Modeling the Ecohydrologic Role of Solar Radiation on Catchment Development in Semiarid Ecosystems

Omer Yetemen

A dissertation
submitted in partial fulfillment of the
requirements for the degree of

Doctor of Philosophy

University of Washington
2014

Reading Committee:
Erkan Istanbulluoglu, Chair
Alison Duvall
Joseph Wartman

Program Authorized to Offer Degree:
Civil and Environmental Engineering

University of Washington

Abstract

Modeling Ecohydrologic Role of Solar Radiation
on Catchment Development in Semiarid Ecosystems

Omer Yetemen

Chair of the Supervisory Committee:
Associate Professor Erkan Istanbulluoglu
Department of Civil and Environmental Engineering

The role of solar radiation on ecohydrologic fluxes, vegetation dynamics, species composition, and landscape morphology has long been documented in field studies. However, these studies miss the value offered by a numerical modeling approach that integrates a range of ecohydrologic and geomorphic processes in exploring the landscape response to multiple controlling factors. This study represented flood generation and solar-radiation-driven echydrologic dynamics in a landscape evolution model (LEM) to investigate how ecohydrologic differences caused by differential irradiance on opposing hillslopes manifest themselves on the organization of modeled topography, soil moisture, and plant biomass. We use the CHILD (Channel-Hillslope Integrated Landscape Development) LEM equipped with a spatially-distributed solar-radiation component, leading to spatial patterns of soil moisture; a vegetation dynamics component that explicitly tracks above- and below-ground biomass; and a runoff component that allows for runoff-runon processes along landscape flow paths.

This study starts with data analysis, and then followed by a modeling part. In the first part, the relationship between land surface properties (e.g. soil, vegetation, and lithology) and landscape morphology quantified by the catchment descriptors: the slope-area (S-A) relation, curvature-area (C-A) relation, and the cumulative area distribution (CAD), in two semiarid

basins in central New Mexico. All three land surface properties were found to have significant influences on the S-A and C-A relations, while the power-law exponents of the CADs for these properties did not show any significant deviations from the narrow range of universal scaling exponents reported in the literature. Among the three different surface properties we investigated, vegetation had the most profound impact on the catchment descriptors.

Following data analysis, the role of solar radiation on landscape morphology was investigated in the second part with a numerical model framework that integrated a range of ecohydrologic and geomorphic processes. Modeled spatial patterns of soil moisture confirmed empirical observations at the landscape scale as well as other hydrologic modeling studies. The spatial variability in soil moisture was controlled by aspect prior to the wet season (North American Monsoon, NAM), and by the hydraulic connectivity of the flow network during the NAM. Aspect and network connectivity signatures were also manifested on plant biomass with typically denser vegetation cover on north-facing slopes than south-facing slopes. Over the long-term, CHILD gave slightly steeper and less dissected north-facing slopes, more dissected south-facing slopes, and overall asymmetry in the modeled morphology of valleys. Aspect influence on hillslope asymmetry was enhanced with greater uplift rates. Model simulations showed how subtle differences in biomass and soil moisture dynamics at annual scales lead to distinct geomorphic differences at both hillslope and catchment scales.

The controls of latitude and mean annual precipitation (MAP) on the development of hillslope asymmetry were investigated in the third part by using the CHILD LEM. In simulations the mean slope of north-facing slopes was steepened towards the poles, while south-facing slopes became gentler toward the poles. As a result of this inverse pattern, the relative differences between north- verses south-facing slopes become larger toward the poles. The model outcomes,

which are compatible with field observations, show north-facing slopes to be steeper (shallower) than south-facing slopes in the northern (southern) hemisphere. Our results underscore the influence of solar radiation as a global control on the development of hillslope asymmetry. Variations in MAP at the same latitude have little impact on hillslope asymmetry in comparison to variations in latitude at the same MAP.

In the last part, the observed spatial patterns in erosion rates caused by aspect-driven microclimatic and ecohydrologic conditions are examined with the CHILD LEM forced with a uniform uplift rate obtained by averaging the erosion estimates from the study site. Climate represented in the model ranges from simple to more realistic. The climate forcing is simulated by: (1) stationary climate represents the recent climate that prevails in the study site; (2) cyclic climate represents the late Pleistocene climate that prevailed in the region; (3) paleo-constructed climate based on paleoclimate proxies. Recent field study in central New Mexico shows that long-term erosion rates (~10,000 years) on south-facing slopes are faster than opposing north-facing slopes. However, CHILD simulations show that the discrepancy in erosion rates on opposing hillslopes is not sustainable over the long-term. Depending on the climate forcing or internal dynamics of erosion mechanism, either north- or south-facing slopes can be more erosive than their counterparts. Over the long-term, however, the fluctuations in spatial erosion rates are averaging out. Hence, under a given uniform uplift, erosion rates on opposing hillslopes are found to be the same.

ACKNOWLEDGEMENTS

I would like to thank my academic advisor Dr. Erkan Istanbulluoglu for his never-ending great support since 2006. His guidance, thoughtful insights, enthusiasms and also patience helped me to accomplish my study and to follow my research passion at the University of Washington.

I am grateful to my committee members, Dr. Alison Duvall, Dr. Joseph Wartman, and Dr. David Montgomery for their feedback, support and guidance. I highly appreciated their thoughtful comments that improve the quality of this work. Their opinions and perspectives expanded my horizon. I am very thankful to Dr. Duvall for her mentoring, lectures, and of course, for her great enthusiasm.

I am thankful to Dr. Homero Flores-Cervantes for his mentoring and helping me learn the CHILD model. His guidance and his expertise in CHILD were indispensable. A huge thank you to Homero.

This dissertation benefited substantially from collaborators. Their expertise and suggestions improved the quality of this dissertation. I am thankful to my collaborators, Dr. Enrique Vivoni, Dr. Hugo Gutierrez-Jurado, Dr. Rafael Bras, Dr. Bruce Harrison, and Dr. Fred Philips.

I appreciated the importance of mentorship during my graduate study. I am especially grateful to Dr. Stephen Burges for his guidance and teaching critical thinking.

I am grateful to my officemates (Wilcox-159), former or recent group members (Istanbulluoglu Ecohydrology Research Group), and colleagues (CEE UW): Nicoleta C. Cristea, Ronda L. Strauch, Xiaochi Zhou, Tiejun Wang, Chris D. Frans, Olivia M. Wright, Sai Nuduripati, Gu Wenquan, Zhuoran Duan, Suvi Ahopelto, Domenico Caracciolo, Christina Bandaragoda, Mark Raleigh, Kael Martin, Susan Dickerson-Lange, Brian Henn, Adam K. Massmann, Abbas Hooshmand, and Liz Clark. I am grateful to these wonderful folks for their friendship, eagerness to help and kindness to make easier to spend my life in the Wilcox Hall.

Finally, last but not least, I am very grateful to roommates: Ahmet Keles and Onur Cem Namli for their friendship and support to complete my study at UW. In addition, I want to express my gratitude to my friends that I met in Seattle, WA and Lincoln, NE for their friendship: Mustafa Gungormus, Serkan Kasirga, Utku Baran, Evren Soylu, Meryem Soylu, John B. Ong, Sami Akin, Ufuk Nalbantoglu, Chris Ayriss, John Horvath, Carlos F. Artieda, Hakan Solak, T. Deniz Yucesoy, Sefa Dag, Divya Nudurupati, Suleyman Gulsuner, and Hilal Unal.

I had a wonderful experience during my Teaching Assistantship. I am very grateful to these wonderful colleagues for their encouragement.

I want to express my gratitude to my family for their support.

DEDICATION

This dissertation is dedicated to my adviser *Erkan Istanbulluoglu* and to my friends, *Ronda Little Strauch, Nicoleta Carina Cristea*, *Christopher Donald Frans* and *Sai Siddhartha Nudurupati* for their great support during my PhD journey.

TABLE OF CONTENTS

LIST OF FIGURES

CHAPTER 5

LIST OF TABLES

CHAPTER 1: INTRODUCTION

1.1. Background

Ecologic, hydrologic and geomorphic differences with respect to hillslope orientation have long been recognized by observers. For example, the Hebrew Bible (~ 1,500 BC) describes the ancient Middle Eastern city of Shechem as a hilly country nestled between the vegetated north-facing slope of Mount Gerizim and barren south-facing slopes of Mount Ebal [*Hillel*, 2006]. A large body of literature has examined the influence of hillslope aspect on the spatial distribution of soil temperature [*Shreve*, 1924], soil composition and chemistry [*Butler et al.*, 1986; *Kunkel et al.*, 2011; *Ma et al.*, 2011], soil moisture [*Geroy et al.*, 2011; *Reid*, 1973], vegetation type, composition, and density [*Ayyad and Dix*, 1964; *Cottle*, 1932; *Kutiel et al.*, 1998; *Sternberg and Shoshany*, 2001], runoff fluxes [*Kidron*, 1999], glacier distribution [*Evans*, 2006a; b], and hillslope morphology [*Burnett et al.*, 2008; *Pierce and Colman*, 1986].

The influence of hillslope aspect on soil and vegetation is most profound in water-limited ecosystems where soil moisture is a critical limiting factor to vegetation growth [*Butler et al.*, 1986; *Noy-Meir*, 1973]. Besides variations in vegetation density, in some climates, ecotone shifts are observed among opposing hillslope aspects. Examples include the Fall Creek in western Wyoming, USA, where a thick forest grows on north-facing slopes, as opposed to grass and scattered shrubs on south-facing slopes [*Walker*, 1963]. In central New Mexico, USA, an ecotone shift from co-existing species of Juniper pine and dense black grama on north aspects to creosote bush and sparser fluff grass on south-facing slopes can be observed [*Istanbulluoglu et al.*, 2008].

Besides the vegetation patterns, manifestations of varying solar radiation on landscapes include aspect-dependence in the dominant erosion processes, hillslope gradients, and landscape-scale valley asymmetry [*Churchill*, 1981; *Gutiérrez-Jurado and Vivoni*, 2013; *Istanbulluoglu et al.*, 2008; *Perron and Hamon*, 2012; *Pierce and Colman*, 1986; *Yetemen et al.*, 2010]. Steeper

north-facing slopes than south-facing slopes are commonly observed in the northern hemisphere below the 45 ^{o}N. Geomorphic differences in the opposing slopes have been typically linked to the feedbacks between aspect-modulated vegetation and erosion dynamics [e.g., *Hadley*, 1969; *Parson*, 1988; *Branson and Shown*, 1989]. In arid and semi-arid climates, denser vegetation on north-facing slopes acts to reduce the erosive impact of runoff, leaving soil creep as the dominant form of hillslope sediment transport. Conversely, south-facing slopes, with less dense vegetation cover, tend to incise more rapidly under erosive flows and form dendritic channels. The hypothesis proposed earlier suggested that under a regionally uniform uplift, lack of (abundance of) erosive flows on north- (south-) facing slopes lead to steeper (shallower) hillslope forms [e.g., *Istanbulluoglu et al*., 2008]. Evidence to this hypothesis came from mostly hillslope- and small-catchment-scale studies, which concurrently document ecologic and geomorphic differences between the opposing hillslope aspects [*Carson and Kirkby*, 1972; *Dohrenwend*, 1978; *Pierce and Colman*, 1986; *Istanbulluoglu et al*., 2008].

While hypotheses have been developed to explain differential hillslope evolution and valley asymmetry, however, the only modeling work that addressed this phenomenon was the hillslope profile development experiments of *Kirkby et al*., [1990], where erosivity differences were used to represent erosion on contrasting north- and south-facing slopes. Some of the key modeling challenges remain, as distilled in the following questions: (1) Can we model the differential hillslope development and valley asymmetry using a landscape evolution model, forced by spatially varying solar radiation? (2) What is the role of tectonic uplift and climatic wetness in valley asymmetry? (3) How strong is the relationship between valley asymmetry and latitude?

1.2. Structure of the Dissertation

This dissertation investigates the ecohydrologic role of solar radiation on catchment development in water-limited ecosystems with a data analysis and numerical modeling approach. Chapter 2-5 are self-contained papers, each with its own abstract, conclusions, and references. Chapter 2 has been published as *Yetemen et al*., [2010]. Chapter 3 has been submitted for journal publication [*Yetemen et al*., submitted manuscript]. Chapter 4 and Chapter 5 are planned to be submitted for journal publication

Chapter 2 examines the relationship between land surface properties (e.g. soil, vegetation, and lithology) and landscape morphology quantified by the catchment descriptors: the slope-area (S-A) relation, curvature-area (C-A) relation, and the cumulative area distribution (CAD), in two semiarid basins in central New Mexico. The first site is composed of several basins located in today's desert elevations with mesic north-facing and xeric south-facing hillslopes underlain by different lithological formations. The second site is a mountainous basin exhibiting vegetation gradients from shrublands in the lower elevations to grasslands and forests at higher elevations. All three land surface properties were found to have significant influences on the S-A and C-A relations, while the power-law exponents of the CADs for these properties did not show any significant deviations from the narrow range of universal scaling exponents reported in the literature. Among the three different surface properties we investigated, vegetation had the most profound impact on the catchment descriptors. In the S-A diagrams of the aspect-controlled ecosystems, we found steeper slopes in north-facing aspects than south-facing aspects for a given drainage area. In elevation-controlled ecosystems, forested landscapes exhibited the steepest slopes for the range of drainage areas examined, followed by shrublands and grasslands in all soil textures and lithologies. The influence of functional types of vegetation detected on observed topography provided some initial understanding of the potential impacts of life on the organization of topography. This finding also emphasizes the critical role of climate in catchment development. We suggest that climatic fluctuations that are capable of replacing vegetation communities could lead to highly amplified hydrological and geomorphic responses.

Chapter 3 investigates the role of solar radiation on landscape morphology with a numerical model framework that integrates a range of ecohydrologic and geomorphic processes. Solar radiation has a clear signature on the spatial organization of ecohydrologic fluxes, vegetation patterns and dynamics, and landscape morphology in semiarid ecosystems. Existing landscape evolution models (LEMs) do not explicitly consider the spatial variability in solar radiation as a model forcing variable to study coupled ecohydrologic and geomorphic processes. In this study, a physically-based solar radiation component is introduced to the Channel-Hillslope Integrated Landscape Development (CHILD) LEM, and its vegetation dynamics component is improved with the aim to represent: (1) seasonal soil moisture, evapotranspiration, and vegetation dynamics on opposing north-facing slopes (NFS) and south-facing slopes (SFS); (2) flood frequency and

magnitudes driven by stochastic rainfall input; and (3) differential evolution of landscape morphology on NFS and SFS consistent with observed landforms in a semiarid ecosystem in central New Mexico, located at the Sevilleta National Wildlife Refuge (SNWR). To examine the role solar radiation on modeled vegetation and landform characteristics, we designed a set of comparative LEM simulations driven by spatially uniform and variable solar radiation and a range of uplift rates. Rainfall climatology is represented by a seasonal rectangular pulse Poisson process model. Modeled local soil moisture, evapotranspiration and vegetation dynamics are confirmed against observations at a SNWR Long-term Ecological Research site. Space-time dynamics of modeled soil moisture and vegetation at the landscape scale are verified with respect to commonly observed patterns in other field and modeling studies. It is found that the spatial variability in soil moisture is controlled by aspect prior to the wet season (North American Monsoon, NAM) as a result of aspect-dependent differences in evapotranspiration, and by the hydraulic connectivity of the flow network during the NAM, when soil moisture is ample. Aspect and network connectivity properties are also manifested on modeled vegetation biomass. NFS produced significantly more biomass than SFS. Interestingly, while greater biomass on NFS was observed on steeper hillslopes with smaller contributing drainage areas, SFS biomass increased as a function of growing drainage area, illustrating the varying role of drainage network on vegetation dynamics in relation to aspect. Modeled NFS and SFS morphologies are found consistent with topographic observations: modeled NFS are steeper, smoother, and longer with limited channelization, while SFS are relatively gentler, shorter, and highly dissected with channels. Differential evolution of opposing aspects has led to asymmetric valley development, as is evident in the field catchment. Understanding and modeling the role of solar radiation on coupled eco-geomorphic landscape evolution is critical for interpreting observed geomorphic patterns, and assessing the impacts of past and future climates on landscape response and morphology.

Chapter 4 explores the control of latitude and mean annual precipitation (MAP) on the development of hillslope asymmetry by using a landscape evolution model. Growing observations at the field, catchment, and continental scales across a range of climates and latitudes reveal aspect-controlled patterns in soil properties, vegetation types, ecohydrologic fluxes, and hillslope and valley morphology. These observations could be indicating eco-geomorphic feedback mechanism driven by micro-climatologic differences shaping landscapes in most glacier free land masses. In

this study, we used a landscape evolution model that couples the continuity equations for water, sediment, and aboveground vegetation biomass at each model element. The model is used to explore the control of latitude and mean annual precipitation (MAP) on the development of hillslope asymmetry. In the model, vegetation growth influences the fluvial incision and transport. Hillslope diffusion is assumed independent of vegetation. Our model results suggest that: 1) hillslope asymmetry can emerge from the competition between soil creep and vegetation-modulated fluvial transport, driven by spatial distribution of solar radiation and uniform rainfall. Consistent with the observations of Parsons [1988] and Poulos et al. [2012] modeled hillslope asymmetry (HA) grows toward northern latitudes. North-facing slopes (NFS) get steeper toward the North Pole while south-facing slopes (SFS) get gentler compared to their corresponding values at the 0° latitude. Modeled topography for the 45°N bears the shallowest SFS and the steepest NFS, and therefore the highest hillslope asymmetry for north- and south-facing slopes (HAN-S) for all rainfall regimes. 2) Hillslope asymmetry can emerge from differential vegetation growth, with NFS supporting more vegetation cover than SFS as latitude increases towards north. Differences in the vegetation cover is related to greater rates of evapotranspiration during the fall and winter season on SFS that led to lower initial soil moisture during the beginning of the growing season, and more rapid vegetation decay during senescence. 3) For a given latitude, MAP is found to have minor control on HAN-S in the low to middle latitudes, where wetter conditions promote slope steepening on SFS with denser vegetation growth. In the simulations, mean slopes of the NFS steepen towards the poles, while SFS become gentler toward the poles. As a result of this counteraction, HAN-S values become larger toward the poles. Our results underscore the influence of solar radiation as a global control on the development of hillslope asymmetry. Variations in MAP at the same latitude have little impact on these in comparison to latitudinal variations.

Chapter 5 utilizes a series of numerical model experiments to examine the climatic and ecohydrologic conditions that would lead to the observed spatial patterns in the Holocene erosion rates in central New Mexico. Based on field observations, south-facing slopes are found to be more erosive than north-facing slopes. We used CHILD (Channel-Hillslope Integrated Landscape Development) LEM (Landscape Evolution Model) equipped with solar radiation and vegetation dynamics components. We forced CHILD with uniform uplift rate obtained by averaging the erosion estimates from the study site. The climate forcing is simulated by: (1) as stationary climate

that represents the observed modern climate in the region using the stochastic rainfall model; (2) cyclic climate forcing replicating a late Pleistocene climate that prevailed in the region. These two simulations were used to bring the landscapes to dynamic equilibrium. Once, the landscapes reached the equilibrium, the modeled elevation fields that correspond to the wet period (e.g., Last Glacial Maximum) were output from the model, and used as an input to a third and final set of forcing using dynamic climate forcing based on paleoclimate proxies. The simulations with variable climate show us how the landscape memory of climate variability alters spatial erosion rates, and finally using the reconstructed paleoclimate followed by cyclic climate will illustrate the role of more accurate representation of climate on the spatial patterns of erosion. LEM also showed that the discrepancy in erosion rates on opposing hillslopes is not sustainable over the long-term. Depending on the climate forcing or internal dynamics of erosion mechanism, either north- or south-facing slopes can be more erosive than their counterparts. Over the long-term, however, the fluctuations in spatial erosion rates are averaging out. Hence, under a given uniform uplift, erosion rates on opposing hillslopes are found to be the same.

References

Ayyad, M. A. G., and R. L. Dix (1964), Analysis of Vegetation - Microenvironmental Complex on Prairie Slopes in Saskatchewan, *Ecological Monographs*, *34*(4), 421-442.

Branson, F.A., Shown, L.M., 1989. Contrasts of vegetation, soils, microclimates, and geomorphic processes between north- and south-facing slopes on Green Mountain near Denver, Colorado. United States Geological Survey, Department of the Interior, Water-Resources Investigations Report 89-4094.

Burnett, B. N., G. A. Meyer, and L. D. McFadden (2008), Aspect-related microclimatic influences on slope forms and processes, northeastern Arizona, *J Geophys Res-Earth*, *113*, F03002, doi:10.1029/2007JF000789.

Butler, J., H. Goetz, and J. L. Richardson (1986), Vegetation and soil - landscape relationships in the North-Dakota Badlands, *American Midland Naturalist*, *116*(2), 378-386.

Carson, M. A., and M. J. Kirkby (1972), *Hillslope form and process*, Cambridge University Press, Cambridge, U. K.

Churchill, R. R. (1981), Aspect-Related Differences in Badlands Slope Morphology, *Annals of the Association of American Geographers*, *71*(3), 374-388,

Cottle, H. J. (1932), Vegetation on north and south slopes of mountains in southwestern Texas, *Ecology*, *13*, 121-134.

Dohrenwend, J. C. (1978), Systematic valley asymmetry in the central California Coast Ranges, *Geol. Soc. Am. Bull.*, *89*, 891–900, doi:10.1130/0016-7606(1978)89<891:SVAITC>2.0.CO;2.

Evans, I. S. (2006a), Local aspect asymmetry of mountain glaciation: A global survey of consistency of favoured directions for glacier numbers and altitudes, *Geomorphology*, *73*(1-2), 166-184, doi:10.1016/j.geomorph.2005.07.009.

Evans, I. S. (2006b), Glacier distribution in the Alps: Statistical modelling of altitude and aspect, *Geografiska Annaler Series a-Physical Geography*, *88A*(2), 115-133.

Geroy, I. J., M. M. Gribb, H. P. Marshall, D. G. Chandler, S. G. Benner, and J. P. McNamara (2011), Aspect influences on soil water retention and storage, *Hydrol Process*, *25*(25), 3836-3842, doi:10.1002/Hyp.8281.

Gutiérrez-Jurado, H. A., and E. R. Vivoni (2013), Ecogeomorphic expressions of an aspect-controlled semiarid basin: I. Topographic analyses with high-resolution data sets, *Ecohydrology*, *6*(1), 8-23, doi:10.1002/Eco.280.

Hadley, R.F., 1961. Some effects of microclimate on slope morphology and drainage basin development. United States Geological Survey, Department of the Interior, Geological Survey Research 1961, B32-B34.

Hillel, D. (2006), *The natural history of the Bible: an environmental exploration of the Hebrew scriptures*, Columbia University Press, New York.

Istanbulluoglu, E., O. Yetemen, E. R. Vivoni, H. A. Gutierrez-Jurado, and R. L. Bras (2008), Eco-geomorphic implications of hillslope aspect: Inferences from analysis of landscape morphology in central New Mexico, *Geophysical Research Letters*, *35*, L14403, doi:10.1029/2008gl034477.

Kidron, G. J. (1999), Differential water distribution over dune slopes as affected by slope position and microbiotic crust, Negev Desert, Israel, *Hydrol Process*, *13*(11), 1665-1682.

Kirkby, M. J., K. Atkinson, and J. Lockwood (1990), Aspect, vegetation cover and erosion on semi-arid hillslopes, in *Vegetation and Erosion: Processes and environments*, edited by J. B. Thornes, pp. 25-39, John Wiley and Sons Ltd., Chichester.

Kunkel, M. L., A. N. Flores, T. J. Smith, J. P. McNamara, and S. G. Benner (2011), A simplified approach for estimating soil carbon and nitrogen stocks in semi-arid complex terrain, *Geoderma*, *165*(1), 1-11, doi:10.1016/j.geoderma.2011.06.011.

Kutiel, P., H. Lavee, and O. Ackermann (1998), Spatial distribution of soil surface coverage on north and south facing hillslopes along a Mediterranean to extreme arid climatic gradient, *Geomorphology*, *23*(2-4), 245-256.

Ma, L., L. X. Jin, and S. L. Brantley (2011), How mineralogy and slope aspect affect REE release and fractionation during shale weathering in the Susquehanna/Shale Hills Critical Zone Observatory, *Chemical Geology*, *290*(1-2), 31-49, doi:10.1016/j.chemgeo.2011.08.013.

Noy-Meir, I. (1973), Desert ecosystems: Environment and producers, *Annual Review of Ecology and Systematics*, *4*, 25-51.

Parsons, A. J. (1988), *Hillslope form*, Routledge, London, U. K.

Perron, J. T., and J. L. Hamon (2012), Equilibrium form of horizontally retreating, soil-mantled hillslopes: Model development and application to a groundwater sapping landscape, *J Geophys Res-Earth*, *117*, F01027, doi:10.1029/2011jf002139.

Pierce, K. L., and S. M. Colman (1986), Effect of height and orientation (microclimate) on geomorphic degradation rates and processes, late-glacial terrace scarps in central Idaho, *Geol Soc Am Bull*, *97*(7), 869-885.

Reid, I. (1973), The influence of slope orientation upon the soil moisture regime, and its hydrogeomorphological significance, *Journal of Hydrology*, *19*, 309-321.

Shreve, F. (1924), Soil temperature as influenced by altitude and slope exposure, *Ecology*, *5*, 128-136.

Sternberg, M., and M. Shoshany (2001), Influence of slope aspect on Mediterranean woody formations: Comparison of a semiarid and an arid site in Israel, *Ecological Research*, *16*(2), 335-345.

Yetemen, O., E. Istanbulluoglu, and E. R. Vivoni (2010), The implications of geology, soils, and vegetation on landscape morphology: Inferences from semi-arid basins with complex vegetation patterns in Central New Mexico, USA, *Geomorphology*, *116*(3-4), 246-263, doi:10.1016/j.geomorph.2009.11.026.

CHAPTER 2: THE IMPLICATIONS OF GEOLOGY, SOILS, AND VEGETATION ON LANDSCAPE MORPHOLOGY: INFERENCES FROM SEMI-ARID BASINS WITH COMPLEX VEGETATION PATTERNS IN CENTRAL NEW MEXICO, USA[1]

This chapter expands on Chapter 2 in *Yetemen* [2008] which investigated the influence of vegetation on topography. In this dissertation, I expanded the investigation to include the influence of soil and geology on topography. Figures in this chapter (Figure 2e, Figure 7a, Figure 7b, Figure 10a, Figure 10b) are reproduced in whole or in part from *Yetemen* [2008].

Yetemen, O., 2008. Topographic analysis of landscape morphology in central New Mexico: Influence of hillslope aspect, geology, vegetation. MSc. thesis, University of Nebraska, Lincoln, NE.

[1] This chapter is published as :

Yetemen, O., Istanbulluoglu, E. and Vivoni, E.R. (2010). The implications of geology, soils, and vegetation on landscape morphology: Inferences from semi-arid basins with complex vegetation patterns in Central New Mexico, USA. Geomorphology, 116, 246-263.

Abstract

This paper examines the relationship between land surface properties (e.g. soil, vegetation, and lithology) and landscape morphology quantified by the catchment descriptors: the slope-area (S-A) relation, curvature-area (C-A) relation, and the cumulative area distribution (CAD), in two semi-arid basins in central New Mexico. The first site is composed of several basins located in today's desert elevations with mesic north-facing and xeric south-facing hillslopes underlain by different lithological formations. The second site is a mountainous basin exhibiting vegetation gradients from shrublands in the lower elevations to grasslands and forests at higher elevations. All three land surface properties were found to have significant influences on the S-A and C-A relations, while the power-law exponents of the CADs for these properties did not show any significant deviations from the narrow range of universal scaling exponents reported in the literature. Among the three different surface properties we investigated, vegetation had the most profound impact on the catchment descriptors. In the S-A diagrams of the aspect-controlled ecosystems, we found steeper slopes in north-facing aspects than south-facing aspects for a given drainage area. In elevation-controlled ecosystems, forested landscapes exhibited the steepest slopes for the range of drainage areas examined, followed by shrublands and grasslands in all soil textures and lithologies. In the C-A diagrams, steeper slopes led to a higher degree of divergence on hillslopes and a higher degree of convergence in the valleys than shallower slopes. The influence of functional types of vegetation detected on observed topography provided some initial understanding of the potential impacts of life on the organization of topography. This finding also emphasizes the critical role of climate in catchment development. We suggest that climatic fluctuations that are capable of replacing vegetation communities could lead to highly amplified hydrological and geomorphic responses.

2.1. Introduction

Topography emerges from the competition of various geomorphic processes under the influence of land surface properties such as rock type, soils, and vegetation. Each of these properties vary naturally in space and time and may lead to differential catchment erosion, resulting in differences in the observed morphology of landscapes (Hancock, 2005; Dietrich and Perron, 2006; Cohen et al., 2008). Whereas rock type may be treated as a constant landscape variable over geomorphically significant time scales, it is arguable that soil and vegetation co-evolve with topography under a changing climate through weathering-erosion-deposition cycles and strong interactions with bedrock (Lavee et al., 1998; Waters and Haynes, 2001; Bierman et al., 2005; Monger and Bestelmeyer, 2006; Buxbaum and Vanderbilt, 2007). The role of rock strength on hillslope and basin relief (Schmidt and Montgomery, 1995, 1996) as well as channel profile properties and rates of channel incision (Stock and Montgomery, 1999; Whipple, 2004; Stock et al., 2005) have long been discussed. Little is known, however, about the role of parent material on different process domains within soil-mantled landscapes under the varying influence of soil production and vegetation dynamics.

Soil development over rock is a precondition for the establishment of soil flora and fauna where climate permits. Once established, biota shifts the form of the dominant soil transport mechanisms from physical (Gabet, 2003) to biotic processes on hillslopes (e.g., Gabet, 2000; Gabet et al., 2003). Recent research further demonstrates how strongly biota alters the type and magnitude of sediment transport on hillslopes (Yoo et al., 2005; Roering, 2008) and in channels (Montgomery et al., 1996; Murray and Paola, 2003; Lancaster and Grant, 2006). Soil formation and the establishment of vegetation also dramatically changes hydrological fluxes by accommodating soil moisture and facilitating the formation of subsurface flow paths (Torres et al., 1998; Montgomery and Dietrich, 2002; Montgomery et al., 2002; Ebel et al., 2007a). These soil and vegetation related alterations in hydrology strongly impact the form and magnitude of erosion, sediment transport (Casadei et al., 2003; Ebel et al., 2007b), and deposition (Molina et al., 2009) across the landscape. As a consequence, numerical models of landscape evolution predict a strong dependence of simulated landscape features to mechanisms generating runoff (Ijjász-Vásquez et al., 1992; Tucker and Bras, 1998; Bogaart et al., 2003), soil and vegetation properties (Casadei et al., 2003; Collins et al., 2004; Istanbulluoglu and Bras, 2005), climate change (Rinaldo

et al., 1995; Tucker and Slingerland, 1997), and spatial variability of landscape erodibility (Moglen and Bras, 1995a,b; Gasparini et al., 2004), and show how such differences may be captured by some quantitative catchment descriptors including the slope-area relation and the cumulative area distribution.

While these model predictions offer testable hypothesis for natural landscapes, little has been done to relate the observed landscape morphology to lithology, soils, and vegetation at the basin scale. Some earlier efforts sought connections between hillslope form and spatial patterns of land surface properties in the opposing hillslope aspects in semi-arid climates. These include comparison of aspect-related differences on the morphology of badland slopes (Churchill, 1981) and terrace scarps (Pierce and Colman, 1986). Generally, in soil-mantled landscapes of the northern hemisphere, wetter north-facing slopes were found to be steeper than south-facing slopes, attributed to the denser vegetation cover on north-facing slopes that restrain runoff erosion (Hadley, 1961; Branson and Shown, 1989; Istanbulluoglu et al., 2008). This observation, however, is often reversed in rock slopes where physical weathering processes outpace bioturbation. In a series of small weathering-limited valleys, Smith (1978) documented steeper southwest- and northeast-facing slopes than those of other aspects and attributed this observation to differential rates of weathering in combination with diurnal cycles of moisture retention and rapid heating and cooling. Recently, Burnett et al. (2008) documented steeper south-facing slopes than north-facing slopes in canyon walls of semiarid northern Arizona. In their field site, Burnett et al. (2008) proposed higher rates of weathering of clay minerals on wetter north-facing slopes as a plausible mechanism leading to shallower north-facing slopes.

At the basin scale, Hancock (2005) demonstrated notable impacts of lithology on some catchment geomorphic descriptors such as the slope-area relation, the cumulative area distribution, and basin hypsometric distribution. His analysis also revealed that catchments with heterogeneous lithology have longer hillslopes than their homogeneous counterparts. In addition to lithology, Cohen et al. (2008) related the spatial variability of types of soils to catchment geomorphic descriptors used by Hancock (2005) and others. They argued that at a subcatchment scale the slope-area relation is closely linked to types of soils observed in the field, and presented a new methodology for explicit calculation of the empirical parameters of the slope-area relation at a pixel scale.

The aforementioned studies provide a preliminary empirical basis for the following related questions that remain to be tackled in quantitative geomorphology: (1) How do soils and biota interact with climate and bedrock, and modulate the geomorphic response of a catchment? (2) How do soils and biota alter the time scales of whole landscape geomorphic response? and (3) How will global warming impact sediment yields and landscape form in relation to projected changes in the ecosystem? One way to address these questions empirically is to investigate the associations between the properties of the land surface and topography by conducting spatial analysis of digital maps of elevation, geology, soils, and vegetation in relation to the regional climate history and records of sediment yield. For this purpose, we studied semiarid landscapes in central New Mexico (USA), where hillslope aspect and elevation control the structure of the ecosystem. The slope-area relationship, the curvature-area relationship, and the cumulative distribution of contributing areas are used as quantitative catchment geomorphic descriptors. This paper builds on some of the earlier findings of Istanbulluoglu et al. (2008) in an aspect-controlled ecosystem in central New Mexico.

2.2. Study areas

This study was conducted using two study areas in central New Mexico, with ecosystems characterized by aspect and elevation control.

2.2.1. Study area for the aspect-controlled ecosystems

We examined the role of lithology and aspect on geomorphic descriptors in eight catchments (1.8 km^2 - 12 km^2 in size) located at the foot of the Ladron Peak in the northwestern corner of the SNWR (Sevilleta Wildlife National Refuge) in central New Mexico (Figs. 1a and 1b), with hillslopes primarily oriented north and south (McMahon, 1998; Gutiérrez-Jurado et al., 2006, 2007). Catchments used in this study are within an elevation range of 1500 m – 1900 m. Mean annual precipitation in the region is approximately 250 mm, and ~50% of this precipitation occurs during the North American monsoon (July to September) (Vivoni et al., 2008). Vegetation is distinctly different between the wetter north- and drier south-facing slopes (Dickie-Peddie, 1993; Gutiérrez-Jurado et al., 2007). The north-facing slopes are typically mesic ecosystems with one-seed Juniper (*Juniperus monosperma*) and dense black grama (*Bouteloua eriopoda*), and deeper soils with higher organic matter, $CaCO_3$, silt and clay contents. The south-facing slopes are xeric ecosystems comprised primarily of creosotebush (*Larrera tridentata*), and sparser fluff grass

(*Erioneuron pulchellum*) (McMahon, 1998; Gutiérrez-Jurado et al., 2007). In addition, north-facing slopes are slightly steeper and longer than south-facing slopes, and have planar mid-slopes with rounded and smoother ridges (Fig. 1c). South-facing slopes on the other hand are typically dissected by rills and gullies (Fig. 1d).

Two units of the Sante Fe Group characterize the geology of the selected catchments: the early Pliocene to middle Pleistocene aged the Sierra Ladrones Formation (SLF), consisting of alluvial fan, piedmont slope, floodplain, and axial stream deposits; and early to late Miocene aged the Popotosa Formation (PF). The PF is the deepest unit within the Santa Fe Group, and is typically overlain by the SLF (Bruning, 1973; Green and Johns, 1997).

Because of the dominant control of aspect on the spatial distribution of vegetation and soils in the region (e.g., McMahon, 1998; Gutiérrez-Jurado et al., 2006, 2007), we use aspect as a surrogate variable for ecosystem classification. We classified north, northwest, and northeast aspects as north-facing mesic ecosystems; and south, southeast, and southwest slopes as south-facing xeric ecosystems. East- and west-facing hillslopes are not considered here as these typically contain the boundaries between the two opposing ecosystems. This classification is also adopted because the publicly available digital data sets with ~ 30 m spatial resolution for soils (e.g., US Department of Agriculture, STATSGO) and vegetation (National Land Cover Data, NLCD) cannot adequately distinguish the observed spatial structure of the soils and the ecosystem in these desert elevation of the central New Mexico.

To examine the influence of lithology and aspect on relatively homogeneous surface conditions, we selected seven basins that are individually underlain by the same lithology (either PF or SLF) and have relatively small elevation differences. Four basins were selected to represent the SLF (Qts/Qtf) (Fig. 1b). Among these, three basins are located at a higher elevation range (1711 m to 1920 m), and one at a lower elevation range (1567 m to 1711 m), enabling to investigate the role of elevation on geomorphic descriptors. Throughout the paper, these basins are called the Higher SLF and the Lower SLF, respectively. Three other small basins were selected on the PF (Tp), all between 1628 m and 1789 m elevation (Fig. 1b). In addition to seven homogeneous basins, we selected a basin composed of different lithologies to examine the influence of geologic heterogeneity on the geomorphic descriptors used in this study. This basin is composed of the piedmont-slope facies of the SLF in its headwaters (Qps), Tp and Qts/Qtf in the middle, and valley

border alluvium (Qp) near the outlet, with an elevation range of 1566 m - 1907 m (Fig. 1b). A 10-m Digital Elevation Model (DEM) derived from Interferometric Synthetic Aperture Radar (IfSAR) is used to derive the local slope, aspect, drainage area, and curvature fields in the basins.

2.2.2. Study area for the elevation-controlled ecosystems

We examined the role of lithology, soil, and types of vegetation on geomorphic descriptors in the Upper Rio Salado (URS) basin. The URS basin is located in the Colorado Plateau physiographic region in west-central New Mexico, 70 km west of the SNWR. The basin covers an area of 464 km^2 within an elevation range of 1985 m to 2880 m. Annual rainfall for the growing season varies between 220 mm at lower, and 325 mm at higher elevations of the URS (Caylor et al., 2005; Vivoni et al., 2009). The location, DEM, geology, soil, and vegetation maps of the basin are presented in Fig. 2.

Two geologic units, including the Crevasse Canyon Formation (Kcc) from Upper Cretaceous, and the Paleogene sedimentary units (Tps) form the dominant lithology in the basin (Fig. 2c) (New Mexico Bureau of Geology and Mineral Resources, 2003). The Quaternary alluvium (Qa) largely underlies the main channel. The Kcc covers majority of the lower elevations, followed by the Tps as elevation increases. Middle Tertiary, Oligocene and upper Eocene, sedimentary and volcaniclastic sedimentary rocks (Tvs) are located on the southern boundaries of the study site. Kgm, from upper Cretaceous, represents Gallup sandstone isolated in the lower elevations of the northeastern part of the basin close to the main stem of the river. Lower Oligocene to upper Eocene aged Tlrp represents pyroclastic rocks and ash-flow tuffs of the Datil Group located through the southeastern edges of the study area.

The soil texture information is obtained from the United States Department of Agriculture (USDA) STATSGO database (Soil Survey Staff, 1994). Soil textures in the URS basin include sandy loam, silt loam, and loam. Silt loam and loam have similar surface areas. Silt loam makes up the majority of the northern tributaries, some of which have sandy loam valley bottoms (Fig. 2d). The south-facing tributaries and the higher elevations of north-facing tributaries are covered by loam.

The 1992 National Land Cover Data (NLCD) (28.5 m grid resolution) is used to identify vegetation patterns in the basin (Vogelmann et al., 2001). The NLCD vegetation map was previously used for ecohydrological analysis in the URS (Caylor et al., 2005). Types of vegetation

are greatly impacted by elevation. Shrubs, primarily creosotebush (*Larrea tridentata*), dominate the lowlands (1985m – 2075m); a combination of grasses (galleta, *Hilaria jamesii* and blue grama, *Bouteloua gracilis*) and shrubs cover the mid-elevations (2075m – 2250m); and forests (woodlands of piñon pine, *Pinus edulis*; and one-seed juniper, *Juniperus monosperma*) cover the upper elevations (2250m – 2880m) (Dickie-Peddie, 1993; Caylor et al., 2005) (Fig. 2e).

2.3. Methods: Quantitative measures of catchment morphology

2.3.1. Slope-area (S-A) relation

A power-law relationship between the local slope of a given point on the landscape and its contributing area in the form: $S = k \cdot A^{\theta}$, is widely observed in natural landscapes. In channels, k and θ are referred to as the steepness index and the concavity index, respectively. The concavity index is the gradient (degree of steepness) of the slope-area (S-A) relation in a log-log plot, ($\log(S) = \log(k) + \theta \log(A)$). In fluvial valleys, most θ values fall in the range between -0.4 and -0.7, although values as low as -0.1 are not uncommon for low-relief alluvial systems and badlands (Howard, 1980; Tarboton et al., 1992). This relationship has been widely used to examine the observed and modeled river profiles in relation to process-based theory (Snow and Slingerland, 1987; Sklar and Dietrich, 1998; Whipple and Tucker, 2002; Whipple, 2004; Gasparini et al., 2007), the impacts of variable rock uplift and rates of erosion (Wobus et al., 2006), and landscape relief (Willgoose, 1994).

The parameters of the S-A relation have been related to the dominant form of sediment transport process in the basin, which can be theoretically described by a geomorphic transport law (GTL). In GTLs, sediment detachment and transport are often represented as a function of certain topographic variables (e.g., slope, curvature, drainage area), and constants that implicitly lump together the role of climate, soils, vegetation, and lithology. In transport-limited soil-mantled landscapes with loose sediments, the long-term average transport of sediment can be described by the following generic GTL, which can be used, with proper parameter values, for modeling fluvial and soil creep transport:

$$Q_s = KA^m S^n \quad , \qquad (1)$$

where Q_s is sediment flux [MT^{-1}]; A is basin drainage area [L^2], S is local slope [L/L] and K is an empirical transport efficiency coefficient that lumps the influence of climate, vegetation,

hydrology, and lithology [$MT^{-1}L^{-2m}$]. The parameters m and n vary with different form of erosion (Kirkby, 1971; Montgomery, 2001). For soil creep m=0 leading to a slope-dependent GTL for hillslopes. Fluvial processes often take m>1 and n>1. A theoretical basis for the slope-area relation was described as the following (Tarboton et al., 1992; Willgoose et al., 1991). If the long-term average rate of denudation (D) is equal everywhere in the basin, the sediment flux in the basin for a given A is:

$$Q_s = D \cdot A. \qquad (2)$$

In a transport-limited landscape, S adjusts to A such that sediment transport capacity is just equal to total sediment flux, leading to a power-law relationship for S (Tarboton et al., 1992):

$$S = kA^{\theta}, \quad k = \left(\frac{D}{K}\right)^{\frac{1}{n}} \quad \theta = \frac{(1-m)}{n}. \qquad (3)$$

Sediment transport in soil-mantled hillslopes where runoff is not erosive is characterized by a transport-limited slope-dependent diffusive process with m = 0. This leads to a positive relationship between S and A ($\theta > 0$), suggesting a convex hillslope morphology (e.g., McKean et al., 1993). For fluvial sediment transport, m and n > 1, in which case (3) predicts an inverse relationship for S with A ($\theta < 0$), representing a concave upward channel profile. Some degree of dependence of these process coefficients on vegetation properties (Gabet and Dunne, 2003; Istanbulluoglu and Bras, 2005), soils (Cohen et al., 2008), and geology (Moglen and Bras, 1995a,b; Hancock, 2005) have been proposed.

2.3.2. Curvature-area (C-A) relation:

Corollary to the slope-area scaling, landscape curvature (i.e. Laplacian of elevation z, $\nabla^2 z$) is another useful measure for the interpretation of dominant sediment transport processes on the landscape (Bogaart and Troch, 2006; Istanbulluoglu et al., 2008; Tarolli and Dalla Fontana, 2009). Total curvature is defined as the sum of planform ($\partial^2 z/\partial x^2$) and profile ($\partial^2 z/\partial y^2$) curvatures:

$$\nabla^2 z = \left(\frac{\partial^2 z}{\partial x^2} + \frac{\partial^2 z}{\partial y^2}\right). \qquad (4)$$

Planform curvature represents the degree of divergence or convergence perpendicular to flow direction. Profile curvature represents the convexity or concavity along the flow direction. In

general terms, divergent-convex landforms ($\nabla^2 z<0$) are formed by hillslope diffusion, while concave-convergent landforms ($\nabla^2 z>0$) result from fluvial sediment transport.

2.3.3. Cumulative area distribution (CAD):

As the third quantitative measure, we used the cumulative distribution of contributing areas in the form of an exceedance plot, calculated as: $P(A \geq a) = n/N$, where n is the number of pixels with contributing area greater than or equal to a selected contributing area, a, and N is the total number of pixels in the basin. This distribution was pioneered by Rodríguez-Iturbe et al. (1992) to examine the aggregation structure of river basins, who showed that the shape of the distribution on a log-log plot forms a straight line following a power-law equation as:

$$P(A \geq a) \propto a^{-\beta} \qquad (5)$$

where, β is scaling exponent often ~0.43 regardless of the type of climate, vegetation, soil, and rock that form the river network (Rodríguez-Iturbe et al., 1992).

2.4. Results

2.4.1. Landform analyses in aspect-controlled ecosystems

First, we use the geomorphic catchment descriptors to investigate relations between landscape morphology and lithology in the SNWR basins. This step is critical to illustrate the background control of lithology at the basin scale before analyzing the role of soils and vegetation at the hillslope scale. The slope-area (S-A) and curvature-area (C-A) relations, and the cumulative area distributions (CAD) of the SNWR basins underlain by the SLF (at two different elevation ranges), the PF, and a heterogeneous lithology are given in Figs. 3 and 4, respectively.

The PF slopes are much steeper than the Lower SLF (difference as high as 0.1 m/m) for the entire range of areas plotted, while the heterogeneous basin, a hybrid of both formations as well as one other formation, plots between the two homogeneous lithologies. The PF and Lower SLF basins are within a very close elevation range, share similar vegetation patterns, and climate. Therefore, we treat the observed differences in the S-A relations as an indication of lithological control on basin morphology.

Up to four different scaling regimes may be observed in a S-A relation (Ijjasz-Vasquez and Bras, 1995; Tucker and Bras, 1998; McNamara et al., 2006). Region I with a positive S-A gradient

(θ>0) corresponds to hillslopes with lower drainage areas where sediment is dominantly transported by soil creep. Fluvial transport overwhelms hillslope diffusion in region II (Ijjasz-Vasquez and Bras, 1995). The steepest slopes on the landscape are located in the boundary between region I and II, where diffusive processes give way to fluvial erosion, marking the location of the valley head. The channel head with definable banks often begins somewhere down the valley with greater contributing areas and lower slopes than the valley head (Montgomery and Foufoula-Georgiou, 1993; Montgomery and Dietrich, 1994). In some landscapes, channels are distinguished by a reduction in the gradient of the S-A relation (Ijjasz-Vasquez and Bras, 1995).

According to the S-A relation in Fig. 3a, valleys begin with a smaller contributing area (~ 300 m^2, location indicated by X) in the PF basin than the lower SLF basin (~ 600 m^2, location indicated by a vertical line), while the turn-over point of the S-A relation of the heterogeneous basin appears between the two homogeneous counterparts. In all basins, the transitions from hillslopes to valleys are manifested by a change in the sign of landscape curvature (Fig. 3b). This suggests a change of the landscape form from convex to concave topography at the valley head. Interestingly, in each basin, change in the sign of curvature is marked with a smaller contributing area than that identified at the point of slope-area turnover, designated by the vertical line for the SLF basins. This may indicate that profile concavity begins slightly downslope of the point where valley planform becomes converging (Eq. 4), resulting in a higher drainage area at the S-A turnover.

Based on our experience in this landscape, channels begin farther down the valley head, and, therefore, the S-A turnover in Fig. 3a does not correspond to the location of channel heads (Istanbulluoglu et al., 2008). To identify and compare the channels among different lithologies, first, we look for a reduction in the gradient of the fluvial portion of the S-A relation as reported in the literature (e.g., Ijjasz-Vasquez and Bras, 1995). Although not very clear, some evidence of that exists in all of the SNWR basins except the Higher SLF. To more closely examine and identify channels theoretically, we relate the S-A relation to the CAD of these basins, as the straight portion of a CAD in a log-log domain designates channels (Fig. 4). CADs of the Higher and the Lower SLF and the heterogeneous basins follow a straight line for areas greater than 2×10^3 m^2 (Figs. 4a, b, d), while the straight portion of the distribution for the PF basin begins with a smaller area value ~1000 m^2 (Fig. 4c). The exponent of a power function fitted to the straight portions of the CADs is nearly identical ~0.43, to the universal value of Rodríguez-Iturbe et al. (1992). When demarked

on the area axis of Fig. 3a (the vertical line at ~2000 m^2 for SLF basins and the letter Y for the PF basin), however, these area thresholds do not correspond to any direct gradient changes in the S-A relations. This may indicate that, the accumulation structure of channels does not leave a clear signature on the S-A relation of the basins developed from binned average data. It is conceivable that this suggests a transitional topographic state such that the landscape is either responding to changes in the external forcing or still incising the alluvial fan that formed the initial condition to the SNWR basins.

To examine the geomorphic impacts of the observed aspect-dependent ecosystem and soil patterns in the SNWR, next, we constrain the S-A and C-A relations to north- and south-facing slopes of the basins in the SLF (Lower basin in Figs. 5a, c; Higher basin in Figs. 5b, d); the PF (Figs. 5e, g), and the heterogeneous lithology (Figs. 5f, h). The analyses are limited to hillslopes (<0.1 km^2) within the selected basins, as the opposing north and south facing hillslopes drain into an east-flowing drainage network. Because of that, the comparisons presented in Fig. 5 are largely limited to low-order channels and headwater valleys in the basins studied in the SNWR.

The plots reveal slightly higher north-facing slopes than south-facing slopes (Figs. 5a, b, e, f) across all lithologies and elevation ranges. For the plotted bin ranges, 71% and 61% of the opposing average slopes have different means at α=0.05 and α=0.01 significance levels, respectively. These subtle but statistically significant differences in slopes are reflected on the C-A relationship. Compared to south-facing slopes, north-facing aspects show slightly higher positive curvature on ridges and higher negative curvature in valleys (Figs. 5c, d, g, h). The differences are statistically significant in 61% (α=0.05) and 45% (α=0.01) of the plotted average curvature data.

Some distinguishable features also occur in the form of the S-A relation of the opposing slopes. A flat region is apparent in the north-facing slopes of the Lower SLF between ~200 m^2 and ~600 m^2 (Fig. 5a), and Higher SLF between ~300 m^2 and ~1100 m^2 (Fig. 5b). This implies planar hillslope morphologies between these area limits on north-facing slopes, consistent with our field observations in the region (Fig. 1c). On south facing slopes such a flat region does not exist and the transition from a positive to a negative θ occurs at smaller drainage areas. As in the case of lithological comparisons, aspect related soils and vegetation differences seem to have a similar

impact on the S-A relations, mediating the slope steepness, valley head positions, and the form of hillslope-valley morphology.

2.4.2. Landform analyses in elevation-controlled ecosystems

2.4.2.1. Individual comparisons of land surface properties and the URS topography

Figs. 6, 7, and 8 illustrate the S-A and C-A relations, and the CAD for the URS basin areas grouped with respect to only lithology, soil, and vegetation, respectively. In all S-A relations, the vertical lines at 900 m^2 and 9000 m^2 designate the three S-A scaling regions, visually defined based on change in the gradient of the S-A relations for Kcc and Tps formations. These formations occupy 55% and 23% of the entire basin area, respectively; while a large fraction of the remaining 22% is occupied by four other lithologies

A clear separation exists among the S-A relations in Fig. 6a. Erosionally resistant volcaniclastic unit Tvs (Chamberlin et al., 1994), shows the highest slopes in the plotted area range, especially in regions I and II, followed by Tlrp. Both lithologies are located in the southern basin divide at high elevations. In addition to rock strength, the steeper slopes of Tvs and Tlrp lithologies may also be related to fault activity. The Red Lake Fault (see RLF in Fig. 2.c) runs through the southeastern boundary of the basin (Chamberlin et al., 1994; Green and Jones, 1997). Stratigraphically located beneath the Kcc formation, the Kgm formation is the third steepest lithology following Tvs and Tlrp, especially in regions I and II. In Region III, the S-A relation of the steeper lithologies blend into each other. These altogether cover approximately 9.7% of the basin area. The shallowest slopes in Fig. 6a belong to Qa (Quaternary Alluvium), confined in the main channel and several tributary basins in the headwater regions of the URS basin. It is likely that the highly erodible nature of the non-cohesive alluvial deposits lead to the observed shallow slopes, as in Eq. (4), a higher value of the transport coefficient K leads to a smaller k (steepness index), and as a result, a lower S. Finally, the two dominant lithologies, Kcc and Tps, not directly associated with faulting, show subtle differences in the S-A relations, with an identical concavity index ($\theta \cong -0.15$) in region III.

Next, we discuss the influences of soil texture on catchment descriptors. In the URS basin, loam occupies much steeper regions on the landscape than silt loam and sandy loam (Fig. 7a). Loam areas are dominantly underlain by Kcc and Kgm lithologies in the northern flank of the basin, and Tvs and Tlrp formations in the southern catchment boundary. Because of the underlying

resistant lithology and proximity to the RLF, the southern region contributes significantly to the overall steepness of the loam S-A plot. The opposite is true for silt loam which lies in less steep regions that contain Qa and Tps lithologies, resulting in shallower slopes and a smaller concavity index than those of loam. Plotting separately the major rock types that underlie the silt loam surface, we identified that the lower θ is caused by the headwater regions of the main channel dominated by Qa lithology which has a nearly flat S-A relation in region III (Fig. 6a). When this highly erodible region is excluded in the S-A plot of silt loam, θ becomes ~-0.15 for silt loam underlain by Tps, consistent with loam regions but with shallower slopes (figure not presented).

Following geology and soil texture, we repeat the same analysis for types of vegetation (Fig. 8). The S-A scaling regimes of the three vegetation species can be clearly distinguished from one another in Fig. (8a). For all ranges of areas from ridges to large valleys, forests show the steepest binned average slopes followed by shrubs and grasses, respectively. The S-A relations for areas less than about 0.6 km^2 are approximately parallel on the log-log plot and the transitions between scaling regimes (from I to II, and II to III) occur at approximately identical drainage areas for each type of vegetation. The θ indices of the plotted S-A relations are: θ=0.44 in region I, θ=-0.33 in region II, and θ=-0.16 in region III. The steepness index, k (Eq. 3), however, changes from grasslands to forests up to twofold in all regions. From a theoretical standpoint, these findings suggest that differences in the type of vegetation do not influence the nonlinear dependence of geomorphic processes to A and S within a given scaling region, but do influence the transport efficiency coefficient K in (Eq. 1). This theoretical interpretation emphasizes the conclusions of Dietrich and Perron (2006) and suggests that same morphologies may exist under different vegetations, but with slightly different scaling properties.

In the curvature-area (C-A) diagram (Fig. 8b), forests show the highest ridge divergence and valley convergence, followed by shrublands. Grasslands have the least divergent ridges and least convergent valleys. We attribute this pattern to variations in the steepness index, k. The larger k observed in forests implies a higher rate of change in gradient along hillslopes and valleys, leading to higher values of curvature across the forest landscape (Eq. 5). In contrast, a smaller k in grasslands would lead to a lower rate of slope change with area indicating a lower curvature on hillslopes and valleys.

A consistent observation in all C-A relations is that, the properties of the land surface that plot steeper throughout all three regions of the S-A relation exhibit a higher degree of ridge divergence in region I, and a higher degree of convergence in regions II and III of their corresponding C-A relations than other groups. This can be clearly observed in Kcc-Tps, loam-silt loam, and forest-shrub-grass comparisons (Figs. 6b, 7b, 8b). Typically, regardless of the surface property examined, the C-A relations show fairly constant gradients in regions I and II; while in region III, they dip down remarkably and reach a global maximum around 5×10^5 m^2. Beyond this point, curvature gradually increases with area. Interestingly, this global maximum in the binned average C-A data does not have a signature in the S-A relation of the basins.

The CADs of all groups follow a power-law function beginning with drainage areas slightly larger than the area threshold for region III in the respective S-A relations. The power-law exponents of the CAD for grasses and shrubs are very close and well within the universal range reported in the literature, while the trees exponent is slightly larger (Fig. 8c).

2.4.2.2. Interactive comparisons of land surface properties and the URS topography

The analyses presented thus far focused on examining the impacts of different types (e.g., tree, grass, shrub) of a given surface property (e.g., vegetation) on some catchment geomorphic descriptors. In reality, landscape morphology emerges from the intertwine linkages among lithology, soils, and vegetation through numerous biotic and abiotic processes forced by climate and tectonics. Here, we propose to compare the S-A relations of different types (e.g., forest, grass, shrub) of a selected landscape surface property (e.g., vegetation) within a domain where the other two types of land surface property remain fixed (e.g., soil: loam; lithology: Kcc). We do this by constraining the coverage of the study domain to the overlapping regions of the two fixed types of land surface property (e.g., soil: loam; lithology: Kcc), and plotting the S-A relation of the different types of the third land surface property observed within that domain (e.g., vegetation: forest, grass, shrub). A combination of these different types of land surface properties will be called a land surface group (LSG) in the remainder of the paper. In this section, we only used Kcc and Tps lithologies in the URS basin. These lithologies underlie approximately 78% of the entire basin area, are away from local faults located in the upper portions of the basin, and their S-A relations do not visually present any significant disparities (Fig. 6a).

First, we investigate the influence of soil texture followed by vegetation. In the left panel of Fig. 9, we plot the S-A relations for types of soil textures only within the basin areas characterized by Kcc geology; and grass (Fig. 9a), shrub (Fig. 9c), and forest (Fig. 9e) vegetation, respectively. In the right panel, the same is repeated for Tps lithology (Figs. 9b, d, f). In the legend of each figure, the areas corresponding to each type of soil textures are given in parenthesis as percentages of the entire basin area. Soil percentages in the Kcc lithology are relatively stable under different types of vegetation, but significantly variable in Tps. Consistently in each LSG, loam has steeper slopes than sandy and silt loam, especially for areas less than 10^6 m^2.

Next, the S-A relations for different types of vegetation, grouped with respect to Tps and Kcc lithology, are presented in Figs. 10a and 10b, respectively. Here, to examine the impact of grouping with respect to lithology only, we did not include the soil groups in the analysis. A clear separation exists between forests, shrublands, and grasslands in Kcc where each type of vegetation has approximately equal proportions within the domain as reported in the legend of the figure. Because of a strong control of elevation on the spatial distribution of the types of vegetation, forests largely dominate the Tps areas located at higher elevations than Kcc. Lower percentages of shrubs and grasses over Tps lithology, lead to highly fluctuating S-A trends for these types of vegetation in Fig. 10b. It is likely that this causes a mixing of slopes of shrubs and forests in region I. Regardless of lithology and elevation, grasses register the shallowest slopes in the basin.

In order to incorporate the soil groups, next we used the Kcc lithology, because of its moderate slopes and approximately equal percentages of soil texture and types of vegetation. The S-A relations are plotted for forests, grasses, and shrubs located on loam (Fig. 11a), silt loam (Fig. 11b), and sandy loam (Fig. 11c), all within the Kcc lithology. Regardless of soil texture, the binned average slope values increase in the grass, shrub, and forest order very consistently in a wide range of drainage areas plotted. As drainage area grows higher than ~10 km^2, the separation becomes less evident because of the decreasing number of data points within each bin.

Figs. 6 through 11 clearly illustrate the differences in the S-A regions analyzed in relation to landscape lithology, soils, and vegetation. The question that arises here is: which of the LSGs are more influential on the observed landscape morphology as quantified by the S-A relation in this paper? To address this question, we first calculate, for each LSG, the mean landscape slope within all three regions of the S-A relation individually. Then, for LSGs having two identical and one

different type of land surface property, we quantify the impact of the third land surface property by subtracting the mean slopes for each S-A region of the comparing pairs. These differences are used for relative comparisons of types of land surface properties on landscape morphology. In this comparison, we assume that the greater the slope difference between the two types of land surface properties (e.g., forest-grass or loam-silt loam), the higher the impact of that land surface property (e.g., vegetation or soil) on landscape evolution.

To quantify the significance of these results, we test the hypothesis that the mean of the slopes in each S-A region is statistically different (α=0.01 using Student's *t*-test) between any two selected LSGs, having only one type of property different and other two identical. Any LSG occupying lesser coverage than 0.5% of the URS basin is excluded from the analysis. Because large differences in sample sizes of the pairing LSGs, and high variations in slope values over a range of drainage areas in small sample sizes lead to ambiguous results. Statistical comparisons are reported in Table 1. The first column presents the LSGs compared in each row with a heading that specifically identifies the compared types of land surface property. In the subsequent columns, mean slopes and slope differences are reported for S-A regions I, II, and III, respectively. Except one comparison, examining forest-grass difference in silt loam and Tps lithology, all other comparisons are statistically significant at α=0.01.

We summarized the results of Table 1 in Fig. 12 by plotting the means of the slope differences for the comparison of each type of land surface property. In Fig. 12, the LSG composed of Loam-Tps-Forest is excluded due to the proximity of this LSG to the resistant rocks and fault activity to avoid any inequalities in the forcing for topographic development. Fig. 12 clearly suggests that on hillslopes (Region I) a change in the type of soil texture (loam to silt loam) and vegetation (forest to grass) has the highest influence on slope steepness, followed by shrub to grass and forest to shrub comparisons. In region I, the least impact on the difference in mean slope is observed in the lithology comparison (Fig. 6a). In regions II and III, the leading impact of forest to grass and loam to silt loam change on slope difference continued, with the former moving up in the rank. Interestingly, change in lithology from Kcc to Tps gradually became more influential in the S-A relation in regions II and III. Shrub to grass and forest to grass changes had a lower impact, though significant statistically.

2.5. Discussions

2.5.1. Measures of catchment morphology

Analysis of the DEMs and field observations suggest that the development and maintenance of perennial channels require greater drainage areas than those observed where the S-A turnover occurs (Montgomery and Dietrich 1989, 1992; Istanbulluoglu et al., 2003). Consistent with this notion, others showed that the log-log linear portion of the CAD begins with a change in the gradient of the S-A relation usually in region III of the S-A relation of fluvial basins (Ijjasz-Vasquez and Bras, 1995) or in region IV in landslide dominated valleys (McNamara et al., 2006). In our analysis in the SNWR and the URS basins, the log-log linear portion of the CADs begins with drainage areas slightly larger than the area threshold for region III in their corresponding S-A relations, without a pronounced break in the gradient of the S-A relation. Subtle separations occur among the CADs for different surface conditions within a basin as well. The CAD of a region with steeper slopes plots below the CAD of shallower slopes, meaning that the exceedance probability of a given area is higher for regions with lower slopes. This suggests that the land surface properties may influence the constant of the power-law distribution, while the scaling exponent of the distribution remains close to 0.43.

The C-A relations used in this paper reveal two important features. The first of these is a change in the sign of curvature with drainage area that approximately corresponds to the S-A turnover point. This is consistent with the view that the location of the valley head corresponds to a transition from divergent to convergent morphology (Montgomery and Foufoula-Georgiou, 1993). The second interesting observation is a global maximum in the C-A relation within the concave portion of the landscape. Interestingly, the drainage area range corresponding to this point does not seem to have a detectable imprint in the S-A relation. Because the S-A relation illustrates how slopes change along the landscape profile, following the local flow direction, absence of a clear signature of maximum convergence on the S-A relation suggests that the maximum point arguably results from, first an initial increase in planform curvature with drainage area, and a subsequent decrease leading to the point of maximum curvature. In the URS where valleys are relatively small, this may indicate valley narrowing downslope of the valley head, followed by widening after reaching the maximum convergence. This would certainly require a process-based explanation in relation to the observed surface properties of the landscape. For example, impacts

of transitions among geomorphic zones with growing drainage area, such as colluvial-bedrock-alluvial channel transition or migrating headcuts, will need to be examined in the landscape to understand the observed C-A trends. We keep this topic, however, for future investigations.

In aspect- and elevation-controlled semiarid ecosystems, we found close associations between catchment morphology and its underlying lithology, soil, and vegetation cover. These land surface properties were found to impact slope steepness, the valley head position, and the beginning of perennial channels on the landscape. In the SNWR sites, the mesic north-facing slopes are found to be typically steeper with planar morphology in comparison to xeric south-facing slopes, which are shallower and more dissected. The S-A and C-A relations are statistically significant (tested for α=0.01 and α=0.05) in the majority of the plotted data (Fig. 5). The S-A model provides a simple but intuitive way to explain these observed differences. The opposing hillslopes in the SNWR site drain into east-west flowing main channels, where the long-term local rate of erosion in both aspects are expected to be identical, and equal to the lowering rate of the main channel. In Eq. (3), S is inversely proportional to K; therefore, under a constant D, steeper north-facing slopes for a given drainage area would imply a lower K (less active wash erosion). Conversely, shallower south-facing slopes would imply a higher K (more active wash erosion) to maintain a constant D. Under the lack of wash erosion, the steeper and planar north-facing slopes suggest dominance of transport by soil creep. These observations imply a strong ecosystem control on landscape morphology.

In soil-mantled landscapes, fluvial erodibility and hillslope diffusivity in the generic slope-area model (Eq. 3) are determined by soil mechanical and hydrological properties as related to soil texture, functional types and dynamics of vegetation, and other biotic activities such as bioturbation and animal burrowing (e.g., Dietrich et al., 2003). In arid and semiarid regions, hydrology is strongly dictated by spatial patterns and connectivity of vegetation between the bare and vegetated patches of the landscape (e.g., Gutiérrez-Jurado et al., 2007; Mayor et al., 2008). As such, in savanna ecosystems with grass cover (e.g., Juniper pine-grass in Fig. 1c), hillslope runoff, sediment, and nutrient fluxes are often lower than shrublands (e.g., Fig. 1d), with interconnected bare soil patches and higher rates of overland flow (Abrahams et al., 1998; Neave and Abrahams 2002; Wainwright et al., 2000). These views have led to the development of conceptual models of ecosystem function differentiating the landscapes between resource conserving, such as savannas,

versus non-conserving (fragmented shrubby landscapes) in semi-arid climate regimes (Davenport et al., 1998; Reid et al., 1999; Wilcox et al., 2003; Saco et al., 2007). Consistent with these views, the south-facing slopes in the SNWR sites, subject to more erosive runoff, could maintain long-term rates of erosion equal to base-level fall with shallower slopes, while more resistant north-facing slopes, with lower runoff potentials, require higher hillslope gradients to keep up with base-level fall, largely with soil creep transport, which is often much less efficient in removing sediment than transport by soil wash. In a recent paper, Gutiérrez-Jurado et al. (2007) reported differences in soil moisture between the north- and south-facing slopes in the headwater slopes of the Lower SLF (Fig. 1b), illustrating the resource conserving and non-resource conserving roles, respectively. These observations suggest an ecohydrological control on landscape evolution facilitated by hillslope aspect in the SNWR basins.

Application of the S-A model is also helpful for understanding the local dynamics of the tectonic setting. In Fig. 3a, the Higher SLF basins plot the steepest, and the Lower SLF basin plots the shallowest slopes as a function of area (difference up to twofold), while the S-A relations of the PF and the heterogeneous basins appear between the two. Theoretically in Eq. (3), a steeper slope for a given A would suggest a higher D or a smaller K. Under the same lithology, climate, and with approximately 200 m of altitude difference, we do not expect the erodibility parameter K to vary significantly between the Higher and Lower SLF basins. Some regional geology maps show a local fault (Silver Creek Fault) that traverses the foothills of the Ladron Peak (Nimick, 1986). It is conceivable that the steep morphology of the Higher SLF basins results from a local base level dynamics rather than lithology and elevation.

Similar arguments maybe made to interpret the S-A separation observed among different types of vegetation on identical lithology and soil texture in the URS basin (Fig. 11). Greater thresholds of erosion, associated with the soil-binding effects of roots and the additive roughness of understory cover as well as arguably enhanced rates of soil infiltration under semiarid vegetation (e.g., Cerdà, 1998), could naturally lead to lower rates of overland flow and runoff erosion. Several studies have demonstrated, although at field-scale experiments, lower rates of runoff erosion in forested landscapes than shrublands and grasslands (under uniform slopes for all ecosystems) in the southwest USA (e.g., Johansen et al., 2001, Breshears et al., 2003, Allen and Breshears, 1998), which could theoretically lead to the observed separation in the vegetation S-A relations. Forest

ecosystems are typically characterized by higher long-term rates of soil creep because of the bioturbation processes that actively take place in forests (Black and Montgomery 1991; Nash 1994; Roering et al., 2002). Despite this, however, in the nonlinear soil creep equation of Roering et al. (1999), forested hillslopes bear greater critical hillslope gradients for threshold slopes than unvegetated slopes or a laboratory sand pile (Roering et al., 1999, 2001). This indicates that soil slips would occur under shallower hillslope gradients on bare or sparsely vegetated surfaces with interconnected bare patches than forested basins, offering an explanation for the steeper maximum slopes observed at the valley head position of the forests in the URS basin than shrubs and grasses (Figs. 8, 11).

The S-A relations of soil textures clearly show that all other land surface properties being identical, loam slopes are steeper than silt loam slopes in the URS basin (Fig. 9). This provides a landscape-scale evidence for higher erodibility for silt loam than loam. Some empirical data exists to support this finding. Field studies conducted to estimate the erodibility factor for the Universal Soil Loss Equation (USLE) demonstrate that all other soil properties being unchanged (e.g. soil organic matter), soil erodibility decreases as soil texture approaches from silt loam to loam in the soil texture triangle (Wischmeier and Mannering, 1969). Field studies conducted to parameterize the runoff erosion component of the WEPP model also report similar trends for the rill erodibility coefficient of the WEPP model (Flanagan and Livingston, 1995).

The comparisons among LSGs suggest that different types of soil texture, vegetation, and lithological units have a detectable impact on the observed morphology of the basin (Table 1, Fig. 12). Interestingly, changes in soil texture (from loam to silt loam) and vegetation (from forest to grass) have shown the greatest increase on slope steepness in the URS basin, while the impact of lithological change gained significance in the fluvial regions of the S-A relation (regions II and III). The growing influence of lithological change on slopes towards downstream maybe related to changes in the hydrological regime and biological processes tied to sediment thickness on rock with increasing drainage area, modulating both the rates and efficiency of soil creep (Yoo et al., 2005; Roering, 2008), and runoff erosion (Istanbulluoglu, 2009). As such, as the drainage area gets larger, one expects increased local soil loss, leading to thinner regolith, partially exposed bedrock, or development of alluvial soils where sediment carrying capacity of the system drops. As a result, lithological differences within the landscape, especially if the parent material responds

differentially to fluvial processes, will likely manifest themselves in the channel profile geometry. The primary rock types for Kcc and Tps are fine- and medium-grained mixed clastic rock, respectively. As a secondary type of rock, Kcc, includes coal, and Tps includes tuff. According to Green and Johns (1997), the Tps lithology has a tertiary type of rock consisting of limestone, sand, and clay. Based on this, it is plausible that fluvial erodibility of Tps would be slightly higher than Kcc. This interpretation is consistent with the S-A relation of different lithologies (Figs. 6a, 12). Kcc slopes plot steeper than Tps with increasing drainage area, implying a lower erodibility than that of Tps according to the S-A model (Eq. 3). Earlier research has extensively discussed the role of bedrock on the form of channel profiles (Stock and Montgomery, 1999; Whipple, 2004; Stock et al., 2005) and cross-sectional geometry (Montgomery, 2004; Finnegan et al., 2005), however, little is known about its relative role on catchment morphology within the hillslope-valley-channel continuum.

Despite the consistencies of our results both aspect- and elevation-controlled ecosystems, we realized that our data sets were relatively coarse. Recently, in a headwater catchment (~0.1 km^2) located in the Lower SLF, Gutiérrez-Jurado and Vivoni (submitted manuscript) compared the S-A and C-A relations derived from a 1-m LiDAR (Light Detection and Ranging) DEM and the 10-m IfSAR DEM used in this study. Their comparison did not reveal any significant differences between the S-A diagrams of the two products, albeit considerable statistical variations in the C-A relations were found.

In interpreting our results, it is crucial to recognize that a great deal of mismatch occurs among the time scales of rock, soil, and vegetation dynamics of the land surface. Rocks act as the parent material for soils, and over geomorphically significant time scales, they may be considered fixed in space. In our study basins, the alluvial fan deposits of the Sierra Ladrones Formation (SLF) are easily older than ~ 1 million years in the SNWR sites, and the rocks in the URS basin are arguably at least several millions (or possibly more) years old. Soils on the other hand develop over much smaller time scales through interactions with vegetation and climate (e.g., Monger and Bestelmeyer, 2006; Buxbaum and Vanderbilt, 2007). The separations in the S-A and C-A relations conditioned on different types of soil and vegetation raise an important question: Are the observed differences in slope caused by modern aspect- and elevation-induced trends in soils and vegetation patterns, or do relict influences occur in the observed topographic patterns? This question is critical

to advance our understanding of climate change impacts on landscape morphology and rates of erosion. We did not further discuss the role of lithology and soil on the observed topography. We do not have a detailed historical view of the rocks and soils in the region, and soil development and age could be highly dependent on geomorphic position on the landscape. We briefly addressed the vegetation and erosion history of the region, because some historical data make this possible.

2.5.2. Climate fluctuations and its impacts on vegetation, rates of erosion, and topography

In the southwestern United States, the late Pleistocene climate (the last ice age, 30,000 – 13,000 yr BP) was wetter and cooler than in the Holocene (last 11,000 years) and today. During that time, current desert elevations (300 – 1700 m) were covered with piñon-juniper-oak woodlands, while higher elevations, including the elevation range of the URS basin, contained spruce-fir, mixed-conifer, and subalpine forests (Betancourt et al., 1990; Thompson et al., 1993). The transition from glacial to inter-glacial periods around 12,000 yr BP triggered major ecological changes in the region, including migration of sparse piñon woodlands to higher elevations, replacing conifer forests; and the establishment of desert vegetation at the present-day elevations. The modern climate regime was developed ~4,000 years ago, which led to creosotebush establishment in the SNWR (Holmgren et al., 2007) and shrubs and grasses in the lower elevations of the URS.

Strong evidence shows that this climate transition and vegetation change enhanced erosion activity in the region. For example, arroyo formation and cut and fill cycles first began around 8,000 yr BP, and intensified in the past 4,000 years (Waters and Haynes, 2001). Vegetation-erosion interactions under a fluctuating climate regime with wet and dry cycles are believed to have significantly contributed to the arroyo cycles in the southwest United States (e.g., Cooke and Reeves, 1976; Bull, 1997; Istanbulluoglu and Bras, 2006). Rapid erosion still continues in the region with contemporary sediment yields closely matching the late Holocene rates on hillslopes and slightly larger in valleys (Gellis et al., 2004; Bierman et al., 2005).

These observations lead us to the following hypothesis that: the observed differences in the landscape morphology in relation to land surface groups result from climate fluctuations that are capable of replacing vegetation functional types. This hypothesis implies that the S-A differences between forest-shrub-grass comparisons have emerged during the alternating wet-dry periods when forests in the low elevations of the URS basin were replaced by shrubs and grasses; and the trees in the south-facing slopes of the SNWR sites are replaced by shrubs. This hypothesis can be

explained conceptually using the S-A model. If erosion is in balance with soil generation by weathering—shown to hold for at least the late Holocene and today, in the Rio Puerco Basin, north of the Rio Salado (Bierman et al., 2005)—then landscapes adjust such that for a given drainage area, all sites erode at similar rates. This implies that steeper slopes will be needed to erode forested landscapes that may have lower runoff erosion potential than shrublands and grasslands (under uniform slopes for all ecosystems) (e.g., Johansen et al., 2001, Breshears et al., 2003, Allen and Breshears, 1998), in approximately at the same rates as grasslands. The same explanation holds for the desert elevations in the SNWR site, where north- and south-facing aspects are lowered by a master channel.

Our hypothesis does not limit the time scale of climate fluctuations to the last glacial-interglacial cycle (or late Pleistocene-Holocene climate transition). Since the beginning of the Pleistocene, glacial-interglacial fluctuations, driven by the Milankovitch cycles with ~20 - ~ 100 kyr periods, have prevailed with varying frequencies, and have resulted in enhanced rates of sedimentation worldwide (Zhang et al., 2001). For as long as the plants existed in this region, we expect that during each dry period, mesic vegetations developed in the north facing slopes of desert elevations and upper elevations of mountains, while xeric species dominated the south facing slopes as well as low elevation bands of pronounced topographies. These proposed long-term periodic shifts in vegetation patterns and differential erosion/deposition events may also contribute to explaining the observed valley asymmetry in the southwest and western United States (e.g., Istanbulluoglu et al., 2008).

2.6. Conclusions

Associations between observed morphologies of several semi-arid catchments in the southwestern United States and the land surface properties (underlying rock type, soils, and vegetation) were examined. In the study catchments, aspect and elevation had a strong control on the observed vegetation patterns. Basin morphologies were quantified by the following catchment geomorphic descriptors: the slope-area relation, the curvature-area relation, and the cumulative distribution of catchment drainage areas. To facilitate comparisons of the impacts of land surface properties, land surface groups (LSGs) were developed in which all, except one type of land surface property, were kept identical. Examining the differences in the catchment geomorphic descriptors with respect to various LSGs, relative impacts of changes in lithology, soils, and

vegetation types were quantified.

Our analysis revealed dependencies between LSGs and landscape morphology. Earlier research studied the impacts of soils and geology within this context (Hancock, 2005; Cohen et al., 2008). In this study, the influence of functional types of vegetation detected on observed topography, provide some initial understanding of the potential impacts of life on catchment organization. This finding also emphasizes the critical role of climate in the landscape processes. We suggest that climatic fluctuations that are capable of replacing vegetation communities could lead to highly amplified hydrological and geomorphic responses. Consistent with this idea, the continuing high sediment losses from many semi-arid basins in the southwestern United States have been related to the Holocene climate change that caused the re-organization of regional vegetation (Bierman et al., 2005). These findings provide testable hypothesis, and underscore the necessity of numerical models as conceptual frameworks to integrate the dynamics of climate and vegetation with Earth surface processes and examine linkages between ecosystem processes and the evolution of landscapes.

References

Abrahams, A.D., Li, G., Krishnan, C., Atkinson, J.F., 1998. Predicting sediment transport by interrill overland flow on rough surfaces. Earth Surface Processes and Landforms 23, 1087-1099.

Allen, C.D., Breshears, D.D., 1998. Drought-induced shift of a forest-woodland ecotone: rapid landscape response to climate variation. Proceedings of the National Academy of Sciences 95, 14839-14842.

Betancourt, J.L., Van Devender, T.R., Martin, P.S., (Eds) (1990). Packrat middens: the last 40,000 years of biotic change. University of Arizona Press, Tucson, Arizona.

Bierman, P.R., Reuter, J.M., Pavich, M., Gellis, A.C., Caffee, M.W., Larsen, J., 2005. Using cosmogenic nuclides to contrast rates of erosion and sediment yield in a semi-arid, arroyo-dominated landscape, Rio Puerco Basin, New Mexico. Earth Surface Processes and Landforms 30, 935-953.

Black, T.A., Montgomery, D.R., 1991. Sediment transport by burrowing mammals, Marin County, California. Earth Surface Processes and Landforms 16 (2), 163–172.

Bogaart, P.W., Troch, P.A., 2006. Curvature distribution within hillslopes and catchments and its effect on the hydrological response. Hydrology and Eart System Sciences 10, 925-936.

Bogaart, P.W., Tucker, G.E., de Vries, J.J., 2003. Channel network morphology and sediment dynamics under alternating periglacial and temperate regimes: a numerical simulation study. Geomorphology 54, 257-277.

Branson, F.A., Shown, L.M., 1989. Contrasts of vegetation, soils, microclimates, and geomorphic processes between north- and south-facing slopes on Green Mountain near Denver, Colorado. United States Geological Survey, Department of the Interior, Water-Resources Investigations Report 89-4094.

Breshears, D.D., Whicker, J.J., Johansen, M.P., Pinder J, E., 2003. Wind and water erosion and transport in semi-arid shrubland, grassland and forest ecosystems: quantifying dominance of horizontal wind-driven transport. Earth Surface Processes and Landforms 28, 1189-1209.

Bruning, 1973. Origin of the Popotosa Formation, north-central Socorro County, New Mexico. Ph.D. dissertation, New Mexico Institute of Mining and Technology, Socorro, NM.

Bull, W.B., 1997. Discontinuous ephemeral streams. Geomorphology, 19 (3-4), 227-276.

Burnett, B.N., Meyer, G.A., McFadden L.D., 2008. Aspect-related microclimatic influences on slope forms and processes, northeastern Arizona. Journal of Geophysical Research 113, F03002.

Buxbaum, C.A.Z., Vanderbilt, K., 2007. Soil heterogeneity and the distribution of desert and steppe plant species across a desert-grassland ecotone. Journal of Arid Environments 69, 617-632.

Casadei, M., Dietrich, W.E., Miller, N.L., 2003. Testing a model for predicting the timing and location of shallow landslide initiation in soil-mantled landscapes. Earth Surface Processes and Landforms 28, 925-950.

Caylor, K.K., Manfreda, S., Rodriguez-Iturbe, I., 2005. On the coupled geomorphological and ecohydrological organization of river basins. Advances in Water Resources 28, 69-86.

Cerdà, A., 1998. The influence of geomorphological position and vegetation cover on the erosional and hydrological processes on a Mediterranean hillslope. Hydrological Processes, 12, 661-671.

Chamberlin, R.M., Kues, B.S., Cather, S.M., Barker, J.M., McIntosh, W.C., (Eds), 1994. Mogollon Slope, West-Central New Mexico and East-Central Arizona, Forty-Fifth Annual Field Conference. Socorro: New Mexico Geological Society, 335 pp.

Churchill, R.R., 1981. Aspect-related differences in badlands slopes morphology. Annals of the Association of American Geographers 71 (3), 374-388.

Cohen, S., Willgoose, G., Hancock, G., 2008. A methodology for calculating the spatial distribution of the area-slope equation and hypsometric integral within a catchment. Journal of Geophysical Research 113, F03027.

Collins, D.B.G., Bras, R.L., Tucker, G.E., 2004. Modeling the effects of vegetation-erosion coupling on landscape evolution. Journal of Geophysical Research 109, F03004.

Cooke, R.U., Reeves, R.W., 1976. Arroyos and Environmental Change in the American South-West. Clarendon, Oxford, U.K.

Davenport, D.W., Breshears, D.D., Wilcox, B.P., Allen, C.D., 1998. Viewpoint: sustainability of piñon-juniper ecosystems-a unifying perspective of soil erosion thresholds. Journal of Range Management 51, 231–240.

Dickie-Peddie, W.A., 1993. New Mexico Vegetation: Past, Present, and Future. University of New Mexico Press, Albuquerque. 244 pp.

Dietrich, W.E., Perron, J.T., 2006. The search for a topographic signature of life. Nature 439, 411-418.

Dietrich, W. E., Bellugi, D.G., Sklar, L.S., Stock, J.D., Heimsath, A.M., Roering, J.J., 2003. Geomorphic transport laws for predicting the form and dynamics. In: Wilcock, P., Iverson, R. (Eds.), Prediction in Geomorphology. AGU, Washington, D.C., pp. 103-132.

Ebel, B.A., Loague, K., Dietrich, W.E., Montgomery, D.R., Torres, R., Anderson, S.P., Giambelluca, T.W., 2007a. Near-surface hydrologic response for a steep, unchanneled catchment near Coos Bay, Oregon: 1. Sprinkling experiments. American Journal of Science 307, 678-708.

Ebel, B.A., Loague, K., Vanderkwaak, J.E., Dietrich, W.E., Montgomery, D.R., Torres, R., Anderson, S.P., 2007b. Near-surface hydrologic response for a steep, unchanneled catchment near Coos Bay, Oregon: 2. Physics-based simulations. American Journal of Science 307, 709-748.

Finnegan, N.J., Roe, G., Montgomery, D.R., Hallet, B., 2005. Controls on the channel width of rivers: implications for modeling fluvial incision of bedrock. Geology, 33 (3), 229-232.

Flanagan, D.C., Livingston, S.J., (Eds), 1995. WEPP User Summary. NSERL Report No. 11, National Soil Erosion Research Laboratory, West Lafayette, Indiana.

Gabet, E.J., 2000. Gopher bioturbation: field evidence for non-linear hillslope diffusion. Earth Surface Processes and Landforms 25, 1419-1428.

Gabet, E.J., 2003. Sediment transport by dry ravel. Journal of Geophysical Research 108(B1), 2049.

Gabet, E.J., Dunne, T., 2003. A stochastic sediment delivery model for a steep Mediterranean landscape. Water Resources Research 39(9), 1237.

Gabet, E.J., Reichman, O.J., Seabloom, E.W., 2003. The effects of bioturbation on soil processes and sediment transport. Annual Review of Earth and Planetary Sciences 31, 249-273.

Gasparini, N.M., Tucker, G.E., Bras, R.L., 2004. Network-scale dynamics of grain-size sorting: implications for downstream fining, stream-profile concavity, and drainage basin morphology. Earth Surface Processes and Landforms 29, 401-421.

Gasparini, N.M., Whipple, K.X., Bras, R.L., 2007. Predictions of steady state and transient landscape morphology using sediment-flux-dependent river incision models. Journal of Geophysical Research 112, F03S09.

Gellis, A.C., Pavich, M.J., Bierman, P.R., Clapp, E.M., Ellevein, A., Aby, S., 2004. Modern sediment yield compared to geologic rates of sediment production in a semi-arid basin, New Mexico: assessing the human impact. Earth Surface Processes and Landforms 29, 1359-1372.

Green, G.N., Jones, G.E., 1997. The Digital Geologic Map of New Mexico in ARC/INFO Format. U.S. Geological Survey Open-File Report OFR 97-0052, U.S. Geological Survey, Denver, Colorado.

Gutiérrez-Jurado and Vivoni (submitted manuscript). Ecogeomorphic expressions of aspect-controlled semiarid basin: 1. Topographic analyses with high resolution datasets. Journal of Geophysical Research – Earth Surface.

Gutiérrez-Jurado, H.A., Vivoni, E.R., Harrison, J.B.J., Guan, H., 2006. Ecohydrology of root zone water fluxes and soil development in complex semiarid rangelands. Hydrological Processes 20, 3289–3316.

Gutiérrez-Jurado, H.A., Vivoni, E.R., Istanbulluoglu, E., Bras, R.L., 2007. Ecohydrological response to a geomorphically significant flood event in a semiarid catchment with contrasting ecosystems. Geophysical Research Letters, 34, L23S25.

Hadley, R.F., 1961. Some effects of microclimate on slope morphology and drainage basin development. United States Geological Survey, Department of the Interior, Geological Survey Research 1961, B32-B34.

Hancock, G.R., 2005. The use of digital elevation models in the identification and characterization of catchments over different grid scales. Hydrological Processes 19, 1727-1749.

Holmgren, C.A., Norris, J., Betancourt, J.L., 2007. Inferences about winter temperatures and summer rains from the late Quaternary record of C_4 perennial grasses and C_3 desert shrubs in the northern Chihuahuan Desert. Journal of Quaternary Science 22(2), 141-161.

Howard, A.D., 1980. Thresholds in river regimes. In: Coates, D.R., Vitek, J.D. (Eds.), Thresholds in Geomorphology. Allen & Unwin, London, pp. 227–258.

Ijjasz-Vasquez, E.J. Bras, R.L., 1995. Scaling regimes of local slope versus contributing area in digital elevation models. Geomorphology 12, 299-311.

Ijjász-Vásquez, E.J., Bras, R.L., Moglen, G.E., 1992. Sensitivity of a basin evolution model to the nature of runoff production and to initial conditions. Water Resources Research 28(10), 2733-2741.

Istanbulluoglu, E., 2009. An eco-hydro-geomorphic perspective to modeling the role of climate in catchment evolution. Geography Compass 3 (3), 1151-1175.

Istanbulluoglu, E., Bras, R.L., 2005. Vegetation-modulated landscape evolution: effects of vegetation on landscape processes, drainage density, and topography. Journal of Geophysical Research 110, F02012.

Istanbulluoglu, E., Bras, R.L., 2006. On the dynamics of soil moisture, vegetation, and erosion: implications of climate variability and change. Water Resources Research 42, W06418.

Istanbulluoglu, E., Tarboton, D.G., Pack, R.T., Luce, C., 2003. A sediment transport model for incision of gullies on steep topography. Water Resources Research 39 (4), 1103.

Istanbulluoglu, E., Yetemen, O., Vivoni, E.R., Gutiérrez-Jurado, H.A., Bras, R.L., 2008. Ecogeomorphic implications of hillslope aspect: Inferences from analysis of landscape morphology in central New Mexico. Geophysical Research Letters 35, L14403.

Johansen, M.P., Hakonson, T.E., Breshears, D.D., 2001. Post-fire runoff and erosion from rainfall simulation: contrasting forests with shrublands and grasslands. Hydrological Processes 15, 2953-2965.

Kirkby, M.J., 1971. Hillslope process-response models based on the continuity equation. In: Brunsden, D., (Ed.), Slopes, Form and Process. Special Publication 3, Institute of British Geographers, London, pp. 15–30.

Lancaster, S.T., Grant, G.E., 2006. Debris dams and the relief of headwater streams. Geomorphology 82, 84-97.

Lavee, H., Imeson, A.C., Sarah, P., 1998. The impact of climate change on geomorphology and desertification along a Mediterranean-arid transect. Land Degradation and Development 9, 407-422.

Mayor, A.G., Bautista, S., Small, E.E., Dixon, M., Bellot, J., 2008. Measurement of the connectivity of runoff source areas as determined by vegetation pattern and topography: a tool for assessing potential water and soil losses in drylands. Water Resources Research 44, W10423.

McKean, J.A., Dietrich, W.E., Finkel, R.C., Southon, J.R., Caffee, M.W., 1993. Quantification of soil production and downslope creep rates from cosmogenic ^{10}Be accumulations on a hillslope profile. Geology 21(4), 343-346.

McMahon, D.R., 1998. Soil, landscape and vegetation interactions in a small semi-arid drainage basin: Sevilleta National Wildlife Refuge. M.S. thesis, New Mexico Institute of Mining and Technology, Socorro, NM.

McNamara, J.P., Ziegler, A.D., Wood, S.H., Vogler, J.B., 2006. Channel head locations with respect to geomorphologic thresholds derived from a digital elevation model: a case study in northern Thailand. Forest Ecology and Management 224, 147-156.

Moglen, G.E., Bras, R.L., 1995a. The effect of spatial heterogeneities on geomorphic expression in a model of basin evolution. Water Resources Research 31(10), 2613-2623.

Moglen, G.E., Bras, R.L., 1995b. The Importance of spatially heterogeneous erosivity and the cumulative area distribution. Geomorphology 12, 173-185.

Molina, A., Govers, G., Cisneros, F., Vanacker, V., 2009. Vegetation and topographic controls on sediment deposition and storage on gully beds in a degraded mountain area. Earth Surface Processes and Landforms 34, 755-767.

Monger, H.C., Bestelmeyer, B.T., 2006. The soil-geomorphic template and biotic change in arid and semi-arid ecosystems. Journal of Arid Environments 65, 207-218.

Montgomery, D.R., 2001. Slope distributions, threshold hillslopes, and steady-state topography. American Journal of Science 301, 432-454.

Montgomery, D.R., 2004. Observations on the role of lithology in strath terrace formation and bedrock channel width. American Journal of Science 304, 454-476.

Montgomery, D.R., Dietrich, W.E., 1989. Source areas, drainage density and channel initiation. Water Resources Research 25 (8), 1907–1918.

Montgomery, D. R., Dietrich, W.E., 1992. Channel initiation and the problem of landscape Scale. Science 255, 826–830.

Montgomery, D.R., Foufoula-Georgiou, E., 1993. Channel network source representation using digital elevation models. Water Resources Research 29(12), 3925-3934.

Montgomery, D.R., Dietrich, W.E., 1994. Landscape dissection and drainage area-slope thresholds. In: Kirkby, M.J. (Ed.), Process Models and Theoretical Geomorphology, John Wiley & Sons, New York, pp. 221-246.

Montgomery, D.R., Dietrich, W.E., 2002. Runoff generation in a steep, soil-mantled landscape. Water Resources Research 38(9), 1168.

Montgomery, D.R., Abbe, T.B., Buffington, J.M., Peterson, N.P., Schmidt, K.M., Stock, J.D., 1996. Distribution of bedrock and alluvial channels in forested mountain drainage basins. Nature 381, 587-589.

Montgomery, D.R., Dietrich, W.E., Heffner, J.T., 2002. Piezometric response in shallow bedrock at CB1: implications for runoff generation and landsliding. Water Resources Research 38(12), 1274.

Murray, A.B., Paola, C., 2003. Modelling the effect of vegetation on channel pattern in bedload rivers. Earth Surface Processes and Landforms 28, 131-143.

Nash, D.B., 1994. Effective sediment-transporting discharge from magnitude-frequency analysis. Journal of Geology 102 (1), 79–95.

Neave, M., Abrahams, A.D., 2002. Vegetation influences on water yields from grassland and shrubland ecosystems in the Chihuahuan Desert. Earth Surface Processes and Landforms 27, 1011-1020.

New Mexico Bureau of Geology and Mineral Resources, 2003. Geologic Map of New Mexico, 1:500,000: New Mexico Bureau of Geology and Mineral Resources.

Nimick, K.G., 1986. Geology and structural evolution of the east flank of the Ladron Mountains, Socorro County, New Mexico. M.S. Thesis, University of New Mexico, Albuquerque, NM.

Pierce, K.L., Colman, S.M., 1986. Effect of height and orientation (microclimate) on geomorphic degradation rates and processes, late-glacial terrace scarps in central Idaho. Geological Society of America Bulletin 97, 869-885.

Reid, K.D., Wilcox, B.P., Breshears, D.D., MacDonald, L., 1999. Runoff and erosion in a piñon-juniper woodland: influence of vegetation patches. Soil Science Society of America Journal 63, 1869–1879.

Rinaldo, A., Dietrich, W.E., Rigon, R., Vogel, G.K., Rodriguez-Iturbe, I., 1995. Geomorphological signatures of varying climate. Nature 374, 632-635.

Rodríguez-Iturbe, I., Ijjász-Vásquez, E.J., Bras, R.L., Tarboton, D.G., 1992. Power law distributions of discharge mass and energy in river basins. Water Resources Research 28(4), 1089–1093.

Roering, J.J., 2008. How well can hillslope evolution models "explain" topography? Simulating soil transport and production with high-resolution topographic data. Geological Society of America Bulletin 120 (9-10), 1248-1262.

Roering, J.J., Kirchner, J.W., Dietrich, W.E., 1999. Evidence for nonlinear, diffusive sediment transport on hillslopes and implications for landscape morphology. Water Resources Research 35(3), 853-870.

Roering, J.J., Kirchner, J.W., Sklar, L.S., Dietrich, W.E., 2001. Hillslope evolution by nonlinear creep and landsliding: an experimental study. *Geology* 29 (2), 143–146.

Roering, J.J., Almond, P., Tonkin, P., McKean, J., 2002. Soil transport driven by biological processes over millennial time scales. Geology 30 (12), 1115–1118.

Saco, P.M., Willgoose, G.R., Hancock, G.R., 2007. Eco-geomorphology of banded vegetation patterns in arid and semi-arid regions. Hydrology and Earth System Sciences 11, 1717-1730.

Schmidt, K.M., Montgomery, D.R., 1995. Limits to relief. Science 270, 617-620.

Schmidt, K.M., Montgomery, D.R., 1996. Rock mass strength assessment for bedrock landsliding. Environmental and Engineering Geosciences 2, 325-338.

Sklar, L., Dietrich, W.E., 1998. River longitudinal profiles and bedrock incision models: stream power and the influence of sediment supply. In: Tinkler, K.J., Wohl, E.E. (Eds.), Rivers over Rock: Fluvial Processes in Bedrock Channels. AGU, Washington, D.C., pp. 237-260.

Smith, B.J., 1978. Aspect-related variations in slope angle near Béni Abbès, western Algeria. Geografiska Annaler 60 A (3-4), 175-180.

Snow, R.S., Slingerland, R.L., 1987. Mathematical modeling of graded river profiles. Journal of Geology 95, 15-33.

Soil Survey Staff, 1994. State Soil Geographic Database (STATSGO) data users guide. USDA Natural Resources Conservation Service Misc. Publ. 1492, U.S. Government Printing Office, Washington, DC, 88–1036.

Stock, J.D., Montgomery, D.R., 1999. Geologic constraints on bedrock river incision using the stream power law. Journal of Geophysical Research 104 (B3), 4983–4993.

Stock, J.D., Montgomery, D.R., Collins, B.D., Dietrich, W.E., Sklar L., 2005. Field measurements of incision rates following bedrock exposure: Implications for process controls on the long profiles of valleys cut by rivers and debris flows. Geological Society of America Bulletin 117(11-12), 174-194.

Tarboton, D.G., Bras, R.L., Rodriguez-Iturbe, I., 1992. A physical basis for drainage density. Geomorphology 5, 59-76.

Tarolli, P., Dalla Fontana, G., 2009. Hillslope-to-valley transition morphology: New oppurtunities from high resolution DTMs. Geomorphology 113, 47-56.

Thompson, R.S., Whitlock, C, Bartlein, P.J., Harrison, S.P., Spaulding, W.G., 1993. Climatic changes in the western United States since 18,000 yr BP. In: Wright, H.E., Jr., Kutzbach, J.E., Webb, T. III, Ruddiman, W.F., Street-Perrott, F.A., Bartlein, P.J. (Eds.), Global Climates since the Last Glacial Maximum. University of Minnesota Press, St. Paul, MN, pp. 468-513.

Torres, R., Dietrich, W.E., Montgomery, D.R., Anderson, S.P., Loague, K., 1998. Unsaturated zone processes and the hydrologic response of a steep, unchanneled catchment. Water Resources Research 34(8), 1865-1879.

Tucker, G.E., Slingerland, R., 1997. Drainage basin responses to climate change. Water Resources Research 33(8), 2031-2047.

Tucker, G.E., Bras, R.L., 1998. Hillslope processes, drainage density, and landscape morphology. Water Resources Research 34(10), 2751-2764.

Vivoni, E.R., Moreno, H.A., Mascaro, G., Rodriguez, J.C., Watts, C.J., Garatuza-Payan, J., Scott., R., 2008. Observed relation between evapotranspiration and soil moisture in the North American monsoon region. Geophysical Research Letters 35, L22403.

Vivoni, E.R., Aragón, C.A., Malczynski, L., Tidwell, V.C., 2009. Semiarid watershed response in central New Mexico and its sensitivity to climate variability and change. Hydrology and Earth System Sciences 13, 715-733.

Vogelmann, J.E., Howard, S.M., Yang, L., Larson, C.R., Wylie, B.K., Van Driel, N., 2001. Completion of the 1990s national land cover data set for the conterminous United States from Landsat Thematic Mapper data and ancillary data sources. Photogrammetric Engineering and Remote Sensing 67, 650-662.

Wainwright, J., Parsons, A.J., Abrahams, A.D., 2000. Plot-scale studies of vegetation, overlandflow and erosion interactions: case studies from Arizona and New Mexico. Hydrological Processes 14, 2921–2943.

Waters, M.R., Haynes, C.V., 2001. Late Quaternary arroyo formation and climate change in the American Southwest. Geology 29(5), 399-402.

Whipple, K.X., 2004. Bedrock rivers and the geomorphology of active orogens. Annual Review of Earth and Planetary Sciences 32, 151-185.

Whipple, K.X., Tucker, G.E., 2002. Implications of sediment-flux-dependent river incision models for landscape evolution. Journal of Geophysical Research 107(B2), 2039.

Wilcox, B.P., Breshears, D.D., Allen, C.D., 2003. Ecohydrology of a resource-conserving semiarid woodland: effects of scale and disturbance. Ecological Monographs 73 (2), 223–239.

Wischmeier, W.H., Mannering, J.V., 1969. Relation of soil properties to its erodibility. Soil Science Society of America Journal Proceedings. 33, 131-137.

Willgoose, G., 1994. A physical explanation for an observed area-slope-elevation relationship for catchments with declining relief. Water Resources Research 30 (2), 151-159.

Willgoose, G., Bras, R.L., Rodriguez-Iturbe, I., 1991. A coupled channel network growth and hillslope evolution model 1. Theory. Water Resources Research 27 (7), 1671-1684.

Wobus, C., Whipple, K.X., Kirby, E., Snyder, N., Johnson, J., Spyropolou, K., Crosby, B., Sheehan, D., 2006. Tectonics from topography: procedures, promise, and pitfalls. In: Willett, S.D., Hovius, N., Brandon, M.T., Fisher, D.M. (Eds.), Tectonics, Climate and Landscape Evolution. GSA, Boulder, CO, pp. 55–74.

Yoo, K., Amundson, R., Heimsath, A.M., Dietrich, W.E., 2005. Process-based model linking pocket gopher (Thomomys bottae) activity to sediment transport and soil thickness. Geology 33(11), 917-920.

Zhang, P., Molnar, P., Downs, W.R., 2001. Increased sedimentation rates and grain sizes 2–4 Myr ago due to the influence of climate change on erosion rates. Nature 410, 891– 897.

Table 1. Statistical comparison of mean slopes in the slope-area relation of different land surface groups (LSG).

Land Surface Group (LSG)	Average Slope (m/m) Region I[&]			Average Slope (m/m) Region II[&]			Average Slope (m/m) Region III[&]		
Shrub – Grass	LSG. I[@]	LSG. II[@]	Diff[#].	LSG. I	LSG. II	Diff.	LSG. I	LSG. II	Diff.
Loam Kcc Shrub - Loam Kcc Grass	0.166	0.144	0.023	0.186	0.157	0.029	0.133	0.112	0.021
Silt Loam Kcc Shrub - Silt Loam Kcc Grass	0.141	0.119	0.022	0.147	0.118	0.029	0.103	0.086	0.017
Silt Loam Tps Shrub - Silt Loam Tps Grass	0.154	0.131	0.023	0.135	0.083	0.052	0.078	0.052	0.026
Forest - Shrub	LSG. I	LSG. II	Diff.	LSG. I	LSG. II	Diff.	LSG. I	LSG. II	Diff.
Loam Kcc Forest - Loam Kcc Shrub	0.202	0.166	0.036	0.258	0.186	0.072	0.187	0.133	0.054
Silt Loam Kcc Forest - Silt Loam Kcc Shrub	0.148	0.141	0.007	0.169	0.147	0.022	0.124	0.103	0.021
Silt Loam Tps Forest - Silt Loam Tps Shrub	0.137	0.154	-0.016	0.120	0.135	-0.015	0.085	0.078	0.007
Forest - Grass	LSG. I	LSG. II	Diff.	LSG. I	LSG. II	Diff.	LSG. I	LSG. II	Diff.
Loam Kcc Forest - Loam Kcc Grass	0.202	0.144	0.059	0.258	0.157	0.100	0.187	0.112	0.075
Silt Loam Kcc Forest - Silt Loam Kcc Grass	0.148	0.119	0.029	0.169	0.118	0.051	0.124	0.086	0.037
Silt Loam Tps Forest - Silt Loam Tps Grass	0.137	0.131	**0.007**[*]	0.120	0.083	0.037	0.085	0.052	0.032
Kcc – Tps	LSG. I	LSG. II	Diff.	LSG. I	LSG. II	Diff.	LSG. I	LSG. II	Diff.
Loam Kcc Forest - Loam Tps Forest[†]	0.202	0.268	-0.066	0.258	0.314	-0.056	0.187	0.219	-0.031
Silt Loam Kcc Forest - Silt Loam Tps Forest	0.148	0.137	0.011	0.169	0.120	0.048	0.124	0.085	0.039
Silt Loam Kcc Shrub - Silt Loam Tps Shrub	0.141	0.154	-0.012	0.147	0.135	0.012	0.103	0.078	0.025
Silt Loam Kcc Grass - Silt Loam Tps Grass	0.119	0.131	-0.012	0.118	0.083	0.035	0.086	0.052	0.034
Loam - Silt Loam	LSG. I	LSG. II	Diff.	LSG. I	LSG. II	Diff.	LSG. I	LSG. II	Diff.
Loam Kcc Forest - Silt Loam Kcc Forest	0.202	0.148	0.054	0.258	0.169	0.089	0.187	0.124	0.063
Loam Kcc Shrub - Silt Loam Kcc Shrub	0.166	0.141	0.025	0.186	0.147	0.039	0.133	0.103	0.030
Loam Kcc Grass - Silt Loam Kcc Grass	0.144	0.119	0.024	0.157	0.118	0.039	0.112	0.086	0.026
Loam Tps Forest[†] - Silt Loam Tps Forest	0.268	0.137	0.131	0.314	0.120	0.193	0.219	0.085	0.134

[†] May be affected by the resistant units and local fault activity.

[*] Not statistically significant at α=0.05.

[@] LSG I and LSG II, aliases for the LSGs explained in the first column in their respective order.

[#] Diff. refers to slope differences between LSG. I and LSG. II.

[&] Drainage area bands covered by the S-A scaling regions are region I: 900-1,900 m^2; region II: 1,900-9,000 m^2, and region III: 9,000 -200,000 m^2, respectively.

FIGURES

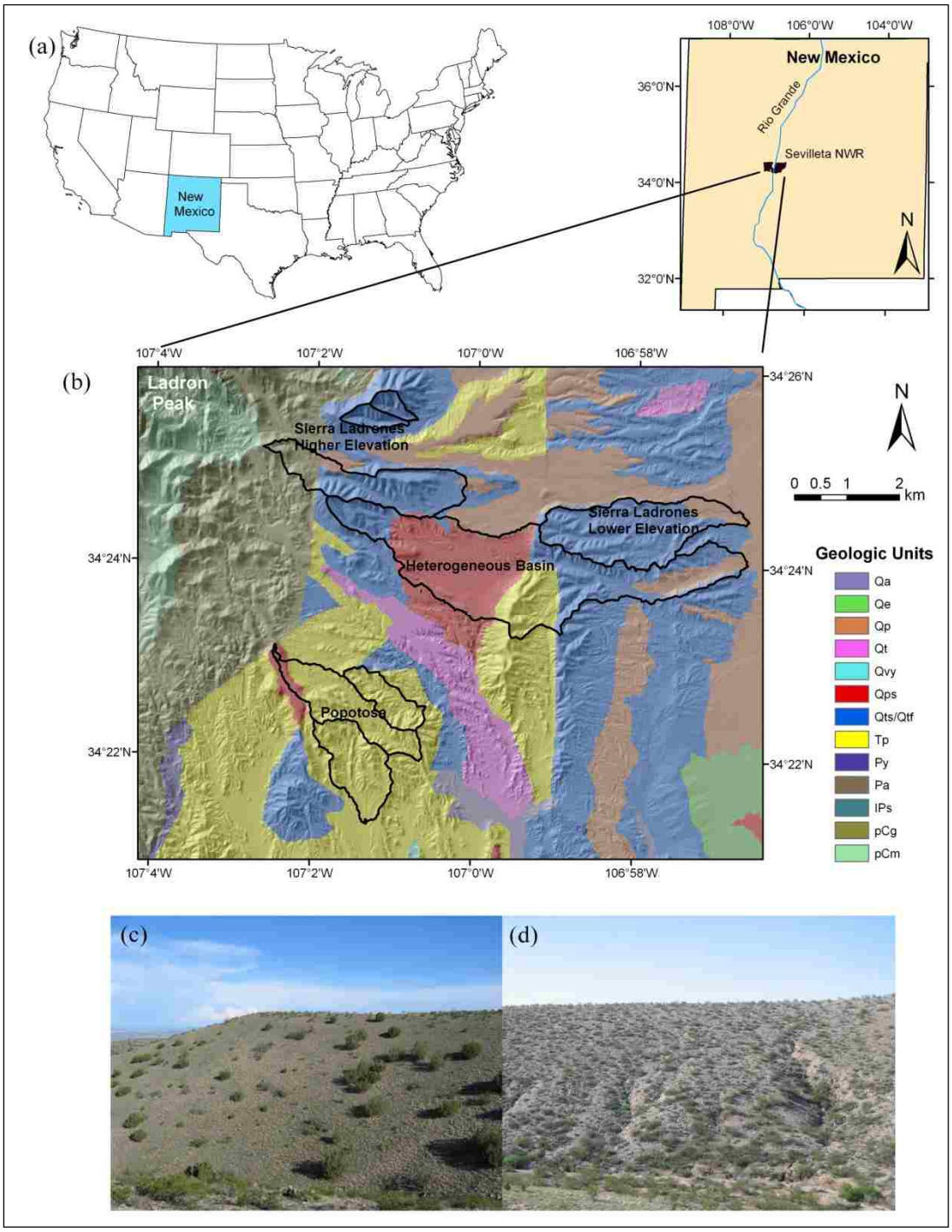

Figure 1. (a) Location map; (b) geology map and the watershed boundaries of the catchments in the Sevilleta National Wildlife Refuge (SNWR) in central New Mexico; (c) a north-facing piñon-juniper and grassland savanna ecosystem with planar hillslope profile; (d) a dissected south-facing slope experiencing active hollow formation through ephemeral gully incision.

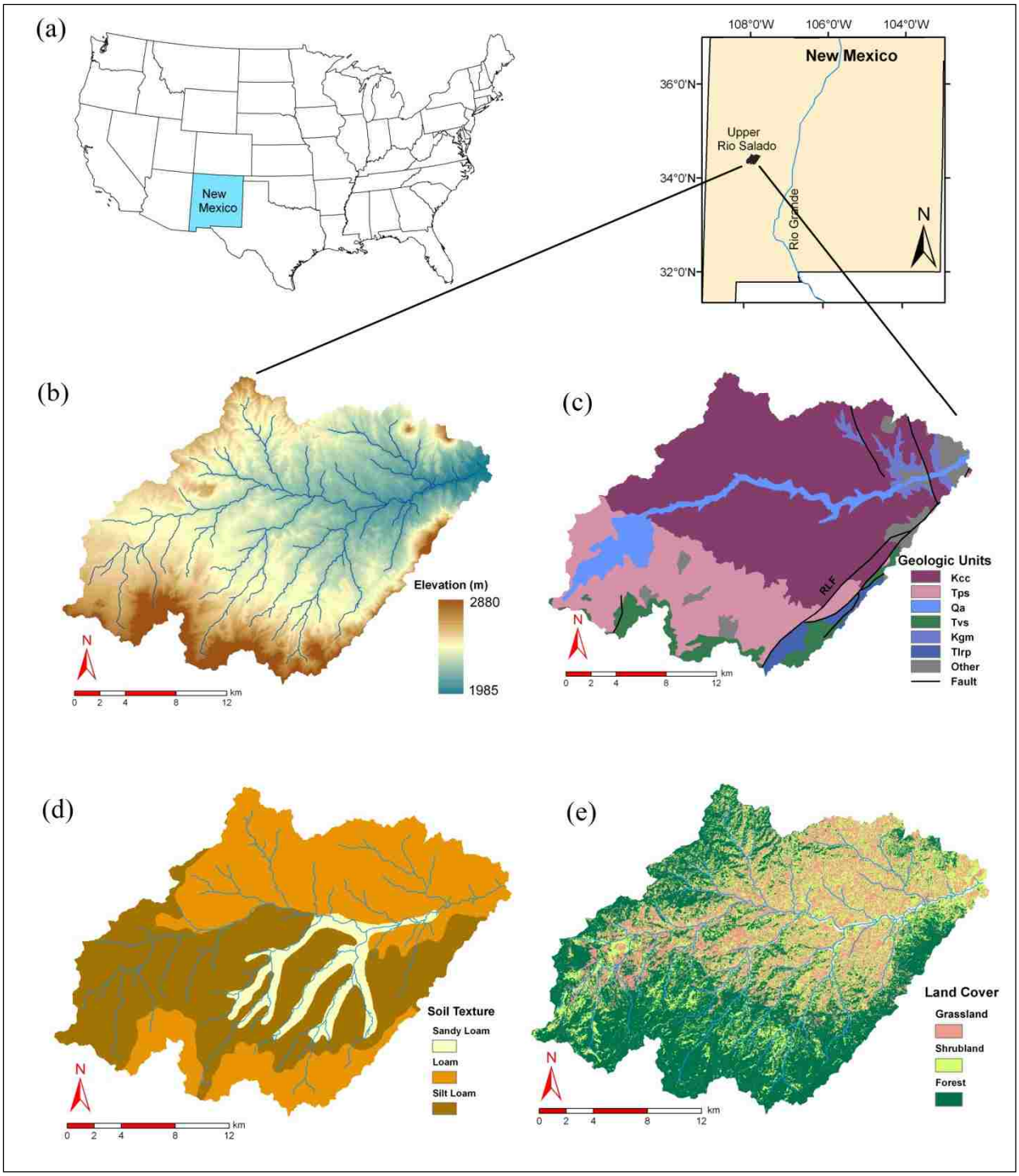

Figure 2. (a) Location; (b) elevation; (c) geology; (d) soil; and (e) vegetation maps of the Upper Rio Salado (URS) basin in central New Mexico.

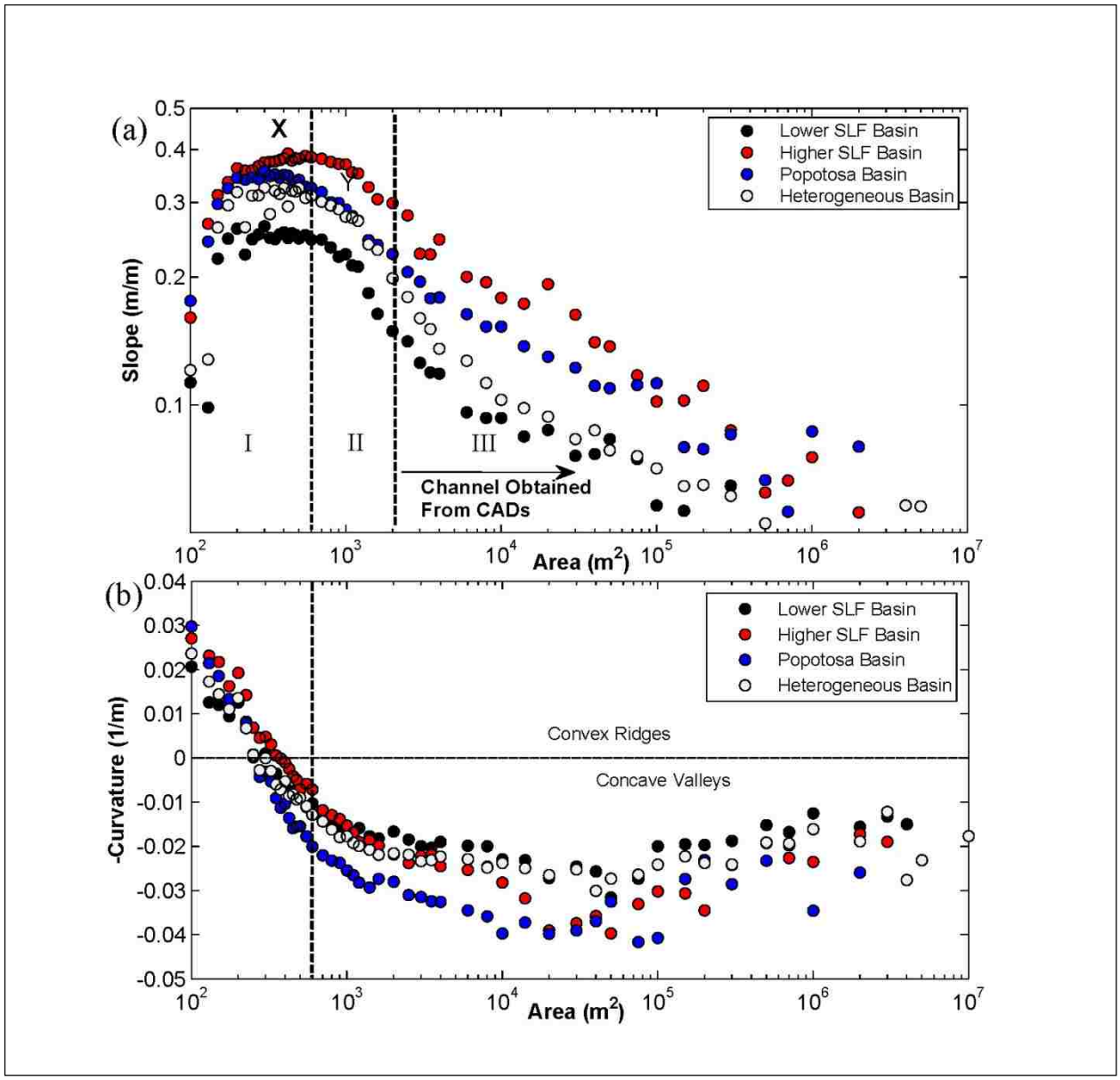

Figure 3. The slope-area (a) and curvature-area (b) relations for basins grouped with respect to different dominant lithologies. The vertical lines designate approximately the limits of the scaling regions I and II identified for the S-A relation of the Sierra Ladrones Formation (SLF) basins, and the letters X and Y show those for the Popotosa Formation (PF) basin, respectively.

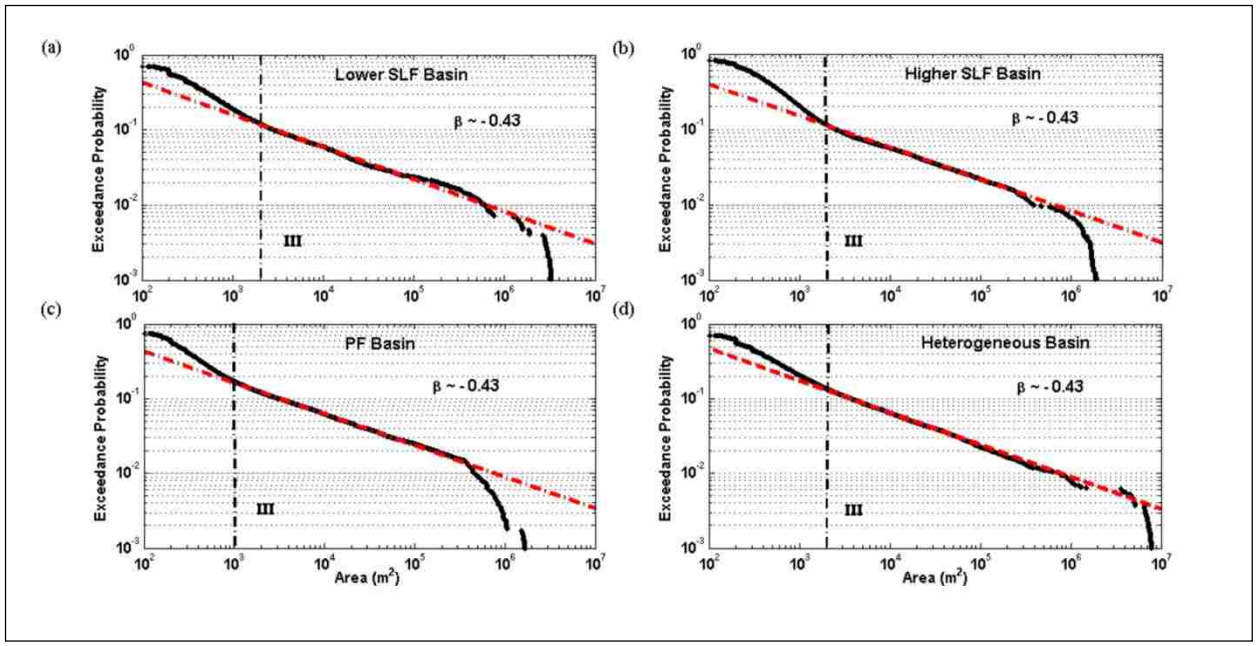

Figure 4. Cumulative area distribution (CAD) for the SLF lower elevation (a) and higher elevation (b) basins; the PF basin (c); and the heterogeneous basin (d). The vertical line in each plot specifies approximately the area above which a power-law distribution holds, and theoretically designates the channel head support area.

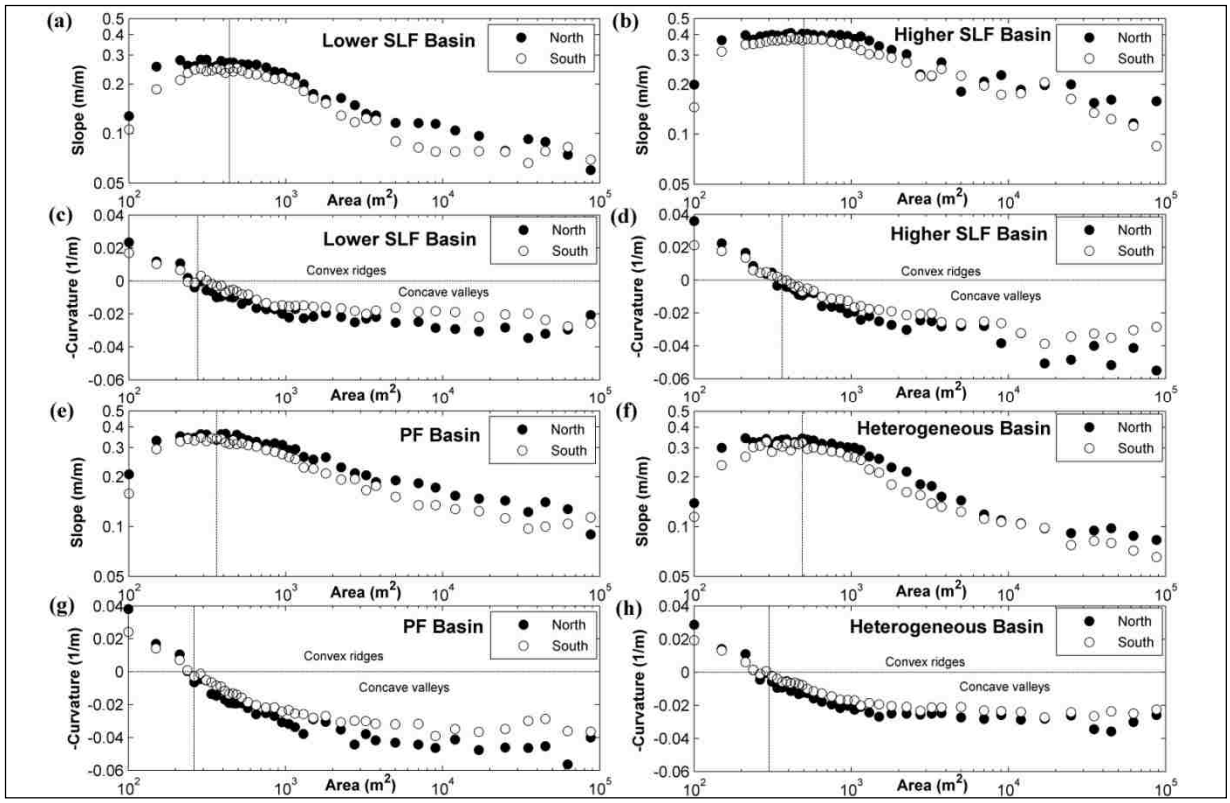

Figure 5. Slope – area (S-A) and curvature – area (C-A) plots of north- and south-facing slopes of the SLF lower elevation (a, c) and higher elevation (b, d) basins; PF basin (e, g); and the heterogeneous basin (f, h). Vertical dashed lines indicates the approximate location of the valley head on the S-A domain, and the area that corresponds to the change in the sign of curvature in the C-A domain.

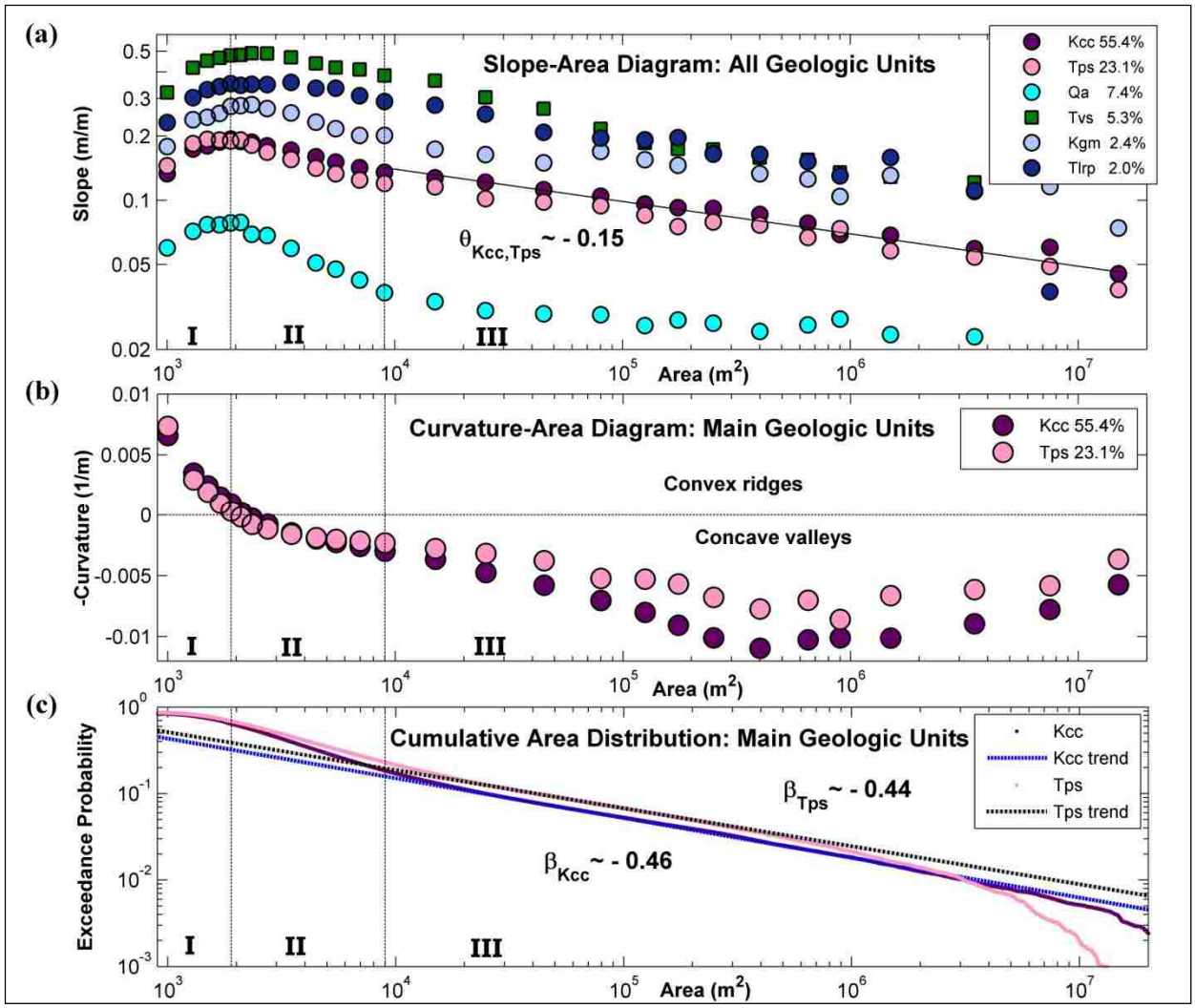

Figure 6. (a) Slope – area (S-A) relation; (b) curvature – area (C-A) relation and; (c) Cumulative area distribution (CAD) of the geologic units in the URS basin.

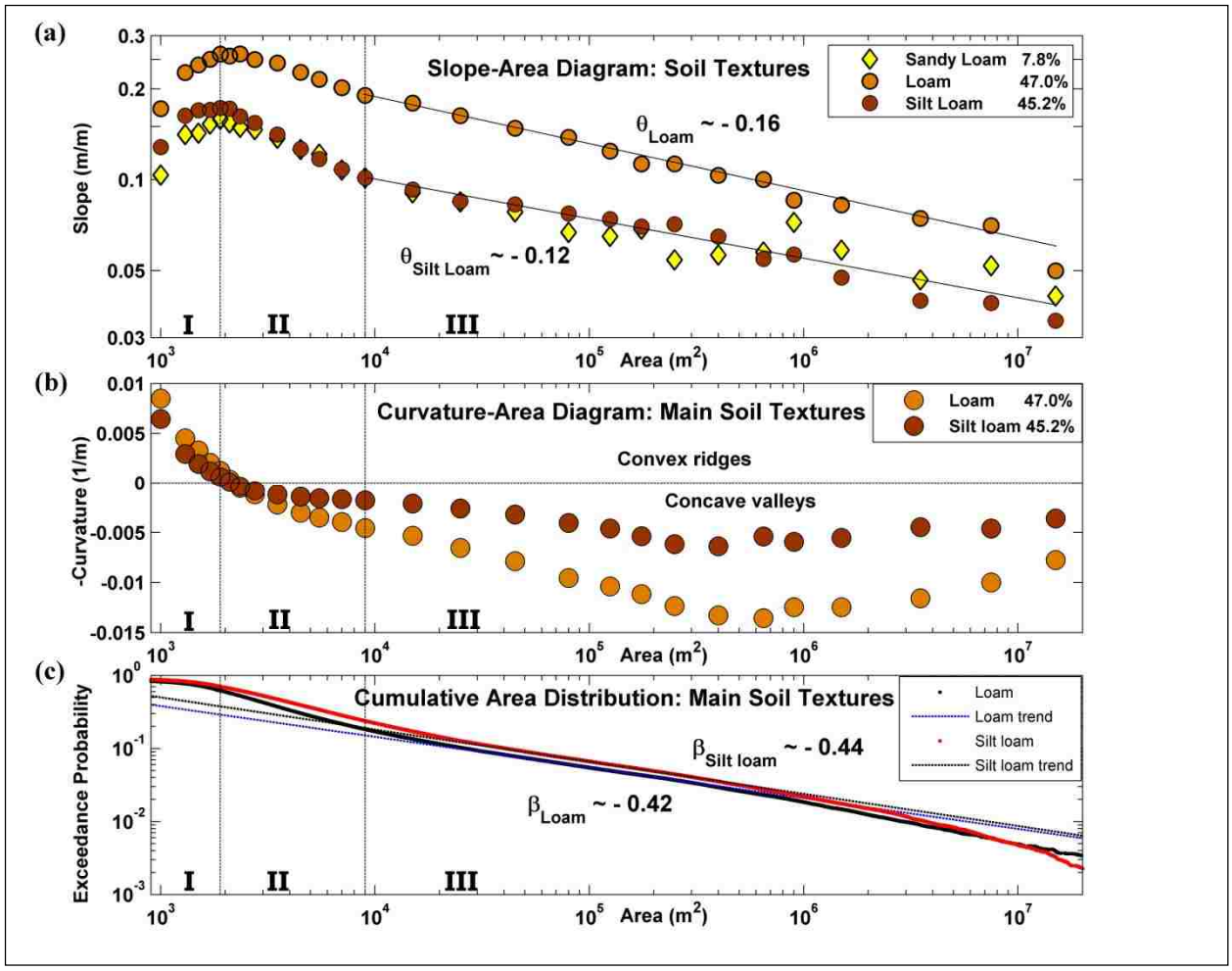

Figure 7. (a) Slope – area (S-A) relation; (b) curvature – area (C-A) relation and; (c) Cumulative area distribution (CAD) of the types of soil textures in the URS basin.

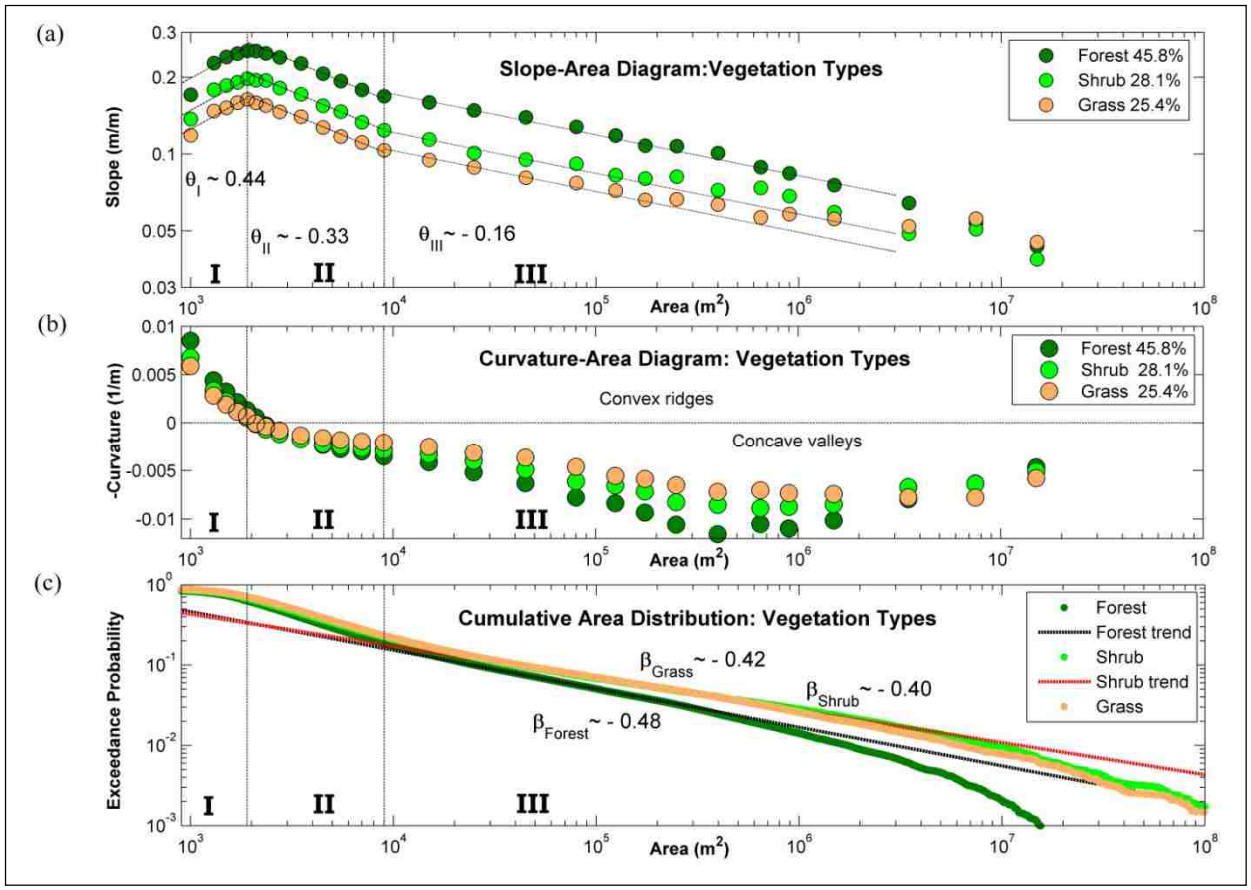

Figure 8. (a) Slope – area (S-A) relation; (b) curvature – area (C-A) relation and; (c) Cumulative area distribution (CAD) of the types of vegetation in the URS basin. Note: The trend line for grass is not given in (c) for clarity purpose.

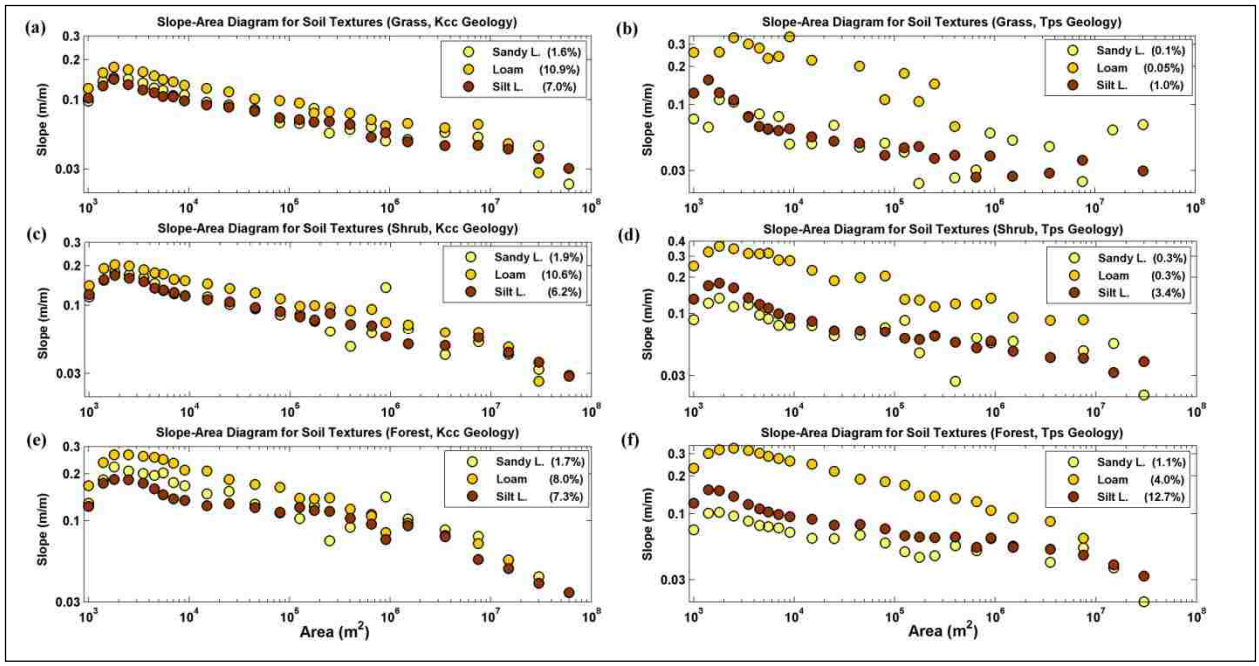

Figure 9. Slope – area (S-A) plots of the types of soil textures with respect to the same type of vegetation and geologic unit in the URS basin (a) Grass and Kcc; (b) Grass and Tps; (c) Shrub and Kcc; (d) Shrub and Tps; (e) Forest and Kcc; (f) Forest and Tps.

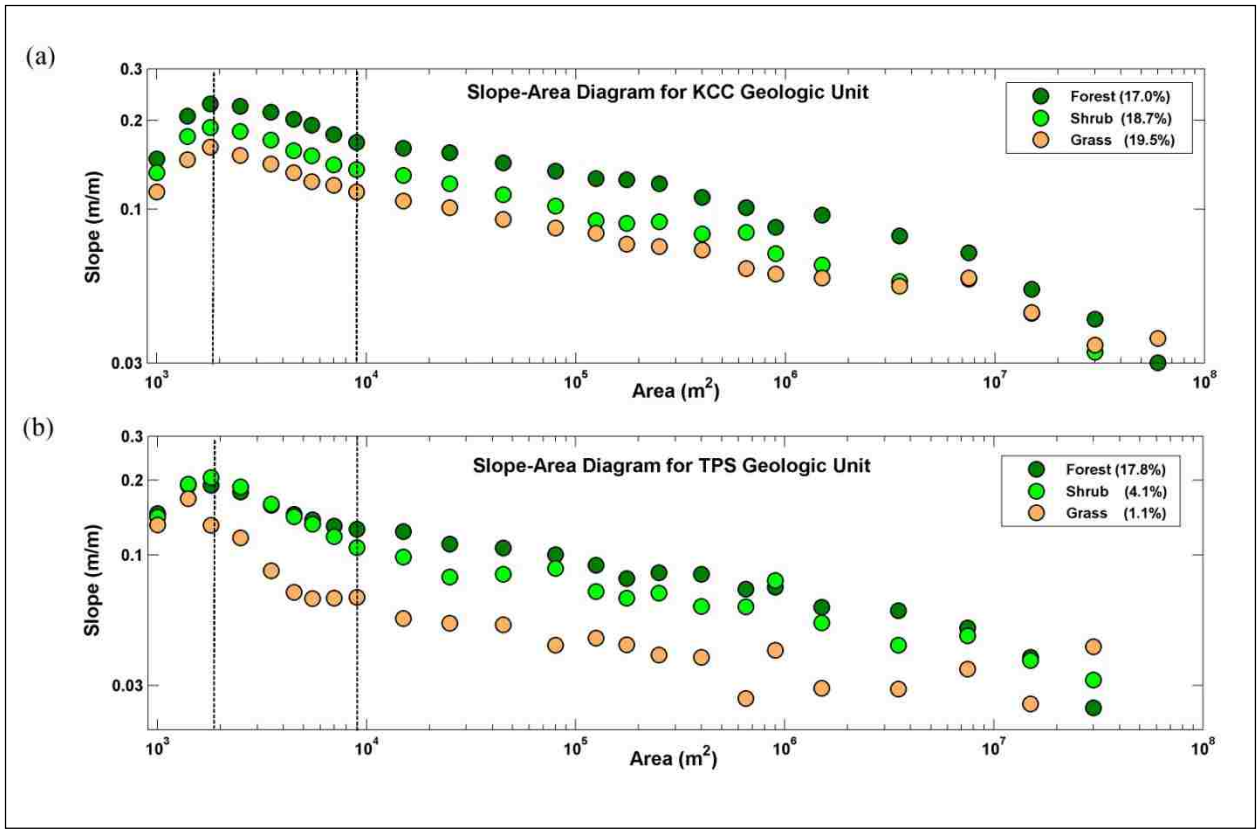

Figure 10. Slope – area (S-A) plots of the types of vegetation for two dominant geologic units in the URS basin (a) Kcc; (b) Tps.

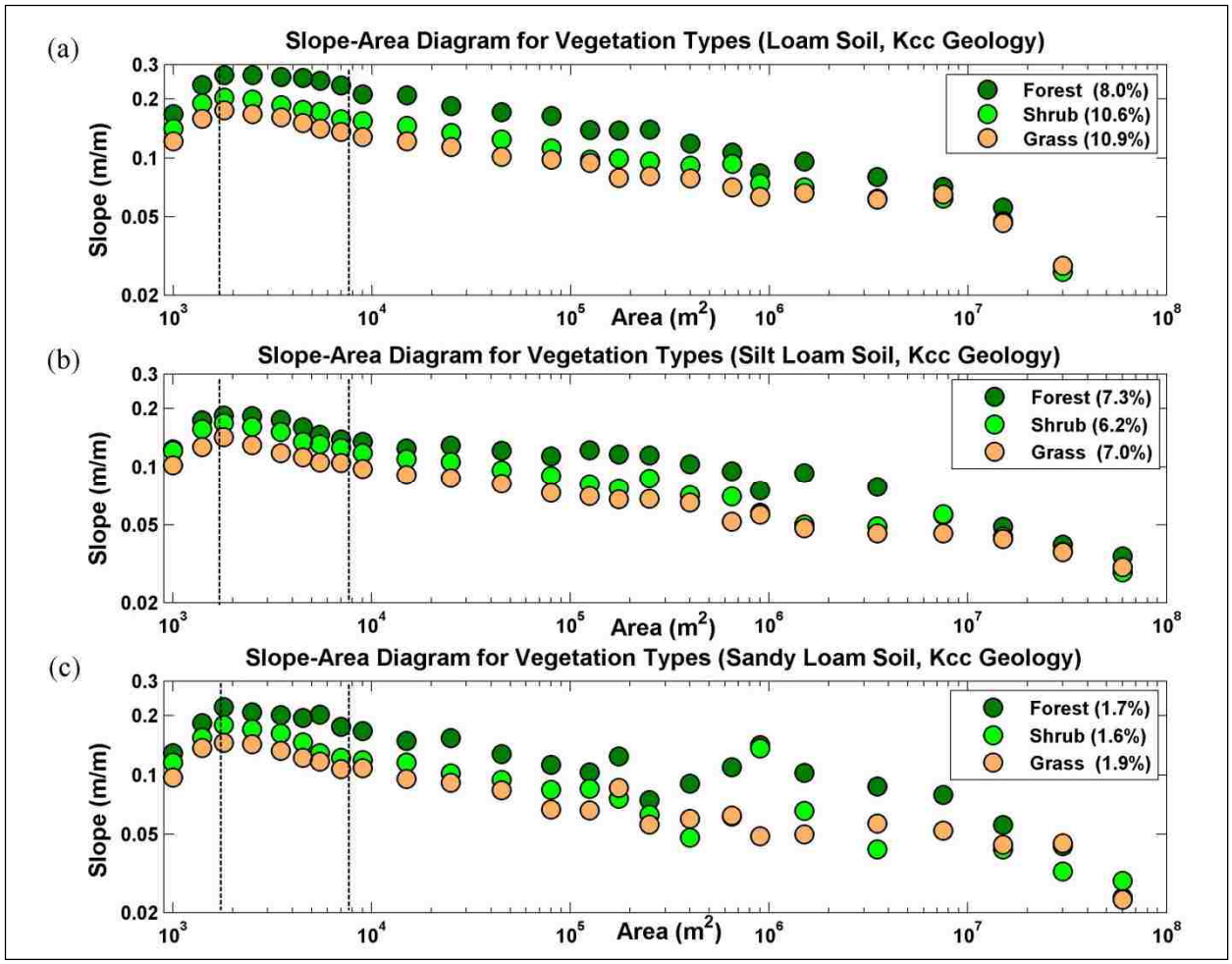

Figure 11. Slope – area (S-A) plots of the types of vegetation for Kcc geologic unit in different types of soil texture (a) loam; (b) silt loam; (c) sandy loam.

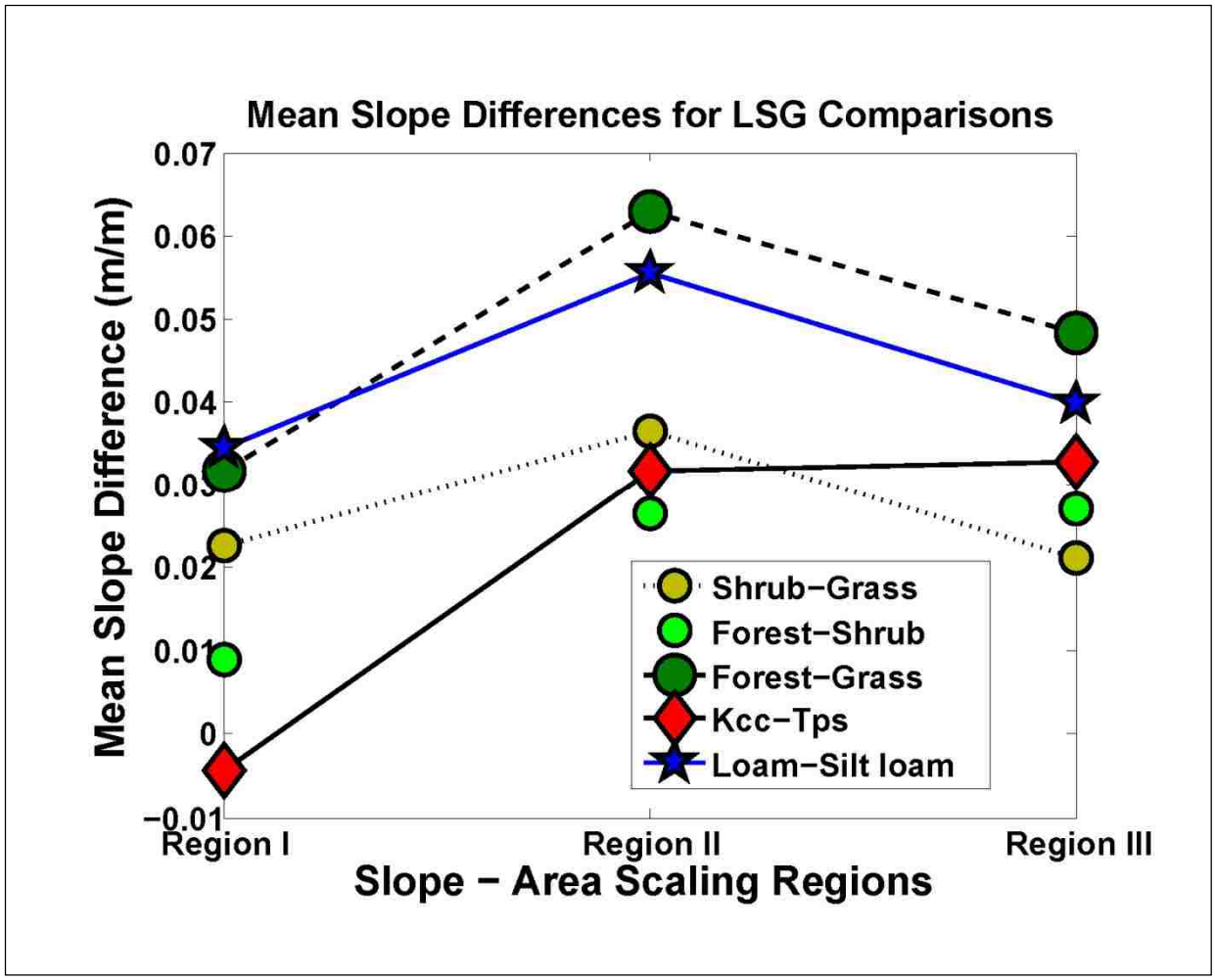

Figure 12. The comparison of the mean slope differences for different land surface groups.

CHAPTER 3: MODELING THE ECOHYDROLOGIC ROLE OF SOLAR RADIATION ON CATCHMENT DEVELOPMENT IN SEMIARID ECOSYSTEMS[2]

Abstract

Solar radiation has a clear signature on the spatial organization of ecohydrologic fluxes, vegetation patterns and dynamics, and landscape morphology in semiarid ecosystems. Existing landscape evolution models (LEMs) do not explicitly consider the spatial variability in solar radiation as a model forcing variable to study coupled ecohydrologic and geomorphic processes. In this study, a physically-based solar radiation component is introduced to the Channel-Hillslope Integrated Landscape Development (CHILD) LEM, and its vegetation dynamics component is improved with the aim to represent: (1) seasonal soil moisture, evapotranspiration, and vegetation dynamics on opposing north-facing slopes (NFS) and south-facing slopes (SFS); (2) flood frequency and magnitudes driven by stochastic rainfall input; and (3) differential evolution of landscape morphology on NFS and SFS consistent with observed landforms in a semiarid ecosystem in central New Mexico, located at the Sevilleta National Wildlife Refuge (SNWR). To examine the role solar radiation on modeled vegetation and landform characteristics, we designed a set of comparative LEM simulations driven by spatially uniform and variable solar radiation and a range of uplift rates. Rainfall climatology is represented by a seasonal rectangular pulse Poisson process model. Modeled local soil moisture, evapotranspiration and vegetation dynamics are confirmed against observations at a SNWR Long-term Ecological Research site. Space-time dynamics of modeled soil moisture and vegetation at the landscape scale are verified with respect to commonly observed patterns in other field and modeling studies. It is found that the spatial variability in soil moisture is controlled by aspect prior to the wet season (North American Monsoon, NAM) as a

[2] This chapter has been submitted for journal publication:

Yetemen, O., E. Istanbulluoglu, J.H. Flores Cervantes, E.R. Vivoni, and R.L. Bras, (submitted manuscript). Modeling the ecohydrologic role of solar radiation on catchment development in semiarid ecosystems. *Water Resources Research*.

result of aspect-dependent differences in evapotranspiration, and by the hydraulic connectivity of the flow network during the NAM, when soil moisture is ample. Aspect and network connectivity properties are also manifested on modeled vegetation biomass. NFS produced significantly more biomass than SFS. Interestingly, while greater biomass on NFS was observed on steeper hillslopes with smaller contributing drainage areas, SFS biomass increased as a function of growing drainage area, illustrating the varying role of drainage network on vegetation dynamics in relation to aspect. Modeled NFS and SFS morphologies are found consistent with topographic observations: modeled NFS are steeper, smoother, and longer with limited channelization, while SFS are relatively gentler, shorter, and highly dissected with channels. Differential evolution of opposing aspects has led to asymmetric valley development, as is evident in the field catchment. Understanding and modeling the role of solar radiation on coupled eco-geomorphic landscape evolution is critical for interpreting observed geomorphic patterns, and assessing the impacts of past and future climates on landscape response and morphology.

3.1. Introduction

Soil and vegetation differences with respect to hillslope orientation have long been recognized. For example, the Hebrew Bible (~1,500 BC) describes the ancient Middle Eastern city of Shechem as a hilly country nestled between the vegetated north-facing slope of Mount Gerizim and barren south-facing slopes of Mount Ebal [*Hillel*, 2006]. Since then, in experimental and modeling studies, vegetation differences on north- and south-facing slopes have been largely attributed to the interplay between the solar radiation-driven evapotranspiration demand and rainfall climatology that controls local soil moisture, and the adjustment of plant type and properties to attain tolerable water stress levels [*Gutiérrez-Jurado et al.*, 2006; *Ivanov et al.*, 2008b; *Pelletier et al.*, 2013; *Zhou et al.*, 2013; *Flores Cervantes et al.*, 2014].

The long-term differences in solar radiation exposure and vegetation have also led to differences in soil composition and chemistry [*Butler et al.*, 1986; *Kunkel et al.*, 2011; *Ma et al.*, 2011], runoff generation [*Kidron*, 1999; *Gutiérrez-Jurado et al.*, 2013], and hillslope morphology [*Pierce and Colman*, 1986; *Burnett et al.*, 2008]. With respect to the geomorphic differences, studies from the northern hemisphere using a range of DEM resolutions (from 1-m LiDAR up to 30-m USGS DEMs) at the watershed-scale repeatedly showed steeper and less dissected north-facing and shallower and more dissected south-facing slopes [*Istanbulluoglu et al.*, 2008; *Poulos et al.*, 2012; *Gutiérrez-Jurado and Vivoni*, 2013a]. Expanding the comparison of hillslope morphologies to the American continents using aggregated DEM data at 90-m resolution, *Poulos et al.*, [2012] developed a hillslope asymmetry index (i.e., log10 of the ratio of median slopes (°) of opposing aspects: N versus S or E versus W) and demonstrated that between the 60°N-60°S latitudes of the Americas hillslope asymmetry is positive between 10°N-49°N latitudes and negative between 15°S-40°S latitudes indicating steeper N (S) and shallower S (N) facing slopes on the northern (southern) hemisphere.

Despite the significant progress that has been made in relating surface processes and vegetation patterns to hillslope aspect, we still have limited understanding of the feedback mechanisms between the transport phenomena (water, sediment, nutrients), controlled by ecohydrologic dynamics and topography, and resulting landscape change that gives rise to differential aspect and slope development, and hence gradually influencing the ecohydrologic dynamics.

By coupling the conservation laws of water and sediment, landscape evolution models (LEMs) provide a numerical framework for studying the role of solar radiation on the evolution of Earth's surface and its ecological and physical components. Most LEM studies have used geomorphic transport laws [see *Dietrich et al*., 2003 for a detailed review] that predict long-term average, reach-scale sediment flux, often with the assumption of a year-around steady-state runoff rate [e.g., *Kirkby* 1971, *Willgoose et al*., 1991; *Tucker and Bras*, 1998; *Perron et al*. 2008]. *Tucker and Bras* [2000] introduced stochastic rainfall forcing in landscape evolution modeling with distinct pulses of storms, each represented by a rate, duration, and interstorm period. This advance brought a realistic "time-clock" to LEMs determined by the intermittency of actual storms.

A more realistic time stepping introduced by storm temporal properties facilitated the development of vegetation growth-death dynamics models within LEMs. Early studies that have coupled vegetation-erosion feedback mechanisms employed simplified vegetation models, which limited vegetation growth to available space (for example, using a logistic growth curve [e.g., *Levins*, 1969]) and related vegetation loss to geomorphic disturbances [*Thornes*, 1990; *Collins et al*., 2004; *Istanbulluoglu and Bras*, 2005]. These studies have predicted strong influences of vegetation dynamics on landscape relief, drainage density, and the spatial extent of geomorphic process domains in modeled landscapes under dynamic equilibrium. However, absence of climatic influence on vegetation dynamics and simplified hydrology (e.g., event-based runoff generation with a generic loss term representing infiltration and evapotranspiration losses) disregard the ecohydrologic controls on the transient evolution of landscapes, and, arguably, limit the use of earlier models only to humid regions where water is not limited.

Modeling of the ecogeomorphic evolution of semiarid systems require a more elaborate treatment of ecohydrology, as evapotranspiration losses grow with aridity, and vegetation dynamics become more tightly coupled with storm frequency and magnitude characteristics [*Sala and Lauenroth*, 1982; *Loik et al*., 2004; *Porporato et al*., 2004; *Istanbulluoglu and Bras*, 2006; *Lauenroth and Bradford*, 2009; *Dunkerley*, 2010]. Initial modeling studies that addressed vegetation-erosion linkages in semiarid climates coupled formulations of one-dimensional water-balance, moisture-dependent transpiration, and transpiration-dependent plant growth [*Istanbulluoglu and Bras*, 2006; *Collins and Bras*, 2008; 2010], and explored some of the well-known empirical concepts and observations of climate geomorphology, such as the sediment yield-precipitation [*Langbein and Schumm*, 1958, *Wilson*, 1973, *Summerfield and Hulton*, 1994], and

drainage density-aridity [*Gregory*, 1976, *Moglen et al*., 1998] relations. However, with respect to solar forcing, the models took a "flat earth" approach, assuming spatially uniform solar radiation. This assumption hampers the use of earlier models to investigate the coupled ecohydrologic and geomorphic outcomes of the spatial distribution of solar radiation within watersheds.

In this paper, we examine the role of solar radiation on the coupled development of landscape morphology and ecohydrologic patterns in a semiarid region by coupling water, energy, and mass conservation laws in the CHILD LEM [*Tucker et al*., 2001a]. CHILD (Channel-Hillslope Integrated Landscape Development) was extended with a solar radiation component [*Flores-Cervantes*, 2010] that calculates the incoming daily solar radiation on a modeled landscape element based on geometric relations between the Sun and the local hillslope position for a given latitude and day of year [*Bras*, 1990]; and an ecohydrology model that simulates vegetation dynamics over daily and/or inter-storm time scales driven by storm pulses and local evapotranspiration demand [*Istanbulluoglu et al*., 2012; *Zhou et al*., 2013]. In the model, the spatial distribution of solar radiation on the landscape leads to spatial and temporal dynamics of evapotranspiration, soil moisture, vegetation biomass, runoff, and erosion potential. Here, we first describe the theory of eco-geomorphic landscape evolution, followed by the validation of the ecohydrology component of the model in central New Mexico. The model is then used in a series of numerical simulations to explore the role of solar radiation on the coupled eco-geomorphic development of modeled landscapes. Modeling experiments are run using varying uplift (and no uplift) for the cases of spatially explicit and spatially uniform solar radiation conditions. Model results are examined by comparing simulated topographies of landscapes, their slope-area and vegetation-area relations, and the space-time variability of soil moisture and vegetation fields on an equilibrium landform. Model findings are discussed with respect to vegetation and landscape observations in central New Mexico, and the ecohydrology literature on the spatial patterns of soil moisture.

3.2. Model Description

The continuity principles of the land surface energy, water, elevation (sediment mass), and vegetation biomass (currently for a single plant type) are coupled in the CHILD LEM [*Tucker et al.*, 2001a, 2001b] on a spatial model domain represented by Voronoi polygons constructed from a TIN (Triangulated Irregular Network) network (Figure 1). For given [x, y, z] coordinates, the

coupled system of continuity equations are illustrated here in "generic" forms, the details of which are discussed throughout this section:

Energy: $$\frac{dS_h}{dt} = R_N\left(S, Asp, t\right) - G - H - \lambda ET\left(R_N, s, LAI\right) \quad (1)$$

Water: $$nD_r \frac{\partial s}{\partial t} = P - \nabla q_w - ET\left(R_N, s, LAI\right) \quad (2)$$

Biomass: $$\frac{dB}{dt} = NPP\left(ET\right)\phi - k_B B \quad (3)$$

Elevation: $$\frac{\partial Z}{\partial t} = U - \nabla q_{sd} - \nabla q_{sf}\left[\tau_f\left(q_w, V_t\right)\right] \quad (4)$$

Energy balance of the land surface can be represented by the rate of change in the surface heat storage S_h, dS_h/dt, driven by R_N: net radiation, and partitioned into G: ground heat flux, H: sensible heat flux, and λET: latent heat flux (λ latent heat of vaporization and ET actual amount of evapotranspiration) components. G and H fluxes are governed by temperature gradients between the surface and the deeper ground, for G, and between the surface and the air above, for H. λET is the latent energy transferred to the atmosphere through ET. In the equations above, environmental variables that regulate fluxes are given in parenthesis. S and Asp are local slope and aspect, respectively, t is time, s is the degree of saturation (between 0 and 1) in the root-zone, D_r, and LAI is vegetation leaf area index estimated from biomass on the land surface.

The water balance component (eqn. 2) tracks the changes in the amount of water in the soil layer [L/T], with a maximum storage of nD_r, where n is soil porosity. The components of water balance are, P: the rate of precipitation; ∇q_w: divergence of water flux (i.e., the sum of incoming overland, q_o, and lateral subsurface, q_l, flows from upstream cells minus outgoing flows divided by cell area); and losses due to local ET. Water and energy balance are coupled through ET and q_w, as changes in one regulates the amount of water available for the other.

In most process-based vegetation dynamics models, the rate of change in biomass (B), dB/dt, is represented as the balance between net primary productivity (NPP), driven by ET, as the source term, and first-order biomass decay (k_B), as sink [e.g., *Montaldo et al.*, 2005]. NPP is the net flux of carbon from the atmosphere to green plants, and ϕ is an allocation coefficient of NPP to aboveground biomass. In CHILD, live and dead constituents of B are represented separately.

Vegetation dynamics is coupled with water balance through *ET*. *B* regulates the amount of *ET*, as *LAI* is estimated from *B*.

Finally, the continuity of sediment follows the Exner equation that gives the rate of change in elevation, *Z*, as a function of a sediment source term (*U*), and divergence of sediment flux by hillslope diffusion (∇q_{sd}) and fluvial transport (∇q_{sf}). In the fluvial component, total vegetation cover fraction (V_t) is used to reduce the efficiency of overland flow shear stress (τ_f) employed in the sediment detachment and transport capacity equations [e.g., *Istanbulluoglu and Bras*, 2005, 2006].

The integration of the ecohydrology (eqns. 1-3) and geomorphology (eqn. 4) components in the CHILD LEM is shown in Figure 2. The model co-evolves fields of *Z*(x,y) and *B*(x,y), driven by pulses of *P* with a variable model time step set by inter-storm duration, t_b. Both observed and statistically generated rainfall data can be used. To simplify the energy balance component over inter-storm time scales (days to weeks in semiarid climates), we assume $dS_h/dt=0$, and use the concept of potential evapotranspiration (*PET*) as the upper limit of *ET* [e.g., *Brutsaert*, 1982]. A solar radiation ratio, R_{solar} (ratio of incoming shortwave radiation on a hillslope element to that of a flat surface) is used to scale *PET* estimated for flat surface on hillslope elements [*Dingman*, 2002]. Local slope (*S*), aspect (*Asp*), and flow directions (*FD*) are derived from *Z* to characterize the topographic attributes of the modeled domain. *S* and *Asp* are used to calculate R_{solar}, and *FD* is used for flow routing.

The model processes *P* as an instantaneous pulse, increasing the soil moisture in the root zone, and routes the excess overland (Q_o) and subsurface flow (Q_l) along flow directions cell by cell. At each cell, effective shear stress (τ_f) is calculated from Q_o and V_t, and used in detachment and transport capacity models. The *Z* field is updated after each storm with the changes in *Z* as a result of erosion and deposition (ΔZ). Erosion is assumed to disrupt vegetation and cause biomass loss ($-\Delta B$), creating a negative feedback to the vegetation state (Figure 2). *ET* and vegetation growth/decay are modeled during the inter-storm period. The *B* field is updated by the net change in vegetation biomass (ΔB) before the arrival of the next storm.

3.2.1. Ecohydrologic Dynamics

This study builds on the ecohydrology [*Collins and Bras*, 2010] and solar radiation [*Flores-Cervantes*, 2010] models previously implemented in CHILD. Only grass vegetation type is

considered in the model. Grassland ecohydrology is introduced with dynamic live and dead grass biomass state variables adopted from recent models designed for long-term simulation experiments with minimalistic input variables sufficient to capture seasonal vegetation dynamics similar to equation (3) [*Istanbulluoglu et al*., 2012; *Zhou et al*., 2013].

Hydrology is modeled as a collection of single-layer storage units, inter-connected along flow paths (Figure 1). Surface runoff is routed cell by cell, and local runoff is generated when the total water input (local rainfall + run-on discharge) exceeds the rate of actual infiltration. The rate of global runoff leaving a model element Q [L^3T^{-1}] is:

$$Q = \max\left[\left\langle p + Q_{in}^{sum} / a_c - I_a \right\rangle a_c, 0\right] \tag{5}$$

where p [LT^{-1}] is rainfall rate, $p=P/t_r$ (t_r is storm duration), Q_{in}^{sum} is the sum of run-on discharge [L^3T^{-1}] from upstream sources $Q_{in}^{sum} = \sum_{1}^{k} Q_{in}$, k is number of upstream cells that drain into a downstream cell, and a_c [L^2] is the cell area. I_a [LT^{-1}] is the actual rate of infiltration. I_a is constrained by three factors: available water flux, infiltration capacity, and the available pore space in the root zone [*Collins and Bras*, 2010]:

$$I_a = \min\left\{P + \frac{Q_{in}}{a_c},\ I_c,\ \frac{nD_r(1-s)}{t_r}\right\} \tag{6}$$

where I_c [LT^{-1}] is the infiltration capacity, n [-] is soil porosity, D_r [L] is the effective root depth, s [-] is saturation degree of soil moisture in the root zone (i.e. volumetric soil moisture divided by n), and t_r is storm duration. In equation (6), no runoff is generated when I_a equals the first term. Infiltration (saturation) excess runoff is generated when I_a equals the second (third) term. Infiltration capacity at a model element, I_c, is modeled similar to [*Dunne et al*., 1991], as the weighted average of I_c of bare soil, $I_{c,bare}$, and a fully vegetated surface, $I_{c,veg}$:

$$I_c = I_{c,bare}(1 - V_t) + I_{c,veg} V_t \tag{7}$$

where V_t [-] is total vegetation cover fraction.

With the influence of run-on from upstream cells incorporated into I_a, a more explicit form of equation (2) is used for water balance similar to [*Collins and Bras*, 2010]:

$$nZ_r \frac{\partial s}{\partial t} = I_a + q_{Lp,in} - q_{Lp,out} - q_{L,n} - ET_a \tag{8}$$

where $q_{Lp,in}$ is the incoming, and $q_{Lp,out}$ is the outgoing lateral soil-moisture flux in the direction parallel to the surface; and $q_{L,n}$ is the normal flux (gravity drainage) [L/T]. $q_{Lp,out}$ and $q_{L,n}$ are non-zero when $s>s_{fc}$ (s_{fc} is field capacity), and calculated based on the leakage, L, model of *Laio et al.* [2001], resolved into lateral and vertical components. The lateral moisture transfer, q_{Lp} is assumed to be in the direction parallel to the surface following [*Cabral et al.*, 1992]:

$$q_{Lp} = L\left[a_r \tan S / (1 + a_r \tan S)\right] \tag{9}$$

where S is local slope angle, a_r is the anisotropy ratio, which is defined as the ratio of the horizontal to vertical saturated hydraulic conductivity. The normal component of the loss is equal to $q_{Ln}=L-q_{Lp}$. In highly anisotropic medium, q_{Ln} is insignificant comparative to q_{Lp}.

Actual evapotranspiration ET_a in equation (8) is estimated considering the limitation of root-zone soil moisture as:

$$ET_a(s) = ET_{\max} \cdot (s - s_w) / (s^* - s_w), \quad s_w < s \le s^* \tag{10}$$

where $ET_{\max}$ [LT^{-1}] is the maximum rate of evapotranspiration from a composite soil-vegetation surface; s_w and s^* are soil moisture thresholds for plant wilting point and reduced transpiration under plant water stress [*Laio et al.*, 2001]. Two other conditions for ET_a are: $ET_a = ET_{\max}$ when $s>s^*$, and $ET_a = E_{min}$ when $s<s_{wp}$. This models gives a linear increase in ET_a with soil moisture between s_w and s^*, which plateaus at a constant rate $ET_a = ET_{\max}$ for further increase in s.

We assumed that the maximum rate of grass transpiration T_{max} will not exceed the transpiration rate of a reference grass (a well-watered, healthy, live-grass at uniform height that completely shades the ground) with a reference leaf area index (m^2 leaf area to m^2 ground area), LAI_{Rmax} of 2.88 [*Allen et al.*, 1989; 1998]. ET_{max} at a model element is estimated as the sum of transpiration from grass and evaporation from bare soil [*Eagleson*, 1978; *Brolsma and Bierkens*, 2007]:

$$ET_{\max} = T_{\max} \frac{LAI_l}{LAI_{R\max}} + E_s \left(1 - \frac{LAI_l}{LAI_{R\max}}\right), \quad LAI_l \le LAI_{R\max} \tag{11}$$

where LAI_l is modeled live leaf area index, and the LAI_l/LAI_{Rmax} is the cover fraction of live grass. E_s [LT^{-1}] is the maximum rate of evaporation from bare soil, reduced from $T_{\max}$ by a coefficient k_s ($E_s=k_sT_{\max}$) [e.g., *Mutziger et al.*, 2005; *Zhou et al.*, 2013]

$T_{\max}$ on sloping model elements, $T^S_{\max}$, is calculated by scaling the $T_{\max}$ estimated for a flat surface, $T^F_{\max}$, with a solar radiation ratio, R_{solar}. R_{solar} is defined as the ratio of clear-sky radiation on sloped surfaces, R^S_{cs}, to that of a flat surface, R^F_{cs}:

$$T^S_{\max} = T^F_{\max} \cdot R_{solar} = T^F_{\max} \cdot \frac{R^S_{cs}}{R^F_{cs}} \tag{12a}$$

$$T^F_{\max} = T^F_{ref}\left(R_N, T_a, v, RH, LAI_R\right) \tag{12b}$$

R_{cs} is estimated as a function of day of year (DOY), latitude, local slope and aspect [*Bras*, 1990; *Dingman*, 2002] (see equations in Appendix A). When the model is run with observed meteorological data, the Penman-Monteith (P-M) equation is used for daily $T^F_{\max}$ for reference grass [*Allen et al*., 1998]. Meteorological variables employed in the P-M equation are net radiation (R_N), air temperature (T_a), wind speed (v), relative humidity (RH), and $LAI_{R\max}$ (eqn. 12b). In long-term geomorphic evolution simulations driven by generated rainfall, we prescribed $T^F_{\max}$ through the use of a cosine function [e.g., *Small*, 2005], fitted to P-M estimated daily $T^F_{\max}$. In both cases, daily estimates of $T^F_{\max}$ are averaged for each inter-storm period. The P-M equation, considerations of radiation balance for estimating R_N, and the cosine function prescribed for $T^F_{\max}$ for long-term simulations are presented in Appendix B.

There are some limitations of our $T^S_{\max}$ model. Equation (12a) neglects the contributions of local variations in meteorological variables, and diffused and reflected radiation fluxes on $T^S_{\max}$. The latter two terms are usually relatively small in comparison to direct radiation [e.g., *Pierce et al.*, 2005], unless the modeled topography has canyon-like morphology. Assuming uniform meteorological variables was deliberately chosen to minimize model input requirement, consistent with most catchment-scale distributed hydrologic models [e.g., *Wigmosta et al*., 1994].

We illustrate aspect control on radiation distribution, by plotting R_{solar} as a function of the day of year (DOY) and local slope for contrasting N (360°) and S (180°) aspects for 34° N latitude and 107° W longitude (Socorro, NM) (Figure 3). Aspect control on incoming solar radiation is clearly more pronounced during the fall and winter months (300>DOY>90) because of the shallow gradient of sunlight [*Zou et al*., 2007]. During this period, slopes steeper than ~10° become have a greater effect on the distribution of solar radiation. N-facing slopes receive less and S-facing slopes receive more solar radiation than a flat surface. In the spring and summer months (growing

season in the region), however, contrasting aspects receive comparable amounts of solar radiation to a flat surface and to each other. The implications of spatio-temporal variability in solar radiation to ecosystem dynamics are discussed later in the paper.

The production of the sum of above- and below-ground grass biomass (net primary productivity, *NPP*) at the ecosystem scale is related linearly with actual *ET* through the use of water use efficiency (*WUE*) [*Swenson and Waring*, 2006]:

$$NPP = 0.75 \cdot (1-\mu) \cdot ET_a \cdot WUE \cdot \rho_w \cdot \omega \qquad (13)$$

This is a relatively simple model that represents biomass production by photosynthesis. *WUE* indicates the amount of carbon gained for each unit of water lost (kg CO_2 / kg H_2O), μ is the ratio of nighttime to daytime CO_2 exchange, ρ_w is water density, and ω is a conversion factor of CO_2 to dry biomass (kg DM / kg CO_2). *NPP* is partitioned between root and aboveground-live biomass using an allocation coefficient that depends on available space (eqn. 14a). Allocation of biomass to live and dead biomass pools and biomass decay are tracked using ordinary differential equations as commonly used in vegetation dynamics models [e.g., *Sitch et al*., 2003].

$$\frac{dB_l}{dt} = NPP \cdot \phi_a - k_{sl} B_l - k_{sf} \xi_{sl} B_l \qquad (14a)$$

$$\frac{dB_d}{dt} = k_{sl} B_l - k_{dd} \xi_{sd} B_d \qquad (14b)$$

where B_l is the aboveground live biomass; and B_d is the aboveground dead biomass; ϕ_a is an allocation coefficient for aboveground live biomass ($0<\phi_a<1$); k_{sl} and k_{dd} are the coefficients for green biomass senescence and dead biomass decay, respectively; k_{sf} is coefficient for the drought-induced foliage loss driven by water stress, ξ_{sl} ($0<\xi_{sl}<1$); ξ_{sd} is a coefficient for climate-influence on the rate of dead biomass loss [*Istanbulluoglu et al*., 2012]. k_{sl} is doubled during the dormancy season to represent unfavorable climatic conditions. Equations used for ϕ_a, ξ_{sl}, ξ_{sd}, and the conversion of live and dead *LAI* (LAI_l and LAI_d) from biomass and the vegetation cover, V_t, fraction from total LAI_t are given in Table 1.

The onset and the offset of the growing season are often triggered when a set of environmental conditions (e.g., soil and air temperature, soil moisture) are satisfied for certain period of time [*Cayrol et al.*, 2000; *Sitch et al.*, 2003; *Ivanov et al.*, 2008a]. For simplicity, we used the 30-day-averaged T_{max}, $T_{max\text{-}30}$, as a surrogate variable for climatic favorability [*Istanbulluoglu et al*., 2012].

The growing season starts when $T_{max\text{-}30}$ is greater than a growth threshold, GT, and ends when $T_{max\text{-}30}$ gets smaller than a dormancy threshold, DT.

Geomorphic events impact vegetation dynamics. Rapid fluvial incision and landslides can scour the vegetation cover, and sediment deposition can cause plant mortality as a result of the burial of actively transpiring leaves [e.g., *Murray and Paola*, 2003; *Collins and Bras*, 2004]. In CHILD, vegetation loss due to fluvial scour is represented with a linear loss function driven by excess shear stress [*Collins et al.*, 2004]:

$$\frac{dV_t}{dt} = -k_v V_t \left(\tau_f - \tau_c\right), \qquad \tau_f > \tau_c \tag{15}$$

where k_v is a vegetation erodibility parameter. It is assumed that loss in live and dead aboveground biomass is proportional to their initial cover fractions. Fluvial-driven vegetation destruction forms a negative feedback in the model between geomorphic and ecohydrologic processes (Figure 2).

3.2.2. Geomorphic Dynamics

The rate of change in elevation due to fluvial processes is set to the lesser of detachment capacity, D_c [L T^{-1}], and the divergence of sediment flux ∇q_{sf} [*Tucker et al.*, 2001a]:

$$\frac{\partial z}{\partial t} = -\min\left[D_c, \frac{q_{s,out} - \sum q_{s,in}}{a_c}\right] \tag{16}$$

where $\Sigma q_{s,in}$ is the total sediment influx to a model element and $q_{s,out}$ is the outgoing sediment flux from a model cell assumed at sediment transport capacity [L^3 T^{-1}]. D_c gives the maximum rate of local erosion. We used excess shear stress-driven parameterization for each flux component (Table 2) [*Istanbulluoglu et al.*, 2003; *Tucker and Hancock*, 2010].

Instead of using the boundary shear stress of the flow acting on the compound surface (vegetation and soil), we use the concept of effective excess shear stress, described as the amount of shear stress that directly acts on soil grains [e.g. *Einstein and Barbarossa*, 1952; *Foster*, 1982]. Effective shear stress, $\tau_{eff,}$ is calculated from the boundary shear stress scaled by a shear stress partitioning ratio, parameterized using Manning's roughness coefficients for bare soil, n_s, and vegetation n_v [*Laursen*, 1958; *Istanbulluoglu and Bras*, 2005]:

$$\tau_{eff} = \tau_b \left(\frac{n_s}{n_s + n_v}\right)^{3/2} \tag{17a}$$

$$\tau_b = \rho_w g C^{0.75} Q^{0.375} S^{0.8125} (n_s + n_v)^{0.375} \qquad (17b)$$

where τ_b is the boundary shear stress formulated for a parabolic flow cross section with a shape constant C, Q is discharge [$L^3 T^{-1}$], S is local slope [*Istanbulluoglu and Bras*, 2005; *Istanbulluoglu et al.*, 2003].

3.2.3. Rainfall Forcing

Model simulations are driven by generated rainfall using a modified version of the Poisson rectangular pulse (PRP) rainfall model [*Eagleson*, 1978]. Each storm event is represented with constant rainfall intensity, p, and a storm duration, T_r, and storms are separated by an interstorm period, T_b. A one-parameter exponential distribution is used to represent the variability in T_r and T_b [*Eagleson*, 1978]. Dependence between storm depth and its duration is well-documented [*Bonta*, 2004; *Grayman and Eagleson*, 1969]. To represent this dependence, storm depths are generated from a two-parameter gamma distribution conditioned by $T_r/\overline{T_r}$ as a dynamic shape parameter that varies with each storm, and $1/\overline{P}$, where $\overline{P}$ is the mean storm depth, as the scale parameter of the gamma distribution [*Ivanov et al.*, 2007]. Rainfall seasonality is simulated by varying the parameters of the distributions based on the observed storm statistics for wet and dry seasons [e.g., *Small*, 2005].

In the PRP model, using the mean rainfall intensity, $\overline{p}$, obtained from rainfall records by dividing the accumulated rainfall during a storm to storm duration often leads to under-predictions of storm runoff, especially in regions where rainfall is highly variable with high-intensity bursts [*Wainwright and Parsons*, 2002]. Most erosive events occur during short-duration high-intensity storm bursts, even though the rainfall event may continue for longer durations with lower intensities. To obtain both realistic values of storm intensities and modeled runoff depths, earlier modeling studies have dealt with this limitation using a scaling factor, α, to calibrate $\overline{p}$ and $\overline{T_r}$ as [*Collins and Bras*, 2010]:

$$\overline{p'} = \alpha \cdot \overline{p}, \qquad \overline{T_r'} = \overline{T_r}/\alpha \qquad (18)$$

where $\overline{p'}$ and $\overline{T_r'}$ are the scaled values of $\overline{p}$ and $\overline{T_r}$, respectively. To preserve the mean number of storms, the reduction from storm duration is added to the mean interstorm duration, $\overline{T_b'} = \overline{T_b} + \left(\overline{T_r} - \overline{T_r'}\right)$.

3.3. Study Site and Ecohydrologic Model Confirmation

To illustrate the role of solar radiation on ecogeomorphic catchment evolution and confirm model predictions, we selected a site at the Sevilleta National Wildlife Refuge (SNWR) in central New Mexico, where hillslope aspect has a marked influence on vegetation patterns and landscape morphology (Figure 4). The catchment was incised on the coarse alluvial fan deposits of the Plio-Pleistocene Sierra Ladrones Formation [*McMahon*, 1998; *Connel and McGraw*, 2007].

The region receives ~250 mm of mean annual precipitation (MAP). High-intensity and short-duration convective thunderstorms during the North American Monsoon (NAM, July to September) claim approximately 50% of the MAP [*Vivoni et al.*, 2008], and show high spatial and inter-annual variability [*Gosz et al.*, 1995]. In the winter, low-intensity frontal storms with occasional snow are typical [*Milne et al.*, 2003]. The site hosts the Sevilleta LTER (Long Term Ecological Research), which aims to study the long-term ecological change in the region (Figure 4). Livestock grazing has not been permitted at the SNWR since 1973 [*Gosz and Gosz*, 1996].

Differences in the vegetation and geomorphology of the contrasting north (N) and south (S) facing hillslopes are illustrated in Figure 4. The N-facing slopes are covered by a mesic ecosystem with one-seed Juniper (*Juniperus monosperma*) and denser black grama (*Bouteloua eriopoda*). S-facing slopes host a xeric ecosystem consisting of creosote bush (*Larrea tridentata*) and sparser fluff grass (*Erioneuron pulchellum*) [*McMahon*, 1998; *Gutiérrez-Jurado et al.*, 2007]. N-facing slopes contain higher proportions of organic matter, $CaCO_3$, silt, and clay than S-facing slopes as a result of higher infiltration rates and deeper infiltration, aeolian sediment deposition, and root respiration [*Gutiérrez-Jurado et al.*, 2006].

Hillslope morphologies of opposing N- and S-facing slopes also exhibit pronounced differences. N-facing slopes have smooth planar forms, devoid of any significant fluvial incisions, and are relatively longer than S-facing slopes. S-facing slopes are highly dissected with active channels, forming regularly-spaced hollows. At the catchment scale, differences in the N- and S-facing morphologies lead to asymmetric network development [*Istanbulluoglu et al.*, 2008].

A plot of local slopes to their contributing drainage areas (*Sl-A* plot) can be used to examine the topographic ramifications of dominant forms of geomorphic transport [e.g., *Tucker and Bras*, 1998]. Hillslope transport processes such as soil creep and bioturbation (e.g., equation 2 in Table 2) lead to a positive *Sl-A* relationship in which *Sl* increases with *A* (i.e., a convex hillslope profile), while fluvial processes dominantly acting on the landscape result in concave valley/channel forms

leading to a negative *Sl-A* relation. Local maxima in a *Sl-A* relation between the two scaling regions indicates the approximate drainage area required to maintain a fluvial network by providing sufficient discharge.

The *Sl-A* relations for N- and S-facing slopes of the catchment in Figure 4b are obtained from a 10m InSAR DEM (Figure 5), by binning the *Sl* data for a defined range of *A* values in the basin, and averaging both *Sl* and *A* data. Consistent with visual observations in the field, the *Sl-A* relation of the basin shows steeper N-facing slopes than S-facing slopes (~ 5% steeper over the whole basin). Under an equilibrium of uplift (or base level fall) and local erosion conditions, a steeper local *Sl* for a given *A* may indicate overall lower fluvial activity on N-facing slopes as a result of higher biomass, such that *Sl* steepens, under continuing base level fall in the main channel, to maintain a constant rate of local erosion by increased slope-dependent hillslope diffusion [*Istanbulluoglu et al*., 2008]. This suggests a testable hypothesis using CHILD as runoff erosion theory presented in the modeling section relates effective shear stress negatively with vegetation cover fraction.

3.3.1. Ecohydrologic Model Confirmation

The ecohydrology component of the model is confirmed against field observations at the McKenzie Flats area, in the north-eastern quadrant of the SNWR. At the site, vegetation is predominantly composed of warm season C4 grass species, such as black grama (*Bouteloua eriopoda*) and blue grama (*Bouteloua gracilis*), and soil is loamy sand [*Moore*, 2012].

Available ecohydrologic data used in this study include: hourly precipitation, temperature, wind speed, and relative humidity between 1990 and 2009 at the Deep Well meteorological station [*Moore*, 2012]; evapotranspiration fluxes between 1996 and 1999 from a Bowen Ratio Energy Balance (BREB) tower located near the Deep Well station [*Gosz*, 2012a]; and soil moisture content of the top 30 cm (i.e., average root depth for grass at the site [*Kurc and Small*, 2004]) measured using vertically-installed TDR (Time-Domain Reflectometry) probes at three different pits adjacent to the meteorological and BREB flux measurements [*Gosz*, 2012b].

MODIS LAI product is used to confirm model predictions of live LAI. MODIS LAI is available at 1 km spatial resolution with 8-day intervals since 2000. A window of 3 by 3 MODIS grid cells overlaying the Deep Well site at the center are obtained from NASA Land Processes Distributed Achieve Center (LP DAAC), and the spatial mean of LAI from the 9 grid cells are calculated to compare against model predictions.

Concurrently measured BREB-derived ET_a and soil moisture can be used to estimate the physical soil parameters (s_{wp} and s^*) of the ET_a model *Kurc and Small*, [2004] and *Chen et al.*, [2008]. The loamy sand soil type is defined as Berino soil in the metadata of the soil moisture observations by *Gosz* [2012b]. The bulk density of Berino soil is given as 1.54 g/cm^3 [*Soil Survey Staff*]. The soil porosity, n, using the particle density of mineral soil (2.65 g/cm^3), is estimated as n=0.42. The ET_a-s relationship (eqn. 10) based on the piecewise linear dependency of ET_a to s is fitted visually to the ET_a-s data pairs, as in *Vivoni et al.* [2008]. For n=0.42, the corresponding values of s_{wp} and s^* found are 0.17, and 0.31, respectively. These values are within the range of s_{wp} and s^* reported in the literature for loamy sand soil [*Laio et al.*, 2001].

To test the ecohydrological component of CHILD, a small flat surface represented with a mesh of 20 nodes is generated and CHILD is run for the period 1990-2009 driven by daily meteorological data obtained by averaging hourly measurements. Model parameters used in this simulation are reported in Table 3, which are selected with minimal model calibration. Experimenting with the model, we identified *WUE*, k_{sl} and k_{dd} as the three most critical parameters that control model response to rainfall. *WUE* defines the amplitude of *LAI* during the growing season, while k_{sl} and k_{dd} control decay rate of live and dead biomass. The values reported for these parameters were identified by varying them within the ranges reported in the literature.

The ecohydrological response of the CHILD model driven by observed meteorological data at the Deep Well site is plotted in Figure 6. Modeled soil moisture is in overall good agreement with observations in the 1996-2006 period (Figure 6b), capturing the magnitudes of soil moisture pulses and the shapes of soil moisture decays reasonably well (Nash-Sutcliffe efficiency, *NSE*=0.76). The model, however, slightly overestimated the soil moisture in the winters of some years (e.g., 2005). This may be attributed to winter greening of some C3 species in the field, lowering the soil moisture through transpiration, while the single species vegetation used in the model does not sufficiently capture this early growth. This argument is supported by the MODIS-*LAI* data which shows early growth in 2005 while the modeled growth is delayed (Figure 6d).

Despite its simplicity, the model generally captures the observed peaks in ET_a during the rainy season (Figure 6c). Most notably, the predictive skill of the model is improved in the wet season of 1999, when a collection of relatively large storm pulses fell during a shorter wet season. With respect to the *LAI*, the model captures the onset of greening, the magnitude of the peak *LAI*, and the onset of senescence of grass vegetation reflected by the MODIS- *LAI* data (Figure 6d). It can

be noted that MODIS-*LAI* does not capture vegetation dynamics when *LAI* goes below 0.2. This discrepancy may be attributed to the insensitivity of MODIS- *LAI* to very low values; in addition for vegetated surface MODIS-*LAI* values start from 0.1 [e.g., *Fang and Lian*, 2005; *Shabanov et al*., 2005].

With this confirmation of the model at the Deep Well site, the role of aspect on modeled vegetation productivity is demonstrated by running CHILD at a small headwater catchment in the SNWR study basin (Figure 4b, location indicated by star), using the Deep Well climate data. Modeled live biomass cover (g/m^2) is presented in two snapshots of the model corresponding to before (end of May) and after (late August) the NAM of 1998 (Figure 7a and 7b, respectively). Modeled time series of mean spatial soil moisture content [m^3/m^3] for 1997-2000 are plotted in Figure 7c. In both cases, north-facing slopes hold more grass biomass than south-facing slopes as a result of greater soil moisture accumulation during the winter (Figure 7c). During the summer, similar soil moisture contents are modeled on north- and south-facing aspects. Given the NAM is the major erosive flood-generating season in the region [e.g., *Gutiérrez-Jurado et al*., 2007], it is anticipated that the differences in the modeled vegetation biomass between the opposing slopes would influence catchment evolution over geomorphic time scales. While the single plant functional type assumption in the current model limits the application of the model at the SNWR study site, where juniper trees and grasses with higher total biomass co-exist on north-facing slopes and shrubs dominate south-facing slopes, the current model is deemed appropriate to examine the ecohydrologic ramifications of aspect on geomorphic evolution as the model gives more plant biomass on north-facing slopes, consistent with observations, than south-facing slopes.

3.3.2. Flood Frequency and Magnitude

Runoff is the main driver of erosion and net sediment export from a catchment. In semiarid regions, most streams are ephemeral, and sediment flux out of ephemeral basins is typically driven by high-magnitude and low-frequency runoff events [*Coppus and Imeson*, 2002; *Polyakov et al.*, 2010]. In this section, we evaluate runoff coefficients, RC (percent of the ratio of mean annual runoff, *MAR*, to mean annual precipitation, *MAP*, or 100**MAR*/*MAP*), and flood return periods modeled by CHILD, with those reported in the literature for the semiarid southwest US and more specifically in central New Mexico. To evaluate the runoff component, the model is run with calibrated soil and vegetation parameters on an evolved catchment, forced by generated climate for 10,000 years. Runoff from each simulated storm is recorded. For this analysis, we run the

model for 5 times, using *MAP* from 200 mm to 400 mm with 50 mm increments to examine the overall model response for semiarid conditions. In each run, the wet season (July, August September), brought ~50% of the *MAP*, as observed in the region during the NAM. The modeled runoff coefficients increased from ~3.1% (*MAP*=200 mm) up to ~4.0% (*MAP*=400 mm).

At the study catchment, *Gutiérrez-Jurado et al.* [2013] reported measured RCs in field plots (4m by 2m) on north- and south-facing slopes as 0.1% and 7%, respectively, which clearly reflects the fundamental role of aspect on runoff generation even at the plot scale. For a small catchment made up equally of N- and S-facing slopes, this would roughly give a 3.5% RC. At the scale of the Rio Puerco (160,000 km^2) and its two major tributaries, *Molnár and Ramirez* [2001] reported RCs between 0.89% and 2.96%. While their values are lower than our simulations, it is highly likely that lower RCs observed in this study can be due to transmission losses in channels and reduced amounts of synchronous runoff-producing storms in larger basins (e.g, *Dunkerley*, 1992; *Mudd*, 2006; *Parsons et al.*, 1999; *Vivoni et al.*, 2006). In an earlier study, *Drissel and Osborn* [1968] reported a RC of 3.3%, in a 173 km^2 basin located in east central New Mexico, consistent with our model runs.

On the wetter end of the simulated climate range, CHILD simulations agree with the RCs observed in various subbasins of the Walnut Gulch Experimental Watershed (WGEW) in southeastern Arizona, with similar climatology (*MAP*=312mm) and coarse soil texture [*Goodrich et al.*, 2008]. In the WGEW, Stone *et al.* [2008] reported RCs of 1.9% and 4.5% for experimental catchments with areas of 8.98 km^2 and 0.06 km^2 respectively. Stone *et al.* [2008] also attributed the observed reduction in the RC with catchment area to growing channel losses.

Return periods of modeled annual maximum daily runoff for *MAP*=250 mm are compared with measured runoff in flume studies of relatively small-scale basins (<10 km^2) at the WGEW. Other existing data for the central New Mexico region are often for much larger basins that generate smaller flood magnitudes, when converted to basin-averaged runoff depth. In headwater catchments, however, most floods are generated with localized high-magnitude storm pulses, leading to larger runoff depths. Although the WGEW catchments receive more *MAP* (312 mm), they also experience a longer NAM [*Goodrich et al.*, 2008]. As such, we anticipate relatively similar flood generating conditions in both NM and AZ sites. Figure 8 plots the modeled and observed annual daily maximum runoff and their return periods. In the WGEW, the peak flow data

were collected from three flumes that drain small catchments of varying sizes for 54 years [*Stone et al*., 2008]. Despite CHILD predicts slightly larger flood magnitudes for return periods of 10 or less years, modeled flood magnitudes are particularly consistent with flumes-4 and -125 of WGEW data for higher return periods. Flume-3 with a larger drainage produces lesser runoff arguably as a result of channel losses and spatial variability of storm intensities. The analysis presented in this section demonstrates the credibility of the model in generating storm runoff at magnitudes commensurate with semiarid basins in the Southwest US.

3.4. Model Experiments

To study the role of solar radiation on landscape and biomass development, we conducted simulations using spatially distributed radiation (Rad-Spatial) and spatially uniform radiation (Rad-Uniform) with CHILD LEM. Model parameter values were selected to represent the environmental conditions in the central New Mexico catchment where aspect-control on ecogeomorphic organization is observed.

Because the Deep Well site has limited (19 years) of meteorological data to parameterize the PRP rainfall model, climate forcing is represented using empirical relations for rainfall climatology developed for the semiarid southwest US as a function of MAP, its distribution between the wet and dry seasons represented by fractions of MAP (F_{wet}, F_{dry}), and the begin and end days of the NAM [*Small*, 2005; *Istanbulluoglu and Bras*, 2006]. Estimated storm intensity, duration, and time between storms for MAP of 250 mm and calculated F_{wet} and F_{dry} from the Deep Well site are listed in Table 3.

PET forcing of the model is obtained from a sinusoidal function of $T^F_{\max}$ for reference grass as a function of DOY. The sinusoidal function is fitted to the 19-year-long calculated daily $T^F_{\max}$ data for the Deep Well site to represent the seasonal changes *PET* forcing. In the Rad-Uniform simulations, solar radiation is assumed to be spatially uniform over the simulated domain, and $T^F_{\max}$ is used directly from the sinusoidal function. In the Rad-Spatial simulations, the clear sky radiation is calculated throughout the year as a function of latitude, local slope, and aspect (see Appendix A), and used in equation (12a) to calculate the clear-sky ratio (R_{solar}). For hillslopes, $T^F_{\max}$ is scaled with R_{solar}, to calculate the $T^S_{\max}$ for a given slope and aspect of a landscape element (eqn. 12a).

The initial domain used in the model simulations is a 900 m by 900 m inclined surface, with a ~7% east facing slope, and 20 m node spacing. Drainage is only permitted on the bottom of the sloping side of the domain. The role of solar radiation on landscape and plant biomass development is examined under the conditions of no uplift, a low rate of uplift (0.05 mm/yr), and a high rate of uplift (0.10 mm/yr), for both Rad-Spatial and Rad-Uniform conditions. These uplift rates are within the ranges of the long-term (ca. 640 ka) average incision [*Dethier*, 2001], and denudation rate estimates in the region [*Bierman et al.*, 2005; *Clapp et al.*, 2001].

In the model, we assumed that the landscape is soil-mantled (no bedrock control), and transport-limited. This assumption is consistent with the regional geology of alluvial fan deposits of the Plio-Pleistocene epoch and our field observations where we observed alluvial sediment deposits in valleys and absence of any rock outcrops on hillslopes. The channel geometry is assumed parabolic for sediment transport calculations [*Istanbulluoglu et al.*, 2003]. Hillslopes in the study site are covered with coarse soil texture with high gravel contents. *McMahon* [1998] reports approximately 60% and 35% gravel content in the surface substrate of the S- and N-facing slopes, respectively. Hence, a fine gravel substrate with the mean grain size diameter, d_{50}=7 mm is used. The critical shear stress, τ_c, for d_{50}=7 mm is 5 Pa according to the Shields equation [*Shields*, 1936]. For simplicity, τ_c = 5 Pa is used for both detachment and transport capacity equations. The transport coefficient of the latter is calculated with d_{50}=7 mm to be consistent with the selected τ_c (Table 3).

Exponents of the sediment transport and detachment capacity models are taken from *Govers* [1992] and *Nearing et al.*, [1999], respectively. *Istanbulluoglu et al* [2003] compared sediment yield estimates from incised gullies against predictions using the *Govers* [1992] equation and found the equation suitable for natural landscapes. *Nearing et al.*, [1999] conducted experiments to relate net detachment rate with shear stress in Walnut Gulch basin where coarse sediments dominate the surface substrate similar to our catchment [*Nearing et al.*, 1999].

3.4.1. Landscape Morphology

Model experiments are run for 800,000 years until approximate uplift-erosion equilibrium is reached. Mean elevation of the simulated landscapes at 5000-year resolution for 800 kyr (Figure 9) and the plan views of modeled topographies colored with respect to the size of the drainage area of each cell (Figure 10) are presented. The high-uplift simulations are used to illustrate the 3D features of the modeled landscapes (Figure 11).

Uplift raises the mean elevation of the modeled landscapes, and leads to a clear separation among simulations (Figure 9). In the absence of uplift, topography decays with a diminishing rate over time, as landscape elevation drops. With uplift, the mean elevation of the basin attains an approximate constant (with some fluctuations), illustrating the dynamic uplift-erosion balance in the basin. Rad-Spatial simulations maintain slightly higher mean elevations than Rad-Uniform simulations. At the end of the simulations, elevation difference between Rad-Spatial and Rad-Uniform increases with uplift from ~0.30 m under no uplift to ~1.37 m with high uplift, corresponding to 3.29% and 5.18% of the mean elevations of their respective Rad-Spatial landscapes. Higher mean elevations under Rad-Spatial suggest overall steeper elevation gradients across the modeled domains. These findings imply: a) spatially explicit solar radiation leads to lower rates of erosion across the landscape for a given slope, and therefore landscapes adjust to occupy higher mean elevations (and steeper slopes) to maintain erosion-uplift balance; b) the spatial control of solar radiation is amplified by uplift.

To provide metrics as the basis of objective comparisons between the modeled and actual field catchments, we use drainage density, D_d, and hillslope asymmetry, *HA*, indices. D_d is the ratio of the total length of channels to catchment area [e.g., *Tarboton et al*., 1991]. A channel network is extracted using a constant support area threshold of 2,400 m^2, approximate inflection point of the *Sl-A* plot (Figure 5). Following *Poulos et al*. [2012], the north-south *HA*, $HA_{N\text{-}S}$, is estimated as the $\log_{10}$ of the ratio of median slopes of the N- and S- aspects (Table 4). $HA_{N\text{-}S}>0$ ($HA_{N\text{-}S}<0$) indicates steeper N-facing (S-facing) slopes. $HA_{N\text{-}S}$ values are tested with the null hypothesis that the calculated values are statistically different than zero ($p<0.01$ using Student's *t*-test). A consistent pattern in the calculated metrics is that both D_d and $HA_{N\text{-}S}$ are higher in the Rad-Spatial simulations and increase with uplift. $HA_{N\text{-}S}$ of 0.1 means that N-facing slopes are 26% steeper than S-facing slopes in the basin. $HA_{N\text{-}S}$ values in Rad-Spatial simulations are different than zero. D_d and $HA_{N\text{-}S}$ values of the field-site catchment fall between the no uplift and low uplift simulations. $HA_{N\text{-}S}$ can be a function of different factors including uplift rate, geology, vegetation and climate. For example, *Poulos et al*. [2012] report regional $HA_{N\text{-}S}$ values for other semiarid basins where hillslope asymmetry is observed. They estimated $HA_{N\text{-}S}$ from 30 m DEMs for the Gabillan Mesa in the central California Coast Ranges located at the 36° N latitude and Dry Creek located at the 44° N latitude within 0.10 – 0.15.

The differences in the metrics discussed above manifest themselves on the modeled landscape structure (Figures 10 and 11). In the no uplift experiments, modeling spatially varying radiation leads to the development of linear and more closely spaced channels (Figure 10a, 10b). In the Rad-Uniform case, upwardly migrating channels branch into both N- and S-facing slopes (see blue arrows), developing wider headwater valleys (Figure 10a), and capturing surface runoff into three major dendritic channels. In the Rad-Spatial case, however, a limited number of channel heads advances into the N-facing slopes as a result of denser vegetation cover in the headwaters of the catchment. This leads to smaller headwater valleys, but a large numbers of linear channels.

Uplift amplifies the control of solar radiation on modeled landscape development. In the Rad-Spatial case, channel tips tend to develop into south-facing slopes, as can be profoundly observed in the first valley on the left (see blue arrow) (Figure 10b, 10d, 10f). Increase in uplift further promotes the northward expansion of the channel network that inhibits the development of the next valley to its north by capturing larger drainage areas in the upland portions of the modeled domain. Northward expansions of channel heads are responsible for the development of hillslope asymmetry. Figure 11 more clearly demonstrates the differences in the development of the valley networks, and elevations between the Rad-Uniform and Rad-Spatial simulations (Figure 11). The red arrow on the left indicates valley development on northward expansion, and formation of branching on south-facing aspects. This expansion inhibits the development of next channel (middle red arrow in Figure 11b). The right arrow on the right indicates an additional valley that fully developed on the Rad-Spatial case.

3.4.2. Slope-Area and Vegetation-Area Relations

Contributing drainage area, A, is a measure of water supply at a point, used for both fluvial transport and plant growth, while slope and aspect regulates the amount of local water loss to *ET*. To examine the associations between modeled vegetation cover and landscape morphology, we plot local values of slope, S_l, and vegetation cover fraction, V_t, with A, grouped with respect to N (315-45 degrees) and S (135-225 degrees) aspects for all simulations (Figure 12). For the *Sl-A* plot, the elevation field at the end of each model run is used, and *Sl* values for each aspect are binned and averaged with respect to given ranges of A. To capture the temporal dynamics of V_t, V_t for each model element is stored after every storm event in the last 100 years of the simulations, and the temporal average of V_t, $\overline{V_t}$, for 100-year is plotted as a function of A in Figure 12 .

In the Rad-Spatial simulations, modeled N-facing slopes have steeper local slopes than S-facing slopes for A<~10^4 m^2 (Figure 12a, 12c, 12e), consistent with the observed *Sl-A* plot of the field catchment (Figure 5). The *Sl-A* data of the Rad-Uniform simulations plot between those of the N- and S-facing slopes of the Rad-Spatial scenarios. Landscapes get steeper, and the separations between the slopes of opposing aspects become more pronounced as uplift increases.

The *Sl-A* and $\overline{V_t} - A$ relations are related (Figure 12). There is clearly a contrasting behavior of vegetation response with A on N- and S-facing slopes. $\overline{V_t}$ on N-facing slopes first shows a slight positive dependence to A on hillslopes (e.g. A<~2x10^3 m^2), attains a local maximum, and drops with further increase in A to a nearly constant value in channels near the outlet. This response is in-phase with the *Sl-A* relation. On N-facing slopes, the local maximums in the *Sl-A* and *V-A* plots correspond to a similar A value.

N-facing slopes (steeper than ~10°) have significantly lower R_{solar}, especially during autumn and winter (Figure 3a), that reduces T_{max} and enhances soil moisture in the beginning of the growing season (discussed in section 4.2), supporting denser vegetation cover throughout the year. The loss of vegetation as *Sl* decreases and A grows on N-facing slopes suggests that an increase in upland moisture input with larger A cannot compensate the growing *ET* losses as a function of an increase in R_{solar}. This leads to foliage loss as a result of increasing plant water stress.

In contrast to N-facing slopes, steep hillslopes of S-facing aspects receive the highest R_{solar} (Figure 3b) than any other aspect on the landscape during autumn and winter. These differences are relatively lower during the growing season than the remainder of the year; however, the excess of incoming solar radiation on S-facing aspects limits vegetation growth on these hillslopes where the source of moisture is largely from local rainfall. Drop in local *Sl* with A in concave S-facing valleys improves soil moisture as a result of larger A and reduced *ET*, resulting in more productive vegetation growth (i.e., positive relationship between V_t and A) in S-facing valleys (Figure 12).

Figure 12 reveals a positive ecohydro-geomorphic feedback mechanism driven by solar radiation and uplift in this modeled semiarid catchment. Higher rates of uplift input drives hillslopes to gradually attain steeper slopes as the landscapes evolve towards an uplift-erosion equilibrium. Slope steepening leads to growing differences in the amount of radiation received by N and S aspects. N- (S-) facing slopes, occupied with denser (sparser) vegetation, adjust to get steeper (gentler) than their opposing aspects through a dynamic geomorphic feedback as shear stress that drives erosion and sediment transport is inversely related to vegetation cover.

Steepening slopes with growing uplift amplify the differences in vegetation growth through impacting the radiation distribution that force ecohydrologic dynamics. These feedback mechanisms lead to larger *Sl* and V_t differences for a given *A* in modeled catchments as uplift grows (Figure 12).

3.4.3. Spatio-Temporal Soil Moisture and Vegetation Dynamics

Because of the importance of soil moisture in the generation of flood response and ecosystem processes, understanding and representing the spatial and temporal patterns of soil moisture is critical in the coupled modeling of ecohydrologic and geomorphic processes [*Gutiérrez-Jurado et al*., 2007; *Vivoni et al*., 2009; *Penna et al*., 2011]. A number of studies have demonstrated that the coefficient of spatial variation of soil moisture θ (volumetric water content), CV_θ, varies as a function of spatial mean θ, $\langle\theta\rangle$. It has been shown that CV_θ attains a maximum within an intermediate $\langle\theta\rangle$ state of the field, and drops towards its lowest values as the watershed dries and wets, producing a convex parabolic $CV_\theta - \langle\theta\rangle$ relationship [*Western et al*., 2003; *Ryu and Famiglietti*, 2005; *Choi and Jacobs*, 2007; *Famiglietti et al*., 2008; *Mascaro et al*., 2011]. When the soil moisture data are plotted in the $CV_\theta - \langle\theta\rangle$ phase space as a function of time (i.e., a trajectory), however, a hysteretic pattern emerges, in which the spatial variability of soil moisture during wetting and drying phases follow different trajectories [*Teuling et al*., 2007; *Ivanov et al*., 2010; *Vivoni et al*., 2010; *Rosenbaum et al*., 2012].

We output fields of root-zone average soil moisture and vegetation cover following each storm in the last 100 years of the model simulations with high uplift, and calculate the mean spatial soil moisture and vegetation cover $(\langle\theta\rangle, \langle V_t\rangle)$ and their coefficients of spatial variations (CV_θ, CV_{Vt}) after each storm event. Soil moisture $CV_\theta - \langle\theta\rangle$ and vegetation $CV_{Vt} - \langle V_t\rangle$ data pairs for both Rad-Spatial and Rad-Uniform scenarios are presented in Figures 13 and 14, along with the maps of selected soil moisture and vegetation states at the high and low ends of their modeled ranges.

The $CV_\theta - \langle\theta\rangle$ relation in Figure 13a is bounded by low CV_θ values on both dry and wet ends of $\langle\theta\rangle$. On the dry-end, $\langle\theta\rangle$ values are generally within the range of hygroscopic water content and plant wilting point (~0.04-0.07), and on the wet-end $\langle\theta\rangle$ values are between field capacity and

porosity. The spatial variability of soil moisture shows fundamental differences between the Rad-Spatial and Rad-Uniform simulations. The $CV_\theta - \langle\theta\rangle$ data pairs of the Rad-Uniform scenario establish a lower limit in the $CV_\theta - \langle\theta\rangle$ space, with a very slight increase (decrease) in spatial variability as basin wets (dries). In the Rad-Spatial simulation, CV_θ generally maximizes about the mid value ~0.12 of $\langle\theta\rangle$ (e.g., point *C*) and decreases towards the wet and dry ends. Distinct differences between the two radiation scenarios suggest that the spatial variability of solar radiation drives the convex parabolic $CV_\theta - \langle\theta\rangle$ relation, consistent with the generally reported patterns in the literature that used field observations [*Ryu and Famiglietti*, 2005; *Choi and Jacobs*, 2007] and numerical modeling [*Lawrence and Hornberger*, 2007; *Vereecken et al*., 2007; *Ivanov et al*., 2010].

To further examine the physical processes that underlie the spatial and temporal evolution of soil moisture, we plot trajectories of CV_θ as a function of $\langle\theta\rangle$ for two years of soil moisture wetting-drying cycles (Figure 13a). For a clear illustration of the annual $CV_\theta - \langle\theta\rangle$ relationship, we start the trajectories with the driest soil moisture condition before the onset of the wet season (i.e., NAM) in July, and end when the minimum soil moisture is reached in the following year prior to NAM. The size of each loop in the figure is characterized by the amount of wet season rainfall. The outer (inner) loop corresponds to a relatively wetter (drier) years with 317 mm (160 mm) of total rainfall (from July to July). To investigate the topographic controls on the CV_θ states, the simulated maps of spatial soil- moisture distribution for the wetter year are shown for the driest and wettest $\langle\theta\rangle$ conditions (*A* and *B* in Figure 13a), and the highest *CV* point (*C* in Figure 13a) in Figures 13b, 13c, 13d.

With the driest mean soil moisture of the year (point *A*, Figure 13a), both aspects are under the plant wilting point, while N-facing slopes have slightly greater soil moisture contents (aspect-controlled pattern) than S-facing slopes (Figures 13b). The onset of NAM wets the topography through several successive storms and $\langle\theta\rangle$ evolves to its highest value of the year during NAM (point *B,* Figure 13a). Interestingly, during this wetting process CV_θ first shows a slight increase with $\langle\theta\rangle$, but then drops with the final storm event as $\langle\theta\rangle$ takes its maximum value by mid September of the simulated year. A similar change in the sign of the $CV_\theta - \langle\theta\rangle$ relation can be

seen in the Rad-Uniform simulation as $\langle\theta\rangle$ gets larger than ~0.23, a value slightly higher than the field capacity of the soil $(\theta_{fc} = 0.22)$. This model response is a result of a growing influence of lateral soil-moisture redistribution over the domain, activated by the exceedance of the field capacity threshold. Enhanced hydrologic connectivity with lateral flow was shown to reduce the spatial variability of soil moisture (i.e., homogenizing effect) [*Ivanov et al*., 2010]. In the mapped soil moisture field for point *B* of the $CV_\theta - \langle\theta\rangle$ relation (Figure 13c), soil moisture is greater than field capacity across the domain, but shows a fairly narrow spatial range (0.3-0.33). The control of topographic convergence (network-controlled pattern) can be clearly seen on modeled soil moisture. Besides the role of lateral transport, lack of aspect influence on the incoming solar radiation during NAM (see wetting range in Figure 3), arguably contributes to the low spatial variability of soil moisture between the points *A* and *B* in the $CV_\theta - \langle\theta\rangle$ domain (Figure 13a) by imposing a relatively uniform $T_{\max}$ across the modeled domain.

Consistent with *Ivanov et al*. [2010], we have identified two phases in the drying process of the catchment (Figure 13a). Starting a few storm events after the wettest point *B*, during phase-1 of drying, CV_θ increases as $\langle\theta\rangle$ drops, until the peak CV_θ is reached at point *C*. In phase-2, CV_θ drops rapidly with further decrease of $\langle\theta\rangle$, to the driest pre-NAM soil moisture state. This hysteric pattern, when viewed in relation to soil moisture thresholds reveals the underlying processes that control soil moisture variability. Starting from point *B* (Figure 13a), as soil moisture dries below the field capacity $(\theta_{fc} = 0.22)$ lateral transport ceases gradually across the catchment. Without the homogenizing effect of lateral flow, the $CV_\theta - \langle\theta\rangle$ relation presents a negative linear response, carrying CV_θ to a maximum value (drying phase 1).

The phase-1 of drying corresponds to the fall-winter time frame (October-March) during which the modeled region gradually grows a large contrast in the incoming radiation between the N- and S-facing slopes (Figure 3). Differential drying leads to a strong aspect control on the modeled soil-moisture (aspect-controlled pattern), taking CV_θ to its highest value at point *C*. In the mapped soil moisture field for point *C* (Figure 13d), S-facing slopes experience near wilting point conditions, while most N-facing slopes are above the threshold soil moisture for stomata closure $(\theta_{s*} = 0.13)$ and therefore lead to evapotranspiration at the potential rate. The drying phase-

2 corresponds to March-July period that triggers a rapid homogenization in the soil moisture field. During this period, the incoming solar radiation equilibrates across aspects, and the growing season begins on N-facing slopes where soil moisture is sufficient for growth (Figure 3). The following dry NAM season also follows a similar wetting-drying cycle (inner loop labeled Dryer Cycle), while the weakness of the NAM limits the size of the cycle.

The model-based results of *Ivanov et al*. [2010] reveal a perturbation size (i.e., rainfall depth) required to activate the hysteric response of CV_θ during the drying phase. This evidently is not the case in our simulations in which aspect-control was dominant at all levels of $\langle\theta\rangle$ less than the field capacity. *Ivanov et al*. [2010] use a relatively small, 30 m by 15 m domain with two gently sloping hillslopes and a trough in the middle under central Arizona climate. It is arguable that lack of a perturbation threshold in our simulations could be due to the larger domain modeled with steeper and longer hillslopes with more pronounced aspect influence.

The relationship between the coefficient of spatial variation of vegetation cover, CV_{Vt}, and the mean spatial vegetation cover, $\langle V_t \rangle$, in the Rad-Spatial simulation resembles an obtuse triangle for each year as illustrated by the two continuous $CV_{Vt} - \langle V_t \rangle$ trajectories (Figure 14a). The outer loop is for the wettest year in the last 100-year period of the modeled data (538 mm, labeled Year 54), with the highest biomass production in the model record. The inner loop is the $CV_{Vt} - \langle V_t \rangle$ response of the same year for which the wetting and drying phases of the $CV_\theta - \langle\theta\rangle$ trajectories were presented in Figure 13, and will be discussed in this section. $CV_{Vt} - \langle V_t \rangle$ trajectories start before the growing season with the lowest value of $\langle V_t \rangle$ (see *A* in Figure 14a) of the year typically in April or early May, and end with the last storm of the dry season in the following year (before the start of NAM). Each point in the plot is plotted after a storm event.

Higher spatial variability of vegetation cover is observed when the mean biomass in the modeled domain is low. Seasonal vegetation growth-decay dynamics, indicated by arrows on Figure 14a, lead to a hysteric response of CV_{Vt} as a function of $\langle V_t \rangle$. To illustrate this behavior, we mapped V_t over the simulated domain (Figures 14 b, c, and d) to select $CV_{Vt} - \langle V_t \rangle$ pairs at points *A*, *B*, and *C* of Figure 14a.

At point *A* with minimum $\langle V_t \rangle$ before the beginning of the growing season (end of April) N-facing slopes have relatively higher vegetation cover (Figure 14b). This vegetation map corresponds to the early stages of the 2nd phase of drying (closer to point *C* in Figure 13a). Soil moisture maps in Figures 13c and d show wetter N-facing slops throughout this drying phase. Starting from point *A* in the $CV_{Vt} - \langle V_t \rangle$ domain, the growing season imposes a homogenizing effect in the modeled vegetation domain. Here, the growing season is identified by general climatological conditions that lead to a net increase in biomass. CV_{Vt} first falls rapidly during growth until $\langle V_t \rangle$ reaches a value in the 0.1-0.2 range. This period occurs before the onset of NAM from end of April to July, and is driven by the available root-zone soil moisture from the 2nd phase of drying and some sporadic rainfall pulses within the dry season. In some cases, excessive biomass that grows during this "early growth" decays rapidly, forming a small growth-decay loop within the yearly evolution of the $CV_{Vt} - \langle V_t \rangle$ domain, as can be seen in the high-biomass year.

As $\langle V_t \rangle$ increases during the modeled wet season (i.e., NAM), CV_{Vt} remains at a relatively low and nearly constant value. In Figure 14a point *B* marks the end of the wet season (DOY=281). The maximum value of $\langle V_t \rangle$ in the $CV_{Vt} - \langle V_t \rangle$ domain was reached soon after the wet season, stimulated by the wet-season soil moisture (DOY=302 late October) (point *C*). During the entire growth period from points *A* to *C* in Figure 14a, soil moisture patterns moved from an aspect-controlled pattern to a network-controlled pattern, starting with moisture states closer to the mapped soil moisture state in Figure 13d, passing from Figure 13b and reaching the wettest point towards the end of the wet season in Figure 13c. Presence of sufficient soil moisture in the root zone after the peak soil moisture, point *B* in Figure 13c, led a delay in the peak value of vegetation biomass.

Figures 14c and d reveal an interesting switch in the control of aspect on modeled vegetation patterns, which can be related to the spatial patterns of solar radiation and soil moisture. During the period when soil moisture is sufficient to support vegetation growth (Figures 13c, 14c) S-facing slopes with slightly higher incoming solar radiation (Figure 3) show denser vegetation cover than N-facing slopes. However, this slight growth advantage on S-facing slopes is short-lived. At point *C* with the highest $\langle V_t \rangle$ of the season (DOY=302) (Figure 14a), there is a clear advantage of N-facing slopes and the converging topographic structure in vegetation productivity (Figure 14c).

From point C in the $CV_{Vt} - \langle V_t \rangle$ domain, until the beginning of the growing season in the forthcoming wet season, N-facing slopes will remain to hold more vegetation biomass which will enhance the spatial variability of vegetation cover.

3.5. Discussions and Conclusions

Two main conclusions can be drawn from the vegetation dynamics part of our modeling study. First of all, consistent with field observations [*McMahon*, 1998; *Flores-Cervantes et al*., 2014] and other ecohydrologic modeling studies [*Ivanov et al*., 2008b; *Gutiérrez-Jurado et al*., 2013; *Zhou et al*., 2013] in the region, our model predicts higher vegetation biomass and denser canopy cover on N-facing slopes than the opposing S-facing slopes. The key finding of our modeling study is that favorability of northern slopes for plant productivity is a result of growing differences in the insolation on opposing slopes, with northern slopes receiving less insolation than southern slopes, starting from August, and continuing in the fall and spring months, while insolation during the summer season (wet period) on all aspects is relatively uniform (Figure 3).

Higher rates of modeled *ET* on S-facing slopes lead to drier soil moisture conditions at the beginning of the growing season (e.g., Figure 13d) and enhanced rates of biomass decomposition during the non-growing season. When environmental factors are suitable for growth, relatively higher initial soil moisture on northern aspects provides more suitable conditions for vegetation productivity in the model for northern aspects. This advantage also continues during senescence, as senescence in northern aspects is delayed because of higher soil moisture and lower solar radiation following the wet season, while dryer conditions on S-facing slopes trigger earlier drought-related biomass loss.

Observations of insolation and *ET* at our field catchment on N- and S-facing slopes clearly show this seasonal contrast [*Gutiérrez-Jurado et al*., 2013]. Depending on the slope angle, S-facing slopes receive as much as five times greater insolation during the non-growing season than N-facing slopes. At the plot scale with comparable local slopes, *Gutiérrez-Jurado et al*. [2013] reported greater rates of *ET* on S-facing slopes during the dry season than N-facing slopes using the Bowen Ratio Energy Balance method. At the same catchment, a series of multiple time-lapse, quasi-3D electrical resistivity (ER) measurements reported by *Bass* [2011] along the N to S ecotone gradient reveal faster soil moisture depletion on S-facing slopes than N-facing slopes

between late November and mid March. Greater evaporation losses and early initiation of transpiration was proposed as an explanation of this observation [*Bass*, 2011].

Besides insolation differences, existing vegetation types may contribute to the differences in soil moisture on opposing hillslopes. *Gutiérrez-Jurado et al*. [2013] reported longer soil-moisture recession on N-facing slopes than that on S-facing slopes and attributed this pattern to a legacy effect on soil moisture by the vegetation phenological differences. Over long time scales, this effect led to deeper and more uniform $CaCO_3$ horizons developed on N-facing slopes, as a result of deeper and higher rates of leakage and greater transpiration rates [*Gutiérrez-Jurado et al*. 2006]. Because we used a single plant species, soil moisture legacy was not related to any phenological differences on opposing slopes.

In years with wetter than average monsoon rainfall, an initially counter-intuitive finding in our simulations is higher vegetation biomass on southern aspects toward the end of the wet season. Mechanistically this model prediction can be explained. When soil moisture is sufficient for unstressed evapotranspiration, slightly higher solar radiation on south-facing slopes leads to a short-lived advantage for plant growth on southern aspect (Figure 14c). This illustrates the high sensitivity of the plant growth model to subtle differences in solar radiation. We have not found any evidence in the literature to support this modeling result. This lack of evidence could potentially be due to the short-lived nature of the S-facing slope advantage for plant biomass and difficulty of quantifying this phenomenon using satellite products. Additionally, aforementioned differences in soil texture and composition on opposing hillslopes may not allow this to happen in the real-world.

A typical characteristic of a semiarid ecosystem is increased vegetation productivity in valleys and channels where runoff water converges, as quantified in various earlier field [e.g., *Svoray and Karnieli*, 2011; *Flores-Cervantes et al*., 2014] and modeling studies [e.g., *Ivanov et al*., 2008b; *Collins and Bras*, 2010; *Niu et al*., 2014]. In central New Mexico, *Flores-Cervantes et al.* [2014] examined the role of topography on grassland biomass estimated from Landsat NDVI images (22 images from April to October, between 1984 and 2001). In all the images they analyzed, biomass increased with drainage area consistently. In our model predictions, however, an increase in vegetation cover along the channel network is observed towards the end of the monsoon season when wetter conditions are attained at the whole catchment scale (Figure 14b, c). Modeled vegetation cover averaged over time for the last 100 years of the model simulation consistently

shows a positive dependence to drainage area on S-facing slopes, although the relation is not very strong. Steep N-facing slopes, however, provide more favorable conditions for vegetation growth than other topographic positions on the landscape, while either greater drainage area or shallower slopes on northern aspects result in reduced vegetation cover (Figure 12f). This model finding suggests that increased lateral flow contribution cannot overcome enhanced water-stress in channels. Lack of a strong drainage area control on vegetation biomass in the model may be attributed to the absence of topographic shading in our solar radiation calculations which can lead to a drier bias in soil moisture, resulting in less productive channels than observed field conditions.

An aspect advantage over drainage area for vegetation growth can be observed in our field catchment where coexisting mesic juniper trees and grasses, which prefer wetter environments [*McMahon*, 1998; *Gutiérrez-Jurado et al*., 2013; *Zhou et al*., 2013], occupy predominantly north-facing slopes but not the main valley network. However in the field, we observed alluvial sand depositions in channels. Even under same amount of rainfall forcing, soil texture can have a strong control on available soil water for plants [*Yu et al., 2001*; *English et al*., 2005; *Ivanov et al*., 2008b; *Vivoni et al*., 2010]. Therefore, it is highly critical that changes in soil texture should be a part of analysis in relating vegetation cover to topography.

The spatial variability of modeled root-zone soil moisture and vegetation cover exhibits a hysteric dependence to their corresponding mean spatial values when plotted over a full year. In regard to spatial soil moisture, such dependence have been discussed based on measured and modeled soil moisture fields and related to insolation on topography, evapotranspiration demand, vegetation, and climate variability [e.g., *Teuling et al.,* 2007; *Ivanov et al*., 2010; *Vivoni et al*., 2010]. While evolving both elevation structure and plant biomass, our model reproduces this fundamental spatio-temporal behavior of soil moisture. We have not discussed this topic in further detail, as similar model-based findings were extensively discussed by *Ivanov et al*. [2010].

The rate of vegetation growth is directly related to *ET* and local soil moisture. The amount of total biomass at any given time during the growing season is a function of cumulative *ET* throughout that season, as well as insolation which dead biomass decomposes faster under higher insolation. Therefore, similar to the soil moisture fields, the spatio-temporal variability of modeled vegetation cover also shows a hysteretic dependence to its mean spatial value. In the $CV_{Vt} - \langle V_t \rangle$ space, the growing phase of the vegetation field corresponds to the wetting phase of the soil moisture field, and the decay/senescence phase in the vegetation field corresponds to the drying

phase of the soil moisture field, however with some time-delay at the end points of the $CV_{Vt} - \langle V_t \rangle$ space where phase changes in the spatial response of vegetation occur. During the wet season, when insolation is relatively uniform in space (Figure 3), modeled vegetation cover and soil moisture show relatively low spatial variability (Figures 13a, 14a). After the wet season, and until the beginning of the next growing season, aspect-driven differences in insolation on opposing slopes become more pronounced (Figure 3) and lead to a rapid increase in the spatial variability of vegetation cover as a result of growing differences in *ET*, soil moisture, and rates of grass senescence (Figure 14). This model behavior can be confirmed with some limited empirical data. Analyzing the spatial variability of grass biomass in central New Mexico obtained from Landsat NDVI data, *Flores-Cervantes et al*. [2014] found greater spatial variability of ecosystem productivity during the dry season (before NAM) than that during the wet season. For the days with the highest (lowest) grass biomass they reported *CV*=0.7 (*CV*=0.2).

The *CV* values reported by *Flores-Cervantes et al.,* [2014] for the dry season is comparable with the modeled values plotted in Figure 14a, while our model gives much more spatially uniform vegetation cover during the wet season (see *CV* values near 0 in Figure 14a). *Flores-Cervantes et al*. [2014] only examined around twenty images. More satellite and field data will be needed to study the spatial dynamics of plant response and its linkages with the spatial variability of soil moisture. To the extent that the limited data reported by *Flores-Cervantes et al.,* [2014] represents spatial vegetation response during end-member cases, we may argue that the more uniform response of the model for high-biomass conditions may be attributed to the lack of spatial representation of soil texture, soil depth, and topographic shading. These factors were reported to influence spatial patterns of soil moisture in the literature, and therefore are likely to play a role in the spatio-temporal response of vegetation fields. Further model development will be needed to improve this behavior. A relatively easier next step will be to incorporate a soil evolution model [e.g., *Cohen et al*., 2010; *Pelletier et al*., 2013; *Vanwalleghem et al*., 2013] to our existing model.

The profound contribution of this modeling study is in advancing the understanding of the eco-hydro-geomorphic evolution of catchments. When the aforementioned aspect-driven spatio-temporal dynamics of vegetation and runoff are used in the fluvial erosion and transport processes over geomorphic time scales, opposing N- and S-facing hillsopes evolve into notably different characteristic morphologies. In summary, radiation-driven ecohydrologic dynamics result in steeper, smoother, and less dissected N-facing slopes; and shallower, and more dissected S-facing

slopes. At the landscape scale, these differences lead to asymmetric valley development. These model results qualitatively agree with the findings of earlier studies that used DEMs for topographic analysis [e.g., *Istanbulluoglu et al*., 2008: *Gutiérrez-Jurado and Vivoni,* 2013a]. Model results further provide insights for field testable hypothesis in the intersection of ecohydrology, climate change, and tectonic geomorphology. For example, the modeling outcomes underscore the influence of uplift in modulating the eco-geomorphic evolution of landforms. When uplift was increased in the simulations, distinct topographic features of N- and S-facing hillslopes became more pronounced and the valleys became more asymmetric.

While the model provided interesting and promising results, the coupling between geomorphology and ecohydrology was limited to fluvial processes. This is an important limitation of our model as mounting field evidences relate colluvial transport and bedrock weathering to vegetation and micro-climatic conditions [*Anderson et al*., 2013]. To incorporate such effects to landscape modeling, *Pelletier et al*., [2013] linked colluvial and fluvial transport and bedrock weathering to effective energy and mass transfer concept which represents the contributions of effective precipitation and biomass production on geomorphic processes.

The fact that our model only operates with a single vegetation type remains to be a critical limitation. In semiarid ecosystems, enhanced sediment transport has been associated with vegetation changes related to the woody plant encroachment into grasslands. Integration of multiple plant types and the ability for modeling the competition among tree, grass, and shrub vegetation will open new avenues of research in regional water, sediment, and nutrient balances in semiarid ecosystems using landscape models.

Appendix A. Distribution of Solar Radiation on Topography

$T_{\max}$ on sloping model elements, $T^S_{\max}$, is calculated by scaling the $T_{\max}$ estimated for a flat surface, $T^F_{\max}$, with a solar radiation ratio, R_{solar}. R_{solar} is defined as the ratio of direct beam solar radiation on sloped surfaces, R^S_{cs}, to that of a flat surface, R^F_{cs}:

$$T^S_{\max} = T^F_{\max} \cdot R_{solar} = T^F_{\max} \cdot \frac{R^S_{cs}}{R^F_{cs}}, \qquad (12a)$$

The amount of direct beam solar radiation reach at the ground level depends on several factors: the geometric relations between the Sun and the Earth's surface, atmospheric attenuation, and

topographic factors [*Piedallu and Gegout*, 2008]. Ground level direct beam solar radiation, R_{gl}, can be estimated as:

$$R_{gl} = \frac{I_{sc}}{(d_{Sun})^2} \cos(\theta_z) \exp\left[-n\left(0.128 - 0.054 \log_{10}(m)\right) m\right], \quad \text{(A.1)}$$

where I_{sc} is the solar constant, 1361 Wm^{-2} [*Kopp and Lean*, 2011], d_{Sun} is the relative distance between the Earth and the Sun in astronomical units, $\cos(\theta_z)$ is the solar angle of incidence (angle between solar beam and the normal to the Earth's surface), m is the optical air mass which is $1/\sin(\Upsilon)$, Υ is solar altitude, n is a turbidity factor of air (n=2 for clear air) [Bras, 1990]. The distance parameter, d_{Sun}, can be approximated as:

$$(d_{Sun})^2 = \left[1 + 0.033 \cos\left(\frac{2\pi \times DOY}{365}\right)\right]^{-1}, \quad \text{(A.2)}$$

where DOY is day of the year [*Duffie and Beckman*, 1991].

Topographic factors (hillslope inclination and aspect) are effective on incoming direct beam solar radiation, R_{gl}, by characterizing the solar angle of incidence. The solar angle of incidence is calculated as:

$$\cos(\theta_z) = \cos(S)\sin(\Upsilon) + \sin(S)\cos(\Upsilon)\cos(\psi - \beta), \quad \text{(A.3)}$$

where S is local slope, Υ is the solar altitude, ψ is the azimuth of the Sun, β is aspect, which is an angle between the direction of the slope face and the geographic North in clockwise rotation. The solar altitude is:

$$\sin(\Upsilon) = \sin(\Lambda)\sin(\delta) + \cos(\Lambda)\cos(\delta)\cos(\tau_h) \quad \text{(A.4)}$$

where Λ is the local latitude, τ_h the hour angle of the Sun, δ is the declination angle of the Sun. The azimuth of Sun is

$$\psi = \arctan\left[\frac{\sin(\tau_h)}{\tan(\delta)\cos(\Lambda) - \sin(\Lambda)\cos(\tau_h)}\right]. \quad \text{(A.5)}$$

The declination of the Sun, δ (°) is

$$\delta = 23.45 \cdot \cos\left[\frac{360}{365}(172 - DOY)\right], \quad \text{(A.6)}$$

where *DOY* is the day of year. The hour angle of the Sun, τ_h, is calculated depending on the location of the Sun. If the sun is east (west) of the local latitude, the hour angle of the Sun is calculated by eqn. A.7a (eqn. A.7b)

$$\tau_h = \left(T_s + 12 - \Delta T_1 + \Delta T_2\right) \times 15, \qquad \text{(A.7a)}$$

$$\tau_h = \left(T_s - 12 - \Delta T_1 + \Delta T_2\right) \times 15, \qquad \text{(A.7b)}$$

where T_s is the standard time in the time zone of the observer, ΔT_1 is the time difference between standard and local magnitude in hours, and ΔT_2 is the difference between true solar time and mean solar time in hours, which is usually neglected [*Bras*, 1990].

The instantaneous direct beam insolation can be integrated for a given finite period of time, when δ and Λ are constant over this period. Direct beam insolation is estimated each hour of the day, and integrated over each day of the year. The ratio of R_{cs}^{S} to R_{cs}^{F} , R_{solar}, is approximately equal to the ratio of incoming solar radiation on inclined surface to the flat surface at noon time $\left(\frac{R_{gl\ noon}^{S}}{R_{gl\ noon}^{F}}\right)$ [*Flores-Cervantes*, 2010]. To reduce the computational burden in simulations, it is assumed that the ratio of daily solar radiation is equal to the ratio at noon-time.

Appendix B. Calculation of Potential Transpiration

$T_{\max}$ is calculated by using the Penman-Monteith (P-M) [*Monteith*, 1965] transpiration equation for reference grass [*Allen et al.*, 1989; 1998]. The P-M equation is:

$$T_{\max} = \frac{\Delta\left(R_N - G\right) + \rho_a c_a \dfrac{\left(e_s - e_a\right)}{r_a}}{\lambda_v \rho_w \left[\Delta + \gamma\left(1 + \dfrac{r_s}{r_a}\right)\right]}, \qquad \text{(B.1)}$$

where R_N is the net radiation at the plant canopy, G is ground heat flux, c_a is the specific heat capacity of air, ρ_a and ρ_w are the density of air and water, respectively, λ_v is the latent heat of vaporization, (e_s-e_a) is the vapor pressure deficit between the leaf and the atmosphere, Δ is the slope of the relationship between the saturation vapor pressure and temperature, γ is the psychrometric constant. r_s and r_a [s/m] represent plant canopy and aerodynamic resistance terms, respectively. r_s is estimated by scaling up the stomatal resistance of a well-illuminated leaf, r_l, with the active (sunlit) live leaf area index, LAI_a,: $r_s = r_l / LAI_a$ where $LAI_a = 0.5 LAI_{Rmax}$, r_l =100 s/m, and LAI_{Rmax}=2.88 [*Allen et al.*, 1998]. r_a is calculated based on the von-Karman logarithmic profile as

a function of vegetation height and heights at which wind and relative humidity were measured [*Allen et al.*, 1998].

As expressed in the first term of the P-M equation, $T_{\max}$ increases with R_N. R_N is composed of net shortwave, R_{ns}, and net longwave radiation, R_{nl}:

$$R_N = R_{ns} + R_{nl}, \tag{B.2}$$

where, R_{ns} is the amount of incoming shortwave radiation received by the surface after a fraction of it is reflected from the surface as defined by albedo, a (Figure 1):

$$R_{ns} = (1-a)R_s, \tag{B.3}$$

The incoming shortwave radiation R_s is the source term in equation (B.3). For reference grass a=0.23 [*Allen et al.*, 1998]. In most land surface models, R_s is estimated from extraterrestrial radiation, R_{ext}, or from the clear-sky radiation R_{cs}. R_{ext} is the radiation received at the top of the atmosphere. R_{cs} is the fraction of R_{ext} retained on the surface after the influence of atmospheric water vapor and dust is taken out. R_s is the fraction of R_{cs} received by the surface reduced by clouds and optical transmission losses. R_s can be estimated from extraterrestrial radiation, R_{ext}, by relating R_s to R_{ext} through empirical relations that involve the difference between the minimum and maximum daily temperatures [*Hargreaves and Samani*, 1992; *Thornton and Running*, 1999] or from the clear-sky radiation, R_{cs}, scaled with a function for cloud cover [*Ivanov et al.*, 2004]. Both R_{ext} and R_{cs} can be estimated as a function of day of year, latitude, local slope and aspect [*Bras*, 1990; *Dingman*, 2002] as described in Appendix A.

The net longwave radiation, R_{nl}, in equation (B.2) is the difference between the incoming longwave radiation from the atmosphere, R_{Lin}, and the outgoing longwave radiation from the Earth surface, R_{Lout} (Figure 1). Assuming that the surface temperature is the same as the air temperature, we approximated R_{nl} from the Stefan-Boltzmann law:

$$R_{nl} = R_{Lin} - R_{Lout} = \sigma T_{Ra}^4 - \sigma\left(T_a + 273.15\right)^4, \tag{B.4}$$

where σ is the Stefan-Boltzmann constant (5.67×10^{-8}Wm^{-2}K^{-4}), T_a [K] is the air temperature, and T_{Ra} [K] is the apparent radiative temperature of the atmosphere, which can be calculated by the empirical relationship of [*Friend*, 1995], $T_{Ra} = T_a - 0.825\exp\left(-3.54\times10^{-2} R_s\right)$ as a function of shortwave radiation.

For long-term geomorphic evolution simulations driven by generated rainfall, the model is forced by prescribed $T_{\max}^{F}$, obtained from a cosine function of *DOY*. The cosine function is fitted to calculated $T_{\max}^{F}$ (by equation (B.1), using observed local climatological data) [*Small*, 2005]:

$$T_{\max,DOY}^{F} = \frac{\Delta_d}{2}\cos\left[2\pi\left(\frac{DOY - L_T - N_d/2}{N_d}\right)\right] + \overline{T_{\max}^{F}}, \qquad \text{(B.5)}$$

where Δ_d [mm d^{-1}] is the difference between maximum and minimum values of calibrated daily $T_{\max}^{F}$ throughout a year, L_T [d] is the lag between the peak $T_{\max}^{F}$ and peak solar forcing, N_d is the number of days in a year, $\overline{T_{\max}^{F}}$ is the mean annual of daily $T_{\max}^{F}$.

References

Allen, R. G., M. E. Jensen, J. L. Wright, and R. D. Burman (1989), Operational estimates of reference evapotranspiration, *Agron J*, *81*(4), 650-662.

Allen, R. G., L. S. Pereira, D. Raes, and M. Smith (1998), *Crop Evapotranspiration - Guidelines for computing crop water requirements. FAO Irrigation and Drainage Paper 56*, FAO, Rome, Italy.

Anderson, S. P., R. S. Anderson, G. E. Tucker, and D. P. Dethier (2013b), Critical zone evolution: Climate and exhumation in the Colorado Front Range, Field Guides, 33, 1-18, doi:10.1130/2013.0033(01).

Bass, B. J. (2011), Seasonal soil moisture dynamics throughout a semiarid valley ecotone using quasi-3D time-lapse electrical resistivity imaging, B.S. thesis, The University of Texas, Austin.

Bierman, P. R., J. M. Reuter, K. Pavich, A. C. Gellis, M. W. Caffee, and J. Larsen (2005), Using cosmogenic nuclides to contrast rates of erosion and sediment yield in a semi-arid, arroyo-dominated landscape, Rio Puerco Basin, New Mexico, *Earth Surf Proc Land*, *30*(8), 935-953, doi:10.1002/Esp.1255.

Bonta, J. V. (2004), Stochastic simulation of storm occurrence, depth, duration, and within-storm intensities, *T Asae*, *47*(5), 1573-1584.

Bras, R. L. (1990), *Hydrology: an introduction to hydrologic science*, Addison-Wesley, Reading, Mass.

Brolsma, R. J., and M. F. P. Bierkens (2007), Groundwater-soil water-vegetation dynamics in a temperate forest ecosystem along a slope, *Water Resour Res*, *43*(1), W01414, doi:10.1029/2005wr004696.

Brutsaert, W. (1982), *Evaporation into the Atmosphere*, Reidel Dordrecht, Norwell, Mass.

Burnett, B. N., G. A. Meyer, and L. D. McFadden (2008), Aspect-related microclimatic influences on slope forms and processes, northeastern Arizona, *J Geophys Res-Earth*, *113*, F03002, doi:10.1029/2007JF000789.

Butler, J., H. Goetz, and J. L. Richardson (1986), Vegetation and soil - landscape relationships in the North-Dakota Badlands, *Am Midl Nat*, *116*(2), 378-386.

Cabral, M. C., L. Garrote, R. L. Bras, and D. Entekhabi (1992), A kinematic model of infiltration and runoff generation in layered and sloped soils, *Adv Water Resour*, *15*(5), 311-324, doi:10.1016/0309-1708(92)90017-V

Cayrol, P., A. Chehbouni, L. Kergoat, G. Dedieu, P. Mordelet, and Y. Nouvellon (2000), Grassland modeling and monitoring with SPOT-4 VEGETATION instrument during the 1997-1999 SALSA experiment, *Agr Forest Meteorol*, *105*(1-3), 91-115, doi:10.1016/S0168-1923(00)00191-X.

Chen, X. Y., Y. Rubin, S. Y. Ma, and D. Baldocchi (2008), Observations and stochastic modeling of soil moisture control on evapotranspiration in a Californian oak savanna, *Water Resour Res*, *44*, W08409, doi:10.1029/2007WR006646.

Choi, M., and J. M. Jacobs (2007), Soil moisture variability of root zone profiles within SMEX02 remote sensing footprints, *Adv Water Resour*, *30*(4), 883-896, doi:10.1016/j.advwatres.2006.07.007.

Clapp, E. M., P. R. Bierman, K. K. Nichols, M. Pavich, and M. Caffee (2001), Rates of sediment supply to arroyos from upland erosion determined using *in situ* produced cosmogenic ^{10}Be and ^{26}Al, *Quaternary Res*, *55*(2), 235-245, doi:10.1006/qres.2000.2211

Cohen, S., G. Willgoose, and G. Hancock (2010), The mARM3D spatially distributed soil evolution model: Three-dimensional model framework and analysis of hillslope and landform responses, *J Geophys Res-Earth*, *115*, F04013, doi:10.1029/2009jf001536.

Collins, D. B. G., and R. L. Bras (2008), Climatic control of sediment yield in dry lands following climate and land cover change, *Water Resour Res*, *44*(10), W10405, doi:10.1029/2007WR006474.

Collins, D. B. G., and R. L. Bras (2010), Climatic and ecological controls of equilibrium drainage density, relief, and channel concavity in dry lands, *Water Resour Res*, *46*, W04508, doi:10.1029/2009WR008615.

Collins, D. B. G., R. L. Bras, and G. E. Tucker (2004), Modeling the effects of vegetation-erosion coupling on landscape evolution, *J Geophys Res-Earth*, *109*, F03004, doi:10.1029/2003JF000028.

Connel SD, McCraw DJ. 2007. Preliminary Geologic Map of the La Joya NW Quadrangle, Socorro County, New Mexico. New Mexico Bureau of Geology and Mineral Resources: Socorro, NM.

Coppus, R., and A. C. Imeson (2002), Extreme events controlling erosion and sediment transport in a semi-arid sub-andean valley, *Earth Surf Proc Land*, *27*(13), 1365-1375, doi:10.1002/Esp.435.

Dethier, D. P. (2001), Pleistocene incision rates in the western United States calibrated using Lava Creek B tephra, *Geology*, *29*(9), 783-786, doi:10.1130/0091-7613(2001)029<0783:PIRITW>2.0.CO;2.

Dietrich, W. E., D. G. Bellugi, L. S. Sklar, J. D. Stock, A. M. Heimsath, and J. J. Roering (2003), Geomorphic transport laws for predicting landscape form and dynamics, in *Prediction in Geomorphology*, Geophys. Monogr. Ser., vol. 135, edited by P. R. Wilcock and R. M. Iverson, pp. 103-132, AGU, Washington, D.C.

Dingman, S. L. (2002), *Physical Hydrology*, 2nd ed., Prentice Hall, Upper Saddle River, N.J.

Drissel, J. C., and H. B. Osborn (1968), Variability in rainfall producing runoff from a semiarid rangeland watershed, Alamogordo Creek, New Mexico, *J Hydrol*, *6*(2), 194-201, doi:10.1016/0022-1694(68)90159-5.

du Boys, P. (1879), Le Rhône et les rivières à lit affouillable. Etude du régime du Rhône et de l'action exercée par les eaux sur un lit à fond de graviers indéfiniment affooulilable, *Annales des Ponts et Chaussees*, *49(2)*, 141-195 (in French).

Duffie, J. A., and W. A. Beckman (1991), *Solar engineering of thermal processes*, 2nd ed., John Wiley and Sons, New York.

Dunkerley, D. L. (1992), Channel geometry, bed material, and inferred flow conditions in ephemeral stream systems, Barrier Range, Western NSW Australia, *Hydrol Process*, *6*(4), 417-433, doi:10.1002/hyp.3360060404.

Dunkerley, D. (2010), Ecogeomorphology in the Australian drylands and the role of biota in mediating the effects of climate change on landscape processes and evolution, *Geological Society, London, Special Publications*, *346*(1), 87-120, doi:10.1144/sp346.7.

Dunne, T., W. H. Zhang, and B. F. Aubry (1991), Effects of rainfall, vegetation, and microtopography on infiltration and runoff, *Water Resour Res*, *27*(9), 2271-2285, doi:10.1029/91WR01585

Eagleson, P. S. (1978), Climate, soil, and vegetation 2. The distribution of annual precipitation derived from observed storm sequences, *Water Resour Res*, *14*(5), 713-721, doi:10.1029/WR014i005p00713.

Einstein, H. A., and N. L. Barbarossa (1952), River channel roughness, *T Am Soc Civ Eng*, *117*, 1121-1132.

English, N. B., J. F. Weltzin, A. Fravolini, L. Thomas, and D. G. Williams (2005), The influence of soil texture and vegetation on soil moisture under rainout shelters in a semi-desert grassland, *J Arid Environ*, *63*(1), 324-343, doi:10.1016/j.jaridenv.2005.03.013.

Engman, E. T. (1986), Roughness coefficients for routing surface runoff, *J Irrig Drain E-ASCE*, *112*(1), 39-53.

Famiglietti, J. S., D. R. Ryu, A. A. Berg, M. Rodell, and T. J. Jackson (2008), Field observations of soil moisture variability across scales, *Water Resour Res*, *44*(1), W01423, doi:10.1029/2006WR005804.

Fang, H. L., and S. L. Liang (2005), A hybrid inversion method for mapping leaf area index from MODIS data: experiments and application to broadleaf and needleleaf canopies, *Remote Sens Environ*, *94*(3), 405-424, doi:10.1016/j.rse.2004.11.001.

Flores-Cervantes, J. H. (2010), The coupled development of terrain and vegetation: the case of semiarid grasslands, PhD thesis, MIT, Boston, MA.

Flores Cervantes, J. H., E. Istanbulluoglu, E. R. Vivoni, C. D. Holifield Collins, and R. L. Bras (2014), A geomorphic perspective on terrain-modulated organization of vegetation productivity: analysis in two semiarid grassland ecosystems in Southwestern United States, *Ecohydrology*, *7*(2), 242-257, doi:10.1002/eco.1333.

Foster, G. R. (1982), Modeling the erosion process, in *Hydrologic Modeling of Small Watersheds*, ASAE Monogr., vol. 5, edited by C. T. Haan, pp. 295–380, Am. Soc. Agric. Eng., St. Joseph, Miss.

Friend, A. D. (1995), PGEN: an integrated model of leaf photosynthesis, transpiration, and conductance, *Ecol Model*, *77*(2-3), 233-255, doi:10.1016/0304-3800(93)E0082-E.

Goodrich, D. C., T. O. Keefer, C. L. Unkrich, M. H. Nichols, H. B. Osborn, J. J. Stone, and J. R. Smith (2008), Long-term precipitation database, Walnut Gulch Experimental Watershed, Arizona, United States, *Water Resour Res*, *44*(5), W05s04, doi:10.1029/2006wr005782.

Gosz, J.R. 2012a. Bowen Ratio evapotranspiration data at the Sevilleta National Wildlife Refuge, New Mexico, 1996-1999. Albuquerque, NM: Sevilleta Long Term Ecological Research Database: SEV079. http://sev.lternet.edu/data/sev-79 (12 Jan 2014).

Gosz, J.R. 2012b. Time Domain Reflectometry at the Sevilleta National Wildlife Refuge, New Mexico, 1996-2005. Albuquerque, NM: Sevilleta Long Term Ecological Research Database: SEV078. http://sev.lternet.edu/data/sev-78 (12 Jan 2014).

Gosz, R. J., and J. R. Gosz (1996), Species interactions on the biome transition zone in New Mexico: Response of blue grama (Bouteloua gracilis) and black grama (*Bouteloua eripoda*) to fire and herbivory, *J Arid Environ*, *34*(1), 101-114, doi:10.1006/jare.1996.0096.

Gosz, J. R., D. I. Moore, G. A. Shore, H. D. Grover, W. Rison, and C. Rison (1995), Lightning estimates of precipitation location and quantity on the Sevilleta LTER, New Mexico, *Ecol Appl*, *5*(4), 1141-1150, doi:10.2307/2269361.

Govers, G. (1992), Evaluation of transporting capacity formulae for overland flow conditions, in *Overland Flow, Hydraulics and Erosion Mechanics*, edited by A. J. Parsons and A. D. Abrahams, pp. 243-273, UCL Press, London.

Grayman, W. M., and P. S. Eagleson (1969), Streamflow Record Length for Modelling Catchment Dynamics*Rep.*, M.I.T. Press, Cambridge, Mass.

Gregory, K. J. (1976), Drainage networks and climate, in *Geomorphology and Climate*, edited by E. Derbyshire, pp. 289-315, John Wiley&Sons, London.

Gutiérrez-Jurado, H. A., and E. R. Vivoni (2013a), Ecogeomorphic expressions of an aspect-controlled semiarid basin: I. Topographic analyses with high-resolution data sets, *Ecohydrology*, *6*(1), 8-23, doi:10.1002/Eco.280.

Gutiérrez-Jurado, H. A., E. R. Vivoni, J. B. J. Harrison, and H. Guan (2006), Ecohydrology of root zone water fluxes and soil development in complex semiarid rangelands, *Hydrol Process*, *20*(15), 3289-3316, doi:10.1002/Hyp.6333.

Gutiérrez-Jurado, H. A., E. R. Vivoni, E. Istanbulluoglu, and R. L. Bras (2007), Ecohydrological response to a geomorphically significant flood event in a semiarid catchment with contrasting ecosystems, *Geophys Res Lett*, *34*(24), L24S25, doi:10.1029/2007GL030994.

Gutiérrez-Jurado, H. A., E. R. Vivoni, C. Cikoski, J. B. J. Harrison, R. L. Bras, and E. Istanbulluoglu (2013), On the observed ecohydrologic dynamics of a semiarid basin with aspect-delimited ecosystems, *Water Resour Res*, *49*(12), 8263-8284, doi:10.1002/2013wr014364.

Hargreaves, G. H., and Z. A. Samani (1982), Estimating potential evapotranspiration, *Journal of the Irrigation and Drainage Division*, *108*(3), 225-230.

Hillel, D. (2006), *The natural history of the Bible: an environmental exploration of the Hebrew scriptures*, Columbia University Press, New York.

Istanbulluoglu, E., and R. L. Bras (2005), Vegetation-modulated landscape evolution: Effects of vegetation on landscape processes, drainage density, and topography, *J Geophys Res-Earth*, *110*, F02012, doi:10.1029/2004JF000249.

Istanbulluoglu, E., and R. L. Bras (2006), On the dynamics of soil moisture, vegetation, and erosion: Implications of climate variability and change, *Water Resour Res*, *42*, W06418, doi:10.1029/2005WR004113.

Istanbulluoglu, E., T. J. Wang, and D. A. Wedin (2012), Evaluation of ecohydrologic model parsimony at local and regional scales in a semiarid grassland ecosystem, *Ecohydrology*, *5*(1), 121-142, doi:10.1002/Eco.211.

Istanbulluoglu, E., D. G. Tarboton, R. T. Pack, and C. Luce (2003), A sediment transport model for incision of gullies on steep topography, *Water Resour Res*, *39*(4), 1103, doi:10.1029/2002WR001467.

Istanbulluoglu, E., O. Yetemen, E. R. Vivoni, H. A. Gutierrez-Jurado, and R. L. Bras (2008), Eco-geomorphic implications of hillslope aspect: Inferences from analysis of landscape morphology in central New Mexico, *Geophys Res Lett*, *35*, L14403, doi:10.1029/2008GL034477.

Ivanov, V. Y., E. R. Vivoni, R. L. Bras, and D. Entekhabi (2004), Catchment hydrologic response with a fully distributed triangulated irregular network model, *Water Resour Res*, *40*(11), W11102, doi:10.1029/2004wr003218.

Ivanov, V. Y., R. L. Bras, and D. C. Curtis (2007), A weather generator for hydrological, ecological, and agricultural applications, *Water Resour Res*, *43*, W10406, doi:10.1029/2006WR005364.

Ivanov, V. Y., R. L. Bras, and E. R. Vivoni (2008a), Vegetation-hydrology dynamics in complex terrain of semiarid areas: 1. A mechanistic approach to modeling dynamic feedbacks, *Water Resour Res*, *44*, W03429, doi:10.1029/2006WR005588.

Ivanov, V. Y., R. L. Bras, and E. R. Vivoni (2008b), Vegetation-hydrology dynamics in complex terrain of semiarid areas: 2. Energy-water controls of vegetation spatiotemporal dynamics and topographic niches of favorability, *Water Resour Res*, *44*(3), W03430, doi:10.1029/2006WR005595.

Ivanov, V. Y., S. Fatichi, G. D. Jenerette, J. F. Espeleta, P. A. Troch, and T. E. Huxman (2010), Hysteresis of soil moisture spatial heterogeneity and the "homogenizing" effect of vegetation, *Water Resour Res*, *46*, W09521, doi:10.1029/2009wr008611.

Kidron, G. J. (1999), Differential water distribution over dune slopes as affected by slope position and microbiotic crust, Negev Desert, Israel, *Hydrol Process*, *13*(11), 1665-1682, doi:10.1002/(SICI)1099-1085(19990815)13:11<1665::AID-HYP836>3.0.CO;2-R.

Kirkby, M. J., Hillslope process-response models based on the continuity equation, *Spec. Publ. Inst. Br. Geogr.,* 3, 15–30, 1971.

Kopp, G., and J. L. Lean (2011), A new, lower value of total solar irradiance: Evidence and climate significance, *Geophys Res Lett*, *38*(1), L01706, doi:10.1029/2010gl045777.

Kunkel, M. L., A. N. Flores, T. J. Smith, J. P. McNamara, and S. G. Benner (2011), A simplified approach for estimating soil carbon and nitrogen stocks in semi-arid complex terrain, *Geoderma*, *165*(1), 1-11, doi:10.1016/j.geoderma.2011.06.011.

Kurc, S. A., and E. E. Small (2004), Dynamics of evapotranspiration in semiarid grassland and shrubland ecosystems during the summer monsoon season, central New Mexico, *Water Resour Res*, *40*, W09305, doi:10.1029/2004WR003068.

Laio, F., A. Porporato, L. Ridolfi, and I. Rodriguez-Iturbe (2001), Plants in water-controlled ecosystems: active role in hydrologic processes and response to water stress II. Probabilistic soil moisture dynamics, *Adv Water Resour*, *24*(7), 707-723, doi:10.1016/S0309-1708(01)00005-7.

Langbein, W. B., and S. Schumm (1958), Yield of sediment in relation to mean annual precipitation, *Transactions, American Geophysical Union*, *39*, 1076-1084.

Lauenroth, W. K., and J. B. Bradford (2009), Ecohydrology of dry regions of the United States: precipitation pulses and intraseasonal drought, *Ecohydrology*, *2*(2), 173-181, doi:10.1002/Eco.53.

Laursen, E. M., The total sediment load of streams, J. Hydraul. Div. Am. Soc. Civ. Eng., 84(1530), 1 – 6, 1958.

Lawrence, J. E., and G. M. Hornberger (2007), Soil moisture variability across climate zones, *Geophys Res Lett*, *34*(20), L20402, doi:10.1029/2007gl031382.

Lee, T. J. (1992), The impact of vegetation on the atmospheric boundary layer and convective storms, Ph.D. dissertation thesis, Colorado State University, Fort Collins, Colorado.

Levins, R. (1969), Some demographic and genetic consequences of environmental heterogeneity for biological control, *Bulletin of the ESA*, *15*(3), 237-240.

Loik, M. E., D. D. Breshears, W. K. Lauenroth, and J. Belnap (2004), A multi-scale perspective of water pulses in dryland ecosystems: climatology and ecohydrology of the western USA, *Oecologia*, *141*(2), 269-281, doi:10.1007/s00442-004-1570-y.

Ma, L., L. X. Jin, and S. L. Brantley (2011), How mineralogy and slope aspect affect REE release and fractionation during shale weathering in the Susquehanna/Shale Hills Critical Zone Observatory, *Chem Geol*, *290*(1-2), 31-49, doi:10.1016/j.chemgeo.2011.08.013.

Mascaro, G., E. R. Vivoni, and R. Deidda (2011), Soil moisture downscaling across climate regions and its emergent properties, *J Geophys Res-Atmos*, *116*, D22114, doi:10.1029/2011jd016231.

McMahon, D. R. (1998), Soil, landscape and vegetation interactions in small semi-arid drainage basin: Sevilleta National Wildlife Refuge, New Mexico, NMTech, Socorro, NM.

Milne, B. T., D. I. Moore, J. L. Betancourt, J. A. Fairchild-Parks, T. W. Swetnam, R. R. Parmenter, and W. T. Pockman (2003), Multidecadal drought cycles in South-central New Mexico: Patterns and consequences, in *Climate Variabililty and Ecosystem Response at Long Term Ecological Research (LTER) Sites*, edited by D. Greenland, D. Goodin and R. Smith, pp. 286-307, Oxford University Press, New York.

Moglen, G. E., E. A. B. Eltahir, and R. L. Bras (1998), On the sensitivity of drainage density to climate change, *Water Resour Res*, *34*(4), 855-862, doi:10.1029/97WR02709.

Molnár, P., and J. A. Ramírez (2001), Recent trends in precipitation and streamflow in the Rio Puerco Basin, *J Climate*, *14*(10), 2317-2328, doi:10.1175/1520-0442(2001)014<2317:RTIPAS>2.0.CO;2.

Montaldo, N., R. Rondena, J. D. Albertson, and M. Mancini (2005), Parsimonious modeling of vegetation dynamics for ecohydrologic studies of water-limited ecosystems, *Water Resour Res*, *41*(10), W10416, doi:10.1029/2005wr004094.

Monteith, J. L. (1965), Evaporation and environment, *Symp Soc Exp Biol*, *19*, 205-234.

Moore, D.I. 2012. Meteorology data at the Sevilleta National Wildlife Refuge, New Mexico. Albuquerque, NM: Sevilleta Long Term Ecological Research Database: SEV001. http://sev.lternet.edu/data/sev-1 (12 Jan 2014).

Mudd, S. M. (2006), Investigation of the hydrodynamics of flash floods in ephemeral channels: Scaling analysis and simulation using a shock-capturing flow model incorporating the effects of transmission losses, *J Hydrol*, *324*(1-4), 65-79, doi:10.1016/j.jhydrol.2005.09.012.

Murray, A. B., and C. Paola (2003), Modelling the effect of vegetation on channel pattern in bedload rivers, *Earth Surf Proc Land*, *28*(2), 131-143, doi:10.1002/Esp.428.

Mutziger, A. J., C. M. Burt, D. J. Howes, and R. G. Allen (2005), Comparison of measured and FAO-56 modeled evaporation from bare soil, *J Irrig Drain E-Asce*, *131*(1), 59-72, doi:10.1061/(ASCE)0733-9437(2005)131:1(59).

Nearing, M. A., J. R. Simanton, L. D. Norton, S. J. Bulygin, and J. Stone (1999), Soil erosion by surface water flow on a stony, semiarid hillslope, *Earth Surf Proc Land*, *24*(8), 677-686, doi:10.1002/(SICI)1096-9837(199908)24:8<677::AID-ESP981>3.3.CO;2-T.

Niu, G.-Y., P. A. Troch, C. Paniconi, R. L. Scott, M. Durcik, X. Zeng, T. Huxman, D. Goodrich, and J. Pelletier (2014), An integrated modelling framework of catchment-scale ecohydrological processes: 2. The role of water subsidy by overland flow on vegetation dynamics in a semi-arid catchment, *Ecohydrology*, *7*(2), 815-827, doi:10.1002/eco.1405.

Parsons, A. J., J. Wainwright, P. M. Stone, and A. D. Abrahams (1999), Transmission losses in rills on dryland hillslopes, *Hydrol Process*, *13*(17), 2897-2905, doi:10.1002/(SICI)1099-1085(19991215)13:17<2897::AID-HYP905>3.0.CO;2-B.

Pelletier, J. D., et al. (2013), Coevolution of nonlinear trends in vegetation, soils, and topography with elevation and slope aspect: A case study in the sky islands of southern Arizona, *J Geophys Res-Earth*, *118*(2), 741-758, doi:10.1002/Jgrf.20046.

Penna, D., H. J. Tromp-van Meerveld, A. Gobbi, M. Borga, and G. Dalla Fontana (2011), The influence of soil moisture on threshold runoff generation processes in an alpine headwater catchment, *Hydrol Earth Syst Sc*, *15*(3), 689-702, doi:10.5194/hess-15-689-2011.

Perron, J. T., W. E. Dietrich, and J. W. Kirchner (2008), Controls on the spacing of first-order valleys, *J Geophys Res-Earth*, *113*(F4), F04016, doi:10.1029/2007jf000977.

Piedallu, C., and J. Gegout (2008), Efficient assessment of topographic solar radiation to improve plant distribution models, *Agr Forest Meteorol*, *148*(11), 1696-1706, doi:0.1016/j.agrformet.2008.06.001.

Pierce, J. K. B., T. Lookingbill, and D. Urban (2005), A simple method for estimating potential relative radiation (PRR) for landscape-scale vegetation analysis, *Landscape Ecol*, *20*(2), 137-147, doi:10.1007/s10980-004-1296-6.

Pierce, K. L., and S. M. Colman (1986), Effect of height and orientation (microclimate) on geomorphic degradation rates and processes, late-glacial terrace scarps in central Idaho, *Geol Soc Am Bull*, *97*(7), 869-885, doi:10.1130/0016-7606(1986)97<869:EOHAOM>2.0.CO;2.

Polyakov, V. O., M. A. Nearing, M. H. Nichols, R. L. Scott, J. J. Stone, and M. P. McClaran (2010), Long-term runoff and sediment yields from small semiarid watersheds in southern Arizona, *Water Resour Res*, *46*, W09512, doi:10.1029/2009WR009001.

Porporato, A., E. Daly, and I. Rodriguez-Iturbe (2004), Soil water balance and ecosystem response to climate change, *Am Nat*, *164*(5), 625-632, doi:10.1086/424970.

Poulos, M. J., J. L. Pierce, A. N. Flores, and S. G. Benner (2012), Hillslope asymmetry maps reveal widespread, multi-scale organization, *Geophys Res Lett*, *39*, L06406, doi:10.1029/2012GL051283.

Roering, J. J., J. W. Kirchner, and W. E. Dietrich (1999), Evidence for nonlinear, diffusive sediment transport on hillslopes and implications for landscape morphology, *Water Resour Res*, *35*(3), 853-870, doi:10.1029/1998wr900090.

Roering, J. J., J. T. Perron, and J. W. Kirchner (2007), Functional relationships between denudation and hillslope form and relief, *Earth Planet Sc Lett*, *264*(1-2), 245-258, doi:10.1016/j.epsl.2007.09.035.

Rosenbaum, U., H. R. Bogena, M. Herbst, J. A. Huisman, T. J. Peterson, A. Weuthen, A. W. Western, and H. Vereecken (2012), Seasonal and event dynamics of spatial soil moisture patterns at the small catchment scale, *Water Resour Res*, *48*, W10544, doi:10.1029/2011wr011518.

Ryu, D., and J. S. Famiglietti (2005), Characterization of footprint-scale surface soil moisture variability using Gaussian and beta distribution functions during the Southern Great Plains

1997 (SGP97) hydrology experiment, *Water Resour Res*, *41*(12), W12433, doi:10.1029/2004WR003835.

Sala, O. E., and W. K. Lauenroth (1982), Small rainfall events: An ecological role in semiarid regions, *Oecologia*, *53*(3), 301-304, doi:10.1007/Bf00389004.

Shabanov, N. V., et al. (2005), Analysis and optimization of the MODIS leaf area index algorithm retrievals over broadleaf forests, *IEEE Transactions on Geoscience and Remote Sensing*, *43*(8), 1855-1865, doi:10.1109/Tgrs.2005.852477.

Shields, A. (1936), Application of similarity principles and turbulence research to bed-load movement (in German), No. 26, Preuss. Vers. Anst. Wasserb. Schiffb. (English translation is available as *Hydrodyn. Lab. Publ. 167*, Hydrodyn. Lab., Calif. Inst. of Technol., Pasadena).

Simons, D. B., and F. Şentürk (1992), *Sediment transport technology: water and sediment dynamics*, Water Resources Publications, Littleton, Colorado.

Sitch, S., et al. (2003), Evaluation of ecosystem dynamics, plant geography and terrestrial carbon cycling in the LPJ dynamic global vegetation model, *Global Change Biol*, *9*(2), 161-185, doi:10.1046/j.1365-2486.2003.00569.x.

Small, E. E. (2005), Climatic controls on diffuse groundwater recharge in semiarid environments of the southwestern United States, *Water Resour Res*, *41*, W04012, doi:10.1029/2004WR003193.

Soil Survey Staff Natural Resources Conservation Service, United States Department of Agriculture. Web Soil Survey. Available online at http://websoilsurvey.nrcs.usda.gov/. Accessed [05/27/2012].

Stone, J. J., M. H. Nichols, D. C. Goodrich, and J. Buono (2008), Long-term runoff database, Walnut Gulch Experimental Watershed, Arizona, United States, *Water Resour Res*, *44*, W05S05, doi:10.1029/2006WR005733.

Summerfield, M. A., and N. J. Hulton (1994), Natural controls of fluvial denudation rates in major world drainage basins, *J Geophys Res-Sol Ea*, *99*(B7), 13871-13883, doi:10.1029/94jb00715.

Svoray, T., and A. Karnieli (2011), Rainfall, topography and primary production relationships in a semiarid ecosystem, *Ecohydrology*, *4*(1), 56-66, doi:10.1002/Eco.123.

Swenson, J. J., and R. H. Waring (2006), Modelled photosynthesis predicts woody plant richness at three geographic scales across the north-western United States, *Global Ecol Biogeogr*, *15*(5), 470-485, doi:10.1111/j.1466-822x.2006.00242.x.

Tarboton, D. G., R. L. Bras, and I. Rodriguez-Iturbe (1991), On the extraction of channel networks from digital elevation data, *Hydrol Process*, *5*(1), 81-100, doi:10.1002/hyp.3360050107.

Teuling, A. J., F. Hupet, R. Uijlenhoet, and P. A. Troch (2007), Climate variability effects on spatial soil moisture dynamics, *Geophys Res Lett*, *34*(6), L06406, 10.1029/2006gl029080.

Thornes, J. B. (1990), The interaction of erosional and vegetational dynamics in land degradation: spatial outcomes, in *Vegetation and Erosion* edited by J. B. Thornes, pp. 41-53, John Wiley and Sons Ltd., Chichester.

Thornton, P. E., and S. W. Running (1999), An improved algorithm for estimating incident daily solar radiation from measurements of temperature, humidity, and precipitation, *Agr Forest Meteorol*, *93*(4), 211-228, doi:10.1016/S0168-1923(98)00126-9.

Tucker, G. E., and R. L. Bras (1998), Hillslope processes, drainage density, and landscape morphology, *Water Resour Res*, *34*(10), 2751-2764, doi:10.1029/98WR01474.

Tucker, G. E., and R. L. Bras (2000), A stochastic approach to modeling the role of rainfall variability in drainage basin evolution, *Water Resour Res*, *36*(7), 1953-1964, doi:10.1029/2000WR900065.

Tucker, G. E., and G. R. Hancock (2010), Modelling landscape evolution, *Earth Surf Proc Land*, *35*(1), 28-50, Doi 10.1002/Esp.1952.

Tucker, G. E., S. T. Lancaster, N. M. Gasparini, and R. L. Bras (2001a), The Channel-Hillslope Integrated Landscape Development model (CHILD), in *Landscape Erosion and Evolution Modeling*, edited by R. S. Harmon and W. W. Doe III, pp. 349-388, Kluwer Academic, New York.

Tucker, G. E., S. T. Lancaster, N. M. Gasparini, R. L. Bras, and S. M. Rybarczyk (2001b), An object-oriented framework for distributed hydrologic and geomorphic modeling using triangulated irregular networks, *Comput Geosci*, *27*(8), 959-973, doi:10.1016/S0098-3004(00)00134-5.

Vanwalleghem, T., U. Stockmann, B. Minasny, and A. B. McBratney (2013), A quantitative model for integrating landscape evolution and soil formation, *J Geophys Res-Earth*, *118*(2), 331-347, doi:10.1029/2011jf002296.

Vereecken, H., T. Kamai, T. Harter, R. Kasteel, J. Hopmans, and J. Vanderborght (2007), Explaining soil moisture variability as a function of mean soil moisture: A stochastic unsaturated flow perspective, *Geophys Res Lett*, *34*(22), L22402, doi:10.1029/2007GL031813.

Vivoni, E. R., R. S. Bowman, R. L. Wyckoff, R. T. Jakubowski, and K. E. Richards (2006), Analysis of a monsoon flood event in an ephemeral tributary and its downstream hydrologic effects, *Water Resour Res*, 42(3), W03404, doi:10.1029/2005WR004036.

Vivoni, E. R., H. A. Moreno, G. Mascaro, J. C. Rodriguez, C. J. Watts, J. Garatuza-Payan, and R. L. Scott (2008), Observed relation between evapotranspiration and soil moisture in the North American monsoon region, *Geophys Res Lett*, *35*, L22403, doi:10.1029/2008GL036001.

Vivoni, E. R., K. Tai, and D. J. Gochis (2009), Effects of initial soil moisture on rainfall generation and subsequent hydrologic response during the North American Monsoon, *J Hydrometeorol*, *10*(3), 644-664, doi:10.1175/2008jhm1069.1.

Vivoni, E. R., J. C. Rodriguez, and C. J. Watts (2010), On the spatiotemporal variability of soil moisture and evapotranspiration in a mountainous basin within the North American monsoon region, *Water Resour Res*, *46*, W02509, doi:10.1029/2009wr008240.

Wainwright, J., and A. J. Parsons (2002), The effect of temporal variations in rainfall on scale dependency in runoff coefficients, *Water Resour Res*, *38*(12), 1271, doi:10.1029/2000WR000188.

Western, A., R. Grayson, G. Blöschl, and D. Wilson (2003), Spatial variability of soil moisture and its implications for scaling, in *Scaling Methods in Soil Physics*, edited by Y. A. Perchepsky, H. M. Selim and D. E. Radcliffe, pp. 119-142, CRC Press: New York, Boca Raton, Fla.

Wigmosta, M. S., L. W. Vail, and D. P. Lettenmaier (1994), A distributed hydrology-vegetation model for complex terrain, *Water Resour Res*, *30*(6), 1665-1679, 10.1029/94wr00436.

Willgoose, G., R. L. Bras, and I. Rodriguez-Iturbe (1991), A coupled channel network growth and hillslope evolution model .1. Theory, *Water Resour Res*, *27*(7), 1671-1684, doi:10.1029/91wr00935.

Wilson, L. (1973), Variations in mean annual sediment yield as a function of mean annual precipitation, *American Journal of Science*, *273*(4), 335-349.

Yu, Z. B., T. N. Carlson, E. J. Barron, and F. W. Schwartz (2001), On evaluating the spatial-temporal variation of soil moisture in the Susquehanna River Basin, *Water Resour Res*, *37*(5), 1313-1326, doi:10.1029/2000wr900369.

Zhou, X., E. Istanbulluoglu, and E. R. Vivoni (2013), Modeling the ecohydrological role of aspect-controlled radiation on tree-grass-shrub coexistence in a semiarid climate, *Water Resour Res*, *49*(5), 2872-2895, doi:10.1002/wrcr.20259.

Zou, C. B., G. A. Barron-Gafford, and D. D. Breshears (2007), Effects of topography and woody plant canopy cover on near-ground solar radiation: Relevant energy inputs for ecohydrology and hydropedology, *Geophys Res Lett*, *34*(24), L24S21, doi:10.1029/2007GL031484.

TABLES:

Table 1. Equations and references of the terms in (14a) and (14b)

Ecophysiological Term	Equation	Source[a]
Allocation coefficient for aboveground live biomass	$\phi_a = \left(1 - \frac{LAI_g}{LAI_{\max} - LAI_d}\right)$	1
Live biomass water-stress coefficient	$\xi_{sl} = \begin{cases} 0 & s^* \le s \\ \left(\frac{s^* - s}{s^* - s_{wp}}\right)^4 & s_{wp} \le s \le s^* \\ 1 & s \le s_{wp} \end{cases}$	2
Climate influence on dead biomass loss coefficient	$\xi_{sd} = \min\left(\frac{T_{\max}}{PET_{d\max}}, 1\right)$	1
Live and dead *LAI*	$LAI_l = c_g B_l$, and $LAI_d = c_d B_d$	1
Total *LAI*	$LAI_t = LAI_l + LAI_d$	1
Total vegetation cover fraction	$V_t = 1 - \exp(-0.75 LAI_t)$	3

[a] Sources are as follows: (1) *Istanbulluoglu et al.*, [2012] , (2) *Laio et al.*, [2001]; (3) *Lee*, [1992].

1

Table 2: Equations of the terms in equations (4, 16, 17a, 17b)

Geomorphological Term	Equation	Source[a]
Nonlinear hillslope diffusion	$q_{sd} = \frac{K_d S}{1-\left(S/S_c\right)^2}$	1
Detachment capacity	$q_d = k_d\left(\tau_{eff} - \tau_{cd}\right)^{pd}$	2
Transport capacity	$q_s = k_f\left(\tau_{eff} - \tau_c\right)^{pf}$	3
Sediment transport coefficient	$k_f = \kappa\frac{\sqrt{g\left(\rho_s/\rho_w - 1\right)d_{50}^3}}{\left[\rho_w g\left(\rho_s/\rho_w - 1\right)d_{50}\right]^{pf}}$	4
Vegetation roughness	$n_v = n_{VR}\left(\frac{V_t}{V_R}\right)^{\omega}$	5

[a] Sources are as follows: (1) *Roering et al*., [1999]; (2) *Nearing et al*., [1999]; (3) *Du Boys*, [1879]; (4) *Simons and Senturk,* [1977]; (5) *Istanbulluoglu and Bras*, [2005].

Table 3: Model parameters definitions and sources for the values used in the model

Parameter Definition	Variable	Value	Method
	Geomorphology Parameters		
Mean grain size diameter	d_{50}	0.007 m	approximated
Manning's roughness for bare soil	n_s	0.05 [-]	*Engman*, [1986]
Manning's roughness for reference vegetation cover	n_v	0.5 [-]	*Engman*, [1986]
Reference vegetation cover	V_R	0.95 [-]	*Istanbulluoglu and Bras*, [2005]
Reference vegetation cover exponent	ω	0.5 [-]	*Istanbulluoglu and Bras*, [2005]
Hillslope diffusivity coefficient	K_d	0.003 $m^2 y^{-1}$	*Roering et al*., [2007]
Hillslope diffusivity critical gradient	S_c	1.2 [-]	*Roering et al*., [1999; 2007]
Sediment transport calibration coefficient	κ	20 [-]	*Simons and Şentürk*, [1992]
Dimensionless critical shear stress	τ^*	0.045 [-]	*Istanbulluoglu et al*., [2002]
Critical shear stress for sediment transport	τ_c	5 Pa	estimated
Detachment-limited exponent	pd	2.377 [-]	*Nearing et al.*, [1999]
Transport-limited exponent	pf	2.5 [-]	*Govers* [1992]
Detachment-limited erodibility coefficient	k_d	0.449 m y^{-1}	*Nearing et al.*, [1999]
Shape constant	C	0.346 [-]	*Istanbulluoglu et al*., [2003]
	Soil Parameters		
Soil texture		loamy sand	[*Soil Survey Staff*]
Porosity	n	0.42 [-]	[*Soil Survey Staff*]
Bare soil infiltration capacity	$I_{c,bare}$	12 mm h^{-1}	approximated
Vegetated infiltration capacity	$I_{c,veg}$	36 mm yh^{-1}	approximated
Anisotropy ratio	A_R	1000 [-]	approximated
Empirical parameter in the Campbell model	b	4.85 [-]	*Laio et al.,* [2001]
Hygroscopic capacity	s_h	0.1 [-]	*Laio et al.,* [2001]
Wilting point	s_w	0.17 [-]	estimated
Incipient stomata closure	s^*	0.31 [-]	estimated
Field capacity	s_{fc}	0.52 [-]	*Laio et al.,* [2001]
	Climate Parameters		
Mean annual precipitation	MAP	249.6 mm y^{-1}	Observation
Fraction of wet season duration	F_{wet}	0.252 [-]	Observation
Fraction of wet season precipitation	F_p	0.496 [-]	Observation
Poisson storm scale factor	α	6.0 [-]	calibrated
Rainfall intensity after scale calibration (wet/dry seasons)	$\overline{p'}$	8.73/2.91 mm h^{-1}	*Small*, [2005]

Interstorm duration after scale calibration (wet/dry)	$\overline{T_b'}$	114.3/253.3h^{-1}	*Small*, [2005]
Storm duration after scale calibration (wet/dry)	$\overline{T_r'}$	0.77/1.71h^{-1}	*Small*, [2005]
Vegetation Parameters			
Plant species		blue grama	*Moore*, [2012]
Effective rooting depth	D_r	0.30 m	*Kurc and Small,* [2004]
Bare soil evaporation coefficient	k_s	0.7 [-]	*Istanbulluoglu et al.,* [2012]
Growth threshold	GT	4.93 mm d^{-1}	calibrated
Dormancy threshold	DT	4.93 mm d^{-1}	calibrated
Natural decay factor for live biomass	k_{sl}	0.012 d^{-1}	*Istanbulluoglu et al.,* [2012]
Natural decay factor for dead biomass	k_{dd}	0.05 d^{-1}	calibrated
Constant for dead biomass loss adjustment	$PETd_{max}$	6.0 mm d^{-1}	calibrated
Water use efficiency	WUE	0.005 kg CO_2 / kg H_2O	approximated
Drought-induced foliage loss factor	k_{sf}	0.04 d^{-1}	*Ivanov et al.,* [2008a]
Specific leaf area for live biomass	c_g	4.7 m^{2}kg^{-1} DM	*Istanbulluoglu et al.* [2012]
Specific leaf area for dead biomass	c_d	9.0 m^{2}kg^{-1} DM	*Istanbulluoglu et al.* [2012]
Maximum leaf area index	LAI_{Max}	5.0 [-]	*Istanbulluoglu et al.* [2012]
Vegetation destruction parameter	k_v	100 Pa^{-1} yr^{-1}	calibrated

Table 4. Drainage density, D_d (km/km^2), and north-south hillslope asymmetry, $HA_{N\text{-}S}$, indices for modeled and field catchments.

Parameter	Field Site	Radiation	No Uplift	Low Uplift	High Uplift
D_d (km/km^2)	10.94	Spatial	9.43	11.00	11.39
		Uniform	(9.87)	(10.33)	(10.61)
$HA_{N\text{-}S}$	0.086	Spatial	0.060	0.098	0.131
		Uniform	(0.037)	(-0.0002)	(0.002)

FIGURES

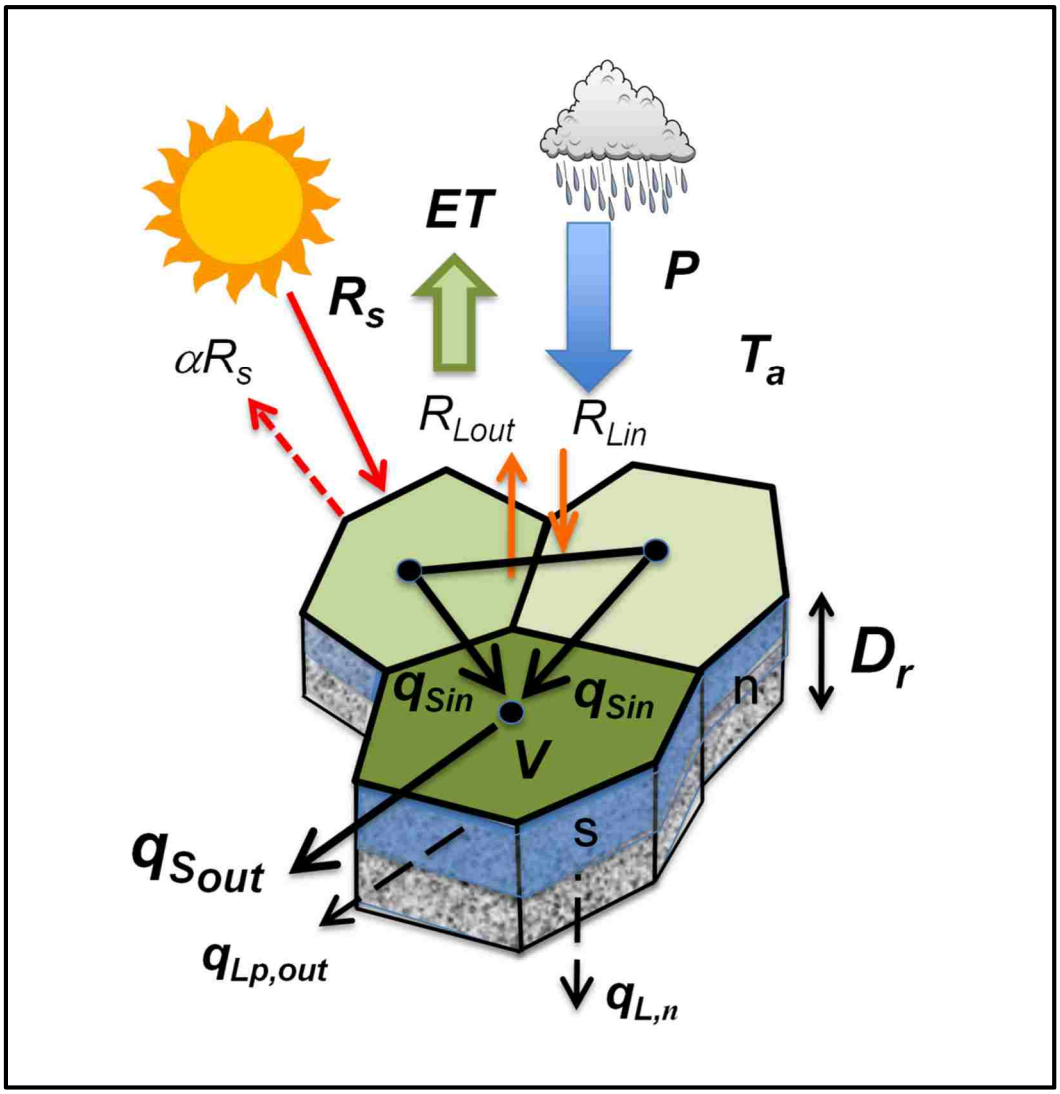

Figure 1. Illustration of the modeled energy, water, and sediment fluxes, and soil water variables in a Voronoi cell used in the CHILD landscape evolution model. Major components of R_N, longwave and shortwave radiation are shown.

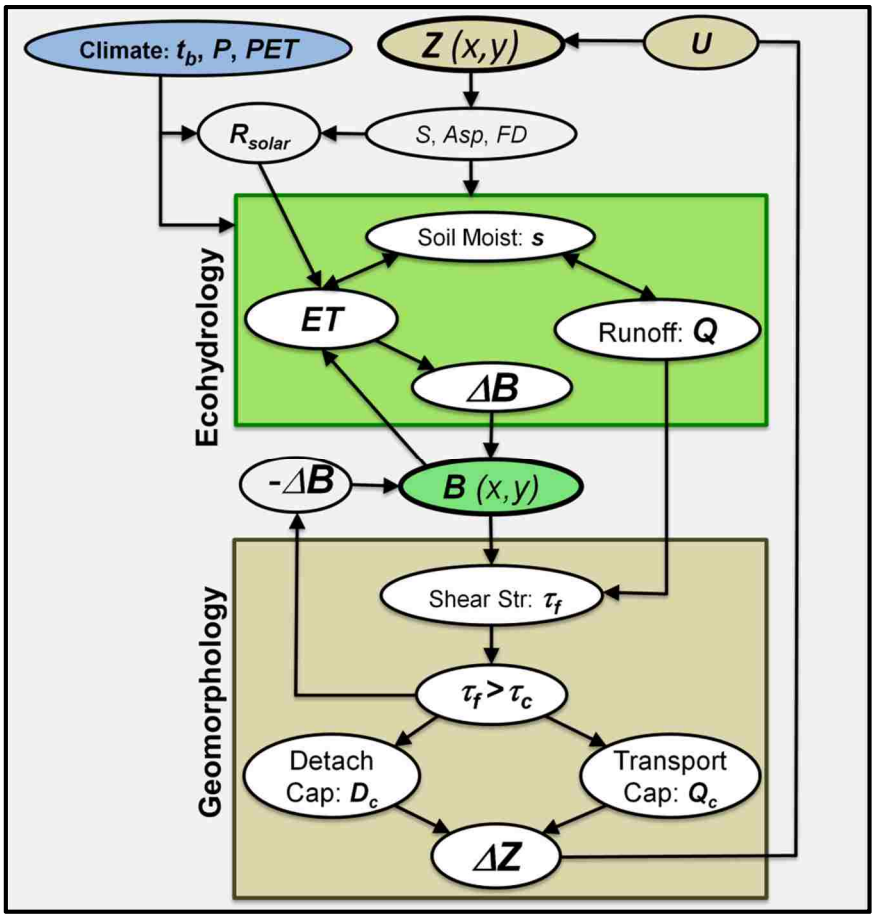

Figure 2. Flow chart for the coupling of the ecohydrology and geomorphology components of the CHILD LEM driven by climate. Biomass (*B*) is the state variable updated and used by both components.

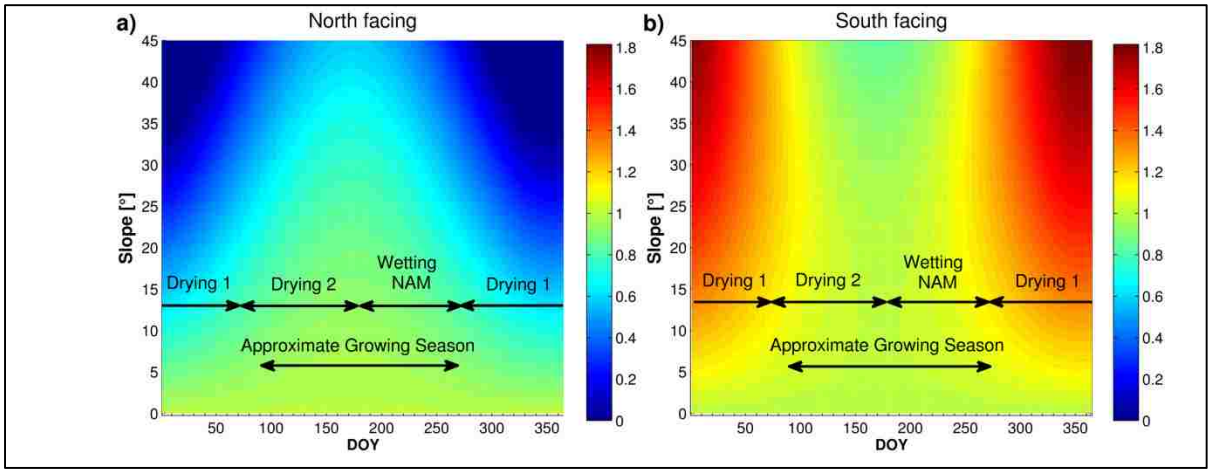

Figure 3. R_{solar} plotted for (a) North- and (b) South-facing slopes as a function of day of year (DOY) and local slope. Drying 1 and 2 periods shown in the figure correspond to different phases of soil moisture loss, and wetting NAM (North American Monsoon) shows the time range for the wet season. These periods were discussed in Figure 13.

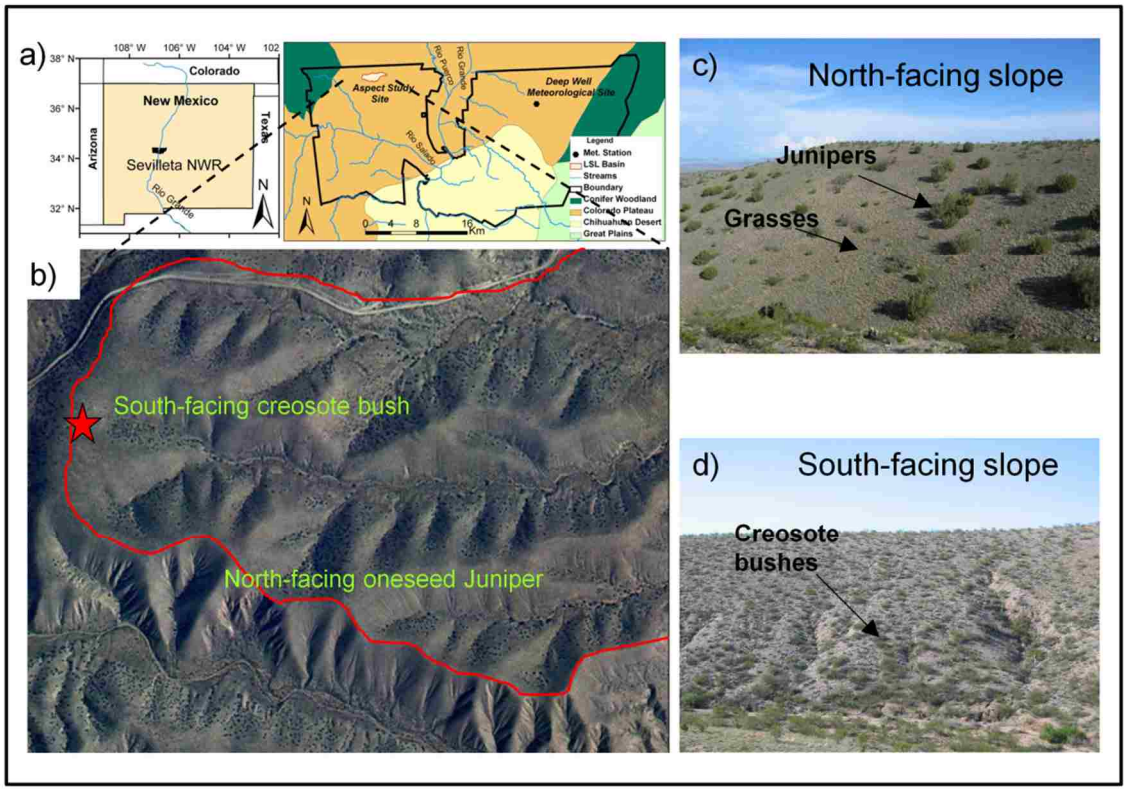

Figure 4. (a) Maps of the state of New Mexico (left), and the Sevilleta LTER (right) with the boundaries of the major ecosystem types and the study catchment, and the location of the weather station used in the model simulations; (b) 2-m aerial orthophoto of the study catchment used to confirm model simulations, red line shows the boundary of west part of the catchment; c) and d) show close-up photographs of segments of north- and south-facing slopes, respectively where aspect control on ecology and geomorphology can be observed.

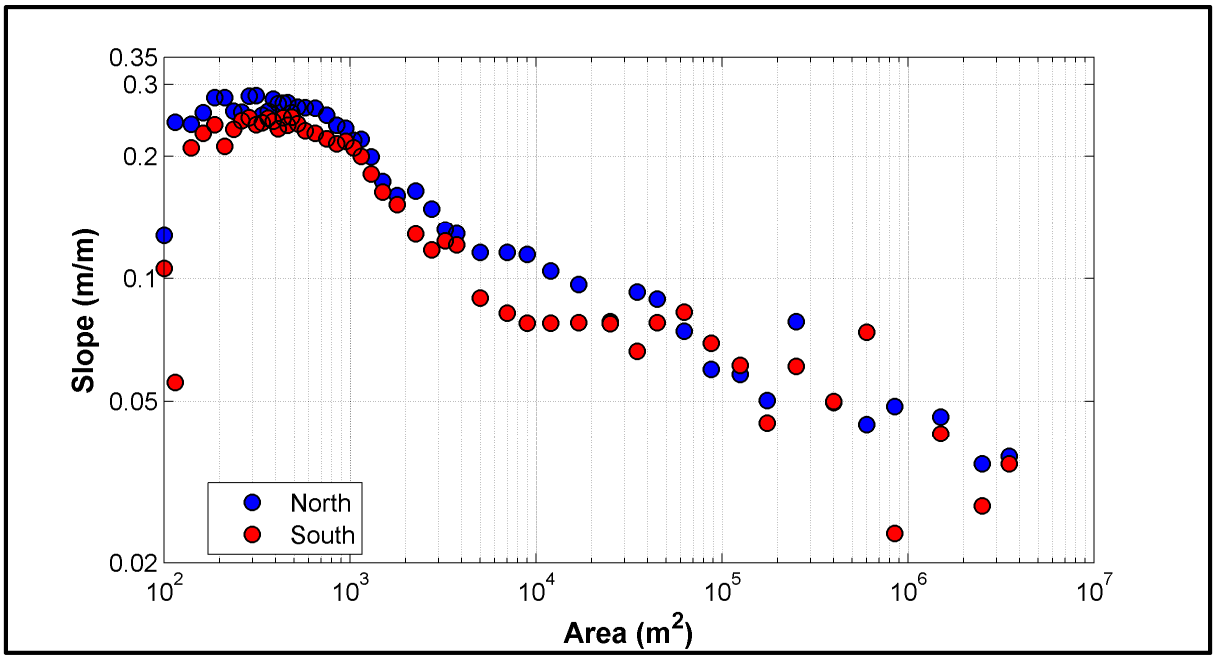

Figure 5. The slope-area plot of the north- and south-facing slopes of the catchment shown in Figure 4a (Aspect Study Site). The plot is produced by binning and averaging the local slope data with respect to their contributing drainage areas.

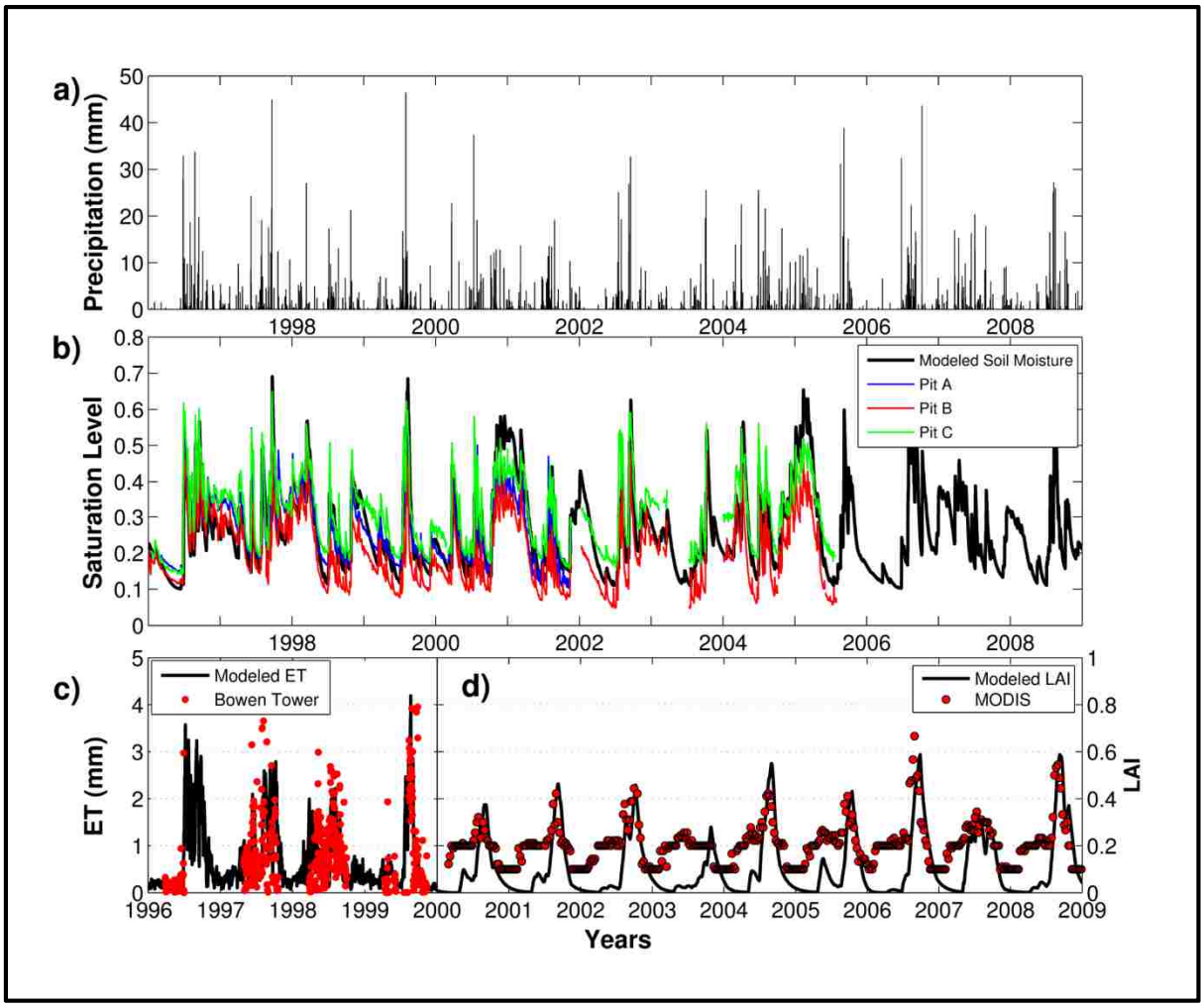

Figure 6. Confirmation of the ecohydrology component of CHILD at the Deep Well site, Sevilleta National Wildlife Refuge. Figures plot time series of: (a) observed precipitation; (b) modeled and measured (in three different soil pits) depth-averaged soil wetness (s) in the 30 cm root zone; (c) modeled and Bowen ratio-estimated evapotranspiration (ET_a); (d) modeled live and MODIS-derived leaf area index (LAI).

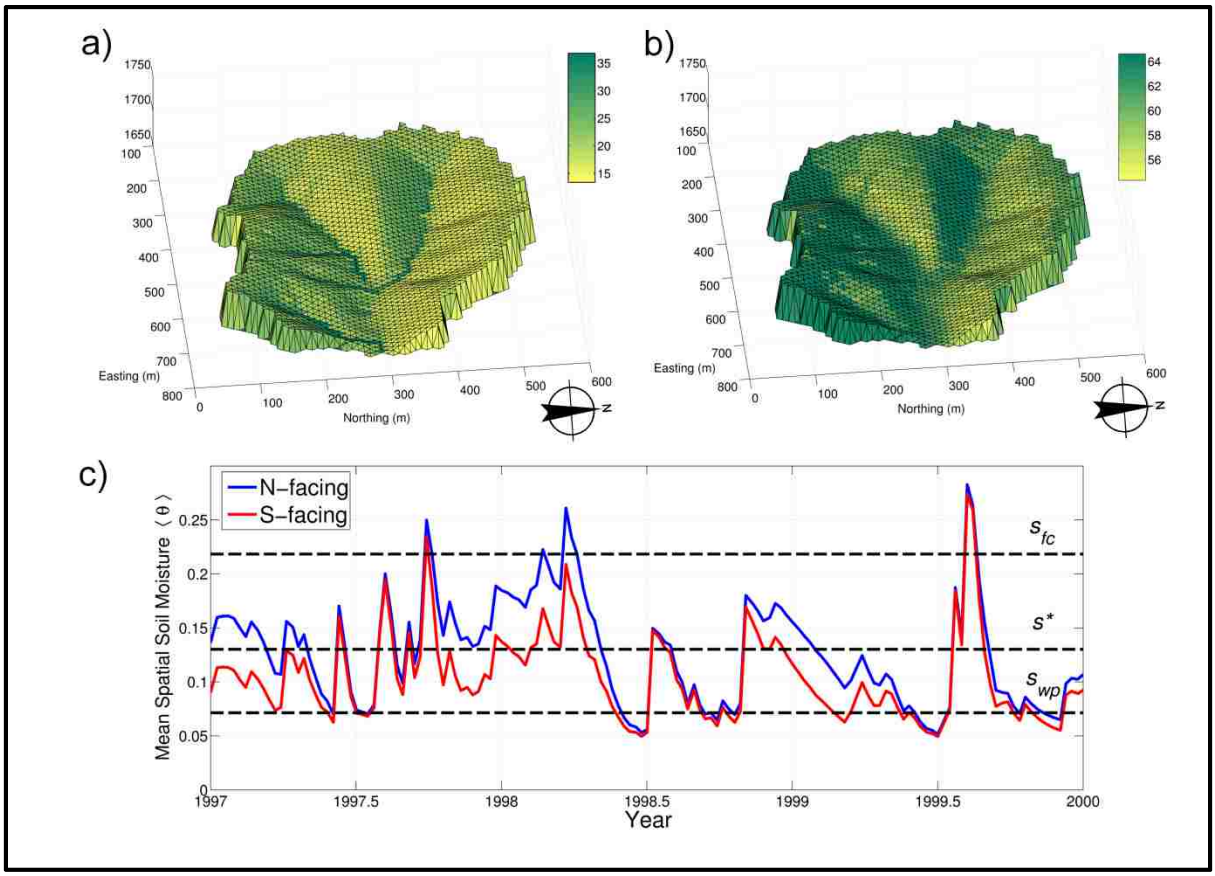

Figure 7. Modeled live biomass cover (g/m^2) at a small headwater valley in the SNWR catchment shown in Figure 4b, (location indicated by a star): (a) pre-monsoon, end of May-1998, and (b) end of monsoon, late Aug-1998; (c) time series of modeled mean-spatial volumetric soil-moisture content $\langle\theta\rangle$ in the root zone at this small headwater valley for the period between 1997-2000. Dashed lines in panel (c) refer to field capacity, s_{fc}, incipient stomata closure, s^*, and plant wilting point, s_{wp}.

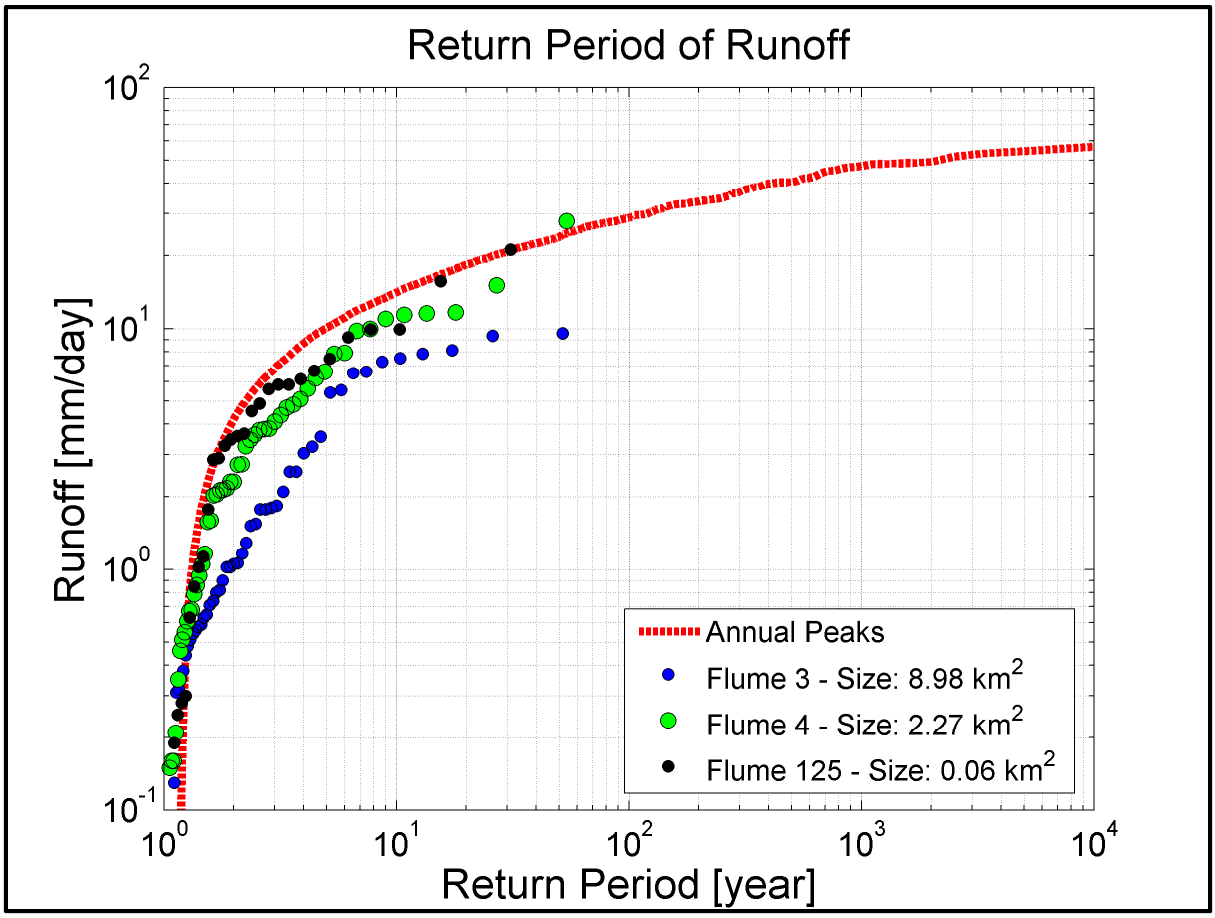

Figure 8. Comparison of the annual maximum daily runoff (mm/d) – return period relations between the CHILD model simulations and observations from several small watersheds at the Walnut Gulch Experimental Watershed, Tombstone, AZ.

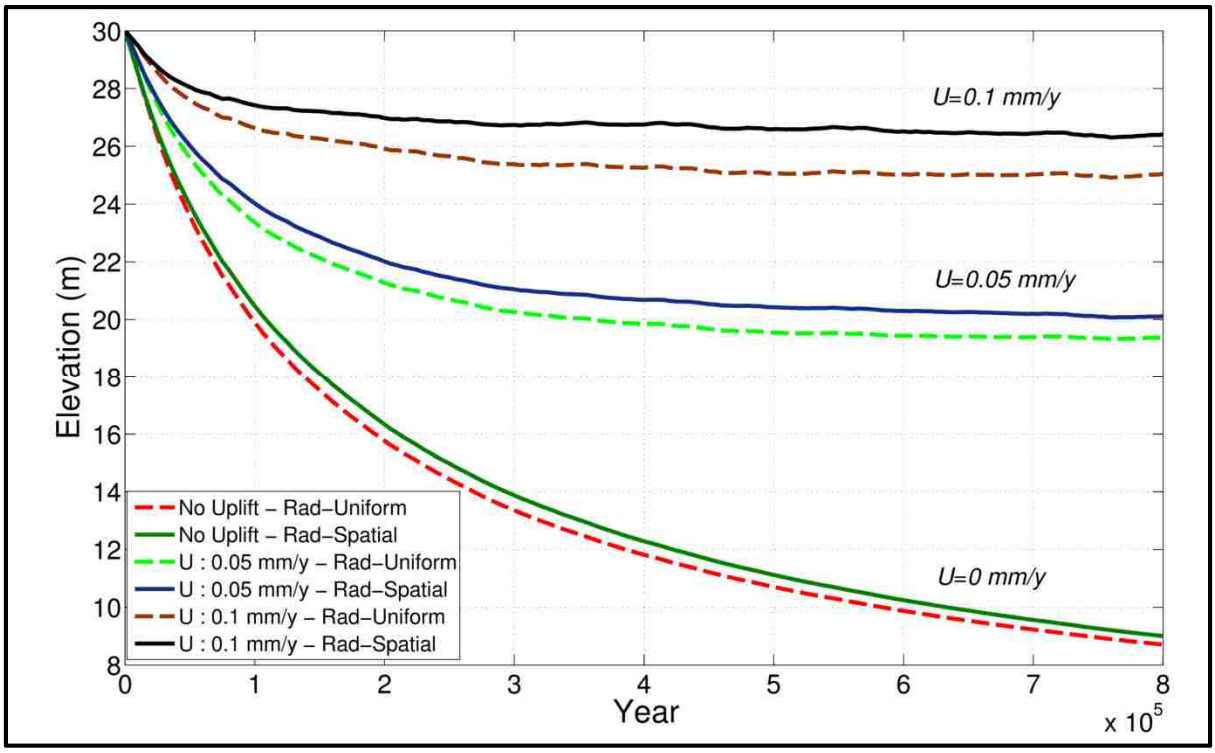

Figure 9. Time series of the mean elevation at 5,000-year resolution of modeled landscapes under spatially uniform (Rad-Uniform) and spatially variable (Rad-Spatial) radiation for 0.00 mm/y, 0.05 mm/y (low), and 0.1 mm/y (high) uplift rates.

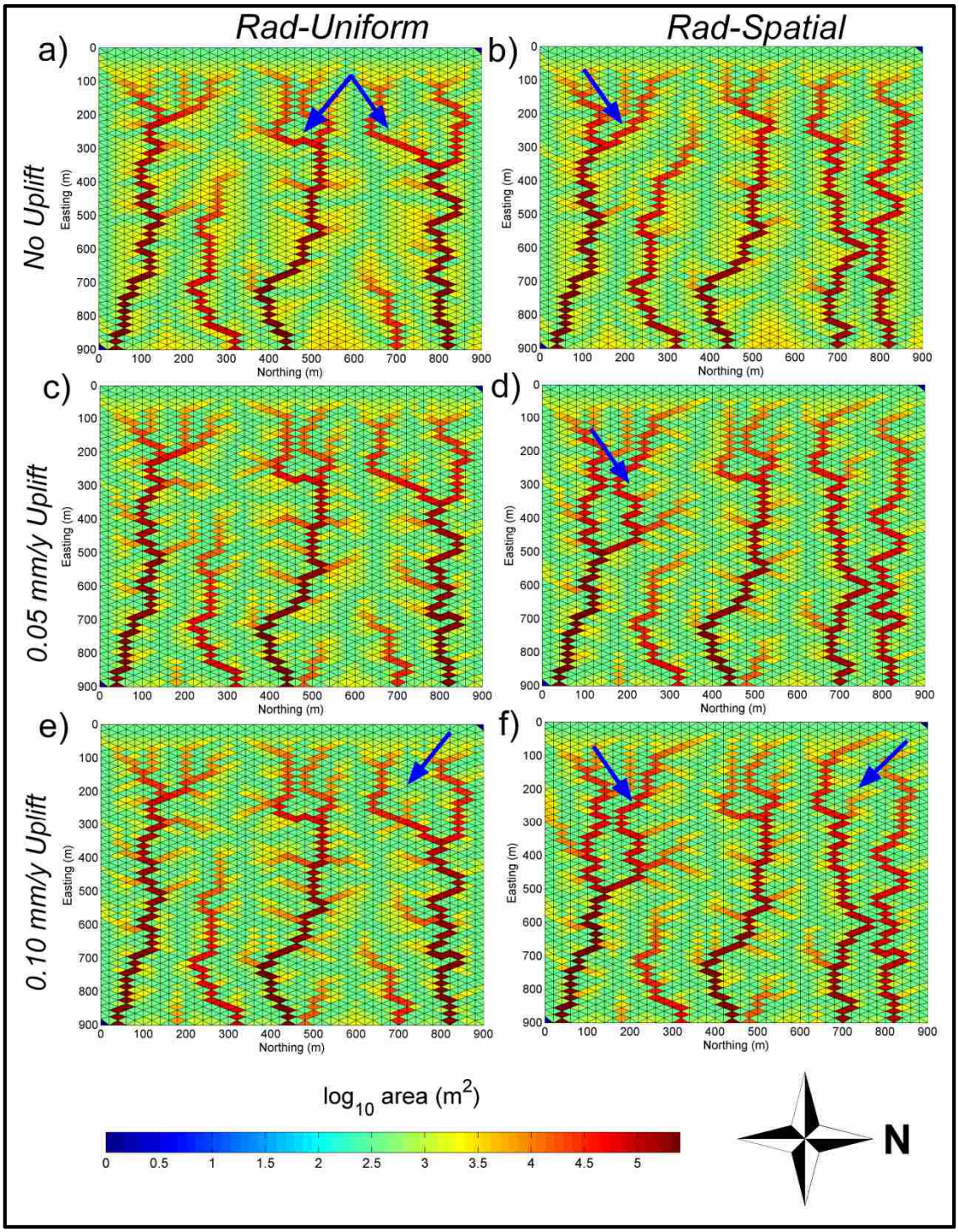

Figure 10. Plan views of numerical experiments for Rad-Uniform (left panel) and Rad-Spatial (right panel) conditions under 0.00 mm/y, 0.05 mm/y, and 0.1 mm/y uplift rates (top to bottom).

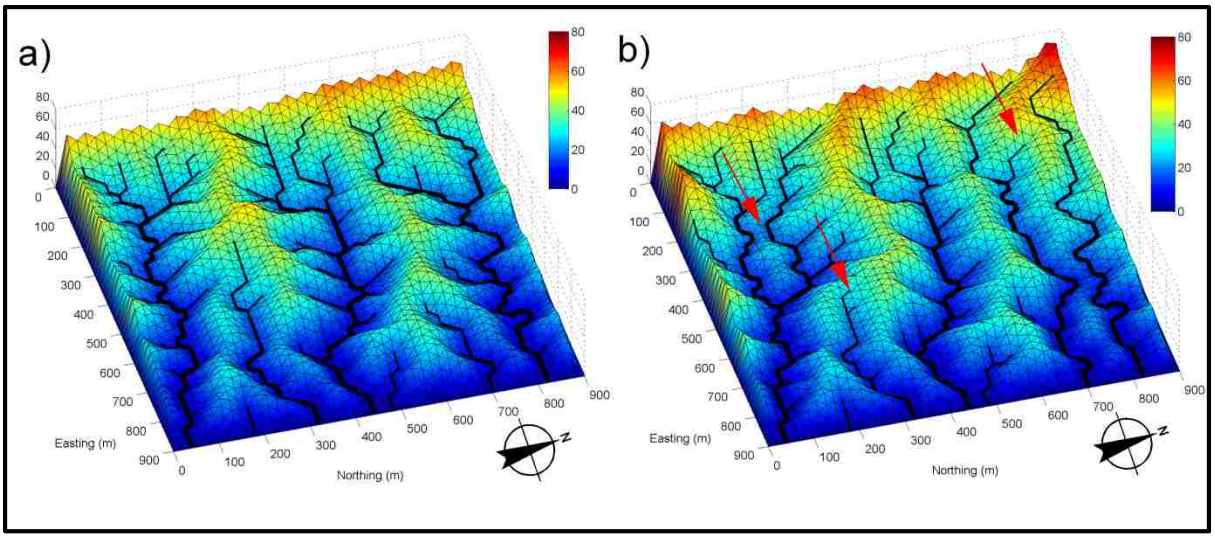

Figure 11. Elevation map (m) of modeled topography driven by high uplift (0.1 mm/y) for: a) Rad-Uniform; and b) Rad-Spatial cases. Channels are mapped using a 2,400m^2 support area threshold.

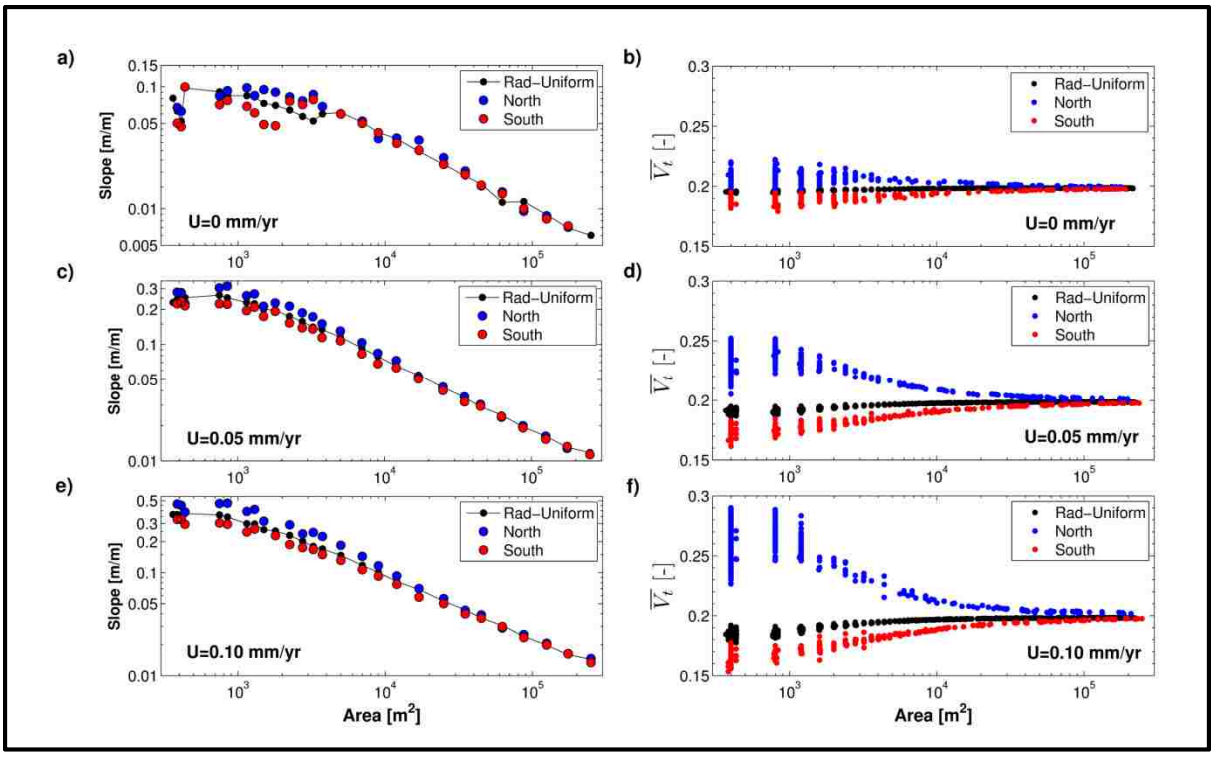

Figure 12. Slope-area, *Sl-A*, (left panel) and vegetation-area, $\overline{V}_t - A$, (right panel) relations for north- and south-facing slopes of the Rad-Spatial simulation and for the whole landscape of the Rad-Uniform simulation for the: (a, b) no-uplift; (c, d) low-uplift (U=0.05 mm/y); (e, f) high-uplift (U=0.1 mm/y) model experiments.

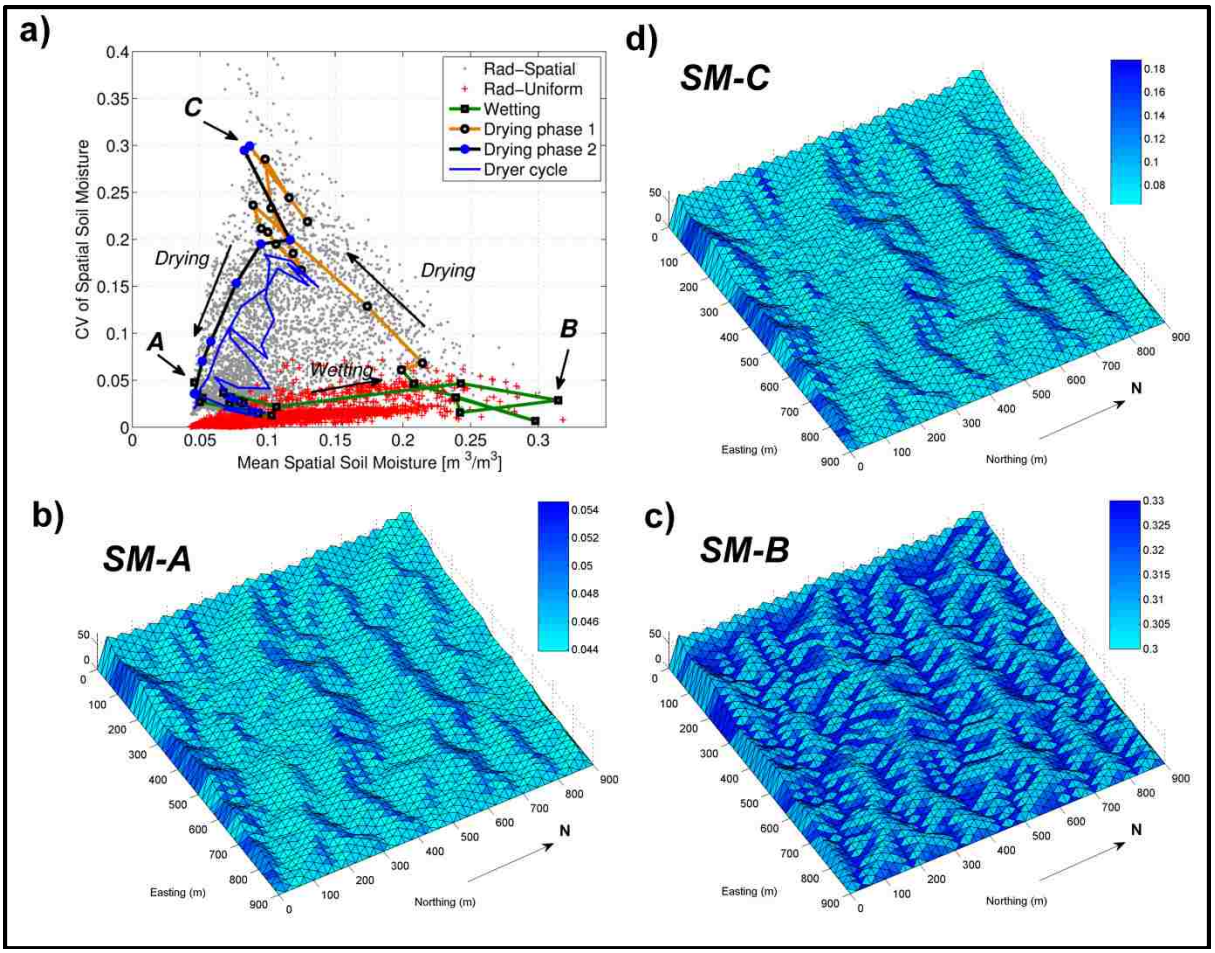

Figure 13. (a) The coefficient of spatial variation of soil-moisture content in the root-zone, CV_θ plotted as a function of its spatial mean $\langle\theta\rangle$ over the modeled domain for Rad-Spatial and Rad-Uniform simulations. Two annual $CV_\theta - \langle\theta\rangle$ trajectories highlighted are from the Rad-Spatial scenario, for years with wetter (outer loop) and drier (inner loop) than average annual precipitation. Modeled soil moisture is mapped on evolved topography for the wetter year (annual precipitation 317 mm) for days with: (b) the driest $\langle\theta\rangle$; (c) wettest $\langle\theta\rangle$; and (d) the highest CV_θ. Note that the ranges of the color bars are different.

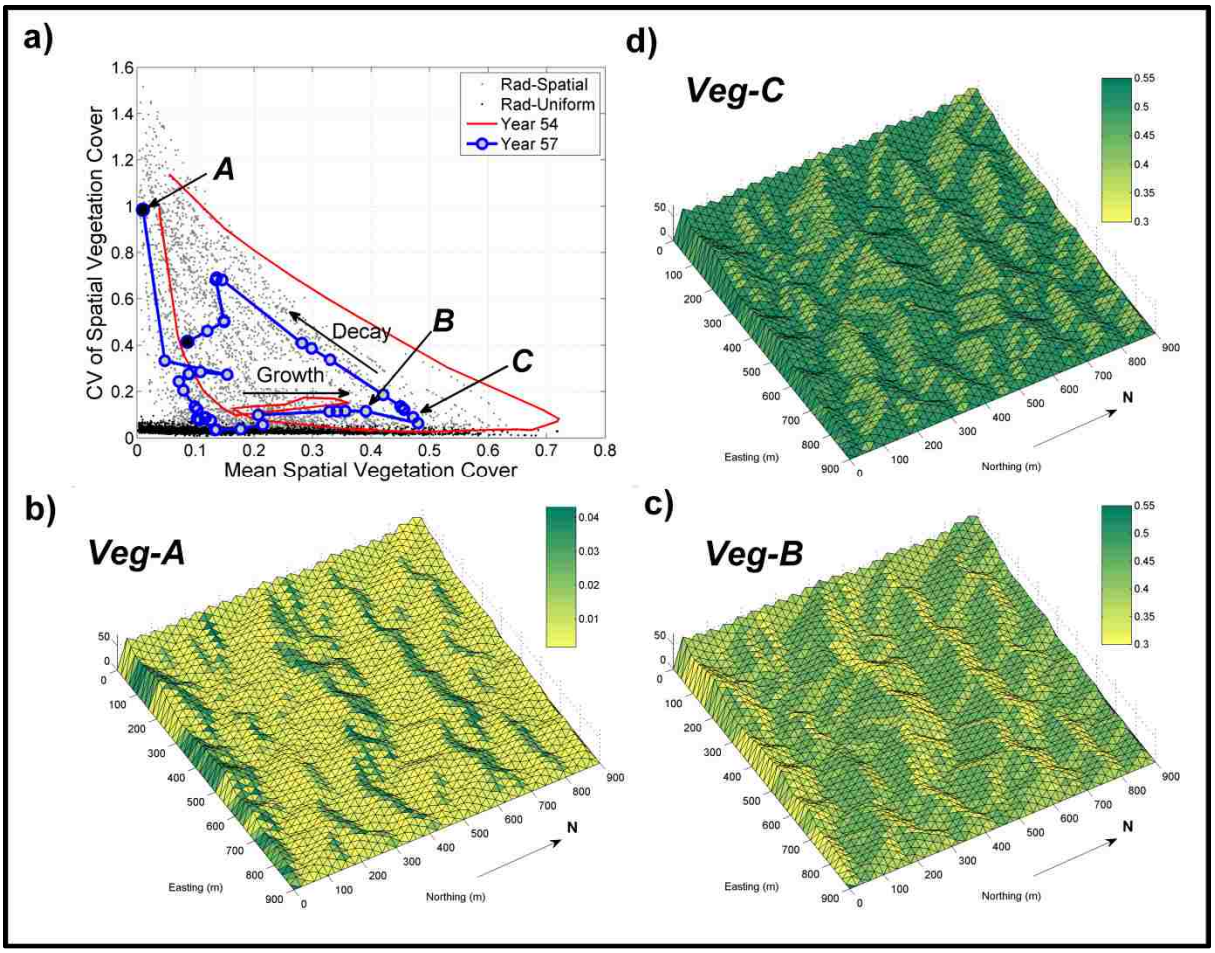

Figure 14. (a) The coefficient of spatial variation of total vegetation cover fraction, CV_{Vt}, plotted as a function of its spatial mean $\langle V_t \rangle$ over the modeled domain for Rad-Spatial and Rad-Uniform simulations. Two annual $CV_{Vt} - \langle V_t \rangle$ trajectories highlighted are from the Rad-Spatial scenario, for years with highest biomass (outer loop) and the wetter than average year (inner loop) used in the soil moisture plots. Modeled vegetation cover is mapped on evolved topography for the wetter year (annual precipitation 317 mm) for days with: (b) the lowest $\langle V_t \rangle$; (c) high $\langle V_t \rangle$ shows south-facing slopes have denser canopy cover than north-facing slopes; and (d) the highest $\langle V_t \rangle$ with low CV_{Vt} that shows north-facing slopes have denser canopy cover than south-facing slopes. Note that the range of the color bar in (b) is different than (c) and (d).

CHAPTER 4: SOLAR RADIATION AS A GLOBAL DRIVER OF HILLSLOPE ASYMMETRY[3]

Abstract

Growing observations at the field, catchment, and continental scales across a range of climates and latitudes reveal aspect-controlled patterns in soil properties, vegetation types, ecohydrologic fluxes, and hillslope and valley morphology. These observations could be indicating eco-geomorphic feedback mechanism driven by micro-climatologic differences shaping landscapes in most glacier free land masses. In this study, we used a landscape evolution model that couples the continuity equations for water, sediment, and above ground vegetation biomass at each model element. The model is used to explore the control of latitude and mean annual precipitation (MAP) on the development of hillslope asymmetry. In the model, vegetation growth influences the fluvial incision and transport. Hillslope diffusion is assumed independent of vegetation. Our model results suggest that: 1) hillslope asymmetry can emerge from the competition between soil creep and vegetation-modulated fluvial transport that is driven by spatial distribution of solar radiation and uniform rainfall. Consistent with the observations of *Parsons* [1988] and *Poulos et al.* [2012] modeled hillslope asymmetry (HA) grows toward northern latitudes. North-facing slopes (NFS) get steeper toward the North Pole while south-facing slopes (SFS) get gentler compared to their corresponding values at the 0° latitude. Modeled topography for the 45°N bears the shallowest SFS and the steepest NFS, and therefore the highest hillslope asymmetry for north- and south-facing slopes ($HA_{N\text{-}S}$) for all rainfall regimes. 2) Hillslope asymmetry can emerge from differential vegetation growth, with NFS supporting more vegetation cover than SFS as latitude increases towards north. Differences in the vegetation cover are related to greater rates of evapotranspiration during the fall and winter season on SFS that led to lower initial soil moisture during the beginning of the growing season, and more rapid vegetation decay during senescence. 3) For a given latitude, *MAP* is found to have minor control on $HA_{N\text{-}S}$ in the low to middle latitudes, where wetter conditions promote slope steepening on SFS with denser vegetation growth. In the simulations, mean slopes of the NFS steepen towards the poles, while SFS become gentler toward the poles. As a result of this counteraction, $HA_{N\text{-}S}$ values become larger toward the poles. Our results underscore the influence of solar radiation as a global control on the development of hillslope asymmetry. Variations in *MAP* at the same latitude have little impact on these in comparison to latitudinal variations.

[3] The coauthor for the planned journal submission is Erkan Istanbulluoglu.

4.1. Introduction

Hillslope-scale studies in soil-mantled semiarid ecosystems of the western US consistently reported steeper and planar morphologies on north-facing slopes (NFS), and less steep, more concave, and highly dissected morphologies on south-facing slopes (SFS) [e.g., *Walker*, 1948; *Melton*, 1960; *Carson and Kirkby*, 1972; *Branson and Shown*, 1989]. In east- and west-flowing streams observed asymmetric forms in valley and drainage networks have been attributed to the differential evolution of opposing hillslope morphologies, and their interactions with channel undercutting at the base of the slopes [*Melton*, 1960; *Parsons*, 1988; *Istanbulluoglu et al*., 2008]. In semiarid soil-mantled ecosystems, aspect-controls on hillslope evolution have been related to greater rates of runoff erosion on less vegetated SFS, and soil moisture storage and dominance of soil creep on vegetated NFS, driven by solar radiation and microclimate differences and their implications on ecohydrologic processes and vegetation dynamics [*Carson and Kirkby*, 1972; *Istanbulluoglu et al*., 2008]. Recent research also suggests freeze-thaw [*West et al*., 2014], frost crack [*Anderson et al*., 2013a], glacial processes [*Naylor and Gabet*, 2007] and weathering [*Burnett et al*., 2008] among micro-climate-driven processes that promote differential hillslope development.

In central New Mexico, USA, where soil, vegetation, and morphologies of NFS and SFS show distinct differences, ecohydrologic field observations revealed wetter and cooler vegetated NFS with greater transpiration rates, and drier and warmer SFS with more frequent and larger runoff magnitudes [*Gutiérrez-Jurado et al*., 2013]. These observations illustrated how aspect-induced micro-climatologic variations lead to ecohydrologic differences, providing strong evidence for earlier hypotheses that advocate the micro-climatic controls on the differential development of opposing hillslopes in semiarid regions.

Coupling a solar radiation-driven ecohydrologic vegetation dynamics model with vegetation-modulated fluvial incision and transport laws in a model of landscape evolution, *Yetemen et al*. [submitted manuscript] has demonstrated that in modeled catchments (~0.8 km^2) spatial and temporal characterization of solar radiation alone is sufficient to reproduce the first-order characteristic of aspect-related observed vegetation distribution, as well as hillslope- and catchment-scale geomorphic patterns in central New Mexico [*Istanbulluoglu et al*., 2008; *Yetemen et al*., 2010]. In their modeling experiments, micro-climatologic effects became more pronounced, leading to greater ecologic and geomorphic (eco-geomorphic) contrasts between opposing slopes

as landscape relief increased as a result of higher rates of uplift used in the simulations. Hillslope diffusion was assumed spatially uniform in their model.

Poulos et al. [2012] investigated hillslope asymmetry (HA) across the American Cordillera from 60°N to 60°S latitude. *Poulos et al*. [2012] described *HA* as log10 of the ratio of median slopes of opposing aspects (N versus S, or E versus W) obtained from a 90-m DEM, using a 5km by 5km sliding window, and averaging the *HA* estimates for each latitude. Based on their observational study, the N-to-S *HA* ($HA_{N\text{-}S}$), is nearly 0 at the Equator, and systematically increases ($HA_{N\text{-}S}>0$) in the Northern Hemisphere indicating steeper N-facing slopes, and decreases ($HA_{N\text{-}S}<0$) in the Southern Hemisphere, indicating steeper S-facing slopes than their opposing counterparts. $HA_{N\text{-}S}$ attains maximum absolute values at mid-latitudes (~30°), and then begins to decrease in the Northern (increase in the Southern) Hemisphere, and finally changes signs above ~49°N (40°S). Their findings were consistent with *Parsons* [1988] who reported steeper NFS up to 45°N and attributed this to the role of micro-climate differences on geomorphic processes at opposing aspects. *Poulos et al*. [2012] argued that the reversal in the $HA_{N\text{-}S}$ at high latitudes may be due to the dominance of periglacial and glacial processes.

Micro-climatic causes have been advocated as a potential driver for differential hillslope development in low-to-mid latitudes [*Parsons*, 1988; *Poulos et al*., 2012]. A large number of environmental variables change with latitude including insolation, local and regional climate (precipitation, temperature, wind speed), vegetation cover, lithology, and tectonic-climate feedbacks, which can influence a wealth of biotic and abiotic processes, contributing to aspect-dependent landform development. Recent studies have quantified micro-climate driven regolith production and transport on opposing hillslope aspects [*Anderson et al*., 2013a; *Ma et al*., 2013; *West et al*., 2013; 2014]. Numerical modeling can be used in a reductionistic approach to systematically explore the impacts of different environmental factors on geomorphic processes and resulting eco-geomorphic properties of landscapes to aid the development of field-testable hypothesis.

While climate and landscape variables besides solar radiation also vary with latitude, we still do not know if the latitude-dependent changes in the spatial distribution of solar radiation alone (keeping annual precipitation, potential evapotranspiration, and types of vegetation and soil constant) can explain hillslope asymmetry. In this paper, we use an ecohydrologic landscape evolution model that varies the spatial distribution of solar radiation with latitude and day of year

(DOY) under identical precipitation and evaporative forcing to address the following research questions: (1) can the observed relationship between $HA_{N\text{-}S}$ and latitude [e.g., *Poulos et al.*, 2012] emerge from the competition between soil creep and vegetation-modulated fluvial transport? If so, (2) what is the influence of latitude on aspect-controlled vegetation productivity? (3) What is the role of precipitation in the $HA_{N\text{-}S}$ and latitude relationship? In this paper, we only consider vegetation impacts on fluvial detachment and transport because of the complexities and uncertainities in the ways of microclimatic controls on regolith thickness and creep transport. Hence we elucidate the unique impacts of fluvial processes under spatially varying ecohydrologic conditions.

4.2. Model Theory

In this study, we used the Channel-Hillslope Integrated Landscape Development (CHILD) landscape evolution model (LEM) framework [*Tucker et al.*, 2001], modified for distributed ecohydrologic simulations [e.g., *Collins and Bras*, 2010; *Flores-Cervantes*, 2010; *Yetemen et al.*, submitted manuscript]. The model couples the continuity equations for water, sediment, and aboveground vegetation biomass at each model element, and evolves fields of soil moisture, s, aboveground biomass, B (currently for grass vegetation type only), and elevation, Z, driven by stochastic rainfall, solar radiation, and landscape uplift. Implicit solar radiation and energy balance calculations were incorporated in the water balance model that resolve evapotranspiration. The coupled system of continuity equations is illustrated here in "generic" forms, these equations are described in detail in *Yetemen et al.* [submitted manuscript].

Water: $$nD_r \frac{\partial s}{\partial t} = I - \nabla q_w - ET\left\{ET_{\max}\left(T^F_{\max}, R_{solar}, LAI^*\right), s\right\} \quad (1)$$

Biomass: $$\frac{dB}{dt} = NPP(ET)\phi - k_B B \quad (2)$$

Sediment: $$\frac{\partial Z}{\partial t} = U - \nabla q_{sd} - \nabla q_{sf}\left[\tau_f\left(q_w, V_t\right)\right] \quad (3)$$

The water balance component in equation (1) tracks the changes in the amount of water within a soil depth of D_r, with a maximum storage capacity of nD_r, where n is soil porosity, and s is the degree of saturation between 0 and 1 ($s=\theta/n$, θ: volumetric soil moisture content). Fluxes in the soil layer in a model element include the rate of infiltration, I (constrained by the minimum of

available water input, infiltration capacity, and available pore space in the root zone [*Collins and Bras*, 2010]); divergence of water flux (sum of incoming overland and lateral subsurface flows minus outgoing flows divided by cell area), ∇q_w; and evapotranspiration, *ET*.

A piece-wise linear relationship is used to model *ET* as a function of *s* and ET_{max} (maximum rate of daily *ET*) at each model element. *ET* is at its upper limit ($ET=ET_{max}$) when *s* is larger than a threshold, *s**. Below *s**, plants experience water stress, and *ET* reduces linearly as soil moisture dries between storms [*Laio et al*., 2001]. In the model, solar radiation and its spatial distribution are incorporated in ET_{max}. ET_{max} is calculated as the weighted average of the rates of maximum transpiration, T_{max}, and soil evaporation, E_s (assumed proportional to T_{max}), using *LAI** as the weighting coefficient: $ET_{max}= T_{max}LAI^*+(1- LAI^*)E_s$, where *LAI** is the ratio of leaf area index, *LAI*, of live vegetation cover to its ecologically limit value [e.g., *Zhou et al*., 2013]. At each model element, T_{max} is obtained by scaling the maximum transpiration rate of vegetation on flat surface, T_{max}^F, by a solar radiation ratio, R_{solar}, $\left(T_{max} = T_{max}^F \times R_{solar}\right)$. R_{solar} is the ratio of incoming shortwave radiation on a hillslope element to that of a flat surface, calculated based on solar geometry as a function of topographic attributes (slope, aspect), latitude, and day of year (DOY) [*Bras,* 1990]. T_{max}^F is calculated by the Penman-Monteith equation using parameters for reference grass following *Allen et al*. [1995] on a flat and planar surface.

Consistent with most process-based vegetation dynamics models, the rate of change in aboveground biomass, *dB*/*dt*, is a result of the balance between the net flux of carbon from the atmosphere to green plants (net primary productivity, *NPP*), and biomass loss due to plant senescence and disturbances. *NPP* is modeled as a function of *ET* following the water use efficiency concept [e.g., *Williams and Albertson*, 2005], and allocated to *B* with a dynamic allocation coefficient, $\phi\left[0 \le \phi < 1\right]$, that relates allocation inversely proportional to *B*. Plant senescence and drought-induced losses are represented by first-order decay equations [e.g., *Montaldo et al*., 2005]. *B* is divided into live and dead biomass pools. Vegetation dynamics is coupled with water balance through *ET* (equations 1 and 2). *B* regulates the amount of *ET*, through *LAI*, estimated from *B*.

Finally, the continuity of sediment follows the Exner equation that describes the rate of change in elevation, *Z*, as a function of a sediment source term (*U*), and divergence of sediment flux by hillslope diffusion (∇q_{sd}) and fluvial transport (∇q_{sf}). Both local detachment and transport capacity

equations are based on power functions of excess effective shear stress, τ_f, $\left(\tau_f - \tau_c\right)$, where τ_c is the critical shear stress for the initiation of detachment and transport. τ_f is the shear stress that acts on sediment grains on the surface, and it is inversely related to total vegetation cover, V_t (live+dead biomass cover) [*Istanbulluoglu and Bras*, 2005]. V_t is calculated from modeled total *LAI*, LAI_t. Hillslope diffusion is not related to vegetation cover and assumed uniform for all aspect in this model to focus on the vegetation impacts on fluvial detachment and transport.

The model is driven by stochastic storms, each storm pulses are characterized by a depth, duration, and an interstorm duration, using a modified rectangular pulse Poisson process method with seasonally varying parameters. $T_{\max}^F$ is first approximated by a sinusoidal function fitted to calculated reference grass transpiration using the Penman-Monteith model from meteorological station data. The sinusoidal function for $T_{\max}^F$ is then used deterministically as a function of time in long-term simulations. Detailed description of the model, confirmation of its ecohydrologic components against observations, and preliminary model experiments that examine the role of solar radiation on landscape development are presented for a field catchment in central New Mexico [*Yetemen et al*., submitted manuscript].

4.3. Numerical Experiment Design

We designed numerical experiments to explore the role of local scale variations in incoming solar radiation on landscape eco-geomorphic evolution across a range of latitudes (from 45°N to 45°S with 15° intervals) driven by mean annual precipitation (*MAP*) from 200 mm to 500 mm with 50 mm increments and an uplift rate of 0.1 mm/y. Only grass vegetation type is considered in the model. The *MAP* range used is consistent with grassland climates globally. All 49 simulations are run for 800,000 years, a sufficient duration to reach uplift-erosion equilibrium.

There are a few critical assumptions made to constrain the simulations such that only the role of spatial solar radiation can be emphasized in the model results. Fixed soil and vegetation parameters are used, selected for a field catchment in central New Mexico (34°N latitude) that produced model results consistent with ecohydrologic and geomorphic conditions in the field [*Yetemen et al*., submitted manuscript]. Central New Mexico receives approximately 250 mm of mean annual precipitation (*MAP*), 50% of which falls during the North American Monsoon (NAM) between July and September [*Vivoni et al.*, 2008]. To simplify climate seasonality for all

*MAP*s, we assumed distinct dry (9-month) and wet (3-month) seasons, each receiving 50% of *MAP*.

As *MAP* changes, storm characteristics are varied according to rainfall climatology of the western US, developed based on empirical relations obtained between storm parameters and *MAP* [*Small*, 2005; *Istanbulluoglu and Bras*, 2006]. The mean annual interstorm duration (T_b) is related negatively, and the number of storms (N_s) is related positively to *MAP* (Fig 1a). Wetter climates generate more storm events, hence interstorm duration shortens. T_b is further adjusted for the wet and dry seasons according to the amount of rain that falls in each season [*Istanbulluoglu and Bras*, 2006]. Based on the empirical relations, mean storm intensities increase with MAP for wet and dry season. (Fig 1b). Also storms in the wet season are more intense than those in the dry season. To achieve reasonable runoff production consistent with semiarid climates, storm durations and intensities are adjusted using a scalar, while storm depth and number of storms in a year are preserved [*Yetemen et al.,* submitted manuscript]. This method has been used in earlier modeling studies in semiarid climates that used the Poisson rectangular pulse method to ameliorate the known deficiencies of the model [e.g., *Collins and Bras*, 2010].

Seasonal changes in $T_{\max}^F$ for grass are represented using a sinusoidal function, calibrated for Penman-Monteith estimates of reference transpiration obtained for central New Mexico (Fig 1c) [e.g., *Small*, 2005]. The seasonal fluctuation of $T_{\max}^F$ is described by three parameters including: the mean of $T_{\max}^F$, the difference between maximum and minimum values of $T_{\max}^F$ throughout the year and the lag between peak solar forcing and peak $T_{\max}^F$ [Small, 2005]. $T_{\max}^F$ is considered to be invariant across northern latitudes. In the Southern Hemisphere, the seasonal distribution of $T_{\max}^F$ is adjusted consistent with the timing of the peak solar forcing. The lag between peak solar forcing (DOY=172) and peak $T_{\max}^F$ (DOY=182) in the Northern Hemisphere is ~10 days, and this lag is preserved for the Southern Hemisphere. For example, this shifts the peak of the sinusoidal function for $T_{\max}^F$ to DOY=2 which is 10 days after the peak solar forcing (DOY=357) for 45°S latitude. In Fig. 1c, the horizontal line denotes a growth threshold for $T_{\max}^F$. When 30-day averaged $T_{\max}^F$ exceeds this threshold, the growing season starts. To reflect the role of *MAP* on evapotranspiration, the annual mean daily value of $T_{\max}^F$ ($MAT_{\max}$) and the annual mean difference in maximum and minimum values of $T_{\max}^F$ throughout the year ($\Delta MAT_{\max}$), parameters of the sinusoidal function for

$T^F_{\max}$, are varied as a function of *MAP*. The inverse relationships between $MAT_{\max}$ and $\Delta MAT_{\max}$ with *MAP* are used which were developed based on data from New Mexico and Nebraska where grass is the dominant vegetation type [*Istanbulluoglu et al*., 2012], (Fig 1d). This assumption is intuitive, due to the cooling effects of evapotranspiration in the lower atmosphere, greater relative humidity, and increased cloudiness as *MAP* grows [e.g., *Cristea et al*., 2012]. To illustrate how $T^F_{\max}$ variability is related to *MAP*, daily $T^F_{\max}$ is plotted for 200 mm and 500 mm *MAP*, where the timing of the wet season (July-September) is highlighted (Fig 1c). The role of climate on the value of live biomass senescence coefficient (k_{sg}) is introduced to the model inversely proportional to *MAP*. This relationship was found to improve the model performance in regional grasslands across a *MAP* gradient in central Nebraska and used in New Mexico (Figure 1e) [*Istanbulluoglu et al*., 2012; *Yetemen et al*., submitted manuscript].

Incision and transport of sediment are driven by effective shear stress, τ_f, in the model, which is inversely related to the total surface vegetation cover, V_t (live+dead biomass cover) [*Istanbulluoglu and Bras*, 2005]. V_t is calculated from modeled total *LAI*, LAI_t [*Yetemen et al*., submitted manuscript]. To illustrate how vegetation influences shear stress, we plot the ratio of τ_f to boundary shear stress, τ_b, (i.e., shear stress without vegetation influence) as a function of LAI_t, with soil and vegetation roughness values selected for the central New Mexico field site (Figure 1f). Vegetation on the ground increases the total roughness of the surface with respect to the grain roughness and decreases the shear stress that directly acts on soil grains. This model was tested using field data from the literature [*Istanbulluoglu and Bras*, 2005]. According to the model, even a small amount of vegetation on the ground can reduce shear stress significantly.

The critical variable for this modeling study is R_{solar}, used to calculate local rates of maximum transpiration from $T^F_{\max}$, $T_{\max} = T^F_{\max} R_{solar}$. $T_{\max}$ is used as the boundary condition to the calculation of actual evapotranspiration in the model as a part of water balance (Equation 1). R_{solar} is the ratio of incoming shortwave radiation on a hillslope element to that of a flat surface, calculated based on solar geometry as a function of topographic attributes (slope, aspect), latitude, and day of year (DOY) [*Bras,* 1990] [see *Yetemen et al*., submitted manuscript for theory]. We demonstrate how R_{solar} varies on NFS and SFS for 0° (the Equator), 45°N, and 45°S latitudes as a function of DOY and local slope (Fig 2). Horizontal arrow indicates the timing of the wet season. The DOY of the begin and end of the wet season in the Southern Hemisphere simulation is moved to the summer

of the Southern Hemisphere consistent with its location in the Northern Hemisphere with respect to the peak of the solar forcing. Adjustment of both the seasonal distribution of $T_{\max}^{F}$ and wet season timing makes the climate forcing identical in both 45°N and 45°S, leaving R_{solar} as the only variable that changes with latitude.

At the 45°N latitude, NFS consistently show lower R_{solar} than SFS for all topographic slopes throughout the year (Fig2 a, b). In particular, during the fall and winter seasons, the contrast in R_{solar} between NFS and SFS grows significantly for slopes steeper than 10°. R_{solar} at the 45°S latitude is the mirror image of R_{solar} at the 45°N with nearly a half-year time lag as a result of the shift of the solar peak from June (DOY=172) to December (DOY=357) in the Southern Hemisphere (Fig2 e, f). Seasonally, like the Northern Hemisphere, R_{solar} contrast is higher during the winter and fall months in the Southern Hemisphere, however with SFS slopes receiving less radiation than NFS. Radiation difference is less pronounced in spring and summer especially for gentle slopes (Fig2 a, b and e, f). Towards the Equator in the Northern Hemisphere, the values of R_{solar} on SFS loose strength on all topographic gradients, while radiation on NFS grows (Fig2 c, d). NFS in the Equator receives more radiation during the summer than SFS. Interestingly, even at the Equator the spatial distribution of R_{solar} throughout the year is not uniform, although the contrast is minimal compared to southern and northern latitudes.

4.4. Results and Discussions

4.4.1. Modeled landscape morphology and hillslope asymmetry across latitudes

The CHILD LEM is run for latitudes from 45°N to 45°S with 15° increments, driven by MAP from 200 mm to 500 mm (ΔMAP=50 mm) and an uplift rate of 0.1 mm/y. Based on previous research results, $HA_{\text{N-S}}$ is enhanced with greater uplift rates [*Yetemen et al.*, submitted manuscript]. Therefore, in this study we used a moderate rate of uplift of 0.10 mm.y^{-1} to avoid landsliding while developing relatively steep slopes shaped by fluvial processes and nonlinear hillslope diffusion. As discussed in detail above, our numerical model experiments were designed to explore the relative distribution of solar radiation in space (R_{solar}) alone under an identical seasonal evaporative forcing with adjusted seasonal behavior from northern to southern latitudes. The initial condition of the model was an eastward sloping ramp-like surface (900 m by 900 m) with an open side boundary condition with a node spacing of 20 m.

Fig 3 presents upslope contributing area maps of sample modeled drainage basins for 0°, 45°N, and 45°S latitudes, driven by 200 mm, 350 mm, and 500 mm of MAP. Darker colors represent the channel network. $HA_{N\text{-}S}$ values calculated for each domain using the method of *Poulos et al*. [2012] are given in the figure. Model results show a clear evidence of latitudinal control on channel network development. In the Northern Hemisphere (45°N), channels preferentially develop on SFS. Enhanced fluvial processes on SFS reduce hillslope gradients, leading to a positive landscape-scale hillslope asymmetry, $HA_{N\text{-}S}>0$ (Figure 3a, b, c). Northward expansion of the fluvial network and $HA_{N\text{-}S}$ becomes slightly more pronounced as the climate got wetter in the intermediate values of MAP (MAP=350 mm). At the Equator (0°), channel branching is nearly symmetrical toward opposing north and south aspects, resulting in $HA_{N\text{-}S}$ values approximately an order of magnitude smaller than those reported for 45°N (Figure 3d, e, f). In the Southern Hemisphere (45°S), the orientation of channel development is reversed, as channels preferentially develop on NFS, leading to landscape asymmetry toward north ($HA_{N\text{-}S}<0$). $|HA_{N\text{-}S}|$ for 45°N and 45°S show consistently similar values under different MAP forcing (Figure 2g, h, i). Comparing Figs 2 and 3 clearly indicates that channels grow into aspects that receive more solar radiation within the modeled semiarid MAP range. At the Equator, hillslope asymmetry is weak as R_{solar} differences between opposing NFS and SFS aspects are much less pronounced.

For a more detailed exploration of the roles of latitude and climate on north-to-south hillslope asymmetry ($HA_{N\text{-}S}$), we plot $HA_{N\text{-}S}$ calculated from modeled landscapes from 45°N to 45°S with 15° increments as a function of latitude (Figure 4a). The latitudinal variation of $HA_{N\text{-}S}$ values for the American Cordillera reported by *Poulos et al*. [2012] based on 90-m DEM is also given in the inset of Figure 4a (figure 2 in *Poulos et al*., [2012]) for comparison with our model results. This figure is complemented by plotting $HA_{N\text{-}S}$ as a function of MAP for each latitude to illustrate the role of precipitation (Figure 4b).

Consistent with the observations of *Parsons* [1988] and *Poulos et al*. [2012], modeled $HA_{N\text{-}S}$ values are positive in the Northern Hemisphere, and negative in the Southern Hemisphere. At a given latitude, differences in MAP manifest itself by a range of $HA_{N\text{-}S}$. Despite the consistency in the signs of $HA_{N\text{-}S}$ between model results and published literature that used DEMs, a close inspection of *Poulos et al*. [2012] values reveal two notable discrepancies between model results and $HA_{N\text{-}S}$ calculated across the American Cordillera (Figure 4a). First, in the modeled landscapes, $HA_{N\text{-}S}$ systematically increases (decreases) toward the poles in the Northern (Southern)

Hemisphere without any discontinuity. This pattern is consistent with *Poulos et al*. [2012] only within the low to mid latitudes. $HA_{N\text{-}S}$ attains maximum absolute values in ~30°N and ~20°S in their data, and then begins to decrease in the Northern (increase in the Southern) Hemisphere, and finally changes the sign from positive to negative above ~49°N, and from negative to positive around ~40°S. Second, modeled $HA_{N\text{-}S}$ values at the landscape scale are nearly an order of magnitude greater than those reported by *Poulos et al*. [2012]. It may be argued that the reversal in the $HA_{N\text{-}S}$ at high latitudes may be due to a change in the dominant form of geomorphic processes from fluvial incisions and landsliding to periglacial and glacial processes, and changes in low- to high-biomass plant species [*Poulos et al*., 2012]. Magnifying the MAP signature on Figure 4a, Figure 4b shows a second-order impact of MAP on $HA_{N\text{-}S}$ mostly in mid-latitudes in the modeled landscapes. Evidence for a relatively small increase in absolute values of $HA_{N\text{-}S}$ can be observed for intermediate values of MAP in 30°N, 45°N, and 45°S latitudes. However such changes are less than ~10% of the mean $HA_{N\text{-}S}$ modeled for any given latitude.

Since our model was initially developed and confirmed against geomorphic and ecohydrologic observations for semiarid conditions in a central New Mexico catchment (34°N, MAP=250 mm) [*Yetemen et al*., submitted manuscript], it is imperative to confirm $HA_{N\text{-}S}$ of modeled landscapes with $HA_{N\text{-}S}$ of actual catchments in the same region. For the central New Mexico catchment (34°N), $HA_{N\text{-}S}$ is calculated as 0.086 (labeled D in Figure 4a). Running the $HA_{N\text{-}S}$ algorithm on a regional 30-m DEM of Upper Rio Salado Basin having an area of 465 km^2, we obtain a regional $HA_{N\text{-}S}$ of 0.094 (labeled C in Figure 4a). Uplift was found to amplify $HA_{N\text{-}S}$ by *Yetemen et al*. [submitted manuscript], and the uplift rate we used in this study is on the higher end of the values reported for central New Mexico [*Pazzaglia and Hawley*, 2004]. To provide more insights about the role of uplift on $HA_{N\text{-}S}$ and to provide further comparisons with $HA_{N\text{-}S}$ of actual topography in central New Mexico in Figure 4a, we report $HA_{N\text{-}S}$ for additional model experiments run by no uplift, intermediate (0.05 mm/y) and high (0.1 mm/y) uplift rates for central New Mexico conditions (34ºN, MAP=250 mm) based on the reported range of uplift rates in the literature (e.g., *Dethier et al*., 1988; *Pazzaglia and Hawley*, 2004). Modeled landscapes with these uplift rates have $HA_{N\text{-}S}$ in the 0.06-0.13 range in the respective order from no to high uplift used in the model, capturing the range of the DEM-derived $HA_{N\text{-}S}$ in central New Mexico. In addition, we also calculated $HA_{N\text{-}S}$ values for several semiarid catchments that show distinct aspect-controlled vegetation differences as reported in the ecological literature in the Northern (A, B, E) and

Southern (F1, F2) Hemisphere (Table 1). The two Southern hemisphere catchments located in Cerro Robles, Chile show good agreement with model results. These catchments have broad-leaved evergreen shrub (known as matorral in Chile) vegetation types and MAP of 593 mm [*Parsons*, 1976]. The Dry Creek Experimental Watershed (DCEW), Boise, Idaho (A in Figure 4a) also agrees with model results. MAP in Dry Creek ranges from 370 mm to 890 mm depending on elevation [*Kunkel et al.*, 2011] with significant snow component [*Smith et al.*, 2011]. The catchment exhibits distinct vegetation and topographic differences as reported by *Poulos et al.* [2012]. Differences between the model and observed $HA_{\text{N-S}}$ values may be attributed to wetter conditions overall and higher snowmelt at the DCEW. $HA_{\text{N-S}}$ values obtained from two other basins (B and E in Figure 4a) do not agree well with the model. This discrepancy may be caused by the orientation of main channels elongated through the N-S direction which lead to not enough hillslope development for N and S aspects or may be caused by other dominant geomorphic processes which are not incorporated into the model.

Theoretically, an increase in $\left|HA_{\text{N-S}}\right|$ with latitude should result from a growing contrast between the steepness of opposing hillslope gradients. To illustrate and examine this behavior, spatial means of local slopes for NFS (Figure 5a) and SFS (Figure 5b) of modeled landscapes are plotted with respect to MAP for latitudes from 45°N to 45°S with 15° increments. The figure clearly shows why $\left|HA_{\text{N-S}}\right|$ is positively related to latitude. Opposing NFS and SFS show the smallest difference in the modeled topography at the 0° latitude. As latitude increases northward (southward) from the Equator, NFS get steeper (gentler) while SFS get gentler (steeper) compared to their corresponding values at the 0° latitude. Modeled topography for the 45°N bears the shallowest SFS and the steepest NFS, while on the contrary, the steepest SFS and the shallowest NFS are predicted for the 45°S latitude. Interestingly, landscape slopes of NFS in southern latitudes (Figure 5a) and SFS in northern latitudes (Figure 5b) first get shallower as MAP increase from 200 mm to 300 mm, and get steeper as climate becomes wetter, while such behavior is not as clear on their corresponding opposite aspects. This may provide an explanation to the observed slight decrease (increase) in $HA_{\text{N-S}}$ with MAP>300 mm in the northern (southern) latitudes (Figure 4b). With this evidence, we ask the following question: what is the mechanism by which solar radiation influences landscape evolution such that the difference between the opposing NFS and SFS enhances with latitude, and for a given latitude slopes show a complex response to MAP?

4.4.2. Latitudinal variations and ecogeomorphic interactions

In our model, vegetation-fluvial incision/transport interactions are the only built-in mechanisms by which slopes evolve differentially as a function of latitude. Therefore quantifying how vegetation responds to latitude and climate on opposing aspects will give direct evidence for the role of aspect on fluvial landscape evolution. To examine the vegetation response to aspect in the Northern Hemisphere, we use the last 100 years of vegetation cover fraction (V_t) outputs at each model element (model grid cell) at a temporal resolution of inter-storm duration. We calculate the 100-year average V_t at each model element $\left(\overline{V_t}\right)$, group the $\overline{V_t}$ data into separate bins for NFS and SFS, and plot each bin data using the Box-Whisker plots for 0°, 15°N, 30°N, and 45°N-latitude simulations, for MAP of 200 mm, 350 mm and 500 mm (Figure 6). To facilitate comparison between NFS and SFS for a given MAP, model outputs for opposing slopes are plotted with some distance between them to avoid overlapping. The observed range in the whiskers show the spatial variability of $\overline{V_t}$ for each aspect. $\overline{V_t}$ values are naturally low as they reflect the average of growing (rainy) and non-growing seasons. This plot can be reproduced for the Southern Hemisphere simulations, however considering that the model response in the Southern Hemisphere is a mirror image of that of the Northern Hemisphere, here we only focus on model results in the Northern Hemisphere.

A clear separation between NFS and SFS can be observed for each MAP plotted, where NFS sustain overall higher and more variable V_t than SFS as latitude grows. At the 0° latitude, V_t values on NFS and SFS are nearly identical and show very small spatial variability while vegetation productivity mainly increases with MAP (Figure 6). This can be directly related to the relatively lower range of seasonal contrast in the spatial distribution of solar radiation on north and south aspects at the 0° latitude (Figure 2 c, d). At higher northern latitudes, growing contrast in the spatial distribution of solar radiation leads to more (less) solar radiation on SFS (NFS) especially during the fall and winter months (Figure 2 a, b). Solar radiation remains to be slightly elevated on SFS during the growing season than NFS. Such differences reduce V_t on SFS and increase V_t on NFS compared to values at the 0° latitude. Loss of V_t on SFS in the Northern Hemisphere has been related to greater soil moisture depletion as a result of higher demand for *ET* during the fall and winter months, leading to drier initial conditions of soil moisture for the growing season than soil moisture on NFS [*Gutiérrez-Jurado and Vivoni*, 2013a; 2013b; *Yetemen et al.*, submitted

manuscript]. Relatively drier soils combined with slightly higher solar radiation exposure during the growing season amplify plant water stress, making SFS less advantageous for vegetation growth than NFS [*Yetemen et al.*, submitted manuscript]. In addition, drier and warmer conditions in SFS were predicted to cause much rapid grass senescence [*Zhou et al.*, 2013; *Yetemen et al.*, submitted manuscript]. These model responses are supported by ecohydrologic field observations on opposing NFS and SFS in central New Mexico [*Gutiérrez-Jurado et al.*, 2013]. Contrasting radiation patterns grow with latitude in the model, leading to highest V_t on NFS and smallest V_t on SFS at the 45°N, for all MAP amounts.

On an evolving modeled topography, emerging vegetation differences on opposing slopes create a feedback mechanism with fluvial erosion and transport rules in the model leading to differential landscape evolution with respect to aspect. The relationship between local slope and upslope contributing area (S-A) can be used to illustrate the role of latitude on catchment organization quantitatively. On a S-A plot, convex hillslopes exhibit a positive S-A relation, while concave valleys and channels exhibit a negative S-A relation [e.g., *Tucker and Bras*, 1998]. Greater convexity in the S-A relation that correspond to intermediate drainage areas can be attributed to unchanneled valleys eroding by a mixture of hillslope diffusion and less frequent fluvial processes [*Istanbulluoglu et al.*, 2008]. The S-A data for 45°N, 0°, and 45°S simulations driven by MAP=350 mm are presented in Figure 7.

Vegetation cover reduces the effective shear stress used for fluvial incision and transport (Figure 1f). Therefore, in an equilibrium landscape on northern latitudes under constant landscape uplift, NFS that are more resistive to fluvial erosion as a result of denser grass cover (Figure 6) tend to get steeper (Figure 7), promoting transport by soil creep to compensate the loss of fluvial transport by hillslope diffusion, and hence maintain uplift-erosion balance. In contrast, more erodible SFS in the Northern Hemisphere can maintain the uplift-erosion balance by adjusting to gentler slopes than their NFS counterparts (Figure 7a) as fluvial transport depends on both discharge and local slope and it is more effective in removing sediments than hillslope diffusion. As solar radiation exposure reverses between NFS and SFS in the Southern Hemisphere, the abovementioned radiation-driven coupled eco-geomorphic processes lead to denser vegetation cover and steeper hillslope gradients on SFS than NFS, resulting in $HA_{N\text{-}S}<0$ (Figure 7c). Consistent with the theory, the relatively low radiation contrast at the 0° latitude does not prompt any significant differences in the S-A relations (Figure 7b).

4.5. Conclusions

Asymmetric development of hillslopes and valley networks has been reported as a global phenomenon. *Poulos et al*. [2012] quantified hillslope asymmetry (HA) as the log10 of the ratio of median slopes of opposing aspects (N versus S, or E versus W) and showed that the N-to-S HA, $HA_{N\text{-}S}$, is nearly 0 at the Equator, and systematically increases ($HA_{N\text{-}S}>0$) in the Northern Hemisphere indicating steeper NFS, and decreases ($HA_{N\text{-}S}<0$) in the Southern Hemisphere, indicating steeper SFS than their opposing counterparts. At the scale of local catchments where strong $HA_{N\text{-}S}$ has been reported, differential hillslope evolution has been attributed to a range of micro-climatic controls altering bedrock weathering [*Burnett et al*., 2008], colluvial transport [*Naylor and Gabet*, 2007; *Anderson et al*., 2013a; *West et al*., 2014], and soil wash [*Parsons*, 1988; *Istanbulluoglu et al*., 2008] on opposing NFS and SFS.

In this study, we used an ecogeomorphic landscape evolution model that couples the continuity equations for water, sediment, and aboveground biomass at each model element. The model is used to explore the control of latitude and mean annual precipitation (MAP) of semiarid climate on catchment evolution, and resulting $HA_{N\text{-}S}$. In the model, vegetation only influences the rates of fluvial incision and transport. Hillslope diffusion is driven by local hillslope gradient, independent of vegetation cover. We have addressed three research questions posed in the introduction section of this paper. First, our modeling experiments reveal that hillslope asymmetry can emerge from the competition between soil creep and vegetation-modulated fluvial transport, driven by spatial distribution of solar radiation and spatially-uniform rainfall. Consistent with the observations of *Parsons* [1988] and *Poulos et al.* [2012], modeled hillslope asymmetry grows with latitude away from the Equator, north-facing slopes (NFS) get steeper (gentler) while south-facing slopes (SFS) get gentler (steeper) compared to their corresponding values at the modeled 0° latitude landscape. Second, the modeled differential evolution of opposing hillslopes is a direct outcome of solar radiation-driven ecohydrologic vegetation dynamics on opposing slopes controlled by latitude. In the model, NFS (SFS) support more (less) vegetation cover than SFS (NFS) as latitude increases towards north (south) from the Equator. In semiarid climates, differences in the vegetation cover of NFS and SFS have been widely observed, and reported in field investigations [*Butler et al*., 1986; *McMahon*, 1998; *Sternberg and Shoshany*, 2001; *Desta et al*., 2004]. Third, for a given latitude, MAP is found to have a secondary control on *HA* in the mid to higher latitudes, where wetter conditions promote vegetation growth on aspects exposed to

higher radiation than their opposing counterparts, leading to differential slope evolution. In the simulations, mean slopes of the NFS increase toward the North Pole (Figure 5a), while those of SFS increase toward the South Pole (Figure 5b). As a result of this counteraction, $HA_{N\text{-}S}$ values become larger (smaller) toward the North (South) Pole. Our results underscore the influence of solar radiation as a global control on the development of hillslope asymmetry. Variations in MAP for a given latitude are shown to have little impact on hillslope asymmetry in comparison to latitudinal variations.

There are several limitations of our model and model scenarios. In the model, the role of solar radiation and vegetation processes are only coupled with fluvial processes. There is growing evidence that aspect-modulated micro-climate can also influence colluvial transport by hillslope diffusion [*West et al*., 2014] and rates of bedrock weathering [*Burnett et al*., 2008]. For example, in a forested catchment in central Pennsylvania (USA), *West et al*. [2014] found hillslope diffusivity on SFS to be nearly twice the value of NFS, and related this to the higher frequency of freeze-thaw cycles on SFS. Their findings can be clearly attributed to significantly higher solar radiation exposure of SFS in winter months in the Northern Hemisphere as we discuss in detail in this paper. Increased efficiency of hillslope diffusion on SFS would further lead to shallower south-facing slopes in the model, increasing the landscape scale $HA_{N\text{-}S}$. Incorporating such effects of hillslope diffusion would arguably amplify the contrast between the opposing hillslope gradients in modeled landscapes.

Our model only incorporates the influence of latitude on the spatial distribution of relative solar radiation throughout the year, while the amount of annual solar radiation as well as other climatic factors (temperature, relative humidity, wind speed) that control T_{max} are assumed to be identical across latitudes, except for the adjustment of the seasonal distribution of T_{max}, consistent with the lag in the solar peak in the Southern Hemisphere. Rainfall climatology is also assumed to be invariant across latitudes. Limitations in the representation of climate across latitudes, and not incorporating more realistic periglacial and glacial processes could have resulted in deviations between modeled and reported hillslopes asymmetry values by *Poulos et al*., [2012] in high north and south latitudes.

References

Allen, R. G., L. S. Pereira, D. Raes, and M. Smith (1998), *Crop Evapotranspiration - Guidelines for computing crop water requirements. FAO Irrigation and Drainage Paper 56*, FAO, Rome, Italy.

Anderson, R. S., S. P. Anderson, and G. E. Tucker (2013a), Rock damage and regolith transport by frost: an example of climate modulation of the geomorphology of the critical zone, *Earth Surf Proc Land*, *38*(3), 299-316, doi:10.1002/esp.3330.

Anderson, S. P., R. S. Anderson, G. E. Tucker, and D. P. Dethier (2013b), Critical zone evolution: Climate and exhumation in the Colorado Front Range, *Field Guides*, *33*, 1-18, doi:10.1130/2013.0033(01).

Branson, F. A., and L. M. Shown (1989), *Contrasts of vegetation, soils, microclimates, and geomorphic processes between north- and south-facing slopes on Green Mountain near Denver, Colorado*, Dept. of the Interior, U.S. Geological Survey :, Denver, Colorado.

Bras, R. L. (1990), *Hydrology: an introduction to hydrologic science*, Addison-Wesley, Reading, Mass.

Burnett, B. N., G. A. Meyer, and L. D. McFadden (2008), Aspect-related microclimatic influences on slope forms and processes, northeastern Arizona, *J Geophys Res-Earth*, *113*, F03002, doi:10.1029/2007JF000789.

Butler, J., H. Goetz, and J. L. Richardson (1986), Vegetation and soil - landscape relationships in the North-Dakota Badlands, *Am Midl Nat*, *116*(2), 378-386.

Carson, M. A., and M. J. Kirkby (1972), *Hillslope form and process*, Cambridge University Press, Cambridge, U. K.

Collins, D. B. G., and R. L. Bras (2010), Climatic and ecological controls of equilibrium drainage density, relief, and channel concavity in dry lands, *Water Resour Res*, *46*, W04508, doi:10.1029/2009WR008615.

Cristea, N. C., S. K. Kampf, and S. J. Burges (2013), Linear models for estimating annual and growing season reference evapotranspiration using averages of weather variables, *Int J Climatol*, *33*(2), 376-387, doi: 10.1002/Joc.3430.

Desta, F., J.J. Colbert, J.S. Rentch, and K. Gottschalk (2004), Aspect induced differences in vegetation, soil, and microclimatic characteristics of an Appalachian watershed, *Castanea*, *69(2)*, 92-108.

Dethier, D.P., C.D. Harrington, and M.J. Aldrich (1988), Late Cenozoic rates of erosion in the western Española basin, New Mexico: Evidence from geologic dating of erosion surfaces, B*ull. Geol. Soc. Am.*, 100 (6), 928–937, doi: 10.1130/0016-7606(1988)100<0928:LCROEI>2.3.CO;2.

Flores-Cervantes, J. H. (2010), The coupled development of terrain and vegetation: the case of semiarid grasslands, PhD thesis, MIT, Boston, MA.

Flores Cervantes, J. H., E. Istanbulluoglu, E. R. Vivoni, C. D. Holifield Collins, and R. L. Bras (2014), A geomorphic perspective on terrain-modulated organization of vegetation productivity: analysis in two semiarid grassland ecosystems in Southwestern United States, *Ecohydrology*, *7*(2), 242-257, doi:10.1002/eco.1333.

Gutiérrez-Jurado, H. A., and E. R. Vivoni (2013a), Ecogeomorphic expressions of an aspect-controlled semiarid basin: I. Topographic analyses with high-resolution data sets, *Ecohydrology*, *6*(1), 8-23, doi:10.1002/Eco.280.

Gutiérrez-Jurado, H. A., and E. R. Vivoni (2013b), Ecogeomorphic expressions of an aspect-controlled semiarid basin: II. Topographic and vegetation controls on solar irradiance, *Ecohydrology*, *6*(1), 24-37, doi:10.1002/Eco.1263.

Gutiérrez-Jurado, H. A., E. R. Vivoni, C. Cikoski, J. B. J. Harrison, R. L. Bras, and E. Istanbulluoglu (2013), On the observed ecohydrologic dynamics of a semiarid basin with aspect-delimited ecosystems, *Water Resour Res*, *49*(12), 8263-8284, doi:10.1002/2013wr014364.

Istanbulluoglu, E., and R. L. Bras (2005), Vegetation-modulated landscape evolution: Effects of vegetation on landscape processes, drainage density, and topography, *J Geophys Res-Earth*, *110*, F02012, doi:10.1029/2004JF000249.

Istanbulluoglu, E., and R. L. Bras (2006), On the dynamics of soil moisture, vegetation, and erosion: Implications of climate variability and change, *Water Resour Res*, *42*, W06418, doi:10.1029/2005WR004113.

Istanbulluoglu, E., O. Yetemen, E. R. Vivoni, H. A. Gutierrez-Jurado, and R. L. Bras (2008), Eco-geomorphic implications of hillslope aspect: Inferences from analysis of landscape morphology in central New Mexico, *Geophys Res Lett*, *35*, L14403, doi:10.1029/2008GL034477.

Istanbulluoglu, E., T. J. Wang, and D. A. Wedin (2012), Evaluation of ecohydrologic model parsimony at local and regional scales in a semiarid grassland ecosystem, *Ecohydrology*, *5*(1), 121-142, doi:10.1002/Eco.211.

Kunkel, M. L., A. N. Flores, T. J. Smith, J. P. McNamara, and S. G. Benner (2011), A simplified approach for estimating soil carbon and nitrogen stocks in semi-arid complex terrain, Geoderma, 165(1), 1-11, doi:10.1016/j.geoderma.2011.06.011.

Laio, F., A. Porporato, L. Ridolfi, and I. Rodriguez-Iturbe (2001), Plants in water-controlled ecosystems: active role in hydrologic processes and response to water stress II. Probabilistic soil moisture dynamics, *Adv Water Resour*, *24*(7), 707-723, doi:10.1016/S0309-1708(01)00005-7.

Ma, L., F. Chabaux, N. West, E. Kirby, L. X. Jin, and S. Brantley (2013), Regolith production and transport in the Susquehanna Shale Hills Critical Zone Observatory, Part 1: Insights from U-series isotopes, *J Geophys Res-Earth*, *118*(2), 722-740, doi:10.1002/Jgrf.20037.

McMahon, D. R. (1998), Soil, landscape and vegetation interactions in small semi-arid drainage basin: Sevilleta National Wildlife Refuge, New Mexico, NMTech, Socorro, NM.

Melton, M. A. (1960), Intravalley variation in slope angles related to microclimate and erosional environment, *Bull. Geol. Soc. Am.*, *71*, 133–144, doi:10.1130/0016-7606(1960)71[133:IVISAR]2.0.CO;2.

Montaldo, N., R. Rondena, J. D. Albertson, and M. Mancini (2005), Parsimonious modeling of vegetation dynamics for ecohydrologic studies of water-limited ecosystems, *Water Resour Res*, *41*(10), W10416, doi:10.1029/2005wr004094.

Naylor, S., and E. J. Gabet (2007), Valley asymmetry and glacial versus nonglacial erosion in the Bitterroot Range, Montana, USA, *Geology*, *35(4)*, 375–378, doi:10.1130/G23283A.1.

Parsons, A. J. (1988), *Hillslope form*, Routledge, London, U. K.

Parsons, D.J. (1976), Vegetation structure in the Mediterranean scrub communities of California and Chile, *J Ecol*, *64(2)*, 435-447, doi: 10.2307/2258767.

Pazzaglia, F. J., and J.W. Hawley (2004), Neogene (rift flank) and Quaternary geology and geomorphology in, Mack, G. and Giles, K., eds., The Geology of New Mexico: New Mexico Geological Society Special Publication 11, Albuquerque, NM, p. 407-437.

Poulos, M. J., J. L. Pierce, A. N. Flores, and S. G. Benner (2012), Hillslope asymmetry maps reveal widespread, multi-scale organization, *Geophys Res Lett*, *39*, L06406, doi:10.1029/2012GL051283.

Small, E. E. (2005), Climatic controls on diffuse groundwater recharge in semiarid environments of the southwestern United States, *Water Resour Res*, *41*, W04012, doi:10.1029/2004WR003193.

Smith, T. J., J. P. McNamara, A. N. Flores, M. M. Gribb, P. S. Aishlin, and S. G. Benner (2011), Small soil storage capacity limits benefit of winter snowpack to upland vegetation, Hydrol Process, 25(25), 3858-3865, doi: 10.1002/Hyp.8340.

Sternberg, M., and M., Shoshany (2001), Influence of slope aspect on Mediterranean woody formations: Comparison of a semiarid and an arid site in Israel, *Ecol Res*, *16*, 335-345, doi:10.1046/j.1440-1703.2001.00393.x

Tucker, G. E., and R. L. Bras (1998), Hillslope processes, drainage density, and landscape morphology, *Water Resour Res*, *34*(10), 2751-2764, doi:10.1029/98WR01474.

Tucker, G. E., S. T. Lancaster, N. M. Gasparini, and R. L. Bras (2001), The Channel-Hillslope Integrated Landscape Development model (CHILD), in *Landscape Erosion and Evolution Modeling*, edited by R. S. Harmon and W. W. Doe III, pp. 349-388, Kluwer Academic, New York.

Vivoni, E. R., H. A. Moreno, G. Mascaro, J. C. Rodriguez, C. J. Watts, J. Garatuza-Payan, and R. L. Scott (2008), Observed relation between evapotranspiration and soil moisture in the North American monsoon region, *Geophys Res Lett*, *35*, L22403, doi:10.1029/2008GL036001.

Walker, E. H. (1948), Differential erosion on slopes of northern and southern exposure in western Wyoming, *Geol Soc Am Bull*, *59*(12), 1360-1360,

West, N., E. Kirby, P. Bierman, R. Slingerland, L. Ma, D. Rood, and S. Brantley (2013), Regolith production and transport at the Susquehanna Shale Hills Critical Zone Observatory, Part 2: Insights from meteoric ^{10}Be, *J Geophys Res-Earth*, *118*(3), 1877-1896, doi:10.1002/Jgrf.20121.

West, N., E. Kirby, P. Bierman, and B. A. Clarke (2014), Aspect-dependent variations in regolith creep revealed by meteoric ^{10}Be, *Geology*, *42*, 507-510, 10.1130/g35357.1.

Williams, C. A., and J. D. Albertson (2005), Contrasting short- and long-timescale effects of vegetation dynamics on water and carbon fluxes in water-limited ecosystems, *Water Resour Res*, *41*(6), W06005, doi:10.1029/2004wr003750.

Yetemen, O., E. Istanbulluoglu, and E. R. Vivoni (2010), The implications of geology, soils, and vegetation on landscape morphology: Inferences from semi-arid basins with complex vegetation patterns in Central New Mexico, USA, *Geomorphology*, *116*(3-4), 246-263, doi:10.1016/j.geomorph.2009.11.026.

Yetemen, O., E. Istanbulluoglu, J.H. Flores-Cervantes, E.R. Vivoni, and R.L. Bras (submitted), Modeling the ecohydrologic role of solar radiation on catchment development in semiarid ecosystems, *Water Resour Res*.

Zhou, X., E. Istanbulluoglu, and E. R. Vivoni (2013), Modeling the ecohydrological role of aspect-controlled radiation on tree-grass-shrub coexistence in a semiarid climate, *Water Resour Res*, *49*(5), 2872-2895, doi:10.1002/wrcr.20259.

TABLE

Table 1: Location of analyzed catchments, their DEM resolution and calculated $HA_{N\text{-}S}$ values, and source of the studies that indicates aspect-related vegetation difference

Location	Latitude (°)	Longitude (°)	$HA_{N\text{-}S}$	DEM Res. (m)	Source
A	N 43.72	W 116.13	0.119	10	*Poulos et al.* [2012]
B	N 40.01	W 105.47	0.024	1	*Anderson et al.* [2013b]
C	N 34.42	W 107.80	0.094	30	*Yetemen et al.* [2010]
D	N 34.41	W 106.98	0.086	10	*Istanbulluoglu et al.* [2008]
E	N 31.72	W 110.03	0.030	10	*Flores Cervantes et al.* [2014]
F1	S 33.05	W 70.92	-0.121	30	*Parsons* [1976]
F2	S 33.05	W 70.92	-0.104	30	*Parsons* [1976]

A: Dry Creek Experimental Watershed, Boise, Idaho; B: Gordon Gulch Boulder Creek Critical Zone Observatory, Boulder, Colorado; C: Upper Rio Salado, New Mexico; D: Sevilleta Long Term Ecological Research Park, New Mexico; E: Walnut Gulch Experimental Watershed, Arizona; F1 and F2: Cerro Robles, Chile.

FIGURES

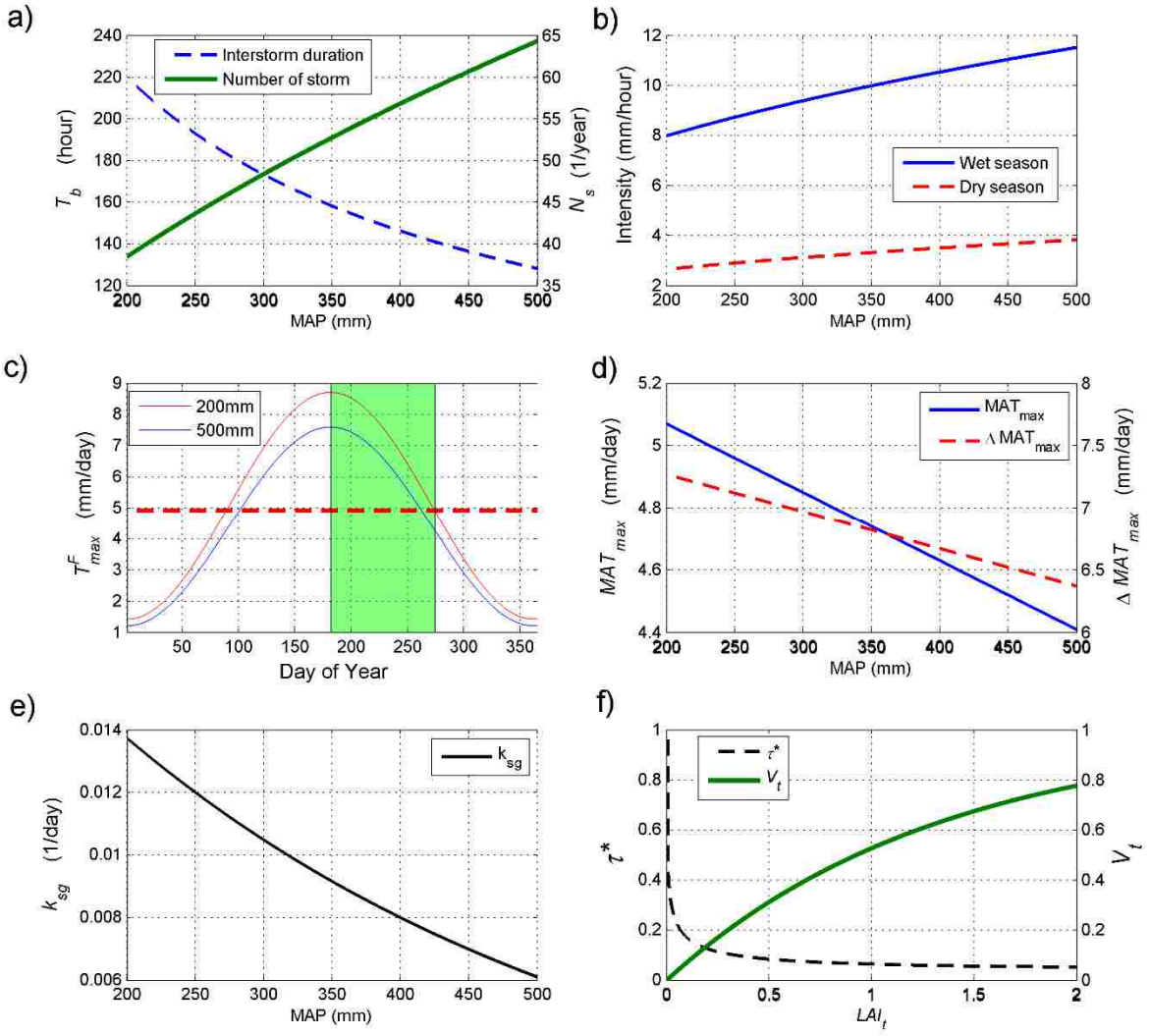

Figure 1. Illustration of several critical model assumptions: a) Empirical relationships for the mean annual interstorm duration (T_b) and annual number of storms (N_s) as a function of mean annual precipitation (MAP). b) Mean storm intensity (mm/hr) for wet and dry season precipitation as a function of MAP, these rates are squeezed by six times to create enough runoff. c) Sinusoidal function used to represent the seasonal variability of T_{max} on flat surface $\left(T^F_{\max}\right)$ as a function of DOY for the wet and dry end-member of modeled MAP. The wet season (Monsoon) is indicated with the green region. The threshold for growing season is represented with a red dashed lines. d) Annual mean daily value of $T^F_{\max}$ ($MAT_{\max}$) and the annual mean difference in minimum and maximum values of $T^F_{\max}$ throughout the year ($\Delta MAT_{\max}$) are predicted as a function of MAP. e) Empirical relationship for decay coefficient for green biomass senescence as a function of MAP. f) Dependence of the dimensionless shear stress τ^* and the total grass cover (V_t) on the total leaf area index LAI_t of the land surface.

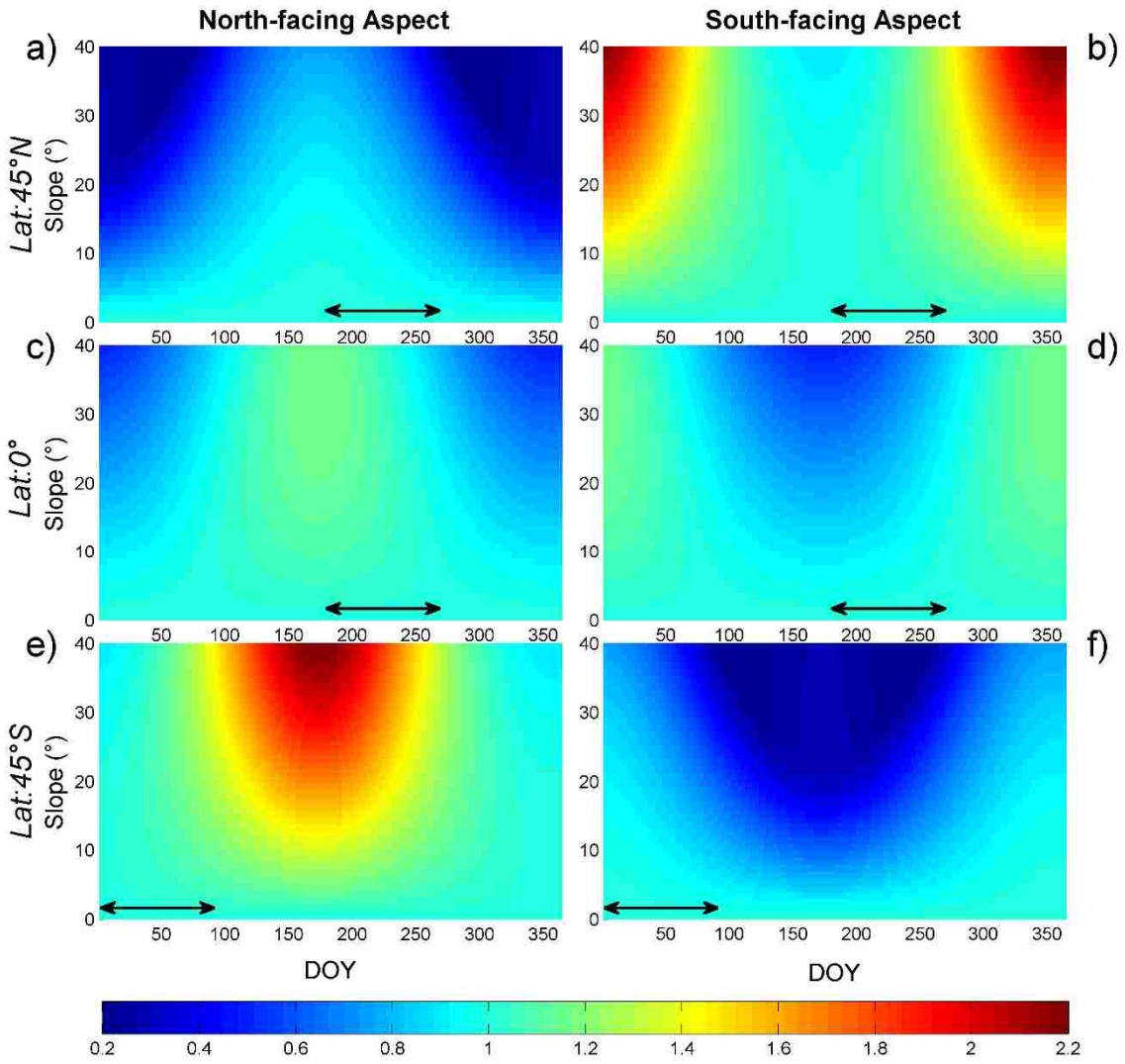

Figure 2. Annual variation in R_{solar} (color bar at the bottom shows the scale) plotted as a function of local slope and day of year (DOY) for north-facing (a, c, e) and south-facing (b, d, f) aspects for 45°N, 0°, 45°S latitudes from top to bottom panels, respectively. Horizontal double-headed arrow indicates the wet season (half of the annual precipitation) used in the model.

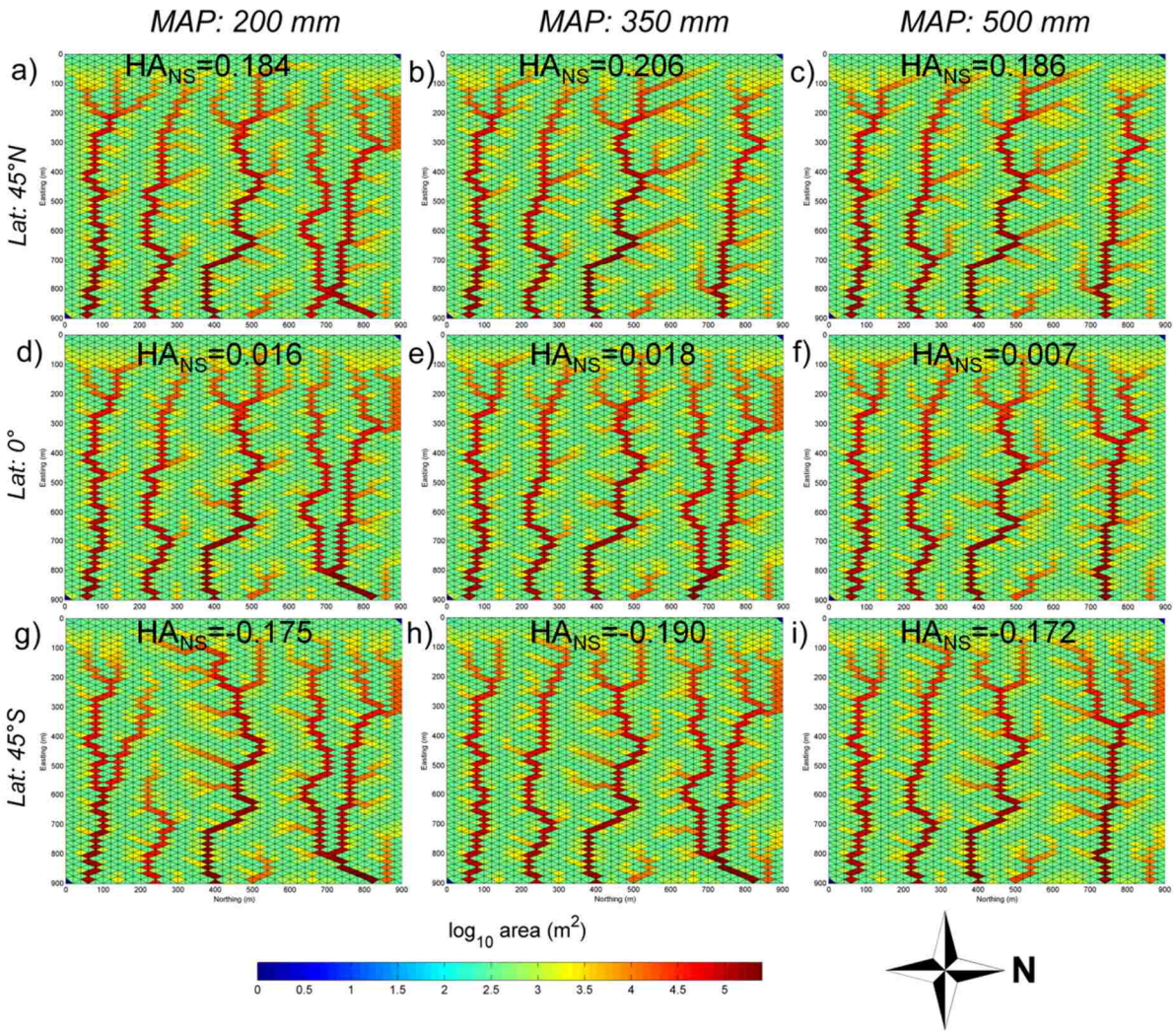

Figure 3. Upslope contributing area maps of modeled landscapes for 200 mm, 350 mm, and 500 mm of MAP for 45°N (a, b, c), 0° (d, e, f), and 45°S (g, h, i) latitudes. Calculated hillslope asymmetry, $HA_{N\text{-}S}$, ($HA_{N\text{-}S}=log_{10}[S_{North}/S_{South}]$) based on *Poulos et al.* [2012] for each modeled landscape is reported.

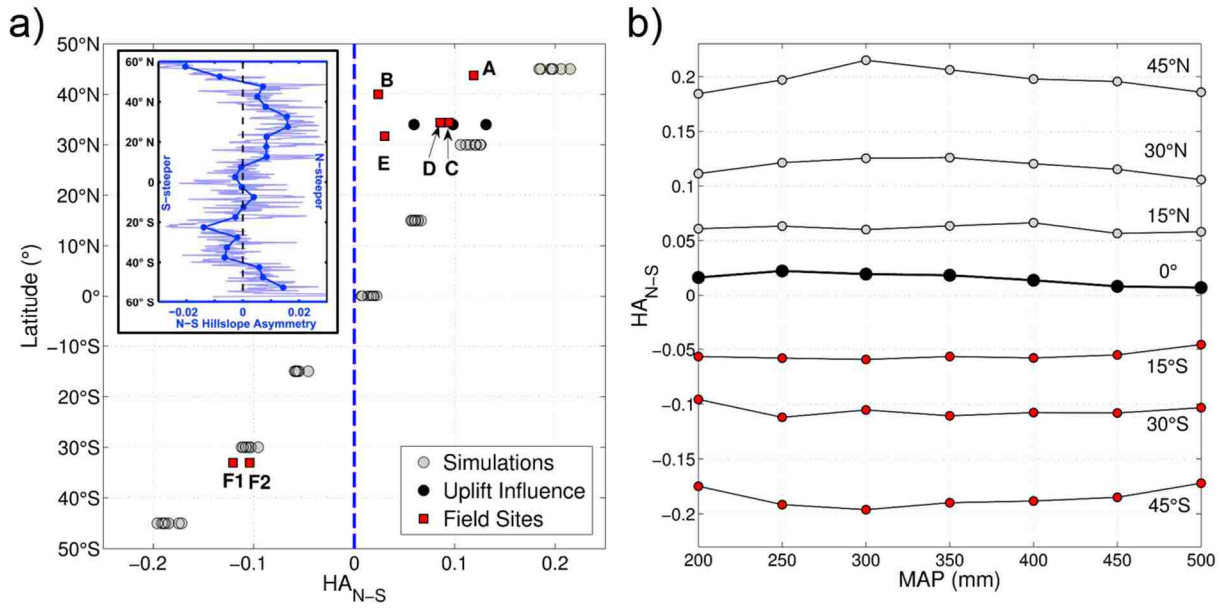

Figure 4. a) Landscape-scale north-to-south hillslope asymmetry ($HA_{N\text{-}S}$) plotted as a function of latitude for all modeled landscapes with 0.1 mm/yr uplift (gray circles) and a range of MAP; landscapes modeled with no, moderate, and high uplift for 34°N for central New Mexico (black circles) with MAP=250 mm; and sample actual semiarid catchments (Table 1) exhibiting aspect-related vegetation and geomorphic difference reported in the literature (red squares). The inset shows the $HA_{N\text{-}S}$ through the American Cordillera calculated by *Poulos et al.*, [2012] (Reproduced from *Poulos et al.*, [2012] with permission of John Wiley and Sons). b) $HA_{N\text{-}S}$ is plotted as a function of MAP, where latitudes in the northern hemisphere, southern hemisphere, and the equator are represented by gray, red, and black circles respectively.

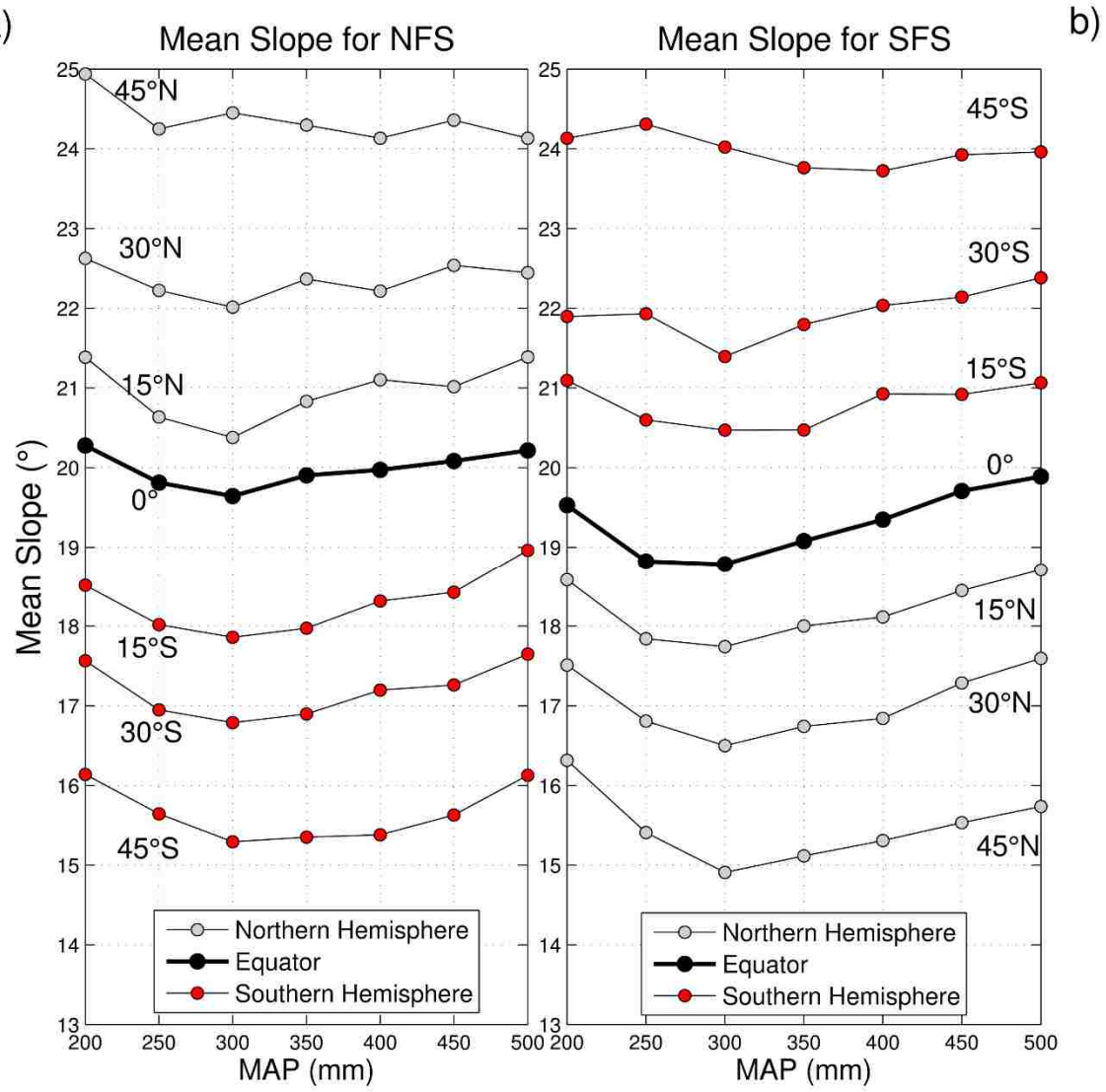

Figure 5. a) Latitudinal variations of spatial mean slopes of modeled landscapes plotted as a function of MAP for north-facing slopes, NFS (a), and south-facing slope, SFS (b). To facilitate cross-comparison of data for NFS and SFS of a model output for a given latitude, latitudes in the northern and southern hemisphere are represented with gray and red circles, respectively; black circles represent data from the equator.

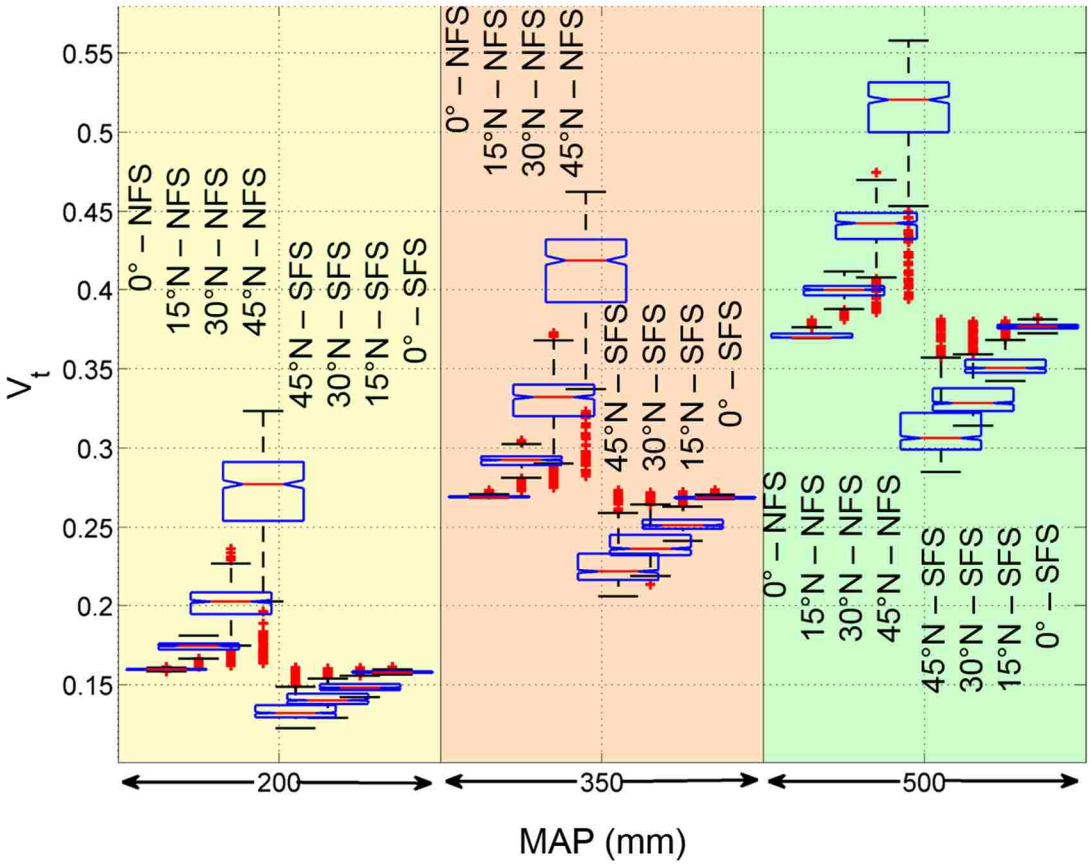

Figure 6. Mean annual total vegetation cover V_t at north- and south-facing slopes for the last 100-yr of the simulations at different latitudes (0°, 15°N, 30°N, and 45°N) are shown in Box-Whisker plots as a function of MAP.

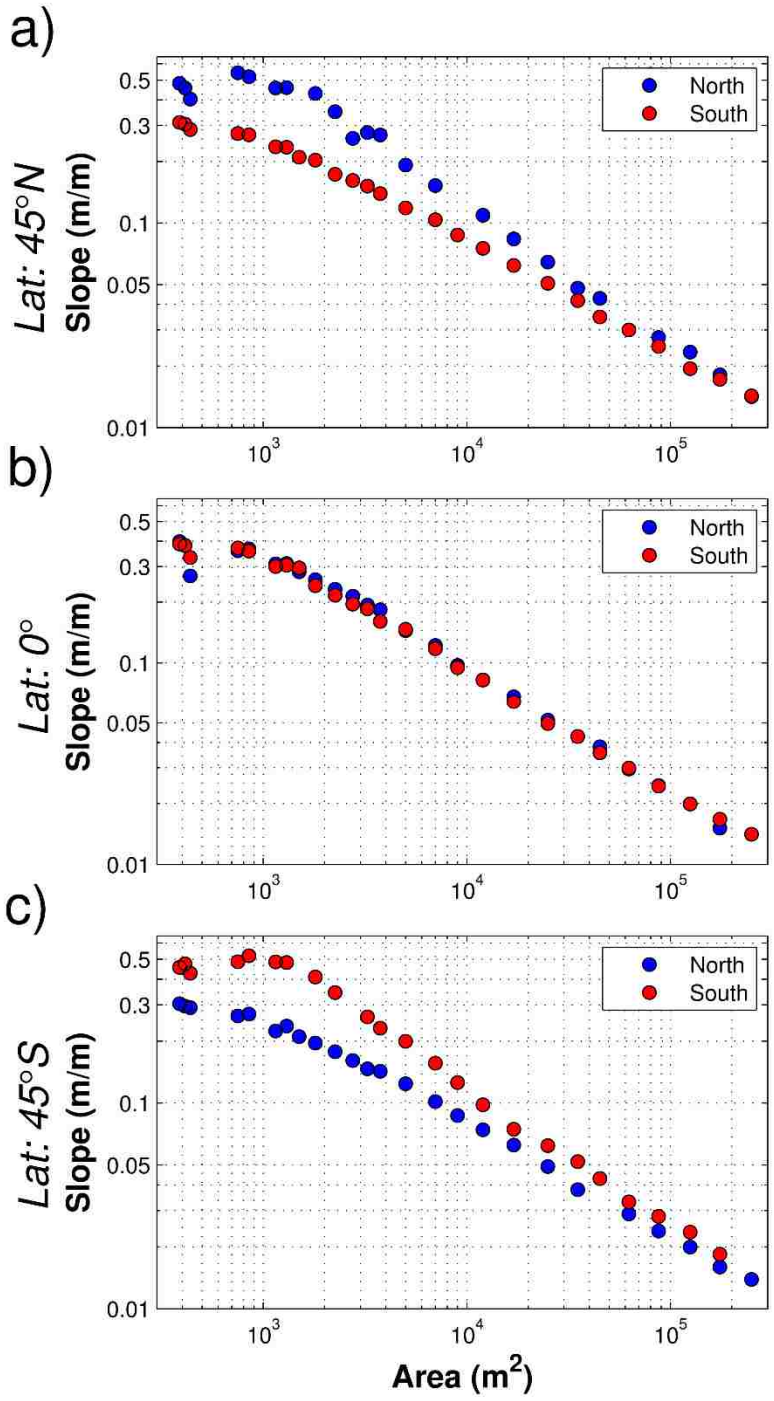

Figure 7. The slope-area relation of modeled landscapes with a MAP=350 mm for (a) 45°N, (b) 0°, and (c) 45°S latitudes. Each data point presents an average slope of binned model elements with respect to area.

CHAPTER 5: CLIMATE AND VEGETATION CONTROL OF HILLSLOPE ASYMMETRY WITH UNIFORM EROSION RATES[4]

Abstract

We designed numerical model experiments to examine the climatic and ecohydrologic conditions that would lead to observed spatial patterns in the Holocene erosion rates in central New Mexico. Based on field observations, south-facing slopes are found to be more erosive than north-facing slopes. We used CHILD (Channel-Hillslope Integrated Landscape Development) LEM (Landscape Evolution Model) equipped with solar radiation and vegetation dynamics components to explore the cases of rate differences. We forced CHILD with uniform uplift rate obtained by averaging the erosion estimates from the study site. The climate forcing is simulated by: (1) stationary climate that represents the observed modern climate in the region using the stochastic rainfall model and (2) cyclic climate forcing replicating a late Pleistocene climate that prevailed in the region. These two simulations were used to bring the landscapes to dynamic equilibrium. Once the landscapes reached equilibrium, the modeled elevation fields that correspond to the wet period (e.g., Last Glacial Maximum) were output from the model, and used as an input to a third and final set of forcing using dynamic climate data based on paleoclimate proxies. The simulations with cyclic climate demonstrate how the memory of landscape follows climate and alters spatial erosion rates. Finally, we illustrate the role of more accurate representation of climate on the spatial patterns of erosion using the reconstructed paleoclimate followed by cyclic climate. LEM also showed that the discrepancy in erosion rates on opposing hillslopes is not sustainable over the long-term. Depending on the climate forcing or internal dynamics of erosion mechanism, either north- or south-facing slopes can be more erosive than their counterparts. Over the long-term, however, the fluctuations in spatial erosion rates average out. Hence, under a given uniform uplift, erosion rates on opposing hillslopes are found to be the same.

[4] The coauthors for the planned journal submission are Erkan Istanbulluoglu, J. Bruce J. Harrison, Fred M. Philips, and Enrique R. Vivoni.

5.1. Introduction

Hillslope asymmetry is a landscape characteristic originated from aspect-driven surface processes that cause opposite facing hillslopes to exhibit differences in gradients at the landscape scale. Global-scale topographic analyses reveal that north-facing slopes (NFS) are steeper (shallower) than south-facing slopes (SFS) in the Northern (Southern) Hemisphere [*Poulos et al.*, 2012]. The reversal in the steeper hillslope gradients from NFS in the Northern Hemisphere to SFS in the Southern Hemisphere has been related to differences in the space-time characteristics of solar radiation and its influence on a range of ecohydrologic and geomorphic processes as a function of latitude [e.g., *Parsons et al.*, 1988; *Burnett et al.*, 2008]. In particular, in soil-mantled water-limited ecosystems in the Northern Hemisphere, steeper hillslope gradients on northern aspects have been related to the geomorphic effects of denser vegetation cover as a result of lower solar insolation, and reduced amounts of surface storm runoff [*Istanbulluoglu et al.*, 2008; *Gutiérrez-Jurado et al.*, 2013].

Recent studies investigating the differences in hillslope morphology on opposing north- and south-facing hillslopes, explained their observations by invoking Hack's concept of equilibrium, and proposed that under a fixed rate of base level fall (i.e., erosion rate in the main channel) opposing hillslope morphologies adjust such that they erode at identical rates, but with different soil fluvial erodibility [*Istanbulluoglu et al.*, 2008; *Yetemen et al.*, 2010] or regolith transport efficiency [*Anderson et al.*, 2013; *West et al.*, 2014]. For example, comparing regolith fluxes in forested north- and south-facing slopes at the Susquehanna Shale Hills Critical Zone Observatory in central Pennsylvania, USA, *West et al.* [2014] found hillslope diffusivity constants on low-gradient SFS with thin soils twice as large as those on NFS, with steep slopes and deeper soils, and related this observation to the higher frequency of freeze-thaw cycles on southern aspects controlled by micro-climatological differences. When long-term average (>10 kiloyear, kyr) erosion rates obtained from meteoric ^{10}Be are compared on opposing slopes *West et al.* [2013] found 19.4 m·Myr^{-1} on north-, and 16.1 m·Myr^{-1} on south-facing slopes, respectively (see table 6 of *West et al.*, [2013]), which may show some evidence that, differences in regolith erodibility may also manifest itself on net erosion rates on opposing hillslopes. In a theoretical modeling study of frost-driven rock damage and transport, *Anderson et al.* [2013] attributed the development of hillslope asymmetry in modeled hillslope profiles to the different transport rates on opposing slopes, which, when multiplied by differences in gradient gives relatively uniform flux on

opposing slopes. These recent studies attribute the development of differences in opposing hillslope steepness and landscape-scale hillslope asymmetry to differences in hillslope erodibility under uniform erosion rates across the landscape.

While recent research demonstrates hillslope asymmetry as a global phenomenon, there is limited research that explore the feedbacks among hillslope-scale soil erodibility, erosion rates, and landscape-scale hillslope asymmetry under a fluctuating climate. To advance our understanding of differential landscape evolution leading to hillslope and valley asymmetry, we must address the following questions: (1) how does short- and long-term climate variability control spatial patterns in erosion rates and resulting hillslope asymmetry under a constant rate of uplift? (2) What is the role of vegetation on modulating spatial erosion rates under a fluctuating climate? (3) Are there any feedbacks between landscape-scale hillslope asymmetry and erosion rates on north- and south-facing slopes? (4) Do the current characteristics of landscapes carry any relict topographic features from past climates that may have an influence on erosion rates? Here, we investigate these questions in a systematic study of numerical model experiments using an ecohydrologic landscape evolution model (LEM) for fluvial landscapes guided by climate and vegetation conditions in a semiarid catchment in central New Mexico, USA, where ecohydrologic processes are tightly coupled with climate. LEM results are corroborated with long-term erosion rates (~10 kyr) obtained from field sediment samples on opposing hillslope aspects.

5.2. Study Site and Erosion Rates

The field site that guided our numerical model simulations is located at the Sevilleta National Wildlife Refuge (SNWR) in central New Mexico, where hillslope aspect shows a marked influence on vegetation patterns and landscape morphology (Figure 1a). The catchment was incised on the coarse alluvial fan deposits of the Plio-Pleistocene Sierra Ladrones Formation [*McMahon*, 1998; *Connel and McGraw*, 2007]. The region receives ~250 mm of mean annual precipitation (MAP) based on observations at Deep Well meteorological station in SNWR. At Deep Well station, hourly precipitation, wind speed and relative humidity have been measured since 1990 [*Moore*, 2012]. Beside climatological data, evapotranspiration fluxes were measured between 1996 and 1999 from a Bowen Ratio Energy Balance tower located near the station [*Gosz*, 2012a], and soil moisture contents in the root zone were measured from 1996 to 2006 using vertically-installed time domain reflectometry probes at three different pits adjacent to the meteorological station and flux tower [*Gosz*, 2012b]. High-intensity and short-duration convective thunderstorms during the North

American Monsoon NAM (July to September) account for approximately 50% of the MAP [*Vivoni et al.*, 2008]. In the winter, low-intensity frontal storms with occasional snow are typical [*Milne et al.*, 2003]. Livestock grazing has not been permitted at the SNWR since 1973 [*Gosz and Gosz*, 1996].

At the catchment NFS are covered by a relatively mesic ecosystem with one-seed Juniper (*Juniperus monosperma*) and denser black grama grass (*Bouteloua eriopoda*). SFS host a more xeric ecosystem consisting of creosote bush (*Larrera tridentata*) and sparser fluff grass (*Erioneuron pulchellum*) [*McMahon*, 1998; *Gutiérrez-Jurado et al.*, 2007]. NFS soils contain higher proportions of organic matter, $CaCO_3$, silt, and clay contents than SFS as a result of higher infiltration rates, deeper infiltration profiles, aeolion sediment deposition, and root respiration [*Gutiérrez-Jurado et al.*, 2006].

Hillslope morphologies of opposing NFS and SFS also exhibit pronounced differences. NFS have smooth planar forms, devoid of any significant fluvial incisions, and are having relative longer hillslopes than SFS. SFS are highly dissected with active channels, forming regularly-spaced hollows. At the catchment scale, differences in the NFS and SFS morphologies lead to asymmetric channel network development [*Istanbulluoglu et al.*, 2008]. We investigated the role of climate on long-term erosion rates on opposing hillslopes at the SNWR, where hillslope aspect has a marked influence on vegetation types and landscape morphology [*Istanbulluoglu et al.*, 2008]. Holocene-averaged erosion-rates on opposing hillslope aspects were estimated using the ^{36}Cl cosmogenic dating technique. A map of the sampling locations for ^{36}Cl measurement is shown in the Figure 1a, and the coordinates and denudation rates, with ranges of uncertainty, are given in Table 1. The exposure times are converted into denudation estimates, ε, based on

$$\varepsilon = \lambda_{36} \Lambda \left[\left(1 - \exp\left(\lambda_{36}\, t \right) \right)^{-1} - 1 \right] \qquad (1)$$

where λ_{36} is the decay constant of the cosmogenic nuclide ($2.30 \cdot 10^{-6}$ yr^{-1}) [*Vermeesch*, 2007], Λ is characteristic attenuation length for neutrons (140 $g.cm^{-2}$) [*Dunai*, 2000], and t is the calculated ^{36}Cl exposure time (yr). Long-term erosion rates that represent the last ~10 kyr to 15 kyr based on sample exposure ages, are in the range of 0.06 to 0.1 $mm \cdot yr^{-1}$, which coincides with the long-term (ca. 640 kyr) erosion rates for the region based on the incision rates [*Dethier, 2001*] as well as other regional denudation estimates [*Dethier et al., 1998*; *Clapp et al., 2001*; *Bierman et al.*, 2005]. Erosion rates and uncertainty for each hillslope pair are compared in Figure 1b. Considering the

uncertainty ranges, SFS show slightly greater net mean annual erosion (between 9-19%, and on average 17.4%) than NFS. This slight difference is consistent with the differences reported on north- and south-facing erosion rates in the forested Susquehanna Shale Hills Critical Zone Observatory catchment by *West et al*., [2013].

5.3. Model Theory and Numerical Experiment Design

In this study, we use the CHILD LEM framework [*Tucker et al*., 2001], which is equipped with solar radiation and vegetation dynamics components [*Collins and Bras*, 2010; *Flores-Cervantes*, 2010]. The model couples the continuity equations for energy, water, aboveground vegetation biomass, and sediment at each model element, and evolves fields of soil moisture, aboveground biomass (currently single plant type of surface vegetation such as grass and shrub), and elevation driven by stochastic rainfall, solar radiation, and landscape uplift. Implicit solar radiation and energy balance calculations were incorporated into the calculation of evapotranspiration (ET). ET and plant water stress, calculated as nonlinear function of soil root-zone moisture deficit below a threshold value [*Laio et al*., 2001], drive vegetation dynamics represented by live and dead biomass. Effective shear stress is inversely related with total vegetation cover, V_t, through a power-law relationship, and it is used for local detachment and sediment transport capacity calculations [*Istanbulluoglu and Bras*, 2005]. Hillslope diffusion is modeled by the nonlinear model of *Roering et al*. [1999], assumed independent of climate and vegetation for simplicity. Therefore, in the current model, differential evolution of the hillslope morphologies is solely driven by the impact of radiation and climate-modulated vegetation on fluvial processes. The coupled system of continuity equations for energy, water, and sediment are described in detail in *Yetemen et al*. [submitted manuscript].

The spatial domain used is a 900 m by 900 m 8% sloping surface with an open-side boundary constructed with Voronoi polygons of 20 m node spacing where sediment can exist the domain. In the model experiments, CHILD is forced by a uniform uplift rate of 0.08 mm/y obtained from long-term erosion estimates at the study site (Table 1). This is done to ensure that the mass provided to the simulated domain will be consistent with the actual denudation rates estimated from field measurements. All simulations were run for 800,000 years to allow the landscape to reach a dynamic equilibrium between erosion rates and uplift. During the simulations, we output elevation fields and total vegetation cover (V_t). Landscape-scale mean erosion rates are calculated

for north- and south-facing slopes using a moving average window of 1,000 and 15,000 years. These different time averages are used to be consistent with the long-term average rates estimated using ^{36}Cl technique from field soil samples. CHILD is driven by stochastic rainfall forcing based on a modified version of Poisson rectangular pulse process model [*Yetemen et al*., submitted manuscript]. Pulses are represented by a rate, duration and interstorm duration [*Tucker and Bras*, 2000]. The Poisson model is represented using empirical relations based on rainfall characteristics developed for semiarid southwest United States [*Small*, 2005; *Istanbulluoglu and Bras*, 2006]. As MAP varies, the rainfall characteristics change based on these empirical relations. The role of MAP on storm characteristics and ecohydrologic parameters are shown in Chapter 4 in this dissertation. The contribution of wet and dry seasons to MAP are represented in the rainfall model based on observation at Deep Well, and the onset and end of wet season mimick the North American Monsoon. Details of rainfall forcing are given in *Yetemen et al*., [submitted manuscript].

To examine the contribution of climate fluctuations on erosion rates and resulting landforms climate forcing scenarios are used systematically in five different simulations including the following cases:

(1) Stationary modern-day climate forcing: observed current climatology at the study site is represented using a stochastic seasonal rainfall model based on the Poisson rectangular pulses theory [e.g., *Zhou et al*., 2013] with a mean annual precipitation (MAP) of 250 mm, and used to evolve landscapes over 800 kyrs. The purpose of using a stationary modern-day climate was to illustrate if erosion rates and hillslope asymmetry carry only the imprint of the modern climate. If that is the case, this would suggest a rapid adjustment of landscapes to climate change over relatively short time scales;

(2) Cyclic climate forcing: a late Pleistocene-like climate regime that has prevailed in NM is illustrated by varying MAP parameter of the stochastic rainfall model between 200 and 600 mm using a sinusoidal function with 40 kyr and 100 kyr periodicity (i.e., time between two subsequent peaks or troughs) [e.g., *Swift*, 1993; *Menking et al*., 2004]. These periodicities are also consistent with well-known Milankovitch climate cycles; axial tilt and eccentricity. These two simulations are used to bring modeled landscapes to dynamic equilibrium from an initial condition of a sloping surface. Cyclic climate simulations are critical to demonstrate how landscape response follow the climate change signal.

(3) Paleoclimate forcing: In the final set of simulations, our aim was to represent paleo-climate forcing to landscape evolution as close to reality as possible. For this purpose annual precipitation forcing in the last 12,800 years is reconstructed based on the work of *Hall and Penner* [2013], who analyzed the $\delta^{13}C$ values of alluvium sequence at Abó Arroyo in central New Mexico (~35 miles north of Sevilleta), and reconstructed the temperature and precipitation records based on a strong relationship between July temperatures and the abundance of C_4 plants showed by *Teeri and Stowe* [1976], and the relationship between $\delta^{13}C$ in topsoil organic matter and July temperatures [*Nordt et al.,* 2007]. The modern climate at Abo Arroyo (MAP=360 mm) is slightly wetter than SNWR. Therefore, the ratio between the mean annual precipitation (MAP) of the Deep Well weather station and Abó Arroyo in central New Mexico is used to scale the reconstructed Abó Arroyo annual precipitation (AP) data to the study site region.

Based on the paleoclimate data of *Hall and Penner* [2013], 12,800 years ago (ie. during the Holocene) climate was 35% wetter than today. This would correspond to an AP of 338 mm at the SNWR study site. Therefore, in the paleoclimate runs the cyclic climate data were replaced with reconstructed AP data from the work of *Hall and Penner* [2013], starting at 782 kyr and 755 kyr (both start with ~338 mm/year AP) for 40-kyr and 100-kyr periodicity, respectively.

To incorporate the differences in rainfall climatology as a function of MAP as climate changes, seasonal rainfall variability, interstorm duration, and number of storms are calculated in the simulations following simple empirical relationships that relate storm climatology to MAP [*Small*, 2005; *Istanbulluoglu and Bras*, 2006]. Beside seasonal variations in potential evapotranspiration (PET), inter-annual variations in annual PET is also considered by relating it to MAP using observations from New Mexico to represent the dry-end, and from central Nebraska, to represent the wet-end of the cyclic climate [*Wang et al*., 2009]. Finally, senescence of live biomass is tied to MAP and represents the role of climate on biomass decay [*Istanbulluoglu et al*., 2012]. In a previous study (Chapter 3, *Yetemen et al*., submitted manuscript) the CHILD LEM was confirmed with observed soil moisture, evapotranspiration, and vegetation biomass observations at the SNWR study site, and with respect to its prediction of flood magnitudes in an experimental catchment in central AZ. The model theory, parameter values for ecohydrologic and geomorphic processes, and the model spatial domain used in the simulations presented in this chapter are the same as those reported in chapter 3 as well as *Yetemen et al*. [submitted manuscript].

5.4. Results and Discussions

5.4.1. Stationary climate

Time series of landscape-scale moving average erosion rates at 1 kyr and 15 kyr temporal resolution are plotted for the last 100-kyr period of the 800 kyr LEM experiments for the modern climate case (Figure 2a, 2b). There is no clear temporal pattern in the 1 kyr erosion rates on opposing NFS and SFS, while SFS erode at slightly higher rates. Moreover, both aspects show a similar year-to-year directional change in 1 kyr-erosion. On the other hand, a cyclic pattern emerges in the 15 kyr erosion rates around the uplift rate, with an alternating pattern of greater erosion rates on NFS and SFS. In both averaging time scales, SFS are more responsive to climate forcing than NFS, as manifested in the greater range of fluctuations in average erosion rates in SFS than NFS. The range of fluctuations of the 15 kyr-average erosion rates (0.075 to 0.084 $mm.y^{-1}$) on both aspects are much narrower than those estimated from field observations with exposure ages in the 8 to 16 kyr range (Figure 1b). The maximum difference in erosion rates between SFS and NFS was found as ~3.2% at year 766 kyr, which is significantly lower than field measurement. The range of variability in erosion rates and the difference between SFS and NFS demonstrate that constant climate cannot reproduce erosion rates observed in the field.

5.4.2. Cyclic climate

Cyclic climate forcing aimed to replicate a late Pleistocene-like climate variability that prevailed in the region by varying annual precipitation (AP) as a function of time between 200 mm and 600 mm, with 40 kyr and 100 kyr periodicities using a sinusoidal function. Time series of model outputs for 40 kyr (left panel) and 100 kyr (right panel) for the last 120 kyr and 200 kyr of the 800 kyr model experiments are given in Figure 3. The total vegetation cover, V_t, linearly follows AP in this water-limited climate, with wetter climate periods producing V_t as high as 0.6 and dry periods as low as 0.05 annual cover (Figure 3c and 3d).

In general, modeled geomorphic response is inversely related to precipitation forcing and vegetation cover. The 1kyr-average erosion rates are out of phase with the AP regime. Wet years characterized by low, and dry years are characterized by high erosion rates (Figure 3e and 3f), which fluctuate between 0.05-0.11 $mm.yr^{-1}$ (Figure 3e) for the 40-kyr, and 0.05-0.13 $mm.yr^{-1}$ for the 100-kyr AP periodicity (Figure 3f). Besides the amount of AP, model results reveal dependence of erosion rates to the direction of climate change. To illustrate this, we classify the model response

to climate in the following four trend categories of AP direction: the periods of AP increase from 400 mm to 600 mm (wet-increasing trend); decrease from 600 mm to 400 mm (wet-decreasing trend); decrease from 400 mm to 200 mm (dry-decreasing trend); and increase from 200 mm to 400 mm (dry-increasing trend). The first two categories form wetter than average, while the latter two categories form drier than average parts of a Milankovicth-like climate cycle. Figure 4 presents the 15 kyr-average erosion rate maps at the end of each of the four trend periods described above during the last 100-kyr of the 800 kyr simulations with a 100-kyr climate periodicity (left panel of Figure 3).

In the wetter-increasing trend of the climate cycle, increase in precipitation from 400 mm to 600 mm, accompanied by V_t increase (Figure 3c and 3d), led to a reduction in erosion rates as a result of denser canopy cover (Figure 3e and 3f). In each simulation, lower spatial average of erosion rates are observed during the peak of the wet period (Figure 3f, at 725kyr). The spatial map of 15 kyr-average erosion for the wet-increasing period ending in 725 kyr show complex spatial patterns. Hilltops erode approximately at the same rate as uplift, hollows and the upper sections of main channels erode at lower rates than uplift, and channels with larger contributing areas close to the catchment outlet erode at rates much greater than the rate of uplift (Figure 4a). The lower rates of erosion in hollows may be explained by both high vegetation cover in valleys (as we have discussed in chapter 3), and shallower hillslope gradients on opposing NFS and SFS, although variations in the NFS and SFS gradients are very small throughout the simulations (Figure 3h).

During the wet-decreasing trend as climate changes from 600 mm to 400 mm (Figure 4b, plotting 15 kyr-average erosion rates corresponding to 750 kyr) an erosion wave propagates from the lower portion of the channel network towards upland channels and valleys, while hilltop erosion reduced slightly below the uplift rate. There is a large degree of spatial variability in erosion rates in this period. This response may be explained by a reduction in V_t as a result of the drying trend in the climate. The shift from high erosion rates on hillslopes (in 725 kyr output) to channels (in the 750 kyr output), and drop in erosion rates on hillslopes led to a positive trend in the mean slope values of NFS and SFS (Figure 3g and 3h).

During the dry-decreasing climate trend as the climate moves towards the driest time of the climate cycle (year 775k in Figure 3b) landscape-scale erosion continuous to increase above the

rate of uplift on NFS and SFS (Figure 3f, 3j). The spatial pattern of the 15 kyr-average erosion shows higher erosion rates in the upland valleys, moderate erosion on ridge-tops and small hillslopes, and lower erosion rates in the second half of the channels towards their outlets (Figure 4c). Hillslope gradients steepened during this stage (Figure 3g and 3h). When climate shifted from the driest point to the dry-increasing trend from 200 mm toward 400 mm of AP, landscape-scale 15 kyr-average erosion rates continued to increase beyond the rate of uplift in year 800 k (Figure 3e and 3f). Channels eroded at much lower rates than the rate of uplift, while hillslopes across the domain eroded markedly faster, much higher than the rate of uplift (Figure 4d).

The 15 kyr moving average erosion rates on NFS and SFS reduced the millennial variability in erosion rates (Figure 3e and 3f) and facilitated the identification of long-term trends to compare with field measurements (Figure 3i and 3j). In both 40-kyr and 100-kyr cycle simulations, 15-kyr moving average erosion rates on NFS and SFS follow a cyclic pattern, and vary in the 0.05-0.105 mm yr^{-1} range (Figure 3i and 3j). This range is more consistent with field-estimated long-term erosion rates at the study site. SFS show a larger amplitude of variation in erosion rates than NFS erosion rates. This naturally leads to an alternating pattern of greater erosion rates on one of the aspects than the other aspect type. When the landscape-scale erosion is at its lowest rates during the wet portion of a climate cycle, NFS consistently show greater erosion rates than SFS with up to 25% difference. The erosion map in Figure (4a) clear demonstrate SFS with lower rates of erosion than NFS. During the driest time of the year with a dry-decreasing trend, SFS show up to 12% greater erosion rates than NFS (Figure 3j), which can be clearly seen in the spatial map of erosion rates in Figure (4c). This can be directly related to lack of surface vegetation, leading to relatively lower amounts of biomass on SFS than NFS. Despite an alternating pattern of greater erosion rates between NFS and SFS, NFS were found consistently steeper than SFS throughout all climate types.

Differences between the hillslope gradients of NFS and SFS can be quantified with the hillslope asymmetry index, HA_{NS} calculated as $\log_{10}$ [median $slope_{North}$/median $slope_{South}$] [*Poulos et al.*, 2012]. Calculated HA_{NS} throughout the simulations also show a cyclic pattern, in-phase with the climate and vegetation cover fraction, and out-of-phase with the cyclic variations of NFS and SFS gradients (Figure 3h). Crest of the HA_{NS} cycles correspond to wet periods when NFS erode faster than SFS, and trough of the HA_{NS} cycle correspond to dry periods when SFS erode faster than NFS. HA_{NS} grows when the differences between NFS and SFS gradients increase (Figure 3

h, g) While the mean HA_{NS} values are similar, values for 40-kyr cycle run (Figure 3k) fluctuate less than that of the 100-kyr cycle run (Figure 3j).

Based on simulation results, cyclic climate forcing yielded results that more closely matched observed variations in erosion rates on opposing aspects than constant climate. For example, the differences in the 15 kyr-average erosion rates between SFS and NFS for the period 761-771 kyr were 12-13.8%, and erosion rates were 0.089 – 0.095 mm.y^{-1} for SFS and 0.080-0.084 mm.y^{-1} for NFS. The difference is slightly less than observed difference; however, simulated erosion rates are in the observed range. Cyclic climate forcing simulations showed that SFS were more sensitive to climate change than NFS. This also reflects in total vegetation-cover elasticity.

Overall, erosion rates at cyclic climate runs followed climate forcing, wet periods mainly generated denser canopy than dry cycles and less erosion rate than the uplift rate. On the other hand, dry cycles caused sparser vegetation and greater erosion rate than the uplift rate. It is also interesting to observe that channels were more active to climate forcing than hillslopes in terms of sediment export from the model domain. Hillslope erosion rates fluctuated about the uplift rate (0.08 mm ± 0.02 mm); however, the erosion rates in the channels were in a much wider range than these values (0.04 mm - 0.16 mm) (Figure 4).

5.4.3. Paleoclimate forcing

A final simulation set was based on paleoclimate proxy. Cyclic climate runs obtained in the previous step were used as an input, and run with reconstructed paleoclimate to compare with the in situ measurements. Based on paleoclimate data, 12,800 years ago climate was 35% wetter than today's climate, which would produce 338 mm of MAP at the SNWR study basin. Therefore, paleoclimate data series were forced to the cyclic climate runs at 782 and 755 kyr for 40-kyr and 100-kyr simulations, respectively. We selected the declining trend in precipitation because of general trend in regional climatology since the Last Glacial Maximum. AP time series reconstructed based on a scaling ratio from Abó Arroyo and a series of synthetically generated annual precipitation in the CHILD LEM (Figure 5a). Erosion rates for different aspects during the last 12,800-yr period were consistent with the exposure ages of estimated erosion rates on opposing hillslopes (Table 1; Figure 5b). Average erosion rates for the modeled paleoclimate reconstruction on NFS and SFS, with the 40-kyr climate periodicity initial landscape condition were 0.085 mm.y^{-1} and 0.095 mm.y^{-1} respectively, and for the 100-kyr initial condition average erosion rates are 0.084

mm.y^{-1} and 0.097 mm.y^{-1}, respectively. The differences in opposing aspect erosion rates (where SFS>NFS) were 11.7% and 15.1% for 40-kyr and 100-kyr, respectively. Based on these results, paleoclimate run on 100-kyr simulations gave results similar to observed rates than the one 40-kyr run.

5.5. Conclusions

In this chapter the role of climate fluctuations on long-term average erosion rates, morphology of opposing NFS and SFS, and hillslope asymmetry were examined for semiarid and subhumid climate conditions using an ecohydrologic landscape evolution model with an explicit solar radiation component. Three types of climate forcing were applied which were a stationary climate based on modern-day observations, cyclic climate represented by a sinusoidal function, and cyclic climate followed by reconstructed climate based on paleoclimate proxies. Model results were averaged using a 15-kyr moving time window. Then, model results were compared against field-based estimates of Holocene-averaged erosion rates over NFS and SFS.

Geomorphic response on SFS was found more sensitive to climate forcing than that on NFS. Hence, erosion rates on SFS fluctuate in a wider range than those on NFS. These fluctuations, however, were much limited under stationary climate and enhanced by the amplitude of cyclic climate forcing. The landscape evolved under a constant climate was not able to reproduce observed patterns in the estimated Holocene-averaged erosion rates. The cyclic climate regime resulted in larger differences in erosion rates, which are in the range of observed values. A more realistic climate forcing obtained from paleoclimate proxies, which reflected the prevailing climate during the last ~15 kyr, led to much closer predictions of mean annual erosion of opposing north- and south-facing slopes observations than smooth cyclic climate forcing. In all the simulations, differences in erosion rates on opposing hillslopes during the cyclic climate compensate each other during the full cycle of climate forcing. Therefore, over the long-term erosion rates on opposing hillslopes are uniform, corroborating an earlier hypothesis [*Istanbulluoglu et al*., 2008].

Interestingly, landscapes that evolved under a more realistic climate regime over the time scale of their development, yielded more realistic aspect-dependent Holocene-averaged erosion rates than the landscapes formed under stationary climate. This suggests that landscapes may carry a geomorphic signature of relict climates that partially control Holocene erosion rates. Our modeling

results suggest that while SFS may erode faster during the Holocene, NFS could have eroded at much higher rates than SFS during periods of greater humidity.

References

Anderson, R. S., S. P. Anderson, and G. E. Tucker (2013), Rock damage and regolith transport by frost: an example of climate modulation of the geomorphology of the critical zone, Earth Surf Proc Land, 38(3), 299-316, doi:10.1002/esp.3330.

Bierman, P. R., J. M. Reuter, K. Pavich, A. C. Gellis, M. W. Caffee, and J. Larsen (2005), Using cosmogenic nuclides to contrast rates of erosion and sediment yield in a semi-arid, arroyo dominated landscape, Rio Puerco Basin, New Mexico, *Earth Surf Proc Land*, *30*(8), 935-953.

Burnett, B. N., G. A. Meyer, and L. D. McFadden (2008), Aspect-related microclimatic influences on slope forms and processes, northeastern Arizona, *J Geophys Res-Earth*, *113*, F03002, doi:10.1029/2007JF000789.

Clapp, E. M., P. R. Bierman, K. K. Nichols, M. Pavich, and M. Caffee (2001), Rates of sediment supply to arroyos from upland erosion determined using *in situ* produced cosmogenic ^{10}Be and ^{26}Al, *Quaternary Res*, *55*(2), 235-245.

Collins, D. B. G., and R. L. Bras (2010), Climatic and ecological controls of equilibrium drainage density, relief, and channel concavity in dry lands, *Water Resour Res*, *46*, W04508, doi:10.1029/2009WR008615.

Connel SD, McCraw DJ. 2007. Preliminary Geologic Map of the La Joya NW Quadrangle, Socorro County, New Mexico. New Mexico Bureau of Geology and Mineral Resources: Socorro, NM.

Dethier, D. P. (2001), Pleistocene incision rates in the western United States calibrated using Lava Creek B tephra, *Geology*, *29*(9), 783-786.

Dethier, D. P., C. D. Harrington, and M. J. Aldrich (1988), Late Cenozoic rates of erosion in the western Española basin, New-Mexico: Evidence from geologic dating of erosion surfaces, *Geol Soc Am Bull*, *100*(6), 928-937.

Dunai, T. J. (2000), Scaling factors for production rates of in situ produced cosmogenic nuclides: a critical reevaluation, Earth Planet Sc Lett, 176(1), 157-169, doi:10.1016/S0012-821x(99)00310-6.

Flores-Cervantes, J. H. (2010), The coupled development of terrain and vegetation: the case of semiarid grasslands, PhD thesis, MIT, Boston, MA.

Gosz, J.R. 2012a. Bowen Ratio evapotranspiration data at the Sevilleta National Wildlife Refuge, New Mexico, 1996-1999. Albuquerque, NM: Sevilleta Long Term Ecological Research Database: SEV079. http://sev.lternet.edu/data/sev-79 (12 Jan 2014).

Gosz, J.R. 2012b. Time Domain Reflectometry at the Sevilleta National Wildlife Refuge, New Mexico, 1996-2005. Albuquerque, NM: Sevilleta Long Term Ecological Research Database: SEV078. http://sev.lternet.edu/data/sev-78 (12 Jan 2014).

Gosz, R. J., and J. R. Gosz (1996), Species interactions on the biome transition zone in New Mexico: Response of blue grama (Bouteloua gracilis) and black grama (*Bouteloua eripoda*) to fire and herbivory, *J Arid Environ*, *34*(1), 101-114, doi:10.1006/jare.1996.0096.

Gutiérrez-Jurado, H. A., E. R. Vivoni, J. B. J. Harrison, and H. Guan (2006), Ecohydrology of root zone water fluxes and soil development in complex semiarid rangelands, *Hydrol Process*, *20*(15), 3289-3316, doi:10.1002/Hyp.6333.

Gutiérrez-Jurado, H. A., E. R. Vivoni, E. Istanbulluoglu, and R. L. Bras (2007), Ecohydrological response to a geomorphically significant flood event in a semiarid catchment with contrasting ecosystems, *Geophys Res Lett*, *34*(24), L24S25, doi:10.1029/2007GL030994.

Gutiérrez-Jurado, H. A., E. R. Vivoni, C. Cikoski, J. B. J. Harrison, R. L. Bras, and E. Istanbulluoglu (2013), On the observed ecohydrologic dynamics of a semiarid basin with aspect-delimited ecosystems, *Water Resour Res*, *49*(12), 8263-8284, doi:10.1002/2013wr014364.

Hall, S. A., and W. L. Penner (2013), Stable carbon isotopes, C_3–C_4 vegetation, and 12,800 years of climate change in central New Mexico, USA, *Palaeogeography, Palaeoclimatology, Palaeoecology*, *369*, 272-281.

Istanbulluoglu, E., and R. L. Bras (2005), Vegetation-modulated landscape evolution: Effects of vegetation on landscape processes, drainage density, and topography, *J Geophys Res-Earth*, *110*, F02012, doi:10.1029/2004JF000249.

Istanbulluoglu, E., and R. L. Bras (2006), On the dynamics of soil moisture, vegetation, and erosion: Implications of climate variability and change, *Water Resour Res*, *42*, W06418, doi:10.1029/2005WR004113.

Istanbulluoglu, E., O. Yetemen, E. R. Vivoni, H. A. Gutierrez-Jurado, and R. L. Bras (2008), Eco-geomorphic implications of hillslope aspect: Inferences from analysis of landscape morphology in central New Mexico, *Geophys Res Lett*, *35*, L14403, doi:10.1029/2008GL034477.

Laio, F., A. Porporato, L. Ridolfi, and I. Rodriguez-Iturbe (2001), Plants in water-controlled ecosystems: active role in hydrologic processes and response to water stress II. Probabilistic soil moisture dynamics, *Adv Water Resour*, *24*(7), 707-723, doi:10.1016/S0309-1708(01)00005-7.

McMahon, D. R. (1998), Soil, landscape and vegetation interactions in small semi-arid drainage basin: Sevilleta National Wildlife Refuge, New Mexico, NMTech, Socorro, NM.

Menking, K. M., R. Y. Anderson, N. G. Shafike, K. H. Syed, and B. D. Allen (2004), Wetter or colder during the Last Glacial Maximum? Revisiting the pluvial lake question in southwestern North America, *Quaternary Res*, *62*(3), 280-288.

Milne, B. T., D. I. Moore, J. L. Betancourt, J. A. Fairchild-Parks, T. W. Swetnam, R. R. Parmenter, and W. T. Pockman (2003), Multidecadal drought cycles in South-central New Mexico: Patterns and consequences, in *Climate Variabililty and Ecosystem Response at Long Term Ecological Research (LTER) Sites*, edited by D. Greenland, D. Goodin and R. Smith, pp. 286-307, Oxford University Press, New York.

Moore, D.I. 2012. Meteorology data at the Sevilleta National Wildlife Refuge, New Mexico. Albuquerque, NM: Sevilleta Long Term Ecological Research Database: SEV001. http://sev.lternet.edu/data/sev-1 (12 Jan 2014).

Parsons, A. J. (1988), *Hillslope form*, Routledge, London, U. K.

Poulos, M. J., J. L. Pierce, A. N. Flores, and S. G. Benner (2012), Hillslope asymmetry maps reveal widespread, multi-scale organization, *Geophys Res Lett*, *39*, L06406, doi:10.1029/2012GL051283.

Roering, J. J., J. W. Kirchner, and W. E. Dietrich (1999), Evidence for nonlinear, diffusive sediment transport on hillslopes and implications for landscape morphology, *Water Resour Res*, *35*(3), 853-870, doi:10.1029/1998wr900090.

Small, E. E. (2005), Climatic controls on diffuse groundwater recharge in semiarid environments of the southwestern United States, *Water Resour Res*, *41*, W04012, doi:10.1029/2004WR003193.

Swift, P. N. (1993), Long-term climate variability at the Waste Isolation Pilot Plant, southeastern New Mexico, USA, *Environ Manage*, *17*(1), 83-97.

Teeri, J.A., and L.G. Stowe (1976). Climatic patterns and the distribution of C4 grasses in North America, *Oecologia*, *23*, 1–12.

Tucker, G. E., and R. L. Bras (2000), A stochastic approach to modeling the role of rainfall variability in drainage basin evolution, *Water Resour Res*, *36*(7), 1953-1964, doi:10.1029/2000WR900065.

Tucker, G. E., S. T. Lancaster, N. M. Gasparini, and R. L. Bras (2001), The Channel-Hillslope Integrated Landscape Development model (CHILD), in *Landscape Erosion and Evolution Modeling*, edited by R. S. Harmon and W. W. Doe III, pp. 349-388, Kluwer Academic, New York.

Vermeesch, P. (2007), CosmoCalc: An Excel add-in for cosmogenic nuclide calculations, *Geochemistry, Geophysics, Geosystems*, *8*(8), Q08003, doi:10.1029/2006gc001530.

Vivoni, E. R., H. A. Moreno, G. Mascaro, J. C. Rodriguez, C. J. Watts, J. Garatuza-Payan, and R. L. Scott (2008), Observed relation between evapotranspiration and soil moisture in the North American monsoon region, *Geophys Res Lett*, *35*, L22403, doi:10.1029/2008GL036001.

Wang, T., E. Istanbulluoglu, J. D. Lenters, and D.T. Scott (2009), On the role of groundwater and soil texture in the regional water balance: An Investigation in the Nebraska Sand Hills, USA, *Water Resour Res*., *45*, W10413, doi:10.1029/2009WR007733.

West, N., E. Kirby, P. Bierman, R. Slingerland, L. Ma, D. Rood, and S. Brantley (2013), Regolith production and transport at the Susquehanna Shale Hills Critical Zone Observatory, Part 2: Insights from meteoric ^{10}Be, *J Geophys Res-Earth*, *118*(3), 1877-1896, doi:10.1002/Jgrf.20121.

West, N., E. Kirby, P. Bierman, and B. A. Clarke (2014), Aspect-dependent variations in regolith creep revealed by meteoric ^{10}Be, *Geology*, *42*, 507-510, 10.1130/g35357.1.

Yetemen, O., E. Istanbulluoglu, and E. R. Vivoni (2010), The implications of geology, soils, and vegetation on landscape morphology: Inferences from semi-arid basins with complex vegetation patterns in Central New Mexico, USA, *Geomorphology*, *116*(3-4), 246-263, doi:10.1016/j.geomorph.2009.11.026.

Yetemen, O., E. Istanbulluoglu, J.H. Flores-Cervantes, E.R. Vivoni, and R.L. Bras (submitted), Modeling the ecohydrologic role of solar radiation on catchment development in semiarid ecosystems, *Water Resour Res*.

Zhou, X., E. Istanbulluoglu, and E. R. Vivoni (2013), Modeling the ecohydrological role of aspect-controlled radiation on tree-grass-shrub coexistence in a semiarid climate, *Water Resour Res*, *49*(5), 2872-2895, doi:10.1002/wrcr.20259.

TABLE

Table 1: Information about ^{36}Cl data collection including details about data location, and estimated exposure ages, denudation and erosion rates.

Sample	Latitude	Longitude	Elevation (ft)	Type	Exposure Ages (kyr)	Denudation Rate ($g.m^{-2}$)	Erosion Rate ($mm.y^{-1}$)
E	34.4066	-106.9862	5517	East-facing	15.26 ± 1.17	93.36	0.059
S1	34.4066	-106.9862	5531	South-facing	11.48 ± 0.44	123.57	0.078
N1	34.4065	-106.9862	5507	North-facing	13.56 ± 0.71	104.86	0.066
S2	34.4065	-106.9857	5510	South-facing	*	*	*
N2	34.4064	-106.9859	5514	North-facing	12.08 ± 0.43	117.51	0.074
S3	34.4063	-106.9846	5491	South-facing	8.90 ± 0.12	158.92	0.100
N3	34.4063	-106.9848	5499	North-facing	9.7 ± 0.57	145.95	0.092
S4	34.4057	-106.9804	5424	South-facing	8.92 ± 0.54	158.57	0.100
N4	34.4050	-106.9807	5394	North-facing	10.5 ± 0.61	134.95	0.085

Note: For erosion-rate calculation, quartz density is 2.65 g/cm^3, and porosity is assumed 0.4.

FIGURES

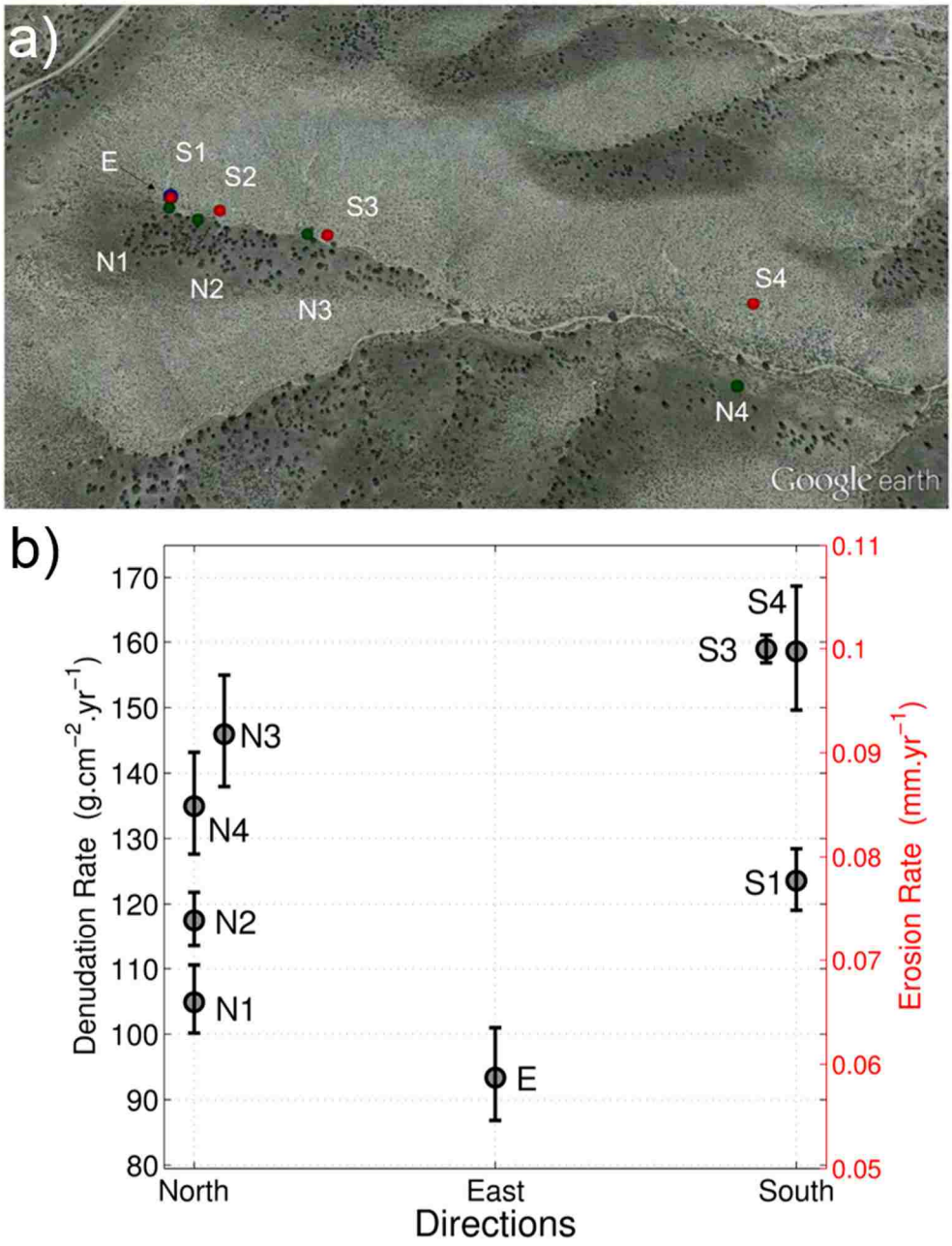

Figure 1: (a) Google earth imagery (taken at 4/Oct/2013) of the study catchment located at the SNWR and locations of paired ^{36}Cl samples on north- and south-facing slopes and on an east-facing slope. Samples from east-facing slope is represented with a green dot; north- and south-facing slopes are represented with blue and red dots (Source: Google Earth); (b) Estimated paired erosion rates with their uncertainty at opposing hillslopes.

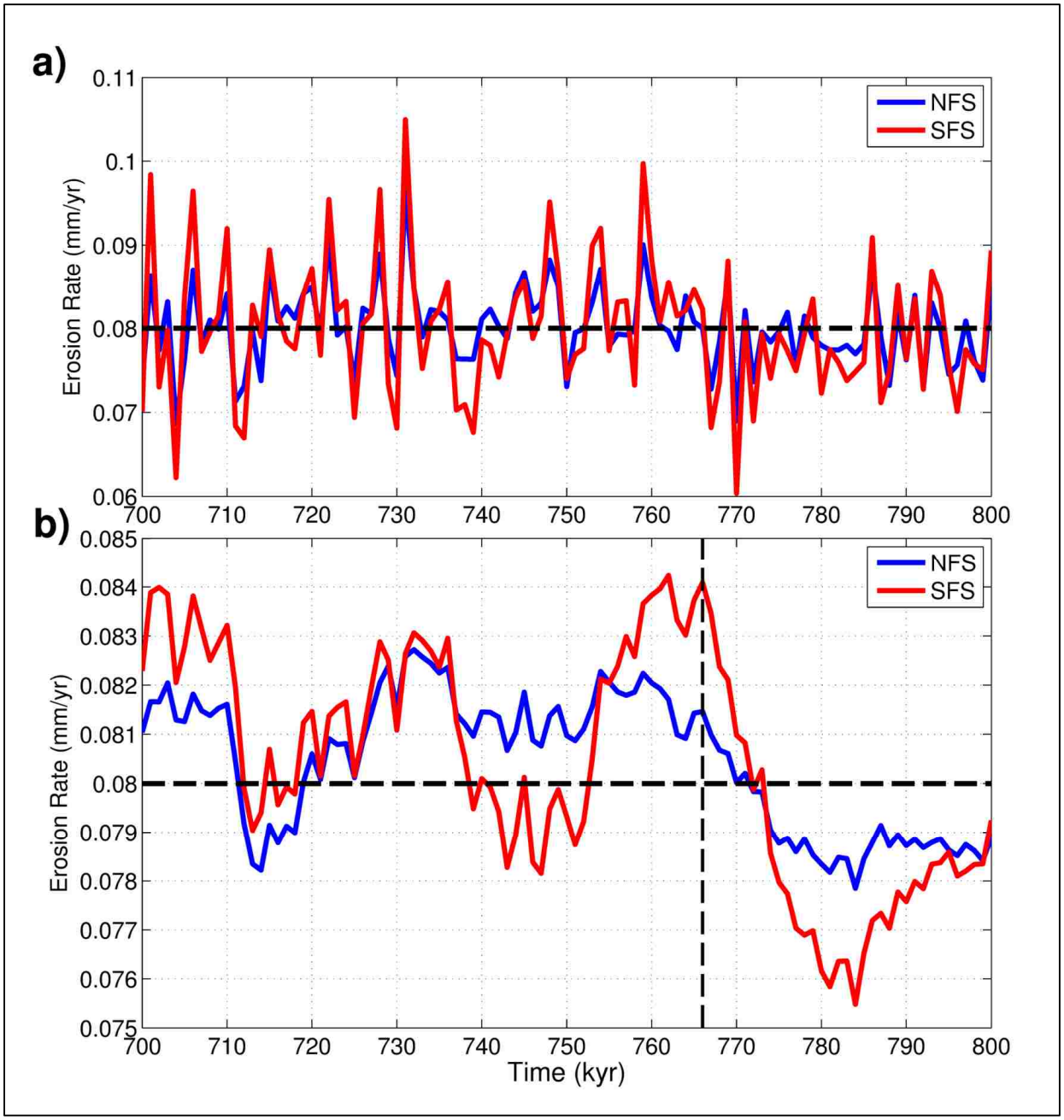

Figure 2: The CHILD model experiments driven by a stationary "modern" climate of the study site based on meteorological station data and a constant uplift rate of 0.08 mm/yr, illustrated by a horizontal dashed line; a) Mean annual landscape-scale erosion rates estimated over a moving time window of 1000 years for north- and south-facing aspects; (b) 15,000-yr moving average erosion rates for north- and south-facing aspects; the vertical dashed line at year=766 represents the time frame used in Figure 5b for comparing with other simulations and field measurements.

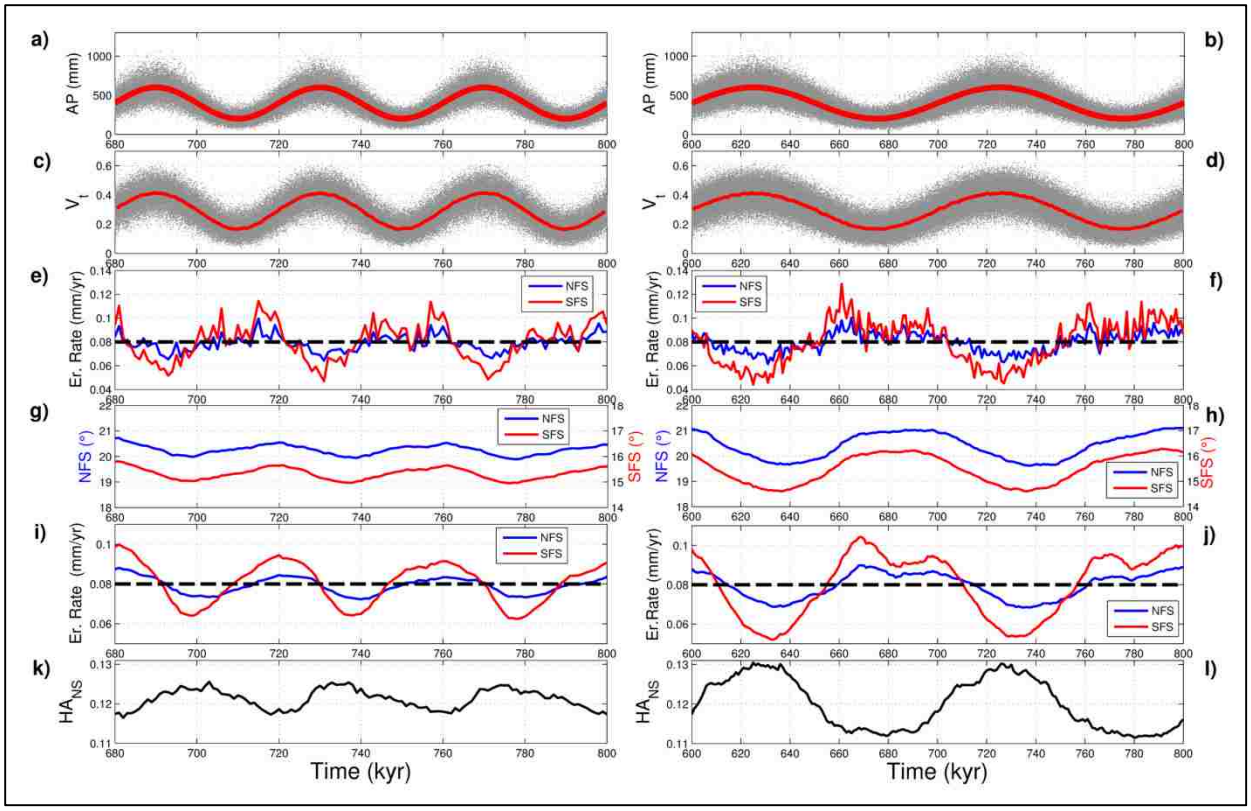

Figure 3: Sample outputs from the CHILD LEM experiments driven by cyclic climate of annual precipitation (AP) illustrating Pleistocene-like climate fluctuations at the study site. Grey dots represent the simulated annual precipitation (AP) for the last (a) 120-kyr of a climate of 40-kyr periodicity, and (b) 200-kyr of a climate of 100-kyr periodicity. For the climate periodicity reported in (a) and (b), plotted variables are: annual average of the total vegetation cover (V_t) in (c) and (d); 1 kyr-average erosion rates in (e) and (f); mean slopes of opposing NFS and SFS slopes in (g) and (h); 15 kyr-average erosion rates for opposing slopes (i) and (j); and north-to-south hillslope asymmetry (HA_{NS}) in (k) and (l), respectively.

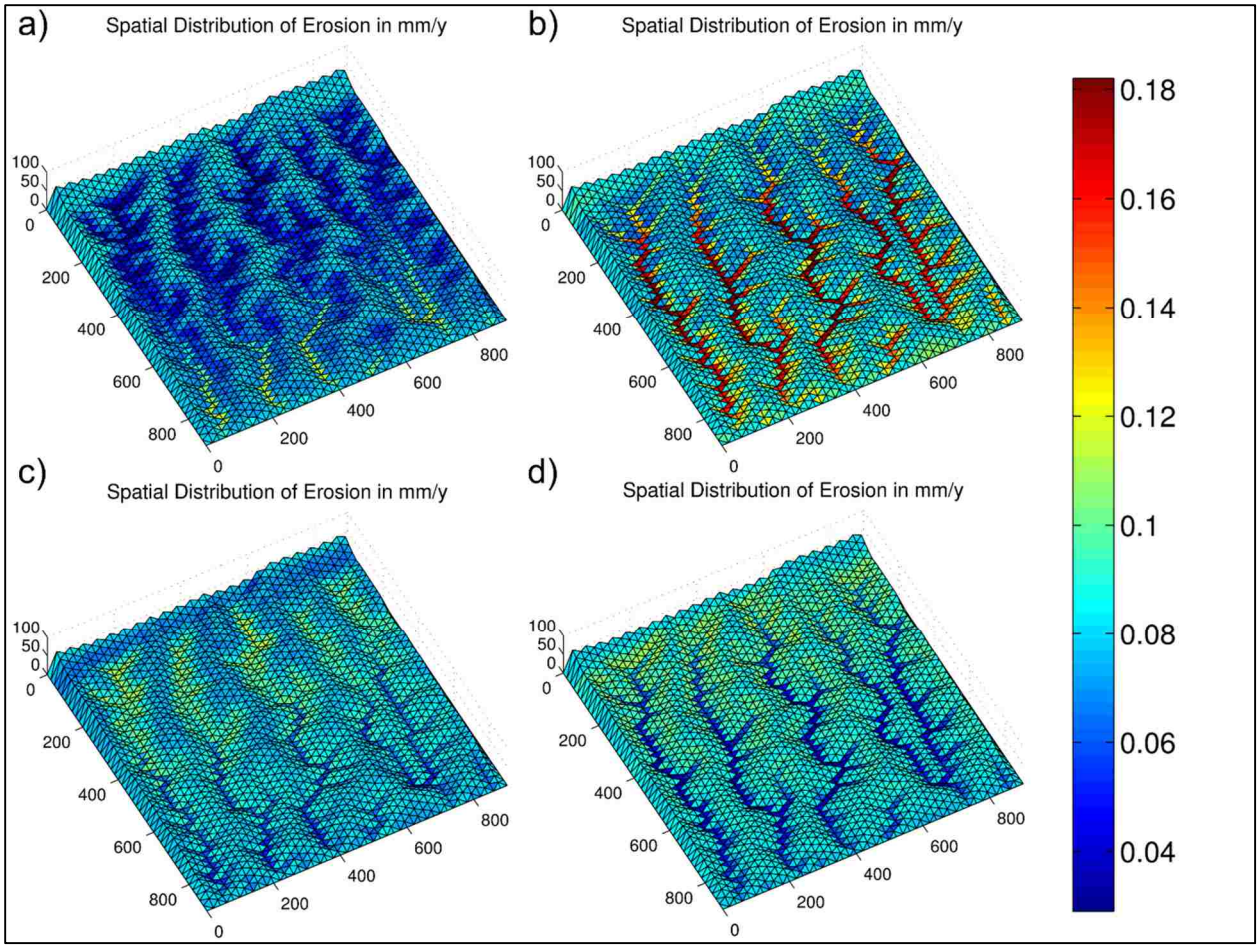

Figure 4: The spatial maps of simulated 15-kyr average erosion rates at 725 kyr (a), 750 kyr (b), 775 kyr (c), and 800 kyr (d) forced with a cyclic climate with 100-kyr cycles. The color bar represents the erosion rates in mm/yr. Warm colors represent higher erosion rates, and cold colors represent lower erosion rates. Corresponding spatial mean 15-kyr erosion rates from (a) to (d) are 0.095 mm/yr, 0.086 mm/yr, 0.071 mm/yr, and 0.068 mm/yr, respectively.

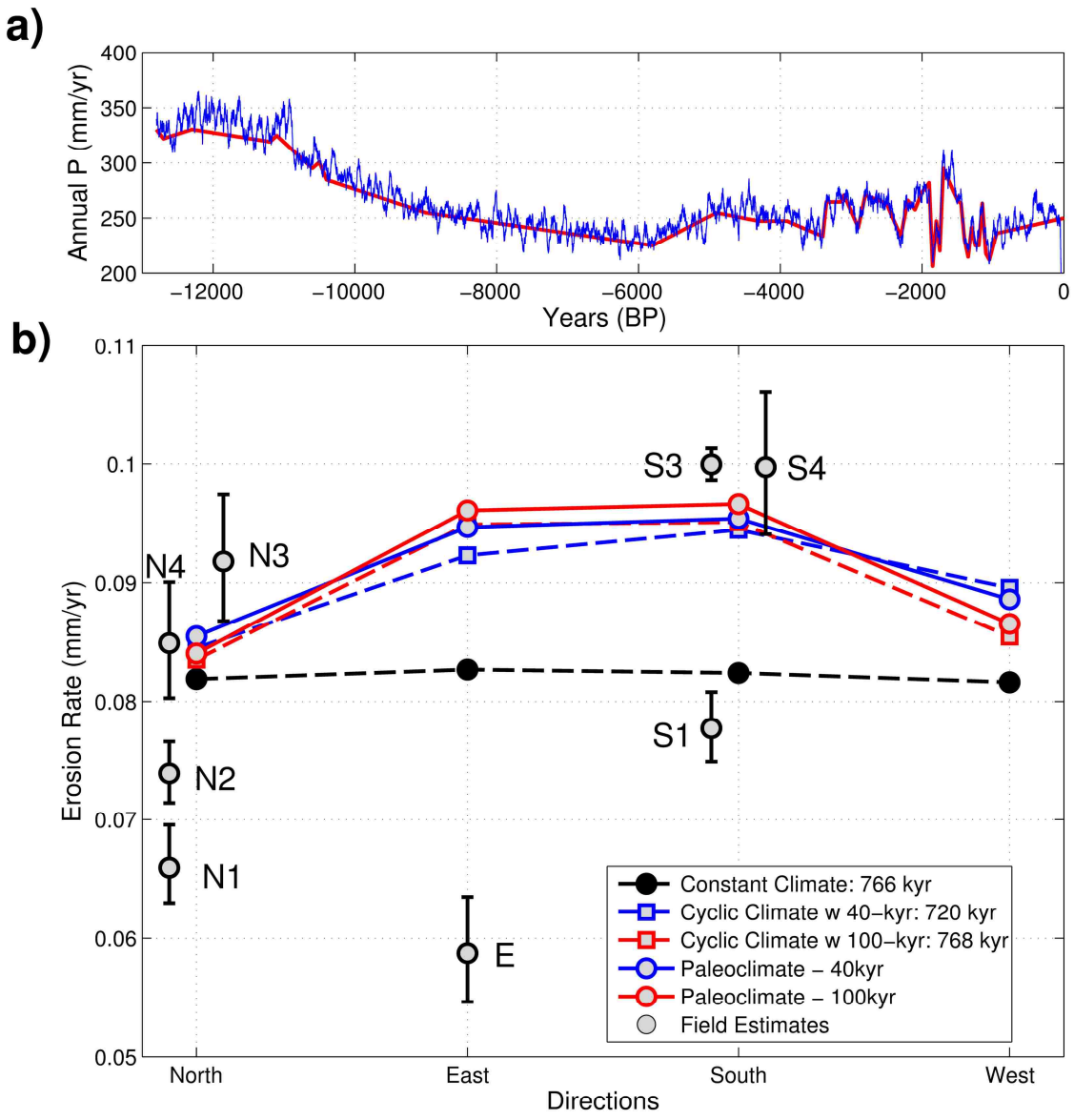

Figure 5: (a) Reconstructed paleoclimate MAP forcing, and synthetically generated annual precipitation in CHILD model; (b) modeled and ^{36}Cl-estimated erosion rates with their uncertainty for the Holocene ~ 12.5 kyr.